NUMERICAL AND EXPERIMENTAL INVESTIGATIONS FOR ELECTROMAGNETIC CRIMPING AND WELDING OF MULTI-MATERIAL TUBULAR COMPONENTS

A Thesis Submitted in Partial Fulfillment of the Requirements for the Degree of

DOCTOR OF PHILOSOPHY

Submitted by

Deepak Kumar

(Roll No. 176103003)

Under the supervision of

Dr. Arup Nandy

DEPARTMENT OF MECHANICAL ENGINEERING
INDIAN INSTITUTE OF TECHNOLOGY GUWAHATI,
GUWAHATI - 781039, ASSAM, INDIA.

FEBRUARY 2023

Dedicated to

My parents

Shreemati Premlata Devi,

Shree Birendra Kumar Roy

for always showing their **SUPPORT** and **LOVE** with enormous **PATIENCE**

DEPARTMENT OF MECHANICAL ENGINEERING
INDIAN INSTITUTE OF TECHNOLOGY GUWAHATI
GUWAHATI 781039, ASSAM, INDIA

DECLARATION

It is declared that the information presented in the dissertation "**Numerical and Experimental Investigations for Electromagnetic Crimping and Welding of Multi-Material Tubular Components**" is entirely my own account of the research performed under the guidance of **Dr. Arup Nandy**. Any part of this work has not earlier been submitted for the award of any degree, diploma, associate-ship, fellowship or its equivalent to any University or Institution. I have not violated any copyright and plagiarism law. All text and figures are my own.

Date: 08/02/2023

Deepak Kumar

Deepak Kumar
Roll No. 176103003
Department of Mechanical Engineering
Indian Institute of Technology Guwahati,
Guwahati-781039, Assam,
India.

DEPARTMENT OF MECHANICAL ENGINEERING
INDIAN INSTITUTE OF TECHNOLOGY GUWAHATI
GUWAHATI 781039, ASSAM, INDIA

CERTIFICATE

It is certified that the work contained in this thesis entitled "**Numerical and Experimental Investigations for Electromagnetic Crimping and Welding of Multi-Material Tubular Components**" submitted by **Mr. Deepak Kumar to** the Indian Institute of Technology Guwahati for the award of the degree of Doctor of Philosophy has been carried out under our supervision in the Department of Mechanical Engineering, Indian Institute of Technology Guwahati. This work has not been submitted elsewhere for the award of any other degree or diploma.

Date:

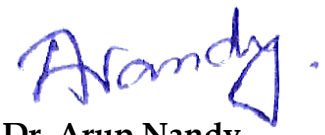

Dr. Arup Nandy
Assistant Professor-
Department of Mechanical Engineering,
Indian Institute of Technology Guwahati,
Guwahati- 781039, Assam,
India.

Acknowledgements

It is a pleasure to express my thanks wholeheartedly to everyone who contributed to making my doctoral research work achievable. Before presenting my research work, I would like to take the opportunity to humbly acknowledge all of them for their constant support and guidance.

First and foremost, I would like to express my sincere gratitude to my supervisor Dr. Arup Nandy for his support and guidance during my PhD. His constant motivation and strong work ethic have been an instruction manual for my PhD. His patience and belief in me have made this PhD journey possible. His excellent organization, planning and management skills taught me a lot and I feel fortunate to have him as my thesis mentor. Special thanks to Prof. Sachin D. Kore for showing tremendous confidence in me and guiding me throughout my PhD journey. I shall always be indebted to him. I would like to appreciate all his contributions, time and ideas to make my doctoral research productive and stimulating.

I would like to thank my doctoral committee members, Prof. Rajiv Tiwari, Prof. Pankaj Biswas and Prof. Sisir Nayak, for their valuable suggestions and encouragement during the period of my research work.

I also like to express my heartful gratitude to the Director, all Deans, and other management of IIT Guwahati, whose collective efforts have made this institute a place for world-class studies and education. I am grateful to the HODs of Mechanical Engineering, Prof S. K. Dwivedy, Prof. S. Senthilvelan and Prof. K. S. R. Krishna Murthy, for extending various facilities during the tenure of my doctoral program. I sincerely thank all members of the central workshop and mechanical department office staff for their help in conducting my experimental work and official requisite.

I am thankful to my seniors, Dr. Sagar Pawar, Dr. Avinish Tiwari, Dr. Chandrahas Patel, Dr. J. K Doley, Dr. Ashish Rajak, Dr. Ramesh Kumar, and Dr. Getu Tilahun Areda for stimulating discussions and motivating to overcome any problems either in work and otherwise. The PhD would have been impossible without my two dear friends and companion, Mr. Gyan Ranjan and Ms. Priyanka Deka. I also sincerely thank my lab mates Mr. Sanjay Raj, Mr. Pradeep Pankaj, Mr. L N Dhara, Mr. Avinash Chetry, Mr. Durgarao, Mr. Dhiraj Bombarde for brotherhood and all the fun we had.

Most importantly, none of this would have been possible without the love and patience of my family. I would like to thank my parents, Mr. Birendra Kumar Roy (Papa) and Mrs. Premlata Devi (Maa), for their unconditional love, support, and encouragement during my research work.

This thesis has become a reality with the kind support and help of many individuals, I would like to extend my sincere thanks to all of them.

Finally, I bow my head to God almighty in most profound gratitude and seek blessings.

February 2022 **Deepak Kumar**

Abstract

Multi-material components have become necessities of the present time because of their ability to offer benefits of properties of multiple materials such as corrosion-resistant, lightweight, higher strength, and electrical conductivity in one single component. Joining multi-material combinations such as Cu-SS, Cu-Al, Al-Steel, and D9-SS 316LN by conventional fusion welding techniques is difficult due to the difference in their mechanical and physical properties, causing hot cracking; therefore, electromagnetic joining (EMJ), which is based on cold forming can be a viable alternative to conventional fusion welding processes. EMJ offers many advantages in the efficient manufacturing of multi-material components, yet it has not been widely adopted in industries. Therefore, this thesis aims to expand upon various forms of the EMJ process for tubular components to expedite its adaptation.

An improved interference-fit multi-material Cu-SS tube-to-tube joint is produced using electromagnetic crimping (EMC) as an alternative to electromagnetic welding (EMW), which requires heavy investments in the form of large capacitor banks. Joints with strength higher than the base Cu tube failure strength are achieved in the case of threaded and knurled surfaced joints without any metallic bond formation.

A coupled multi-step FEM model is developed to replicate the experimental investigation or predict the strength of the smooth-surfaced Cu-SS tube-to-tube joint. The model produces results of strength tests of the EMC crimped joint within an error range of 5-7 %. The obtained results are further investigated by a detailed experimental and numerical analysis of threaded surfaced joints. Threaded surfaced joints are studied by varying the thread pitch, thread angle and discharge energy, and it is observed that in this case, optimum results are obtained with the thread having 60° thread angle and 1 mm thread pitch. The developed multi-step non-coupled FEM model produces pull-out strength results within an error range of 2-9 %. The FEM model is further simplified by fitting into an empirical relationship.

Furthermore, a novel hybrid joining technique has been developed to overcome the shortcomings of the EMC tube-to-tube joint by combining the EMC process with adhesive joining named as electromagnetically assisted adhesive joining (EAAJ). A comparative experimental investigation is performed between the smooth surfaced EAAJ and EMC

Cu-SS tube-to-tube joint. An increment in pull-out and compressive strength by 2 to 3 times is observed, along with an improvement in leak tightness by 1000 times in the case of the EAAJ joint compared to EMC joint. Statistical Analysis is also performed to study the relative effect of various parameters. A detailed experimental investigation further optimises the EAAJ process, and the effect of various process parameters on the joint strength and leak tightness is studied.

The discussed work proposes a tubular joint with high strength and leak tightness. However, if higher grades of leak tightness are required (for example, for nuclear applications), which can not be obtained from the EAAJ process, then the electromagnetic welding (EMW) process which is based on high-velocity EMF to create a metallic bond, can be recommended. Therefore, a detailed experimental and numerical investigation has been performed to further widen the understanding of the EMW. An SPH-based FEM model is developed for D9 tube-to-SS 316 LN end plug joining EMW. To find the weldability window, SPH simulations are performed for different contact angles and contact velocity, considering waviness formation as the weldability criteria. The effect of contact angle and contact velocity on amplitude and wavelength of waviness morphology is also studied. The taper angle of 8° and impact velocity of 500 m/s is observed to be optimum.

This current work has traversed through different horizons of EMJ for creating tubular joints. Depending upon resource availability and different application requirements (joint strength and leak tightness), the process can be chosen among EMC, EMW and EAAJ. The current work further explains the effect of various process parameters on these three techniques; various numerical models are developed, which have been validated with experimental results; In a nutshell, a better understanding of the relative standings of these techniques is obtained.

Keywords: Electromagnetic forming; Electromagnetic Crimping; Electromagnetically assisted adhesive joining; Electromagnetic welding; tube-to-tube; tube-to-end plug; Strength prediction; SPH; Finite Element Analysis;

List of Abbreviations and Symbols

Abbreviations

CMF	Conventional metal forming
HERF	High energy rate forming
EXF	Explosive forming
EHF	Electrohydraulic forming
EMF	Electromagnetic forming
EMC	Electromagnetic crimping
EMW	Electromagnetic welding
EMJ	Electromagnetic Joining
AJ	Adhesive joining
FEM	Finite element method
BEM	Boundary element method
J-C	Johnson-Cook
UTM	Universal testing machine
EMCT3	Electromagnetically crimped threaded surfaced tube-to-tube
EAAJ	Electromagnetically assisted adhesive joining
OM	Optical microscope
SEM	Scanning electron microscope
EDX	Electron discharge spectroscopy
SPH	Smooth particle hydrodynamics
EOS	Equation of state

Latin symbols

A	Johnson-Cook coefficient (Material constants- governing strength)
A_1	Surface area of the contact zone
B	Johnson-Cook coefficient (Material constants-pre-exponential factor)
B_m	Magnetic field density
C	Johnson-Cook coefficient (Material constants- strain rate factor)
C_C	Capacitance of the circuit
D_i	Internal diameter
D_e	External diameter
e	Euler number
E	Charging energy
F	Lorentz force
F_1	Strength of an interference-fit joint
H	Magnetic field intensity
T	Temperature
$I\ (t)$	Flowing current
J	Total current density
Js	Source current density
k	Electrical conductivity
l	Coil length
L	Inductance of the circuit
L_i	Internal inductance
L_{res}	Resultant inductance
M	Mutual inductance
n	Strain hardening coefficient
N	Number of turns
P	Magnetic pressure
P_1	Pressure
p	Interference stress
p_f	Maximum pressure
Q	Ratio of the inner and outer diameter
rw	Radius of the workpiece

R	Inner radius of the flyer tube
R_i	Resistance of the circuit
R_{res}	Aggregate resistance
s	thickness of the flyer
Tm	Melting temperature
Tr	Room temperature
U	Discharge voltage

Greek Symbols

δ	Damping coefficient
δ_s.	Skin depth
σ	Electrical conductivity
μ	Magnetic permeability in vacuum
μr	Relative permeability
μ_1	Friction coefficient
ω	Current frequency
ω_0	Un-damped frequency
λ	Wavelength
θ	Diffraction angle
σ	Stress
σ_f	Yield strength
a	Thermal coefficient
ε	Plastic strain
$\dot{\varepsilon}$	Plastic strain rate
εe	Electrical permittivity
ρ	Total charge density
ϑ	Poison's ratio

Contents

Acknowledgements ..... **vii**

Abstract ..... **ix**

List of Abbreviations and Symbols ..... **xi**

Contents ..... **xv**

List of Figures ..... **xxiii**

List of Tables ..... **xxxv**

1 Introduction **1**

1.1 Conventional Metal Forming Process 1

1.2 High Energy Rate Forming Process 1

1.2.1 Explosive Forming 2

1.2.2 Electrohydraulic Forming 3

1.2.3 Electromagnetic Forming 3

1.2.3.1 Principles of EMF 4

1.2.3.2 Types of EMF Process 7

1.2.3.3 Advantages and Limitations of EMF Process 8

2 Literature Review **11**

2.1 Introduction 11

2.2. Electromagnetic crimping 14

2.2.1. Interference-fit joining (EMC) 16

2.2.1.1 Factors affecting interference-fit joining (EMC) 17

2.2.2 Form-Fit Joining (EMC) 22

2.2.2.1 Factors affecting form-fit joining (EMC) 23

2.3 Electromagnetic welding 26

2.3.1 Factors affecting the EMW process 27

2.4 Hybrid joining 29

2.5 Motivation 30
2.6 Objectives of Work 31
2.4 Novelty of the Work 31
2.7 Structure of Thesis 32
3 Experimental Investigation of Electromagnetic Crimping 35
3.1 Introduction 35
3.2 Experimental and testing procedures 35
3.2.1 Experimental setup 35
3.2.2 Tube geometry and material compositions 37
3.2.3 Destructive testing for joint quality evaluation 38
3.2.3.1 Pull-out test 38
3.2.3.2 Torsion test 39
3.2.3.3 Compression test 40
3.2.3.4 Sample preparation for characterisation of EMC crimped joints 40
3.3 Results and discussion 41
3.3.1 Mechanical Pull-out testing 41
3.3.2 Compression test 45
3.3.3 Torsion test 47
3.3.4 Macrostructural and deformation analysis 51
3.3.5 Interface analysis 54
3.3.6 Micro-hardness test 56
3.3.7 Surface Roughness 57
3.4 Conclusions 59
4 Finite Element Modelling of Smooth-Surfaced EMC Joints 61
4.1 Introduction 61
4.2 Methodology 61
4.2.1 Process parameters 61

4.2.2 Finite Element Modelling 62
4.3 Results and discussion 65
4.3.1 Effect of discharge energy 66
4.3.1.1 Magnetic field 66
4.3.1.2 Radial displacement 66
4.3.1.3 Impact velocity 66
4.3.1.4 Effective plastic strain 67
4.3.2 Effect of field shaper slit 68
4.3.3 Outer diameter and thickness 71
4.3.4 Strength prediction and validation of predicted results 74
4.4 Conclusions 77
5 Electromagnetic Crimping on Threaded Surface 79
5.1 Introduction 79
5.2 Methodology 80
5.2.1 Process parameters 80
5.2.2 Sample preparation for characterisation of EMCT3 joints 81
5.2.3 Numerical simulation for destructive testing 81
5.2.3.1 Electromagnetic analysis using ANSYS Maxwell 82
5.2.3.2 Structural deformation analysis using ANSYS Explicit Dynamics 83
5.2.3.3 Strength prediction for EMCT3 joints 84
5.3 Results and Discussion 85
5.3.1 Experimental validation of FEM simulation for predicting deformation and strength of EMCT3 joint 87
5.3.1.1 Deformation analysis for EMCT3 joint 87
5.3.1.2 Experimental validation of deformation analysis of EMCT3 joint 88
5.3.1.3 Strength prediction, along with experimental validation of EMCT3 joint 90
5.3.1.4 Expressing the effect of pitch and discharge energy on deformation and strength of EMCT3 joint in empirical relations 95

Deriving Empirical relations from experimental data of deformation 95

Validation of the obtained empirical relation with simulation 97

Deriving Empirical relations from experimental data of pull-out strength 98

5.3.1.5 Effect of thread angle on deformation height (***hc***) 100

5.3.1.6 ANOVA analysis to address the relative contribution of different process parameters on the pull-out strength of the EMCT3 joint 103

5.4 Conclusions 105

6 Electromagnetically Assisted Adhesive Joining (EAAJ) 107

6.1 Introduction 107

6.2 Working Principle 109

6.3 Materials and Methods 111

6.3.1. Formation of the electromagnetically assisted adhesive tube-to-tube joining between Cu and SS tubes 111

6.3.1.1 Geometry and Materials of the Constituent Cu and SS tubes and Loctite 638 adhesives 111

6.3.1.2 Experimental Set up for the formation of joint 112

6.3.1.3 Preparation of Surface and Application of adhesives 113

6.3.1.4 Other process parameters 113

6.3.2 Experimental analysis of strength, hardness and leak-tightness for the electromagnetically assisted adhesive tube-to-tube joint 114

6.3.2.1 Strength testing: (i) pull-out test, (ii) compression test, microhardness and deformation analysis 114

6.3.2.2 Leak testing setup 114

6.4 Results and Discussion 115

6.4.1 Pull-out testing results 116

6.4.1.1 Pull-out load variation and failure mode analysis 116

6.4.1.2 Statistical analysis 117

6.4.2 Compression testing results 119

6.4.2.1 Compressive load variation and failure mode analysis 119
4.2.2 Statistical analysis 120
6.4.4 Deformation analysis 121
6.4.3 Micro-hardness analysis 124
6.4.5 Leak test results 125
6.5. Conclusions 127
7 Effect of Process Parameters on the Joint Strength and Leak Tightness in EAAJ 129
7.1 Introduction 129
7.2 Preparation of Electromagnetically Assisted Adhesive Cu-Ss Tube-To-Tube Joining Process 129
7.2.1 Tube and adhesive materials 129
7.2.2 Process parameters 131
7.2.3 Experimental procedure 133
7.2.3.1 Surface preparation 133
7.2.3.2 Adhesive application 134
7.2.4 Testing methods 134
7.2.4.1 Mechanical pull-out testing 134
7.2.4.2 Leak test 134
7.2.3 Characterisation of the hybrid joint 136
7.3 Results and Discussions 136
7.3.1 Mechanical pull-out test and compression test 136
7.3.1.1 Effect of adhesive application length 138
7.3.1.2 Failure mode 139
7.3.1.3 Effect of discharge energy 141
7.3.1.4 Effect of curing time 142
7.3.1.5 Statistical analysis of pull-out test results 143
7.3.2 Leak test 146
7.3.2.1 Effect of discharge energy 146

7.3.2.2 Effect of adhesive application length 146

7.3.2.3 Effect of curing time..... 147

7.2.4 Statistical analysis 148

7.2.5 Microhardness analysis.....149

7.2.6 Deformation analysis 150

7.3 Conclusions..... 152

8 Electromagnetic Welding of D9 Steel Tube to SS316LN End Plug 155

8.1 Introduction 155

8.2 Numerical Simulation Setup with Finite Element Lagrangian Model and Smoothed Particle Hydrodynamics (SPH)..... 156

8.2.1 Electromagnetic analysis using ANSYS Maxwell 157

8.2.2 Structural deformation analysis using ANSYS Explicit Dynamics 159

8.2.3 Fluid dynamics modelling of Welding morphology using Smoothed Particle Hydrodynamics in ANSYS Autodyne.....161

8.3 Experimental setup 162

8.4 Results and discussions..... 166

8.4.1 Lagrangian Finite element model.....166

8.4.2 Experimental validation of Lagrangian simulation model.....166

8.4.3 SPH results along with experimental validation.....167

8.4.4 Hydraulic burst test.....174

8.4.5 Micro-hardness test 175

8.4.6 X-ray computer tomography.....175

8.4.7 Optical micrography and Scanning electron microscopy 177

8.5 Conclusions..... 179

9 Conclusions and Scope of Future Work 181

9.1 Conclusions..... 181

9.2 Scope of Future work 183

List of Publications.....185

International Journals 185

Book Chapters 186

Presentations / Conference attended 186

References 189

List of Figures

Fig. 1.1	Explosive forming	3
Fig. 1.2	Electrohydraulic forming	3
Fig. 1.3	Electromagnetic forming of the tube	4
Fig. 1.4	Equivalent circuit diagrams: (a) detailed version and (b) reduced version [12]	4
Fig. 1.5	Various types of the coil for the pulsed electromagnetic forming method [12]	8
Fig. 2.1	Sample assemblies joined by electromagnetic welding a) Boeing 777 torque tube, b) 4" drive shaft, for Ford, and c) high voltage fuse [25]	11
Fig. 2.2	Components of automotive sector obtained with :(a) drive shaft (Al/steel joint), (b) fuel filter (Al/Al joint), (c) automotive A/C receiver-dryer, (d) automotive earth connector [26]	11
Fig. 2.3	(a) aircraft flight torque tubes [27], (b) aircraft flight control tubes in use [28]	12
Fig. 2.4	(a) Electromagnetically crimped driveshafts; (b) demonstrator space frame [31]	12
Fig. 2.5	Examples of applications for EMJ joints. (a) Lightweight frame structure, (b) driveshaft with a welded (left) and a crimped (right) joint manufactured and (c) oil expansion vessel sealed by a compressed aluminium ring [32]	13
Fig. 2.6	(a) Al/steel crimped tube for instrumental panel beam (b) crimped air suspension, (c) crimped drive shaft [33].	13
Fig. 2.7	Schematic diagram for EMC	15
Fig. 2.8	Mechanism of interference-fit joining by compression: (a) Initial positioning, (b) plastic deformation of the outer and elastic deformation of the inner tube and (c) elastic recovery leading to interference pressure build-up	17
Fig. 2.9	Joint strength (pull-out load) in a tube-to-rod joint with different target workpiece (rod) materials [57]	19

Fig. 2.10	Tube-to-hollow shaft joining by EMC (compression) (a) without supporting shaft and (b) with supporting shaft [64]	20
Fig. 2.11	Example of some of the mandrel surfaces. Left to right: coarse knurl, fine knurl, fine screw thread with axial grooves, and coarse screw thread [52]	21
Fig. 2.12	Form-fit joint produced with (a) minimum discharge energy required to fill the groove and (b) higher discharge energy [32]	22
Fig. 2.13	Geometrical design parameter for the groove of a form-fit joint [53]	23
Fig. 2.14	Radioscopic picture showing the angle *a* at the groove edge with different groove shapes [32]	24
Fig. 2.15	Distribution of stress in a double-grooved form-fit joint under tensile load [77]	25
Fig. 3.1	Schematic diagram showing the dimensions of various parts in EMC setup	36
Fig. 3.2	Current waveform with time in the solenoid coil at five different discharge energy values	36
Fig. 3.3	Model representation of the stainless-steel inner tube having (a) Threaded, (b) Knurled, and (c) Smooth surface profile	37
Fig. 3.4	(a) Experimental setup of pull-out/compression test, (b) schematic diagram of pull-out test for Cu-SS tubular joint and (c) metal plug used in the pull-out test	39
Fig. 3.5	Schematic diagram of a free-end sample for the torsion test	39
Fig. 3.6	Schematic diagram of the torsion test setup for SS-Cu-SS free-end type tubular joint	40
Fig. 3.7	Schematic of (a) cutting pattern for a joined sample and (b) obtained sample for characterisation of the joint	41
Fig. 3.8	Crimped samples for three different surface profiles prepared at 6.2 kJ of different discharge energy levels	41
Fig. 3.9	Separation failure (Joint failure) in (a) threaded, (b) knurled and (c) smooth-surfaced sample	42
Fig. 3.10	Crack failure (Tube failure) in (a) threaded and (b) knurled surfaced samples due to weaker tube (copper) failure	43
Fig. 3.11	Variation of maximum pull-out load with discharge energy for three different surface profiled samples	44

Fig. 3.12	Pull-out load-extension plot at six different discharge energies for (a) threaded, (b) knurled and (c) smooth-surfaced samples	44
Fig. 3.13	Sliding failure during compression test in (a) Threaded-surfaced sample at 4.4 kJ, (b) Knurled surfaced sample at 5.5 kJ and (c) Smooth-surfaced sample at 6.2 kJ of discharge energy	46
Fig. 3.14	Buckling failure in a threaded-surfaced sample at discharge energy of 5.0 kJ	46
Fig. 3.15	Variation of maximum compressive load with discharge energy for three different surface profiled samples	46
Fig. 3.16	Load-extension curve obtained during compression test for threaded, knurled and smooth-surfaced samples prepared at discharge energy of 5.5 kJ	47
Fig. 3.17	Sliding failure in (a) threaded and (b) smooth-surfaced SS-Cu-SS fixed-end type joint prepared at 6.2 kJ of discharge energy	48
Fig. 3.18	Failure due to buckling of parent copper tube followed by crack propagation for the knurled-surfaced sample prepared at 6.2 kJ of discharge energy	49
Fig. 3.19	Failure due to buckling in parent copper without any crack for the knurled-surfaced sample prepared at 5.0 kJ of discharge energy	49
Fig. 3.20	Variation of maximum torque with discharge energy for three different surface profiled samples	50
Fig. 3.21	Torque-twisting angle plot for threaded, knurled and smooth-surfaced fixed-end type sample prepared at 6.2 kJ of discharge energy	50
Fig. 3.22	Variation of the outer diameter of the tubular joint with discharge energy for threaded, knurled and smooth-surfaced samples after crimping	52
Fig. 3.23	Variation of the thickness of the outer (copper) tube after crimping in the crimping zone with discharge energy for threaded, knurled and smooth-surfaced sample	52
Fig. 3.24	Higher magnification (400×) macrographic image of Cu-SS tubular joint interface prepared at 6.2 kJ of discharge energy for (a) threaded (crest side), (b) threaded (root side), (c) knurled and (d) smooth-surfaced sample	53

Fig. 3.25	Higher magnification (400×) macrographic image profile of Cu-SS tubular joint cross-section prepared at 6.2 kJ for (a) threaded, (b) knurled and (c) smooth-surfaced sample	53
Fig. 3.26	Microstructural image of the threaded-surfaced sample at 500× magnification on (a) crest side and (b) root side	54
Fig. 3.27	Microstructural image of the knurled-surfaced sample at 6.2 kJ of discharge energy at (a) 500× and (b) 100× magnification	55
Fig. 3.28	Microstructural image of the smooth-surfaced sample at 6.2 kJ of discharge energy at (a) 500 and (b) 100× magnification	55
Fig. 3.29	EDS elemental mapping demonstrating (a) Cu-Fe distribution, (b) Cu distribution and (c) Fe distribution at the Cu-SS interface of a smooth-surfaced sample prepared at 6.2 kJ of discharge energy	56
Fig. 3.30	Vicker's micro-hardness variation for 6.2 kJ of discharge energy across the cross-section of Cu-SS tubular joint interface using a load of 100 gm and a dwell time of 20 s	57
Fig. 3.31	Variation of micro-hardness for the copper tube at 200 µm from the interface in the crimping zone with discharge energy for threaded, knurled and smooth-surfaced sample	57
Fig. 3.32	3D fringe pattern for (a) threaded, (b) knurled and (c) smooth-surfaced sample prepared at 6.2 kJ of discharge energy	59
Fig. 4.1	Flow chart of the coupled simulation in LS Dyna	62
Fig. 4.2	Sectional view of the simulation model showing meshing of parts for electromagnetic and mechanical analysis	63
Fig. 4.3	Deformation stages of EMC crimped joint at three different times at 5.5 kJ of discharge energy observed in the simulation model	65
Fig. 4.4	Variation of (a) impact velocity and (b) effective plastic strain with time for different mesh sizes at 3.9 kJ of discharge energy during simulation	65
Fig. 4.5	Selected nodes for measurement of parameters in the coupled simulation model	66
Fig. 4.6	Variation of (a) magnetic field, (b) displacement, (c) velocity and (d) effective plastic strain in the outer tube with time in the crimping zone in the coupled simulation model	67

Fig. 4.7	Effective plastic strain variation along the axis of the outer tube in the crimping zone at 5.5 kJ of discharge energy in the coupled simulation model	68
Fig. 4.8	Distribution of Lorentz force vector in the outer tube along the circumference in the crimping zone in the simulation at 5.5 kJ of discharge energy	69
Fig. 4.9	Distribution of Lorentz force vector in the outer tube along the axis of the outer tube in the crimping zone in the simulation at 5.5 kJ of discharge energy	69
Fig. 4.10	Variation of the effective plastic strain of the outer tube in the slit region along the circumference in the simulation at 5.5 kJ of discharge energy	70
Fig. 4.11	Uneven radial deformation of the copper tube in the region near and opposite to the field shaper slit along with the circumference in (a) experiment (b) simulation at 5.5 kJ of discharge energy	70
Fig. 4.12	Comparison of radial deformation of the electromagnetically crimped sample in the simulation and experiment at 5.5 kJ of discharge energy	71
Fig. 4.13	Comparison of (a) outer diameter and (b) thickness of the outer tube in the crimping zone for various discharge energy values in the case of experiment and simulation	72
Fig. 4.14	Comparison of the shape of the electromagnetically crimped sample in the simulation and experiment at 5.5 kJ of discharge energy	72
Fig. 4.15	Variation of the thickness of the outer tube along the length in the crimping zone at 5.5 kJ of discharge energy	73
Fig. 4.16	Boundary conditions applied on the EMC crimped joint in the simulation model for prediction of strength	74
Fig. 4.17	Comparison of (a) maximum pull-out load and (b) maximum compressive load at various discharge energy values for simulation and experiment	76
Fig. 4.18	Comparison of pull-out load vs extension curve at 5.5 kJ and 6.2 kJ of discharge energy for simulation and experiment	77

Fig. 4.19	Sliding failure of EMC crimped joint at 5.5 kJ of discharge energy in experiment and simulation	77
Fig. 5.1	(a) Detailed Dimensioning of various components (b) Images of ISO M10 threaded surfaced SS 304 inner tube with the various pitch size	80
Fig. 5.2	Schematic of (a) cutting pattern for a joined sample and (b) sectional views of the inner (SS) and outer (Cu) tubes	81
Fig. 5.3	Flow chart for the non-coupled multi-step simulation model	82
Fig. 5.4	Simulation model for electromagnetic field analysis (a) current curve, (b) ANSYS Maxwell model, (c) mesh cluster showing the vacuum enclosed model and (d) current density for 5.0 kJ at 15 µs showing induced current at the Cu tube surface in the middle of the crimping zone	83
Fig. 5.5	(a) 3D Cu-SS tube-to-tube assembly, (b) front sectional view of the meshed model, (c) back sectional view of the meshed model and (d) zoomed view of the meshing	84
Fig. 5.6	Representation of boundary conditions for strength prediction simulation as per experimental conditions	85
Fig. 5.7	(a) Maximum magnetic field and (b) maximum magnetic pressure variation at the time of maxima ($1.4\times10-5s$) along the axis of Cu-SS EMCT3 joint and (c) magnetic field and corresponding (d) magnetic pressure variation with time, average out over the crimping zone	87
Fig. 5.8	EMC crimped samples at 3.9 kJ of discharge energy for four different pitches (a) 0.75 mm, (b) 1 mm, (c) 1.25 mm, and (d) 1.5 mm	87
Fig. 5.9	Sectional view of simulated Cu-SS crimped sample showcasing deformation of Cu tube material in between SS threads to calculate deformation height *hc*	88
Fig. 5.10	Experiment and Simulation values of *h*c for a pitch of thread (a) 0.75mm (b) 1 mm (c) 1.25mm (d) 1.5mm	90
Fig. 5.11	Comparison of the experimentally obtained transverse cross-section of the EMCT3 joint sample with the simulated sample in the crimping zone at 4.4 kJ of discharge energy and 1 mm of pitch	90

Fig. 5.12	Comparison of radial deformation of experimentally obtained EMCT3 joint sample with the simulated sample at 4.4 kJ of discharge energy and 1 mm of pitch	91
Fig. 5.13	Comparison of experimental and simulation values of the maximum pull-out test at (a) 3.9 kJ and (b) 4.4 kJ of discharge energies for all the pitches	92
Fig. 5.14	Detachment failure mode in (a) experiment and (b) simulation for 1 mm threaded pitch for 3.9 kJ of discharge energy	92
Fig. 5.15	Crack failure mode in (a) experimental and (b) simulation for 1 mm threaded pitch for 4.4 Kj of discharge energy	92
Fig. 5.16	Pull-out load vs extension plot (experimental) at (a) 3.4 kJ, (b) 3.9 kJ and (c) 4.4 kJ of discharge energy for thread profiles of different pitch	93
Fig. 5.17	Pull-out load vs extension plot (experimental) at (a) 0.75 mm, (b) 1 mm, (c) 1.25 mm and (d) 1.5 mm of pitch for three different discharge energies	94
Fig. 5.18	Separation failure mode	94
Fig. 5.19	Crack failure mode obtained for samples at 4.4 kJ of discharge energy for the pitch of (a) 1 mm and (b) 1.25 mm	95
Fig. 5.20	Obtained solution surface through curve fitting using bisquare method	96
Fig. 5.21	Obtained solution surface through curve fitting using LAR method	97
Fig. 5.22	Deformation vs discharge energy for different pitches	98
Fig. 5.23	Deformation vs pitch of thread for different discharge energies	98
Fig. 5.24	Obtained solution surface through curve fitting using bisquare method	99
Fig. 5.25	Obtained solution surface through curve fitting using LAR method	99
Fig. 5.26	Variation of deformation height with thread angle for (a) 0.75mm, (b) 1mm, (c) 1.25mm and (d) 1.5mm of thread pitch values	101
Fig. 5.27	Comparison of maximum pull-out load results obtained from experiment and simulations for five different thread angles and at 1 mm of thread pitch at (a) 3.4 kJ and (b) 3.9 kJ and (c) 4.4 kJ of discharge energies	102

Fig. 5.28	Image showcasing (a) dependency of the axial component of the frictional force on the thread angle and (b) variation of contact length due to variation in thread angle	103
Fig. 6.1	Pictorial representation of the experimental setup demonstrating (a) the placements of various components on setup, (b) Zoomed view showing the details and (c) mechanism of EAAJ indicating the flow of adhesives	110
Fig. 6.2	The first pulse of the current waveform in the coil for three discharge energy values observed through an oscilloscope	110
Fig. 6.3	Schematic diagram showing the dimensions of various parts in the EAAJ setup	112
Fig. 6.4	Schematic diagram of the air leak test setup	113
Fig. 6.5	Cu-SS tube-to-tube joined sample at 4.4 kJ of discharge energy by (a) EAAJ and (b) EMC method	115
Fig. 6.6	(a) Pull-out load vs extension plot and (b) maximum pull-out load comparison for with and without adhesive joint at three different discharge energy values	115
Fig. 6.7	Sliding failure sample at 4.4 kJ of discharge energy for (a) EAAJ sample, (b) EMC sample	117
Fig. 6.8	(a) Compressive load vs compression plot and (b) maximum compressive load comparison plot for EAAJ and EMC joint at three different discharge energy values	119
Fig. 6.9	Sliding failure behavior being demonstrated by compression test sample (a) before the test and (b) after test	120
Fig. 6.10	Variation of (a) outer diameter and (b) thickness of copper tube with discharge energy for two processes in the working zone (for EAAJ measurements are taken in the adhesive zone)	122
Fig. 6.11	Cu-SS interface at 5.0 kJ of discharge energy for (a) EAAJ and (b) EMC	123
Fig. 6.12	Axially cut Cu-SS interface at 5.0 kJ of discharge energy for (a) EAAJ sample showcasing non-adhesive and adhesive regions, (b) EMC sample showcasing crimping zone	124
Fig. 6.13	Micro-hardness variation at 5.0 kJ of discharge energy across the interface at 100 gm load with 20 s of dwell time	125

Fig. 6.14	Variation of micro-hardness of Cu tube along the length in the working zone for both processes (EAAJ and EMC) at 5.0 kJ of discharge energy	125
Fig. 6.15	Electromagnetically assisted adhesive Cu-SS joint sample at 3.4 kJ of discharge energy for leak test	126
Fig. 7.1	Schematic diagram showing the dimensions of various parts in the EAAJ setup	132
Fig. 7.2	Three-dimensional surface topology (a) before grinding, (b) after grinding and surface roughness variation with the length (c) before grinding, (d) after grinding	134
Fig. 7.3	Air leak test sample	135
Fig. 7.4	Schematic diagram of the air bubble test	136
Fig. 7.5	Schematic diagram of the air pressure decay test	136
Fig. 7.6	EAAJ samples at 5.0 kJ of discharge energy for three different adhesives (a) adhesive 638, (b) adhesive 567, and (c) adhesive SI 596	137
Fig. 7.7	Variation of pull-out load with the adhesive application length for three adhesives at (a) 3.9 kJ, (b) 4.4 kJ and (c) 5.0 kJ of discharge energy	138
Fig. 7.8	(a) Pull-out load vs extension and (b) Compressive load vs compression plot for adhesive 638 samples with 5 mm of adhesive application length	140
Fig. 7.9	EAAJ samples for adhesive 638 at 5 mm of adhesive application length after pull-out testing at (a) 3.9 kJ, (b) 4.4 kJ and (c) 5.0 kJ of discharge energy demonstrating the sliding failure	141
Fig. 7.10	Representation of (a) adhesive and (b) cohesive failure mode of an adhesive joint	141
Fig. 7.11	Zoomed view of EAAJ substrate 2 after the pull-out test for (a) 5.0 kJ, (b) 4.4 kJ and (c) 3.9 kJ	141
Fig. 7.12	Variation of (a) maximum pull-out load and (b) maximum compressive load with discharge energy across three adhesives for 5mm adhesive application length	142

Fig. 7.13	Variation of (a) maximum pull-out load and (b) maximum compressive load with curing time at three discharge energy values	143
Fig. 7.14	Variation of leak rate with adhesive application length at three discharge energy values at 96 hours of curing time	147
Fig. 7.15	Variation of leak rate with curing time for adhesive 638 with 5 mm of adhesive application length for three discharge energy	148
Fig. 7.16	Variation of micro-hardness with distance and discharge energy	150
Fig. 7.17	Cu-SS interface for Loctite EAAJ sample at 5.0 kJ of discharge energy for (a) axial view and (b) circumferential view	151
Fig. 7.18	(a) Representation of Lorentz force distribution in the working zone and (b) zoomed view showcasing the impact of the slit on the distribution along with (c) experimental image	151
Fig. 8.1	Brief Flow Chart for Numerical Modelling for Electromagnetic analysis (ANSYS Maxwell), Structural deformation (ANSYS Explicit dynamics) and Welding morphology (ANSYS Autodyne)	157
Fig. 8.2	Dimensions of various parts of the components of the magnetic pulse welding setup	157
Fig. 8.3	Simulation model for electromagnetic field analysis (a) current curve, (b) ANSYS Maxwell model, (c) grid details showing the sectional view and (d) current density for 18 kV at 15 µs showing induced current at the Cu driver tube surface in the middle of the working zone	158
Fig. 8.4	(a) 3-D model showcasing the arrangement of components and (b) Axisymmetric meshed simulation model for ANSYS explicit dynamics	160
Fig. 8.5	Geometry used for the SPH numerical model	161
Fig. 8.6	Machine used: (a) 70kJ/25kV magnetic welding machine, (b) Welding tool consisting of Bitter coil with disposable copper field shaper	163
Fig. 8.7	Copper field shaper (a) top view, (b) experimental sample	164
Fig. 8.8	Deformation stages showing the effective plastic strain fringe pattern of EMW joint at four different times (a) 0 µs, (b) 5 µs, (c) 10 µs and (d) 15 µs at 18 kV of discharge voltage	166

Fig. 8.9	Outer diameter comparison of the D9 tube-SS 316LN end plug joint in the working zone	167
Fig. 8.10	SPH interface morphologies during simulation at (a) 0.12 μs, (b) 0.46 μs, (c) 0.64 μs and (d) 0.72 μs	168
Fig. 8.11	Formation of wave structure and jetting during magnetic pulse welding simulation using SPH	169
Fig. 8.12	Predicted field variables at 1 μs for impact angle 8 degrees (a) effective plastic strain, (b) pressure and (c) temperature	170
Fig. 8.13	Predicted (a) effective plastic strain and (b) von Mises stress fringe pattern at 3 μs for an impact velocity of 500 m/s and 8 impact angle of 8 degrees	171
Fig. 8.14	Comparison of results of SPH simulation with the Bahrani-Black-Crossland wave formation model	172
Fig. 8.15	Comparison of waviness morphology in (a) Experiments and (b) Simulation	173
Fig. 8.16	(a) Optical micrograph showcasing waviness pattern of the welded interface in experiments (b) Comparison with SPH (zoomed view) at 8-degree, 18 kV discharge voltage	173
Fig. 8.17	(a) Pressure profile with time obtained from hydraulic burst test indicating the failure of the tube at 108 MPa and (b) Hydraulic burst sample failed at D9 tube near the TIG joint	174
Fig. 8.18	Micro-hardness distribution near the bonding interface for the MP welded sample	175
Fig. 8.19	(a) X-ray tomography of one of the samples and (b) high-resolution optical image indicating uniformity in the welded region	176
Fig. 8.20	(a) Half-cut sample micro-tomography, (b) reconstructed voxel (volume pixel) of the sample and (c) zoomed view showing opening/non-uniformity in welding at the D9-SS 316LN interface	176
Fig. 8.21	Optical micrographs at (a) 200× and (b) zoomed view at 500× showcasing the waviness pattern at the interface	177
Fig. 8.22	SEM micrographs of the interface between SS 316LN and D9 at (a) 2.0K ×, (b) 5.0 K ×, (c) 10 K × and (d) 15.0 K ×	178

Fig. 8.23 EDS measurement in the D9-SS 316LN interface region showing composition at the interface 179

List of Tables

Table 3.1	Circuit parameters of electromagnetic forming machine	36
Table 3.2	Mechanical and electrical properties of the copper and SS 304	38
Table 3.3	Chemical composition of the copper tube (wt. %)	38
Table 3.4	Chemical composition of SS 304 tube (wt. %)	38
Table 3.5	Variation of failure modes with crimping parameters in pull-out test	44
Table 3.6	Variation of failure modes with crimping parameters in the compression test	48
Table 3.7	Representation of failure modes with crimping parameters for torsion test	51
Table 3.8	Average surface roughness (R_a) in μm in the crimped zone for threaded, knurled and smooth-surfaced samples prepared at higher discharge energy levels (5.0 kJ – 6.2 kJ)	58
Table 4.1	Constants of J-C material model for Cu and SS 304 [27, 28]	64
Table 4.2	Constants of linear polynomial EOS of copper [28]	64
Table 4.3	Comparison of outer diameter and thickness of copper tube for experiment and simulation	73
Table 4.4	Comparison of maximum pull-out and the compressive load of smooth-surfaced samples for experiment and simulation at various discharge energy levels	76
Table 5.1	Dimensions of the thread at various pitch	88
Table 5.2	Maximum pull-out load variation with discharge energy and pitch of the thread in the experiment	91
Table 5.3	Coefficients of empirical relation fitted using bisquare method	96
Table 5.4	Coefficients of empirical relation fitted using LAR method	97
Table 5.5	Coefficients of empirical relation fitted using bisquare method	100
Table 5.6	Coefficients of empirical relation fitted using LAR method	100
Table 5.7	Influencing factors and levels affecting the EMCT3 joining process	100
Table 5.8	Variation of experimental value of maximum pull-out load (in kN) at three discharge energy values with four thread pitch values	104

Table 5.9	Analysis of Variance for Transformed Response	104
Table 6.1	Properties of Loctite 638 adhesive used [27]	112
Table 6.2	Influencing factors and levels affecting the Cu-SS tube-to-tube joining process	118
Table 6.3	Maximum pull-out load values in kN at both influencing factors (type of process and discharge energy) for three repetitions	118
Table 6.4	Analysis of Variance for Transformed Response	119
Table 6.5	Maximum compressive load values in kN at both influencing factors (type of process and discharge energy) for three repetitions	120
Table 6.6	Analysis of Variance for Transformed Response	120
Table 6.7	Results obtained from deformation analysis for EAAJ samples	121
Table 6.8	Air leak rate in mbarl/sec at three different discharge energy for two different processes at three repetitions of experiment	125
Table 7.1	Properties of adhesives used in the experiment [114]	130
Table 7.2	Influencing factors and levels affecting the Cu-SS tube-to-tube joining process	144
Table 7.3	Variation of maximum pull-out load (in kN) at three discharge energy values with four adhesive application lengths for three different adhesives	144
Table 7.4	Analysis of Variance for Transformed Response	145
Table 7.7	Air leak rate in mbarl/sec at three different discharge energies for adhesive 638 samples at 5mm of adhesive application length	146
Table 7.8	Influencing factors and levels affecting the leak tightness of Cu-SS tube-to-tube joint	149
Table 7.9	Analysis of Variance for Transformed Response for leak test results	149
Table 8.1	Constants of J-C material model for Cu, D9 and SS 316LN [137, 138]	160
Table 8.2	Constants of linear polynomial EOS of copper [139]	160
Table 8.3	Chemical composition of D9 tube and SS 316LN metallic plug	165
Table 8.4	Process parameters of the experiment	165
Table 8.5	Mechanical and electrical properties of driver and flyer material	165

Table 8.6 Variation of Wavelength (λ) and Amplitude (A) of waviness morphology in μm with impact velocity and impact angle 174

1 Introduction

A modern leaning towards decreasing the weight of the structure is achieved by executing multi-material schemes along with recently improved and exceedingly advanced materials, as discussed by Schurmann et al. [1]. Heavyweight reduction capacity of multi-material schemes and aerospace structures are confronted by complicated requirements on joining techniques for such structures [2]. Often disagreements in the mechanical properties of the workpiece materials make it unable to join by conventional joining methods. For Example, if melting temperatures and thermal conductivity of the materials to be joined are significantly different, then fusion welding cannot be practiced generally due to internal stress build-up in intermetallic zones, which further influence joint strength. Usually, to obtain connection strength comparable to the parent metal, further heat treatment is essential, as described by Barnes et al. [3]. However, joining by metal forming can be an alternative for manufacturing multi-material lightweight components. Metal forming is a set of manufacturing processes in which an external force is applied to the material to induce stress which is more than its yield stress but less than its ultimate stress resulting in plastic deformation of the material. Typically, it can be divided into two categories (conventional and high-energy rate forming).

1.1 Conventional Metal Forming Process

Conventional metal forming (CMF) uses a punch and a die system to deform the workpiece (stock or blank). The workpiece can be in the shape of a sheet, plate, rod or tube of different cross-sections. A typical example of conventional forming will include rolling, forging, bending, and extrusion. The strain-rate values during conventional forming are usually in the range of 0.1 to 5.0 s^{-1}. The process has a higher operation time, low strain rate and high spring back [4].

1.2 High Energy Rate Forming Process

High energy rate forming (HERF) utilises a high energy pulse for a short period of time to deform the workpiece material. The strain rate in the high energy rate forming is in the range of 10^3 s^{-1}. The process has a lower operation time and spring back, and even the material which is difficult to deform by the conventional process can be formed by high energy rate forming.

The spring back is reduced in HERF processes compared to CMF processes, which can be summarised as,

- Plastic deformation: At high strain rates, the material undergoes more plastic deformation, which results in a more significant amount of permanent deformation. This permanent deformation counteracts the spring back effect, leading to a reduction in spring back, as also discussed by Barner et al. [5].
- Dynamic recovery: At high strain rates, the material experiences a more significant amount of dynamic recovery, which is the recovery of the material's elastic strain energy due to rapid deformation. This dynamic recovery also contributes to a reduction in spring back [6].
- Temperature effects: At high strain rates, the material experiences an increase in temperature due to rapid deformation. This increase in temperature can lead to a reduction in the material's yield strength and an increase in its ductility, which can also contribute to a reduction in spring back, as also investigated in detail by Barner et al. [5] and Osakada et al. [7].
- Microstructural effects: At high strain rates, the microstructure of the material can be altered due to rapid deformation. This alteration of the microstructure can lead to changes in the material's mechanical properties, such as an increase in strength and a reduction in ductility, which can also contribute to a reduction in spring back, as discussed by Dalal et al. [8], Skubisz et al. [9] Yan et al. [10].

Some examples of high energy rate forming would be explosive forming, electrohydraulic forming and electromagnetic forming [11].

1.2.1 Explosive Forming

Explosive forming (EXF) utilises chemical energy produced from the explosive (a substance that produces bursts of gas) to deform the workpiece material plastically, as shown in Fig. 1.1. Some typical explosives are cyclonite, pentolite and trinitrotoluene. A long setup preparation time and specialised explosive handling skills are required for explosive forming. Therefore, the process is only suited for specialised low-volume products [12].

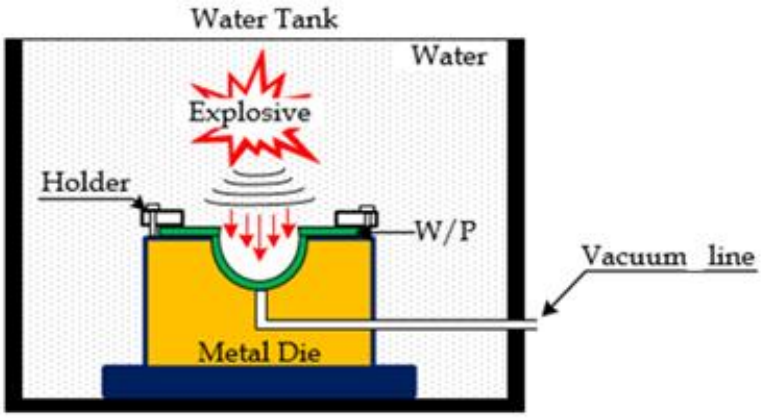

Fig. 1.1 Explosive forming

1.2.2 Electrohydraulic Forming

Electrohydraulic forming (EHF) utilises shock waves generated inside a fluid to deform the workpiece plastically, as shown in Fig. 1.2. During the process, a capacitor bank is discharged in a very short interval of time through two electrodes placed in proximity which generates a high-temperature plasma channel causing vapourisation of the surrounding fluid leading to a shock wave generation which deforms the workpiece [13].

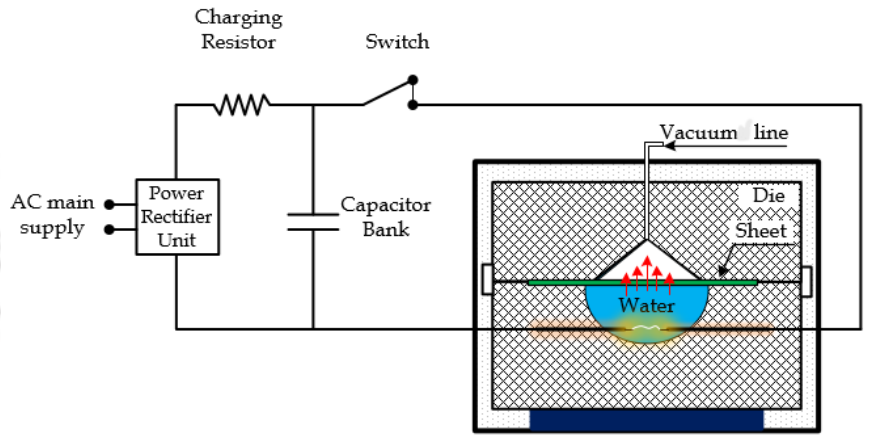

Fig. 1.2 Electrohydraulic forming

1.2.3 Electromagnetic Forming

Electromagnetic forming (EMF) is a non-contact high-speed forming method which utilises an electromagnetic field to deform highly electrically conductive materials assisted by controlled discharge energy from a capacitor bank as described by Daehn et al. [14] as shown in Fig. 1.3. This electromagnetic effect is governed by Maxwell's equation [15].

The basics of this process lie in the fact that an altering magnetic field can induce electric currents in conductive material in contact with the magnetic field leading to applying forces (Lorentz force) to conductors. The early work on EMF of metals has been reported

by Brower et al. [16]. As the current area of this work is EMF, it has been discussed in detail.

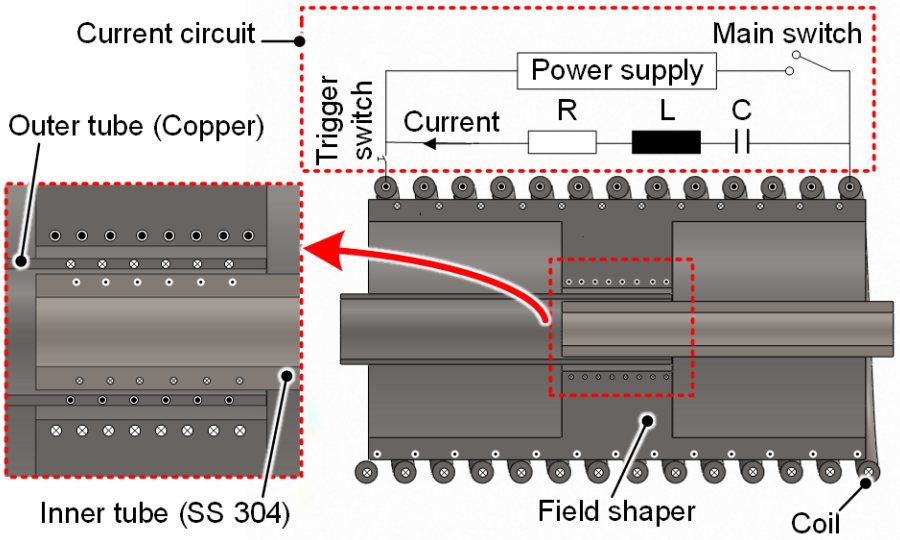

Fig. 1.3 Electromagnetic forming setup

1.2.3.1 Principles of EMF

A prevailing EMF setup can be described as one RLC circuit, a capacitor bank which acts as a power source, a high current discharge switch and a working coil. The setup can be symbolised as the inner resistance R_i, the internal inductance L_i and the capacitance C_c. An equivalent circuit diagram is shown in Fig. 1.4. Here, the capacitance represents the number of capacitors that can be used to store the required energy for the EMF process before the discharge. The charging energy E used in this process is estimated with the help of capacitance C and discharge voltage U as

$$E = \frac{1}{2} C_c U^2. \tag{1}$$

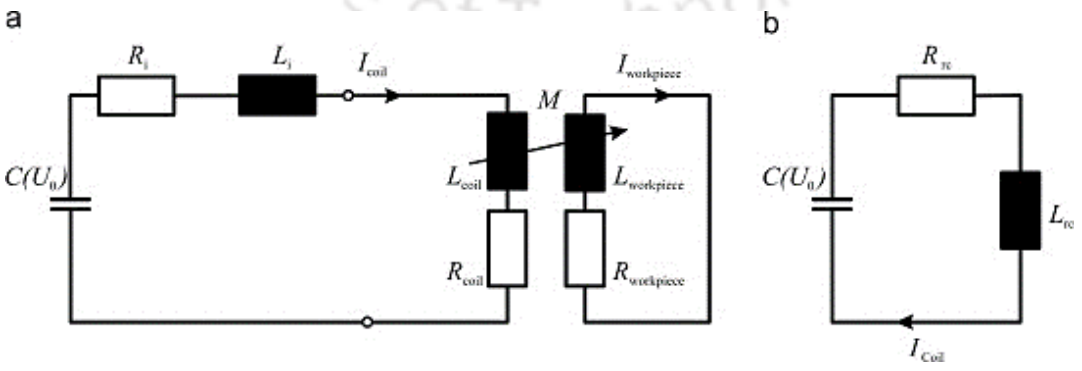

Fig 1.4 Equivalent circuit diagrams: a) detailed version and b) reduced version [18]

The combination of the workpiece and the tool coil is taken as the load of the circuit setup. The abrupt instant discharge of the capacitor causes a damped sinusoidal current *I (t)* to run through the coil. As per Maxwell's law [15], flowing current *I (t)* through a coil generates a magnetic field *H* (r,t,z) across the coil. However, this magnetic field induces a secondary current in the workpiece, which flows opposite to the primary current (Lenz's law). The current induced in the workpiece flow typically close to the surface because of the skin effect [17]. The distance between the surface of the workpiece at which the current density is decreased to *1/e* of its value at the surface (maximum value) is called the skin depth δ_s. In this relation, *e* is the Euler number. Based on the frequency of discharged current ω, permeability μ of the material and the specific electrical conductivity k of the workpiece material used, the value of skin depth δ_s can be represented as [18]

$$\delta_s = \sqrt{\frac{2}{\omega \mu k}}. \tag{2}$$

A magnetic field is focused in between the coil and workpiece. High current density causes high Lorentz forces to be acted orthogonally on the workpiece, which causes plastic deformation of the tube after the stress reaches the yield stress of the material. In general, the entire process takes around 10-100 µs. As per Psyk et al. [19], during the process, the material deforms with a strain rate up to 10^4 s^{-1} and velocities are in the range of 250 m/s or more.

As explained by Psyk et al., various resistances and inductances of the setup (RLC) circuit are considered for the calculation of the discharge current $I(t)$ [19]. Hence, if capacitance *C*, the resultant inductance L_{res}, and the aggregate resistance R_{res} are available, then the current $I(t)$ in the equivalent RLC circuit can be calculated by a damped sinusoidal function as

$$I(t) = \frac{U}{\omega L_{\text{res}}} e^{-\delta t} \sin(\omega t), \tag{3}$$

since the workpiece is continuously deforming during the process, the resistance R_{res}, and the inductance L_{res} becomes a time-dependent variable. This time dependency would prevent a proper analytical solution of the differential equation of the specified RLC circuit, which is why the movement of the workpiece is neglected, and both the variables are considered constant for calculating the discharge current flowing through the coil.

In the equation mentioned above, the variable ω represents the damped angular frequency of the sinusoidal current profile, and it can be easily calculated by subtracting the value of damping co-efficient δ to the ideal un-damped frequency ω_0 of the specified circuit of the setup [19] as

$$\omega^2 = {\omega_0}^2 - \delta. \tag{4}$$

The value capacitance C and inductance L_{res} of the RLC circuit can be used to determine the un-damped angular frequency as

$${\omega_0}^2 = \frac{1}{R_{\text{res}} C}. \tag{5}$$

The damping co-efficient δ of the sinusoidal current function is calculated based on the resultant resistance and inductance of the circuit as

$$\delta = \frac{R_{\text{res}}}{2L_{\text{res}}}. \tag{6}$$

The Lorentz force $\vec{F}$, which acts on the workpiece as a volume force, can be calculated with the [20]

$$\vec{F} = \vec{J} \times \vec{B}. \tag{7}$$

As the magnetic flux density can be expressed in terms of permeability μ_{m} and magnetic field strength $\vec{H}$ as

$$\vec{B} = \mu_{\text{m}} \vec{H}. \tag{8}$$

Disregarding the magnetic field strength component $\vec{H}$ in the workpiece thickness direction, i.e. the radial component in the case of the tube as a workpiece (tube forming) and the z-component in the case of the sheet as a workpiece (sheet forming). The current density $\vec{J}$ is equal to the negative derivative of the magnetic field strength $\vec{H}$ with respect to radius r (in tube forming), as shown in Eq. 9 as

$$\vec{J} = -\frac{\partial \vec{H}}{\partial r}. \tag{9}$$

Therefore, the Lorentz force F_{r} acting on the surface of the tubular workpiece can be determined easily as

$$F_r = -\mu\vec{H}\frac{\partial\vec{H}}{\partial r} = -\frac{1}{2}\mu\frac{\partial|H|^2}{\partial r}, \tag{10}$$

and the current density $\vec{J}$ is equal to the negative derivative of the magnetic field strength $\vec{H}$ with respect to z-coordinate (in sheet forming), respectively, as shown in Eq. 11 as

$$\vec{J} = -\frac{\partial\vec{H}}{\partial z}. \tag{11}$$

similarly, the Lorentz force F_z acting on the surface of the sheet metal workpiece can be expressed as

$$F_z = -\mu\vec{H}\frac{\partial\vec{H}}{\partial z} == -\frac{1}{2}\mu\frac{\partial|H|^2}{\partial z}. \tag{12}$$

The Lorentz force $\vec{F}$ acting as a volume force can be used to calculate magnetic pressure p acting on the surface of the workpiece by integrating the volume force over the thickness of the workpiece as,

$$p(r,t) = \int_{ro}^{ri} F(r,t)dr = \frac{1}{2}\mu\left(H_{\text{gap}}^2(t) - H_{\text{pen}}^2(t)\right). \tag{13}$$

If skin depth is smaller than the thickness, the infiltrated magnetic field can be generally ignored so that magnetic pressure is determined as,

$$p(t) = \frac{1}{2}\mu H_{\text{gap}}^2(t). \tag{14}$$

As per Psyk et al. [19] and Dietz et al. [21], this simplification of the pressure calculation can be only allowed if the ratio of wall thickness and skin depth is at least two and the ratio of skin depth and inner radius is less than 0.2 based on experimental and analytical calculations for compression of the tube. The air space occupied between the surface of the workpiece and the coil is neglected for calculations because the permeability is almost equal to free space, so it causes a negligible effect on the magnetic field as per Thibaudeau et al. [22].

1.2.3.2 Types of EMF Process

EMF process can be classified into three categories based on coil and workpiece arrangement; i) electromagnetic compression, ii) electromagnetic expansion, and iii) electromagnetic sheet metal forming [23]. Electromagnetic compression and expansion

utilise a helical coil to form axisymmetric tubular components, as shown in Fig. 1.5. Bely et al. [24] have added that tubes with a diameter varying from 3 mm to 2 m and thickness up to 5 mm can be easily formed using the EMF process depending upon the mechanical property of tube material. However, the amount of discharge energy required depends upon the area to be processed, so processing large tubes or sheets requires a machine with a higher charging energy/capacitor bank. Electromagnetic sheet metal forming utilises a spiral coil to form sheet metals.

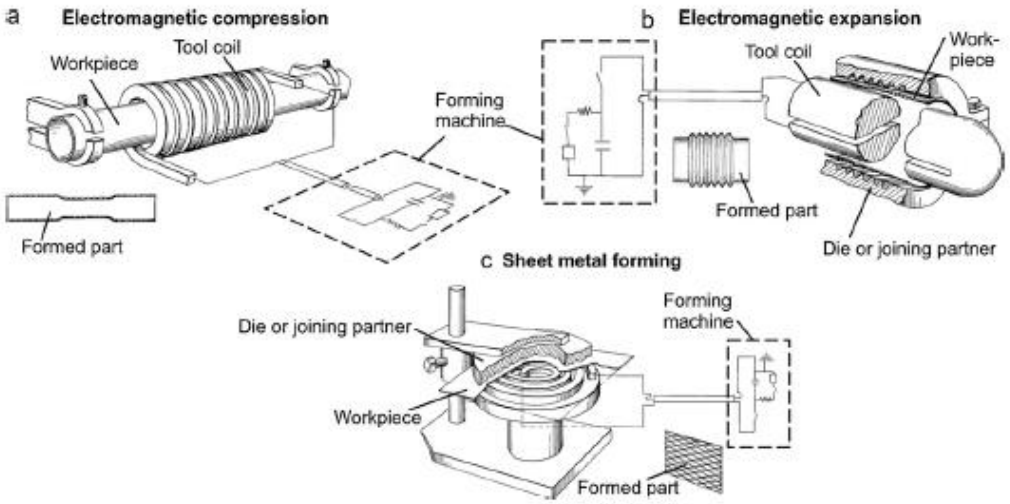

Fig. 1.5 various types of the coil for the pulsed electromagnetic forming method [18]

Bühler et al. [25] have discussed about the application of electromagnetic compression in tubular connections. The authors have further said that only compression by electromagnetic forming is advantageous over conventional forming applications. The EMF process has several advantages and limitations as compared to the CMF process.

1.2.3.3 Advantages and Limitations of EMF Process

The EMF process has many advantages compared to the conventional process, which can be summarised as discussed below,

- EMF is a no-contact process; therefore, it is possible to deform covered/coated parts without destroying the surface layer [26].
- During the EMF process, spring back is significantly reduced (as discussed in section 1.2) compared to the CMF process, which helps simplify the designing process.
- The process is eco-friendly as it does not have any application of lubricants or any external waste material [27]

- The process has high repeatability as it is easy to control the process parameters involved.
- High production rates can be achieved and easily automated and mechanised [28].
- As it is a high speed and high strain rate process, it offers an improvement in the mechanical properties (as discussed in section 1.2) of the workpiece being involved compared to the conventional process.

The EMF process also has some limitations, which can be summarised as discussed below,

- The EMF process is suitable for only highly electrical conductive and low flow stress materials [29]. However, materials with lower electrical conductivity can also be formed with the help of an external driver.
- A tiny portion of the discharged energy from the capacitor bank is actually used for forming the workpiece material. Bertholdi et al. [26] have explored that the efficiency of the process is not higher than 20%.
- The EMF process requires a heavy initial investment in terms of large capacitor banks and disposable tool coils.
- Safety is another concern for the EMF process as it deals with high current and voltage leading to a high magnetic field.

2 Literature Review

2.1 Introduction

EMF technologies have been implemented in the automotive and aerospace industries. Balanethiram et al. [30] have reported that high-speed techniques like pulsed electromagnetic forming, in contradiction to conventional forming, have uniform pressure distribution and thinning during forming. At the same time, formability is observed to increase in various metals. As Birdsall et al. [31] have reported, joining tubes by EMF has several applications, as shown in Fig. 2.1.

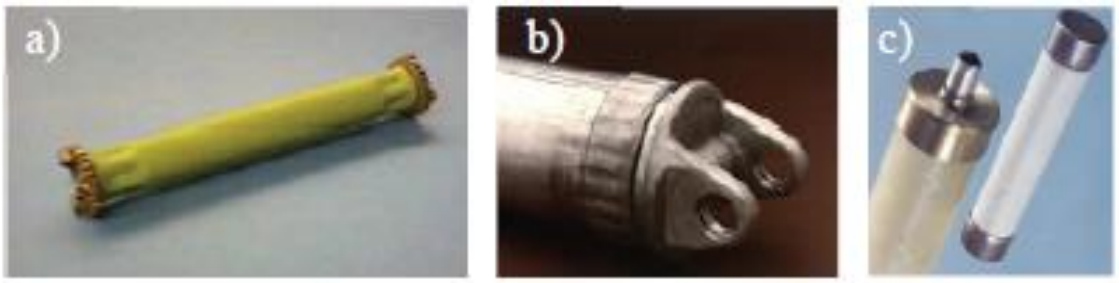

Fig. 2.1 Sample assemblies joined by electromagnetic welding a) Boeing 777 torque tube, b) 4" drive shaft, for Ford, and c) high voltage fuse [31]

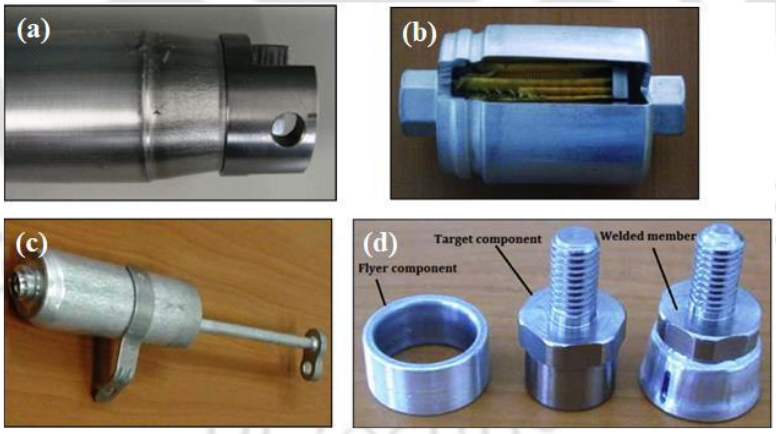

Fig. 2.2 Components of automotive sector obtained with :(a) drive shaft (Al/steel joint), (b) fuel filter (Al/Al joint), (c) automotive A/C receiver-dryer, (d) automotive earth connector [32]

The electromagnetic joining (EMJ) technology has been used for various development in the automotive industry, such as the joining of drive shafts made of aluminium/steel joints, automotive aluminium fuel filters, components of air conditioners, and automotive earth connectors, as shown in Fig. 2.2. [32].

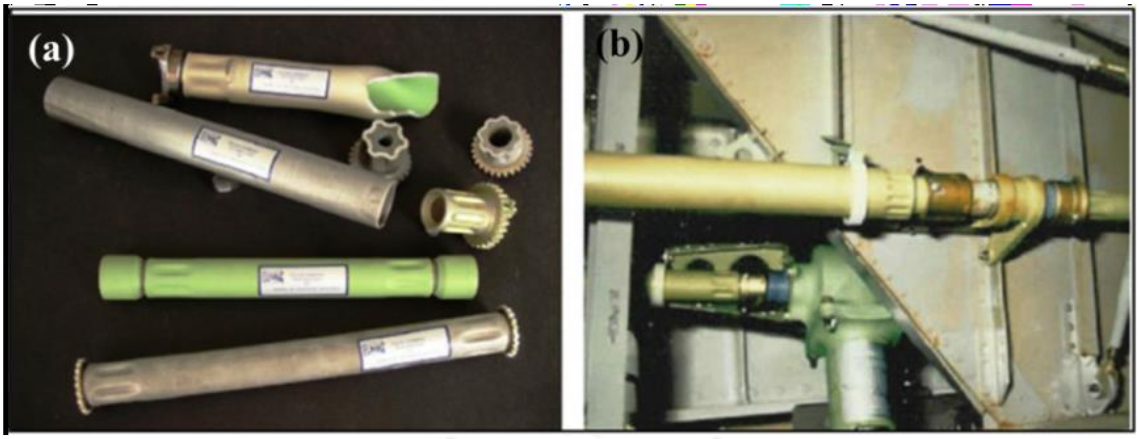

Fig. 2.3 (a) aircraft flight torque tubes [33], (b) aircraft flight control tubes in use [34]

In addition, EMJ has recently gained importance and has already been successfully used in the aerospace industry [33]. For instance, the EMJ process has been used to join aircraft control tubes which can resist torque tests (Fig. 2.3). The EMJ can also be used to join flexible printed circuit boards [35], high voltage cables, and copper tubes on coaxial cables [36]. Weddeling et al. [37, 38] have also proposed the application of EMJ in electric vehicle (EV) body components and drive shaft as a lightweight and high-strength alternative, as shown in Fig. 2.4 and Fig. 2.5.

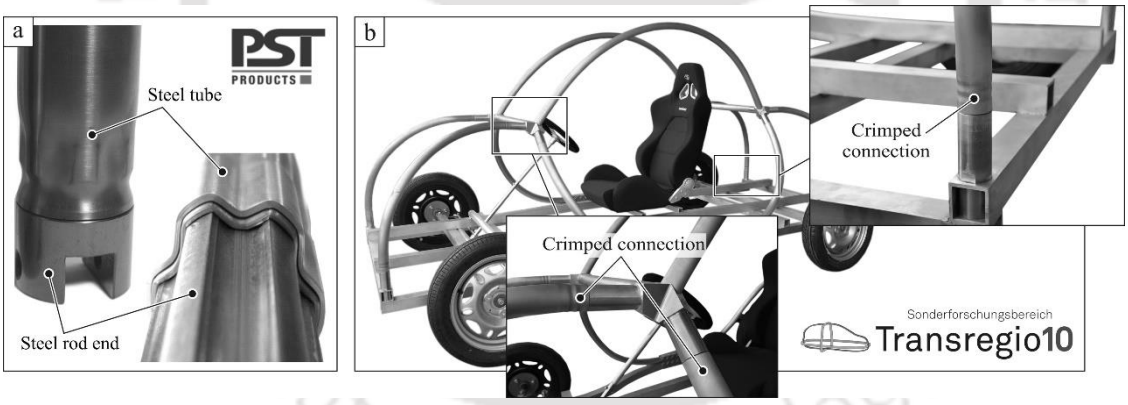

Fig. 2.4 (a) Electromagnetically crimped driveshafts; (b) demonstrator space frame [37]

Besides, the application of the EMJ configuration also flourishes in processing crimped parts for different applications [39], as shown in Fig. 2.6. Rowland et al. [40] have also proposed the application of EMJ in the automotive industry, like locking rubber boots to ball joint housing and assembling an air brake hose.

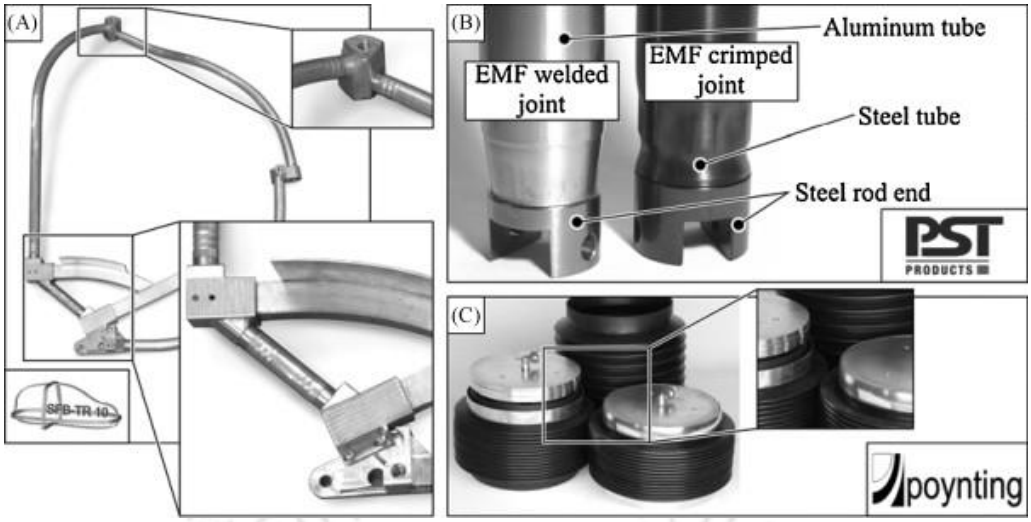

Fig. 2.5 Examples of applications for EMJ joints. (a) Lightweight frame structure, (b) driveshaft with a welded (left) and a crimped (right) joint manufactured and (c) oil expansion vessel sealed by a compressed aluminium ring [38]

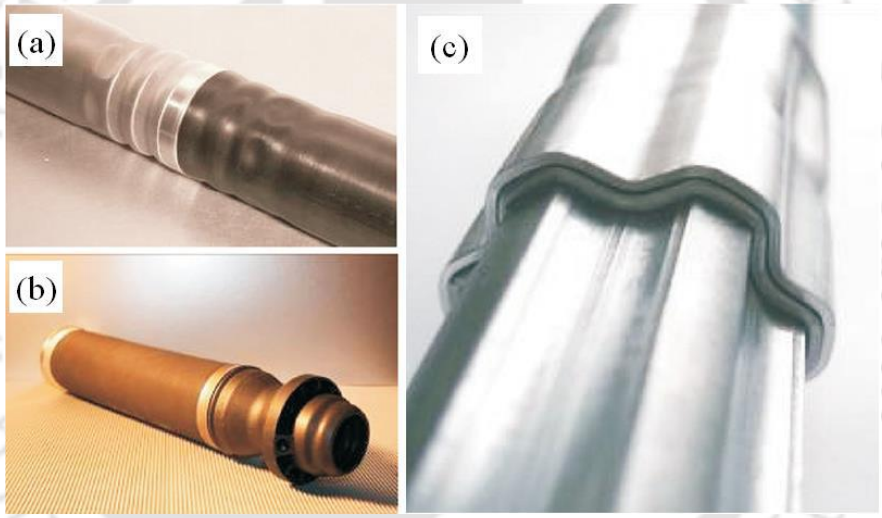

Fig. 2.6 (a) Al/steel crimped tube for instrumental panel beam (b) crimped air suspension, (c) crimped drive shaft [39]

Similarly, EMJ offers many advantages in efficient manufacturing of dissimilar material/multi-material components, which have become necessities of the present time because of their ability to offer benefits of properties of multiple materials such as corrosion-resistant, lightweight, higher strength, and electrical conductivity in one single component [41-42]. Joining a range of multi-material combinations by conventional fusion welding techniques are often very challenging due to the difference in their mechanical and physical properties. For Example, Aluminium (Al) and Steel have a difference of 800-900 °C in their melting temperatures. Therefore, at the point of reaching the melting point of steel, Al may get completely destroyed during fusion welding [43]. Copper-steel (Cu-steel) is also one such multi-material combination that offers electrical and thermal

conductivities of copper combined with higher strength and toughness of steel, which have applications in electrical components, heat sinks, and power generation areas, as discussed by Simoen et al. [42] and Patra et al. [44]. The conventional joining of Cu-Steel through melting is complex because of the lower solubility of copper in iron, leading to hot cracking [43]. Similar challenges are for conventional fusion welding of different austenitic stainless steel (ASS), as it leads to hot cracking defects due to the formation of low-melting-point eutectics arising from impurities such as sulphur and phosphorous [45-46]. Galvanic corrosion (an electrochemical process leading one metal to erode in electrical contact with another metal in the presence of an electrolyte) combined with localisation of stress possesses another issue when joining the multi-material combination using conventional mechanical fastening techniques as it causes irreparable structural damage [47]. Therefore, unconventional solid-state joining techniques can offer weight reduction, higher strength and lower heat sensitivity without any additional mechanical elements, would be an ideal choice for developing multi-material components. Electromagnetic Joining (EMJ) can be a desired alternative to conventional thermal and mechanical joining techniques [48]. EMJ technique minimises the problems associated with metallurgical incompatibilities of components to be joined [49] and can be applied for a large combination of materials such as Al-Ni, Al-Steel, Al-Mg, Cu-Al, Cu-Brass, Cu-Steel, Steel-Steel, Ti-Ni, and Al-Ti [50-51]. The current work concentrates on creating tubular axisymmetrical components/joints using the EMJ technique, which can be classified into three major categories depending on the dominating joining mechanism into i) Electromagnetic crimping (EMC), ii) Electromagnetic welding (EMW), and iii) Hybrid joining [52]. EMC can be further classified into a) Interference-fit joining and b) Form-fit joining [53].

In this literature review chapter, a detailed literature survey has been performed on experimental and numerical investigations associated with all these joining mechanisms under EMJ, along with parameters affecting these mechanisms.

2.2. Electromagnetic crimping

EMC is one of the process variants of EMJ, which is a non-contact high-speed forming method. It utilises an electromagnetic field to deform highly electrically conductive materials, assisted by controlled discharge energy from a capacitor bank. EMC is primarily used in joining tubular components. The physics of the process is the same as discussed in EMF. A prevailing electromagnetic crimping setup can be described as an RLC circuit,

a capacitor bank C, which acts as a power source, a high current discharge switch and a working coil and one field shaper to improve the performance, as shown in Fig. 2.7.

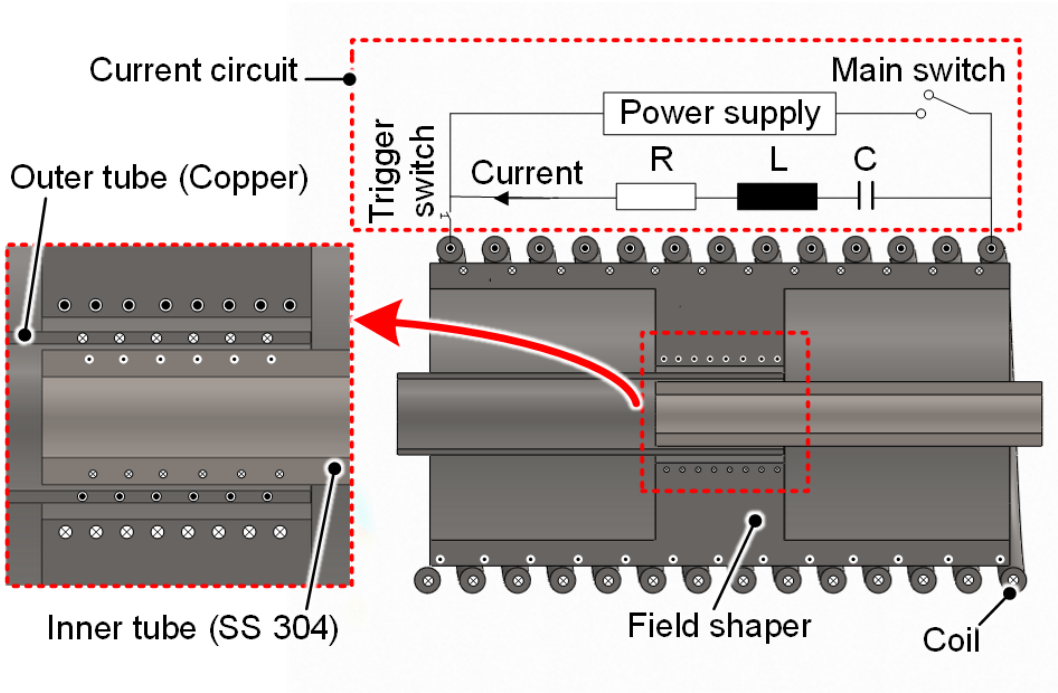

Fig. 2.7 Schematic diagram for EMC

The combination of copper and steel workpiece and the tool coil act as the circuit setup load. The abrupt instant discharge of the capacitor causes a damped sinusoidal current to run through the coil, which is measured with an oscilloscope and a Rogowski coil. As per Maxwell's law, flowing current I (t) through a coil generates a magnetic field H (r,t,z) surrounding the coil. A field shaper is inserted between the coil and outer tube to concentrate and intensify the magnetic flux in the joining region [54]. However, this magnetic field induces a secondary current in the field shaper and that current flow in the opposite direction to the primary current (Lenz's law) and flows close to the surface because of the skin effect [17]. This secondary current further induces another secondary current in the adjacent conductor, i.e. workpiece. Interaction of the magnetic fields leads to high radial Lorentz forces, which causes plastic deformation of the outer tube and crimps over the inner tube. The zone going through the process is referred to as the crimping zone. The entire process generally takes around 10–100 μs, and most of the deformation usually occurs in the first half pulse of the current waveform [53]. It is to be noted that no metallic bond formation takes place during EMC as two workpieces (flyer and target) are brought together at a high velocity below the critical velocity for metallic bond formation; the materials will bounce off each other or deform plastically without

forming a metallic bond. At velocities above the critical velocity, the materials will experience a sufficient level of plastic deformation and plastic flow to allow the atoms of one material to intermix with the atoms of the other material. These atoms intermixing leads to a metallic bond formation between the two materials. The critical velocity for metallic bond formation is determined by the balance between the kinetic energy of the colliding materials and the work required to deform and intermix the materials. At velocities below the critical velocity, the kinetic energy is insufficient to overcome the resistance to deformation and to intermix, so no bond is formed. At velocities above the critical velocity, the kinetic energy is sufficient to overcome this resistance and allow the materials to bond. Much more discharge energy is required to accelerate the flyer workpiece beyond critical velocity compared to the crimping joint formation during EMC.

The joining of the outer (flyer) tube onto the inner (target) tube in EMC can be explained by the following two dominating mechanisms of deformation [53].

- The interference-fit joining, which is based on elastic-plastic deformation between flyer and target workpiece and mechanical interlocking at the microscopic level.
- Form-fit joining is based on fitting the flyer workpiece in an undercut in the target workpiece. Therefore, joint strength is mainly because of the mechanical interlock at the macroscopic level. In this case, the joint is prone to stress concentration.

2.2.1. Interference-fit joining (EMC)

An interference fit joint, also known as a force-fit joint, primarily depends on the dissimilarities between the elastic recoveries of two workpieces being joined, leading to an interference pressure between the workpieces after deformation [55]. The process can be executed by both electromagnetic compression and electromagnetic expansion, depending on the design requirement and placement of the tool coil [56].

Considering the scenario of interference-fit joining by electromagnetic compression, the outer workpiece (tube) is plastically deformed by Lorentz force proportional to the current flowing in the solenoid coil. When resultant stress in the workpiece due to Lorentz force reaches the flow stress value of the outer workpiece material, the outer tube starts deforming plastically towards the inner tube, as shown in Fig. 2.8. Once the gap between both the tubes is covered, the outer tube touches the inner tube and then both start compressing together as the forming pressure increases and reaches maxima due to an increase in the current amplitude value with time.

The outer tube goes to elastic and then plastic deformation, while the inner tube only goes to elastic deformation. When the magnetic pressure is released, both the tube starts recovering elastically. However, elastic recovery of the inner tube is prohibited by the plastic deformation of the outer tube leading to interference pressure build-up, given that an inner tube of higher stiffness and strength than those of the outer tube material is being used. [57]. Hence, higher joint strength with the interference fit is achieved. Apart from interference pressure, interlocking at the microscopic level also contributes to EMC crimped joint strength. Plastic deformation of the outer tube leads to breaking contamination layers and oxide films, which results in high-pressure bonding of clean surfaces. A similar explanation can be proposed for interference-fit joining by electromagnetic expansion.

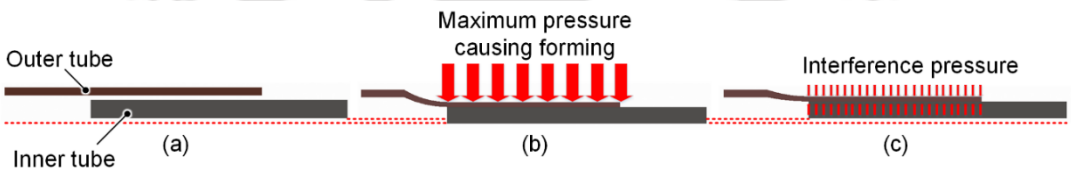

Fig. 2.8 Mechanism of interference-fit joining by compression: (a) Initial positioning, (b) plastic deformation of the outer and elastic deformation of the inner tube and (c) elastic recovery leading to interference pressure build-up

A natural force-fit is developed by high-velocity motion during tube-to-tube or tube-to-rod EMJ, which resists any relative movement, and by forming the outer tube onto the inner tube/rod with an undulating outer surface, a joint having the strength of the weaker workpiece can be produced [58]. The EMC technique can be used in the interference-fit joining of a broad range of electrically conductive materials onto metallic (steel) [59] and non-metallic (polyurethane) [60] materials.

2.2.1.1 Factors affecting interference-fit joining (EMC)

Factors affecting the interference-fit joining process are impact velocity, stand-off distance, the surface area of contact, coefficient of friction between the workpieces, and mechanical properties of the workpiece material. Many factors are interdependent.

The joint strength between two workpieces to be joined is dependent on the impact velocity, which is the velocity with which the outer workpiece impacts the inner workpiece during joining by electromagnetic compression, and the inner workpiece impacts the outer workpiece during joining by electromagnetic expansion [61]. It is observed in a free-forming experiment by measuring the impact velocity that a workpiece

is accelerated to a definite maximum velocity and then decelerates. The impact velocity is dependent on the discharge energy and the gap between the two workpieces.

The gap is referred to as standoff distance, and a zero-gap situation can lead to a significant loss of joint strength as the standoff distance provides the necessary distance for the workpiece to accelerate under the influence of Lorentz force [62]. To obtain maximum deformation at a specific discharge energy, the standoff distance should be optimised for maximum impact velocity, and to get high impact velocities at small gaps, higher discharge energies are required, as Kliener et al. explained [63]. Therefore, an optimum standoff distance results in higher impact velocity leading to higher joint strength [64]. However, this is accurate only for joints having a metallic target workpiece as for joints having a non-metallic target workpiece (for Example, Al tubes to CFRP rods by electromagnetic compression), Hwang et al. have observed that the standoff distance contributes to loss of joint strength compared to a zero-standoff distance joint [60].

Furthermore, an increase in contact between the inner surface of the outer tube and the outer surface of the inner tube (Fig. 2.7) leads to an increase in the contact area of the surface asperities at the microscopic level, which gives rise to friction at the interface in the crimping zone causing mechanical interlock at microscopic level [65].
Columb's friction law can quickly determine the strength of an interference-fit joint. The strength of such joints can be expressed by,

$$F_1 = \mu_1 p A_1, \tag{15}$$

F_1 is the strength of an interference-fit joint, μ_1 is the friction coefficient, p is the interference stress between the tubes, and A_1 is the surface area of the contact zone. Furthermore, an analytical expression for the interference stress of an interference-fit joint is proposed by Marre et al. [61], which is as

$$p = \frac{\dfrac{p_f - \sigma_{f,O} \ln \dfrac{1}{Q_O}}{E_I}\left(\dfrac{1+Q_I^2}{1-Q_I^2} + \vartheta_I\right) + \dfrac{2 \times Q_O^2 \times \sigma_{f,O} \ln Q_O}{E_O(1-Q_O^2)}}{\dfrac{1}{E_I}\left(\dfrac{1+Q_I^2}{1-Q_I^2} + \vartheta_I\right) + \dfrac{1}{E_O}\left(\dfrac{1+Q_O^2}{1-Q_O^2} + \vartheta_O\right)}, \tag{16}$$

where, σ_f is the yield strength, ϑ is poison's ratio, E is Young's modulus, Q is the ratio of the inner and outer diameter, p_f is the maximum pressure in the forming process; also, suffices O and I stand for outer and inner tubes, respectively. Therefore, to have higher

residual stress/interference stress in EMC, a target tube of higher stiffness and strength than the flyer tube material is preferred. The elastic recovery will be higher with higher stiffness, leading to higher radial reaction force [66]. Eguia et al. [58] have further observed that at the same parameter, higher interference stress is observed in the case of the elastomeric target tube. However, irrespective of the target tube material, an increase in discharge energy leads to increased interference stress due to higher deformation at higher energy, as discussed by Hwang et al. [60], while longer joining length and higher flyer tube thickness at the same discharge energy produces lower interference stress. Hence, joining length and thickness should also be considered essential parameters when designing such joints [67]. The authors have also notified that radial shrinkage of elastomeric components need to be considered while estimating the pull-out force of metal-polymer joints.

Furthermore, the authors also establish that multiple shots may improve the overall roundness of a tube-to-rod joint up to a deformation limit and beyond which it creates an adverse effect on joint strength and roundness [67]. Eguia et al. [58] have also confirmed that multiple shots do not add up to the joint strength of a tube-to-rod joint. Although increasing the joining length/crimping length can increase the strength in a non-linear way.

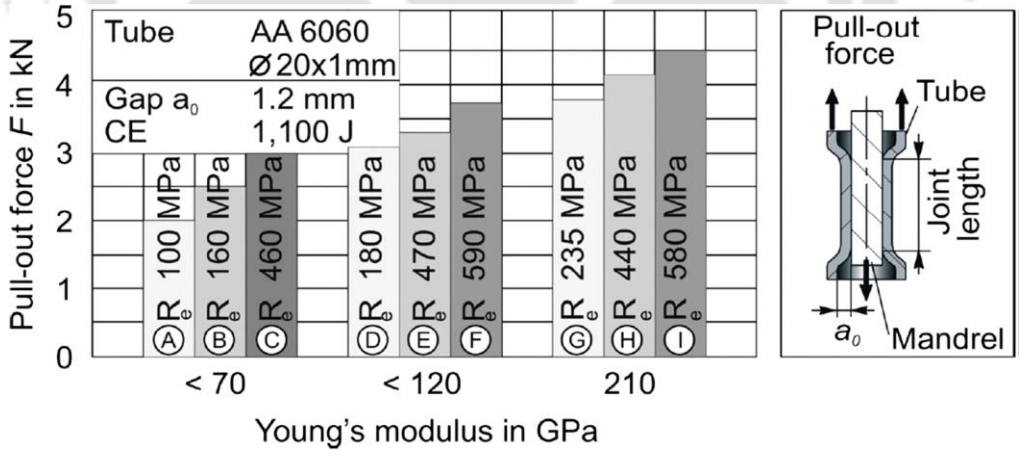

Fig. 2.9 Joint strength (pull-out load) in a tube-to-rod joint with different target workpiece (rod) materials [63]

Kleiner et al. [63] have established that yield strength and stiffness (Young's modulus) of target workpiece also play an essential role in deciding joint strength as lower stiffness (higher Young's modulus) of target workpiece leads to higher elastic recovery causing higher interference stress build-up, which eventually results in higher joint strength (Fig. 2.9).

To examine the effect of stiffness of the target workpiece, Bühler et al. have proposed the term Q, which is the ratio of the internal diameter (D_i) and external diameter (D_e) of the target workpiece. It is conclusive that $Q = 0$ represents a rigid solid target workpiece of higher stiffness, while $Q = 1$ would represent an infinite thin-walled hollow target workpiece of lower stiffness. At the value of Q near zero, the target workpiece has high stiffness causing lower interference stress, resulting in lower joint strength. However, increasing the Q value to a specific limit increases the joint strength, but beyond that, further increments only cause a loss in joint strength. Higher Q implies lower wall thickness and stiffness, resulting in elastoplastic deformation of the target workpiece instead of only elastic deformation, and any plastic deformation of the target workpiece negatively affects the joint strength [68]. Kleiner et al. have further validated this hypothesis in the case of the Al-steel tube-to-rod EMC joint [63].

Weddeling et al. [69] have proposed an analytical expression for the critical inner diameter of the hollow target workpiece in the case of joining by EMC (compression). If the inner diameter is lower than the critical value, an excellent interference-fit joint is produced, but if the inner diameter is more than the critical value, a significant loss in joint strength is observed. The hollow target workpiece has advantages like weight reduction but drawbacks like structural integrity and can deform easily during the EMC process. Therefore, the use of supporting shafts for hollow target workpieces is proposed by Weddeling et al. [70], as shown in Fig. 2.10, which reduces the plastic deformation of the target workpiece.

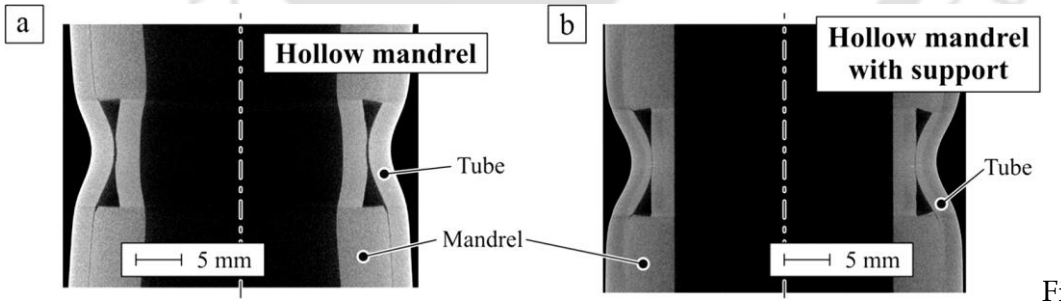

Fig. 2.10
Tube-to-hollow shaft joining by EMC (compression) (a) without supporting shaft and (b) with supporting shaft [70]

Going back to Eq. 15, apart from interference stress, joint strength can also be affected by the coefficient of static friction between the joining partners, which can be increased by changing the surface texture of the target workpiece. Hammers et al. [71] have used shot peening with glass beads and Al_2O_3 particles to harden the target workpiece surface and

five-axis milling to provide a surface texture to the target workpiece. The authors have observed that an increment in surface texture and surface hardening of the target workpiece leads to an increment in pull-out strength of the EMC joint. Psyk et al. [72] have also reported a critical method to increase the strength of an EMC interference-fit joint between a tube and an internal shaft by applying an elastomeric layer to increase the friction coefficient between the workpiece. However, the maximum achievable joint strength is generally equal to the strength of the weaker workpiece if the process is performed at an optimum parameter [61].

After interference stress and coefficient of friction, the third parameter which can optimise the EMC joint strength is the surface area of the contact zone, which depends upon the size of the contact zone [66]. Eguia et al. [58] and Kumar et al. [73-674] have used textured surfaces for the outer surface of a tube-to-shaft joint as textured surfaces have a higher surface area and have observed significant improvement in the strength. Eguia et al. [58] have suggested using a textured surface with finner features and pitch for better joint strength. Bühler et al. [75] have also investigated tube-to-shaft joining by EMC (compression), in which the internal shaft is textured with narrow channels with different pitch sizes. The authors have observed that increased depth causes incomplete filling of the outer tube while increased pitch causes improved filling and increases joint strength (Fig. 2.11).

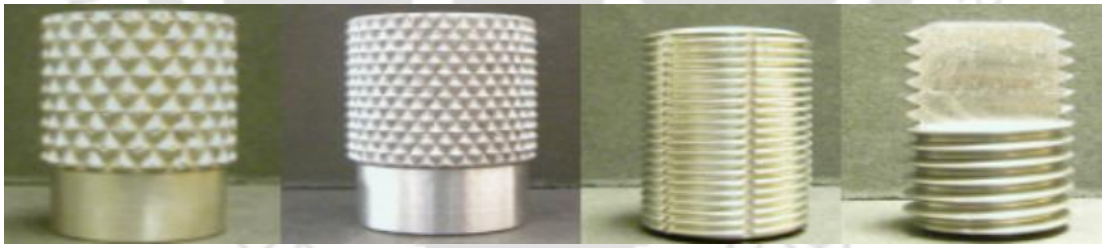

Fig. 2.11 Example of some of the mandrel surfaces. Left to right: coarse knurl, fine knurl, fine screw thread with axial grooves, and coarse screw thread [58]

Establishing a mathematical relation between the joint strength and the variables involved in the process has been challenging. Although tribology tests can quantify friction, microscopic inspections show that the contact between the electromagnetically joined partners is far from ideal. Only a few zones connect along the joint length, and the remaining gap is not constant along its perimeter [55].

Kumar et al. [76] and Rajak et al. [77] have developed coupled simulation model for EMC (compression) using LS-Dyna ™ and validated it with experimental findings. The model

utilises An FEM-BEM combination to solve the EMC problem in two parts (electromagnetic and mechanical). BEM is used for solving Maxwell equations in the regions not having eddy currents, and that is why the FEM-BEM technique is very advantageous because it eliminates air/insulator meshing.

Kaushik et al. [78] discuss the importance of FEM models in process optimisation and how analytical methods can predict the crimping profile. The authors have developed a non-coupled model using the analytical method for the EM part and the FEM method for the mechanical part.

Sofi et al. [79] have developed an analytical model to investigate Lorentz force and corresponding magnetic pressure generation during EMC (compression) process. The authors have developed a mathematical formulation to calculate the self-inductance and resistance of the parts involved along with their mutual inductance. A similarity in results is observed between analytical and numerical simulation models. Furthermore, this work establishes the requirement of developing analytical models as it has lesser computational demand than simulation models.

2.2.2 Form-Fit Joining (EMC)

When the surface profiles (knurls, threads, slots), as discussed in the previous section, are increased from the micro-level to the macro-level, a transition in the joining Mechanism occurs from force-fit to form fit during EMC. The mechanism of form-fit joining is based on the undercut formation by forming the flyer workpiece onto the surface structures (grooves) of the target workpiece [80].

The early work on form-fit joining (EMC) is done by Bühler et al. [80]. The authors have used circumferential grooves of various variations, and the discharge energy is adjusted so that the formed flyer tube touches the bottom of the groove of the target workpiece. The better filling of the grooves leads to stronger form-fit joints. The minimum pressure required to initiate plastic deformation of the flyer workpiece onto the grooves of the target workpiece is analytically calculated based on a piecewise linear approximation of acting pressure and usual plastic metal behaviour along with plane strain, expressed as,

$$p_{min} = \sigma_y \left[3 \left(\frac{s}{w} \right)^2 + \frac{s}{R} \right], \tag{17}$$

here, σ_y , s and R are the strength, thickness and inner radius of the flyer tube, respectively. w is the groove width of the target tube [80]. However, Weddeling et al. [38] have established that the predicted minimum pressure value does not entirely match the experimentally obtained data. The authors have observed that the analytical values are lower than the experimental values. Therefore, it can be used as a lower limit for the minimum magnetic pressure required to initiate plastic deformation [38]. As shown in Fig. 2.12, it has also been observed that the form-fit joints produced with the minimum energy required to fill the groove may not have sufficient joint strength.

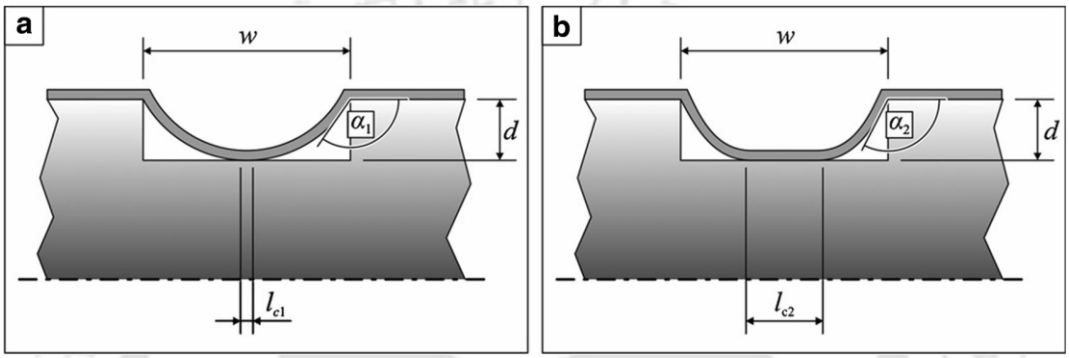

Fig. 2.12 Form-fit joint produced with (a) minimum discharge energy required to fill the groove and (b) higher discharge energy [38]

2.2.2.1 Factors affecting form-fit joining (EMC)

Apart from the discussed factor in 2.2.1.1, groove geometry affects the strength of a form-fit joint which involves groove width, depth and shape. The effect of the geometrical dimension of the groove on the strength of a form-fit joint can be analysed in three sections: the effect of i) groove radius, ii) groove width, and iii) the groove depth, as shown in Fig. 2.8.

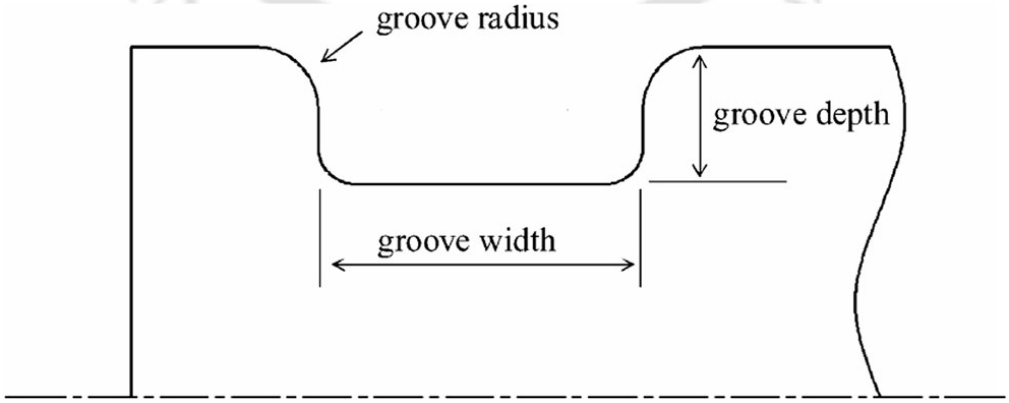

Fig. 2.13 Geometrical design parameter for the groove of a form-fit joint [59]

The parameters can have positive and negative effects on joint strength as there are optimum values of the parameters and increasing the dimension beyond the values will

lead to loss of joint strength [59]. Increasing the groove radius value decreases the thinning of the flyer tube on the groove profile. However, it facilitates the separation of parts during strength testing leading to separation failure of the joint. Increasing the groove depth contributes to the strength. However, excessive depth increment leads to excessive thinning of the flyer tube, causing a reduction in joint strength. Furthermore, increasing the width of the groove increases the joint strength as it leads to an increase in frictional contact, but further increment causes loss in joint strength as it leads to a wrinkling effect in the flyer tube [59].

Increasing the depth and decreasing the width cause higher deformation of the flyer tube, leading to a lower angle (α) and higher stiffness, as shown in Fig. 2.14. Further increasing the discharge energy leads to decreasing the angle (α), and upon contact of the flyer tube with the groove base, a force-fit joint gets created in addition to form-fit, as discussed by Weddeling et al. [38]. The optimum width of the groove depends on the thickness and hardness of the flyer tube [80]. Golovashchenko et al. [81] have also suggested the joint design with minimum groove width (four times the flyer tube thickness). However, increased groove width requires increased discharge energy to fill the groove, leading to higher joint strength.

Weddeling et al. [38] have also experimented on the shape of the groove geometries (rectangular, circular and triangular), as shown in Fig. 2.14. The authors have observed that the highest strength is achieved in the rectangular groove while the lowest strength is achieved in the triangular groove, as the interference stress is highest in the case of the rectangular groove. However, narrower and deeper (decreasing width and increasing depth) grooves lead to higher joint strength for both circular and rectangular shapes [82]. Similar observations have been made by Bühler et al. for rectangular-shaped grooves [80], and authors have further observed that at constant discharge energy and groove shape, having two grooves gives higher joint strength than one groove.

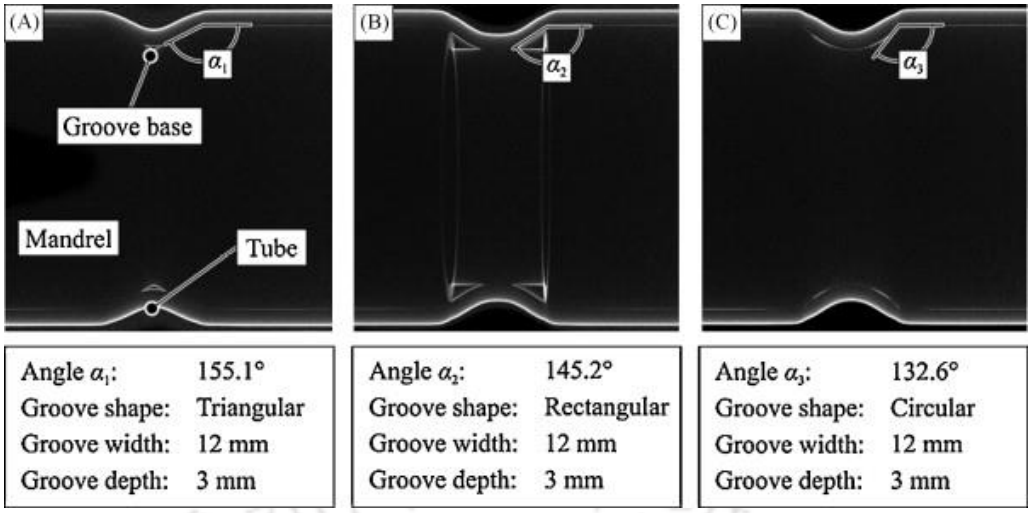

Fig. 2.14 Radioscopic picture showing the angle *a* at the groove edge with different groove shapes [38]

Vanhusel et al. [83] have also proposed that having two grooves adds to the joint strength. The authors have further developed a FEM simulation model and discussed that the highest stress concentration in the mandrel is at the upper corner of the groove, as also shown in Fig. 2.15.

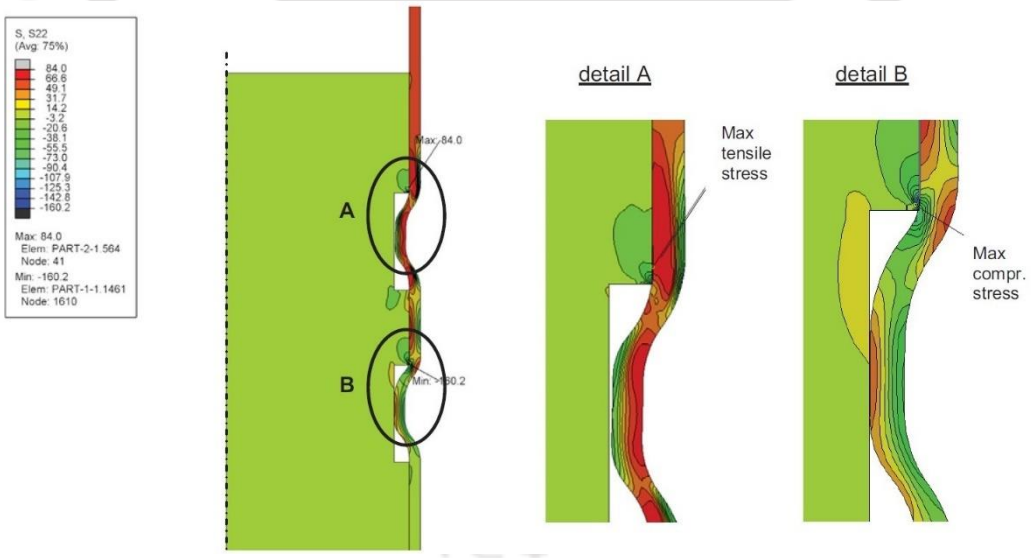

Fig. 2.15 Distribution of stress in a double-grooved form-fit joint under tensile load [83]

Weddeling et al. [37, 69] have further developed an analytical model to predict the strength of a form-fit joint by considering groove geometry, shape (circular, rectangular and triangular), and material properties of the workpiece as process parameters and validated it with experimental results. The authors have further suggested that applying the analytical approach can avoid solving complex finite element simulations and extensive experimental studies. Hence, this approach leads to a less expensive, time-

consuming design process and can be used as a valuable tool for optimising the EMF systems.

Park et al. [59] have discussed that the surface of the groove also has an impact on the joint. Therefore, joint strength (F_{joint}) can be expressed as,

$$F_{joint} = F_{friction} + F_{groove}, \quad (18)$$

here $F_{friction}$ and F_{groove} is the strength due to frictional resistance and groove resistance, respectively. However, frictional resistance is insufficient to sustain the form-fit joint load; therefore, the groove filling must be maximised to obtain a strong joint.

As far as using internal shafts is concerned for hollow target workpieces, Weddeling et al. [69] have observed that the use of supporting shaft increases the joint strength.

2.3 Electromagnetic welding

Electromagnetic welding (EMW) is also a high-speed, high strain-rate joining technique based on the principle of EMJ; when the impact velocity of the flyer tube exceeds the critical velocity in such a way that instead of a force-fit or form-fit bond, it forms a metallic bond with the target workpiece.

Brown et al. [84] have described in their early works that the metal going through the high-strain rate during EMW can be characterised as a high viscosity fluid despite being solid. Shribman et al. [85] have proposed that the welding phenomenon in EMW is due to forcing the atoms towards each other with heavy force to such extent that they surpass their neutral repulsion and achieve a stable equilibrium as they have exchanged and shared electrons.

Therefore, two popular explanations can be considered as joining mechanisms of EMW; a) solid-state and b) quick melting followed by solidification. Brown et al. [84] have discussed that EMW is achieved without reaching the melting point. Although entrapped melt pockets can be observed at the interface during tube-to-end plug joining by EMW. Shribman et al. [85] and Hisashi et al. [86] have further emphasised that the joining Mechanism during EMW is based on the acting pressure and not heat. Hisashi et al. [86] have developed a numerical simulation model to confirm that the heat produced during EMW is insufficient to cause any melting, which has been further verified by Uhlmann et al. [87] and Kore et al. [88] have further validated it with their numerical and experimental

investigations, respectively. Kore et al. [88] have not found any intermetallics and eutectic microstructure during EMW of aluminium with magnesium. The same has been concluded by Fan et al. [89] during Al-Fe joining by EMW, where the authors observed that the temperature at the interface is insufficient to melt Al and Fe.

Wu et al. [90] have investigated Al-Cu tubular joining using EMW and observed that high-temperature rise occurs at the welding interface, and the surface topology of the driver workpiece plays an essential role in waviness formation and mixing of materials at the interface.

Okagawa et al. [91] also talk about the occurrence of an immediate rise in temperature at the interface during EMW, but the heating of the workpiece is localised. It does not affect the larger area of the workpiece, which is further supported during a metallographic investigation of the Al-Cu tube-to-shaft EMW joint by Göbe et al. [92]. The authors have not discovered any diffusion layer and thus conclude that only localised melting is involved during the bonding and phase forming process, which also depends on the discharge energy and melting point of both the workpieces. Geng et al. [93] have studied the Al-Fe EMW process by numerical and experimental investigation and observed a transition recrystallisation zone caused by localised melting along with a low cooling rate. The authors have concluded that localised melting affects the phase formation and bonding phenomenon during the EMW process.

2.3.1 Factors affecting the EMW process

EMW process depends upon impact velocity, stand-off distance, impact angle and mechanical properties of the workpiece material.

EMW welds are usually high-strength welds as, during tensile testing, most of the failures occur in the workpiece material and not in the welding zone. Although, Okagawa et al. [91] have emphasised that it is only applicable when the standoff distance (as discussed in the previous section of EMC) is optimised as an optimum standoff distance is required for the flyer workpiece to accelerate. However, if the standoff distance is increased further, it might cause deacceleration and loss of kinetic energy.

Okagawa et al. [91] have believed that the current flowing through the coil after the impact can still assist positively by offering the joule heating effect to the weld, and therefore standoff distance should be chosen carefully, acknowledging the thickness of the

workpiece and discharge energy. As discussed in section 2.2.1.1, an increment in discharge energy increases the joint strength if all other parameters are constant, as confirmed by Kore et al. [94].

As we understand from section 2.2.1.1, the electrical conductivity of the flyer workpiece is one of the factors affecting the impact velocity, and therefore it is very challenging to directly accelerate a flyer workpiece having very low electrical conductivity. In these situations, an external driver workpiece of high electrical conductivity is used, which accelerates under the influence of magnetic pressure and impacts and transfers its kinetic energy to the flyer workpiece, which then accelerates and collides with the target workpiece as also suggested by Okagawa et al. [91] and Kore et al. [95]. Al and Cu are preferable choices for driver material.

Brown et al. [84] discuss that EMW welds have waviness morphology at the interface, which is the primary characteristic of impact welding. An investigation indicates that an increase in discharge energy causes an increase in impact velocity, which leads to an increase in amplitude and wavelength of the waviness morphology up to a certain point [96, 97]. Nassiri et al. [98] and Cui et al. [99] have supported this and have claimed that the instability causes the waviness formation in EMW.

Furthermore, Ben-Artzy et al. [100] have emphasised that waviness morphology in tubular EMW joints follows the Kelvin-Helmholtz instability mechanism and proposes the generated shock waves to be the origin of interference at the weld interface. The authors have validated that the wavelength of waviness morphology at the weld interface depends on the free path of propagation of shock waves in the target workpiece.

On the formation of intermetallics during EMW of certain material combinations, Göbe et al. [92] have concluded that it cannot be avoided, contrary to the popular belief of no intermetallic formation in EMW, as also supported by Lee et al. [101]. Psyk et al. [102] and Aizawa et al. [103] have also found an inhomogeneous layer at the weld interface. However, its significance can be limited during EMW, as intermetallics are controlled in melting pockets in waviness morphology [104]. Raoelison et al. [105] have also observed an intermetallic layer during Al-Cu joining, which has random pores and cracks in multiple directions, and the authors have claimed that the cavitation is the cause of pores.

However, in a condition of flat morphology, intermetallics takes the form of a film of varying thickness [106]. Wu et al. [90] have also observed intermetallic formation during Al-Cu tubular EMW joining; the authors propose the mass transportation and interdiffusion of materials to be the reason for intermetallic formation. Fan et al. [89] have also observed a 10 nm amorphous layer during Al-Fe joining by EMW due to the interdiffusion of materials.

A thin layer of intermetallics is created during EMW with lower discharge energy. However, an increase in discharge energy causes an increase in intermetallic layer thickness along with cracks and pores [92] which is further supported by Psyk et al. [102] as authors have discussed that increasing the discharge energy beyond a point might lead to microfracture.

Although Yu et al. [107-109] have examined discharge energy requirement during Al-Fe tube-to-tube joining using EMW and observed that minimum discharge energy is required to create the metallic bond. The authors have further studied different zone formations, observed transition zones, and hardness variations along different zones. As per Faes et al. [109], welding zones have three different regions, and actual welding occurs in the middle, where wavy morphology can be observed. The wavelength of waviness morphology increases towards the end of the weld.

Faes et al. [109] have also observed during the joining of Cu-brass tube-to-shaft using EMW that improper selection of process parameters can cause brittle intermetallic formation.

2.4 Hybrid joining

Hybrid joining (HJ) refers to the joining technique which has been developed by combining two or more different joining techniques, and in this context, it refers to the combination of techniques where one of the techniques is EMJ. Hybrid joining techniques can be beneficial in these scenarios to overcome the disadvantages of a multi-material joint while maintaining the advantages [110]. It offers more flexibility along with better control over joining.

Schmidt et al. [111] proposed an HJ technique combining electromagnetic and thermal joining for a metal-to-porcelain tubular joint, as the lower formability and strength of porcelain make it difficult to joint metallic tube to porcelain shaft by conventional EMJ

technique. In this process, metallic tubes are heated, followed by electromagnetic compression onto a porcelain shaft at elevated temperature. The heating of the metallic tube makes it softer and ensures its compression without fracturing the inner porcelain shaft. However, the strength of the joint is achieved after cooling the metallic tube, causing its shrinking and development of higher interference stress between two workpieces.

Alf et al. [112] have suggested utilising the induction heating method to heat the workpiece in the same setup that Uhlmann et al. [113] have further extended. The authors have combined inductive heating and electromagnetic compression to create a tubular joint of magnesium tubes which has very low formability at room temperature, and elevating the temperature extends its formability. The authors have used two different coils focused on the same working area for heating and forming purposes, and joints with good strength are observed. Belyy et al. [24] have also confirmed the addition of extra interference stress by heating during the EMJ process. Therefore, this section builds upon the benefits and necessities of developing and optimising hybrid joining methodologies for multi-material structures.

2.5 Motivation

The detailed literature review shows that a fair amount of work has been done in the EMJ domain to create tubular joints. However, despite all the work done, the process has not been widely adopted in industries. We feel that the heavy initial investment required in terms of a large capacitor bank and lack of in-depth analysis for various aspects of tubular joints can be a few of the contributing reasons. Therefore, this thesis aims to achieve better results (joint strength and leak tightness) at lower discharge energy by improving the factors involved in the process or developing a new process. EMC process is a form of EMJ and uses lower discharge energy to create interference-fit and form-fit tubular joints, but very few works have been done with an extensive investigation on joint integrity and failure modes.

Furthermore, using FEM models to replicate experimental investigations can save a lot of time and resources in a time of high computational ability. Therefore, extensive work is needed to develop the FEM models which can investigate joint integrity by predicting joint strength. Furthermore, EMC joints can only be used for structural applications as the produced joints are not leak-tight. Therefore, an improvement in the process is required to overcome the shortcomings of produced joints. Furthermore, finding the optimum

parameters requires a lot of initial trials in experimentation during EMW and developing a numerical strategy for identifying optimum parameters will expedite its adaptation.

2.6 Objectives of Work

The main objective of this work is to investigate (experimentally and numerically) various forms of the EMJ process. To improve the understanding of these processes. The primary objective is divided into the following subpart for the accomplishment.

1. Producing an improved interference-fit Cu-SS tube-to-tube joint
2. Development of a FEM model to predict the strength of an EMC joint
3. Studying the effect of various process parameters on the joint strength of an EMC joint through experimental and numerical investigations.
4. Developing a hybrid joining method to overcome the shortcomings of an EMC joint and perform a comparative analysis.
5. Studying the effect of various process parameters on the joint strength and leak tightness in the developed hybrid joining method.
6. Developing an SPH model to establish a weldability window and replicate experimental investigations during tubular joining using EMW

2.4 Novelty of the Work

After studying the available literature, we wish to put forward the following aspects as the novelty of the current thesis work.

1. A detailed experimental investigation has been discussed on the effect of various factors involved on different joint failure modes during different destructive testings of interference-fit tube-to-tube joints produced by EMC.
2. A multi-step FEM model is developed to simulate the destructive testing on an EMC tubular joint to predict the joint strength. Discussions on the effect of a straight slit of field shaper on circumferential Lorentz force distribution casing circumferential non-uniformity in EMJ of tubular components.
3. The current work addresses all the factors involved during tube-to-tube joining using EMC on the threaded surface with detailed experimental investigations, replicating all results with the numerical investigation and further analysing their relative contribution to strength with statistical analysis.
4. A novel hybrid joining process has been developed to improve the EMC process, which provides joints with high strength and leak-tightness and, therefore, proposes

the adaptation of produced joints for piping applications apart from structural applications.

5. The current work extensively discusses the joining of nuclear grade steels using the EMW process and uses a numerical strategy of developing an SPH model to predict the weldability window. This information improves the joint quality in the experimentation process.

2.7 Structure of Thesis

This thesis is organised into eight different chapters. The first chapter provides the introduction along with the working principle of the electromagnetic forming process, and the second chapter provides an extensive literature review on tubular joining by the EMJ process. Each chapter in this thesis ends with a summary outlining the achievements and findings which have been either obtained through experimental or numerical investigations. The remainder of this thesis is organised as follows:

- In chapter 3, a detailed experimental investigation is performed with various process parameters to produce an improved interference-fit multi-material Cu-SS tube-to-tube joint using the EMC process.
- In chapter 4, the FEM model is developed to predict the strength of an EMC joint. A coupled FEM model produces results of pull-out and compression tests of smooth surfaced EMC crimped Cu-SS tube-to-tube joint.
- In chapter 5, a further improvement is proposed on the previously discussed chapters by a detailed experimental and numerical investigation. Optimum process parameters are obtained by experimental, numerical and statistical analysis. The FEM model is further validated by fitting into an empirical relationship.
- In chapter 6, a novel hybrid joining technique is developed to overcome the shortcomings of an EMC tube-to-tube joint by combining the EMC process with adhesive joining named as EAAJ. A comparative experimental investigation is performed between EAAJ and EMC process for the smooth-surfaced Cu-SS tube-to-tube joint.
- In chapter 7, a detailed experimental investigation is performed to elaborate on the EAAJ process further to study the effect of various parameters (discharge energy, adhesive application length, types of adhesives and curing time) on EAAJ joint characteristics leading to the optimisation of the process.

- In chapter 8, the third aspect of tubular joining by EMF is also investigated. An SPH-based FEM model is developed for D9 tube-to-SS 316 LN end-plug joining EMW process to establish a weldability window by considering waviness formation as the criteria.

Conclusions and the scope of future work are presented in Chapter 9, followed by a list of publications and references.

3 Experimental Investigation of Electromagnetic Crimping

3.1 Introduction

This chapter explores the possibility of producing an improved interference-fit tubular joint between pure copper and stainless-steel tube by electromagnetic crimping (EMC). Successful joints are obtained with optimal parameters consisting of the outer surface profile of the inner tube and discharge energy. Joints exceeding the strength of the parent tube are formed without any metallic bond formation. Three destructive testings, pull-out, compression and torsion tests, have confirmed the successful joint formation as the failure occurs in the copper base tube. Analysis of failure mechanisms has revealed joint character at various discharge energies and surface profiles. Among smooth, knurled and threaded surface profiles with different discharge energy levels, the knurled surface provides the best joint strength at 6.2 kJ, showing a failure in the parent Cu tube during all three destructive testings. Radial deformation of the tubes is measured and compared for different discharge energy and surface profile. During microstructural analysis, no metallic bond formation and the wavy interface is observed between the joining partners. Furthermore, no elemental overlapping is observed during energy dispersive spectroscopy mapping analysis indicating an absence of diffusion. Higher micro-hardness is observed near the Cu-SS tubular joint interface due to strain hardening caused by high-velocity impact.

3.2 Experimental and testing procedures

3.2.1 Experimental setup

EMC working principle and setup are discussed in section 2.2. The experiments are performed on an EMF machine with circuit parameters, as shown in Table 3.1. When the tube is longer than the solenoid coil, then we have a non-uniform magnetic field in the crimping zone, whereas the equal length of coil and workpiece does not have such a problem as reported by Yu et al. [114]. Therefore, the requirement of an optimum coil length is necessary for uniformity of magnetic field distribution [115, 116]. Furthermore, magnetic flux is intensified and concentrated in the working zone by a single-step field shaper [117, 118], and it is effective even though the field shaper causes energy dissipation [119, 120]. A copper solenoid coil having an inner diameter of 49 mm and 13 turns distributed over a coil length of 91 mm is used as an inductance coil. A single-step copper field shaper, which concentrates and intensifies the magnetic flux from a total length of 90

mm to a working length of 20 mm, is also used. The detailed description of the dimensions of various parts in this EMC process is demonstrated in Fig. 3.1. Copper and stainless-steel tubes are placed coaxially with the coil and field-shaper using Polytetrafluoroethylene (PTFE) fixtures while high-temperature resistant Kapton tape is used as a spacer between the tubes. The discharged pulse current frequency is measured with an oscilloscope and a Rogwoski coil, as shown in Fig. 3.2.

Table 3.1 Circuit parameters of electromagnetic forming machine

Capacitance (C)	Maximum voltage	Maximum energy	Circuit inductance (L)	Circuit resistance (R)	Frequency
90 µF	15 kV	10 kJ	0.7 mH	12.5 m Ω	20 Hz

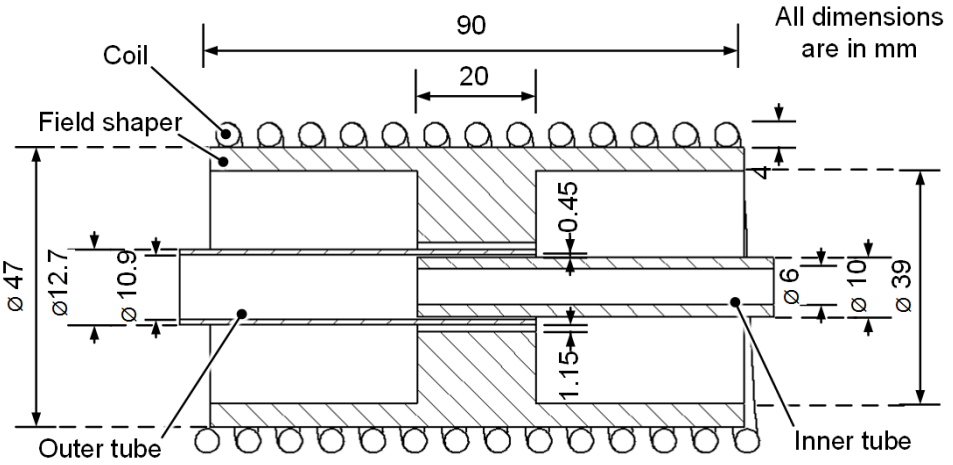

Fig. 3.1 Schematic diagram showing the dimensions of various parts in EMC setup

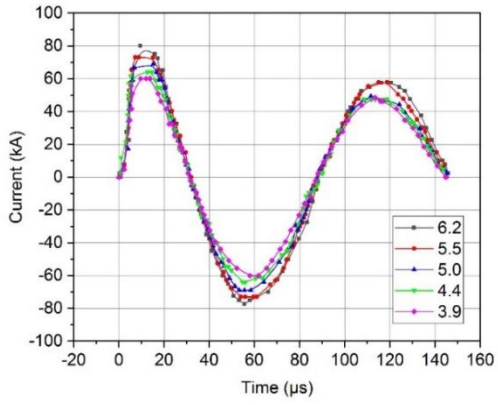

Fig. 3.2 Current waveform with time in the solenoid coil at five different discharge energy values

3.2.2 Tube geometry and material compositions

A copper tube of thickness 0.9 mm and a stainless-steel tube of thickness 2 mm are used as flyer and target tube, respectively. Dimensions of the flyer and target tube are shown in Fig. 3.1. A tensile test is performed on the tubes to determine various mechanical properties using a universal testing machine (UTM) at room temperature, and the results are tabulated in Table 3.2. Energy-dispersive X-ray spectroscopy is used to calculate the chemical composition of the Cu and SS 304 tubes, and the values are shown in Table 3.3 and Table 3.4, respectively. The radial gap between both the tubes, i.e. the stand-off distance, has been kept constant at 0.45 mm in all experiments. As our present work focuses on tube-to-tube joints, so efforts have been made to ensure the minimum gap between the inner diameter of the outer tube and the outer diameter of the inner tube to ensure a realistic tubular joint of similar diameters. However, having zero gaps may lead to a significant loss of joint strength as insufficient acceleration distance is available, causing insufficient deformation. Therefore, the minimum available stand-off distance is used and kept constant throughout the experiment. If we further reduce the stand-off diameter, the joint strength at specific discharge energy will significantly reduce, and upon increment in stand-off distance, the strength may increase, but to minimise the stand-off distance and maximise the inner tube size, the stand-off distance is not increased further.

The initial gap between the field shaper and the outer or flyer tube should be carefully controlled to achieve optimal results. A gap that is too small may result in a higher magnetic field strength, which can lead to a stronger weld, but it may also result in more significant distortion of the materials and a less aesthetically pleasing appearance, as also discussed by Cui et al. [121]. A gap too large may produce a weaker weld, but it may also result in less distortion of the materials and a more aesthetically pleasing appearance [122]. The initial gap of 1.15 mm is kept constant throughout the experiment to have some flexibility in terms of varying the outer diameter of the outer tube, as increasing the gap beyond that may lead to a significant loss of energy.

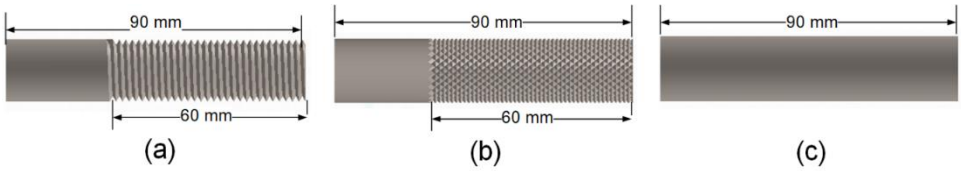

Fig. 3.3 Model representation of the stainless-steel inner tube having (a) Threaded, (b) Knurled, and (c) Smooth surface profile

Three different surface profiles (smooth, threaded and knurled) are used for the outer surface of the target tube. Model representation of the stainless-steel tube with varying surface profiles is shown in Fig. 3.3. ISO metric thread M10×1 thread and general-purpose righthanded diamond knurls with the helix angle of 60° is used.

Table 3.2 Mechanical and electrical properties of the copper and SS 304

Materials	Ultimate tensile strength (MPa)	Young's modulus (GPa)	Poisson's ratio	Electrical conductivity (S/m)
Copper	251	130	0.34	59.6×10^6
SS 304	505	193	0.29	1.389×10^6

Table 3.3 Chemical composition of the copper tube (wt. %)

Zn	Mn	Fe	Sn	P	Ni	Cu
0.01	0.1	0.02	<0.1	<0.1	0.02	>99.6

Table 3.4 Chemical composition of SS 304 tube (wt. %)

S	P	Si	Mn	Ni	Cr	C	Fe
< 0.03	< 0.045	< 1	< 2	8-11	17.5-20	< 0.08	Rest

3.2.3 Destructive testing for joint quality evaluation

3.2.3.1 Pull-out test

In this destructive testing, joint strength is evaluated by applying an axial tensile load or pull-out load on Cu-SS tubular joint samples. EMC experiments are performed at six different discharge energy levels for three different surface combinations (smooth, knurled and threaded). All these eighteen sets of experiments are repeated thrice to ensure repeatability. The pull-out test is performed at a constant pulling-out speed of 0.5 mm/sec on a Universal Testing Machine (UTM). A cylindrical metal plug is used at the end of the copper tube to facilitate the UTM machine's jaw to grip the copper tube without crushing it. No metallic support is required for the SS tube as SS has higher strength. Plug and pull-out test specimen design is considered from ASTM A370 [123], as shown in Fig. 3.4.

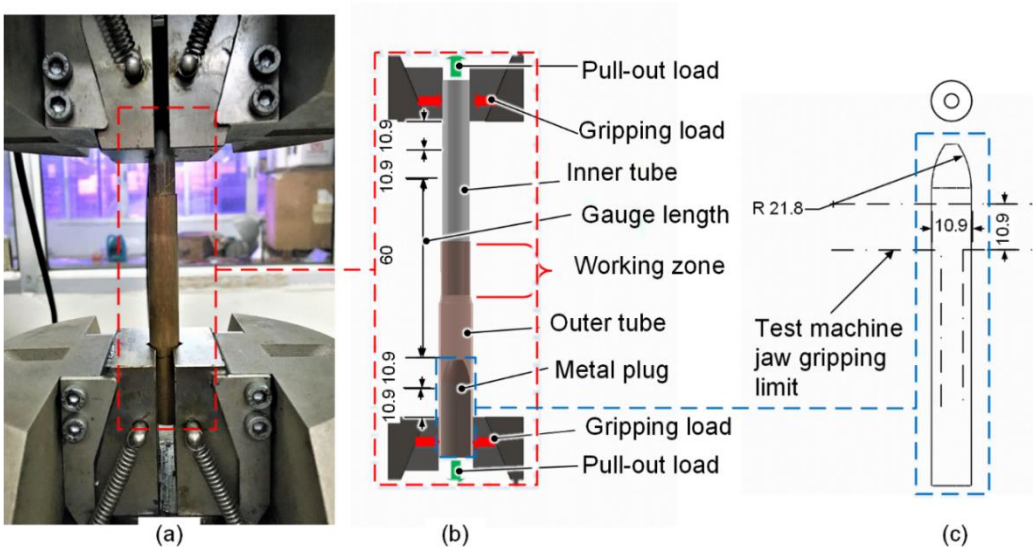

Fig. 3.4 (a) Experimental setup of pull-out/compression test, (b) schematic diagram of pull-out test for Cu-SS tubular joint and (c) metal plug used in the pull-out test

3.2.3.2 Torsion test

Torsion tests are carried out on a free-end type SS-Cu-SS tubular joint, as shown in Fig. 3.5, which is proposed by Park et al. [59] for proper gripping as to avoid any axial crack formation during the torsion test as discussed by Faes et al. [124]. SS tube is milled to flat at the ends for proper gripping by the torsion testing machine jaws. For three different surface combinations, (smooth, knurled and threaded) EMC experiments are performed at four different discharge energy levels. All these twelve sets of experiments are repeated. Schematic diagrams for a free-end sample and torsion test setup are shown in Fig. 3.5 and Fig. 3.6, respectively.

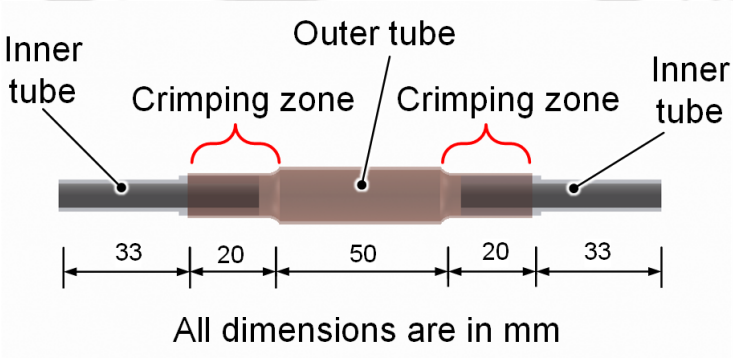

Fig. 3.5 Schematic diagram of a free-end sample for the torsion test

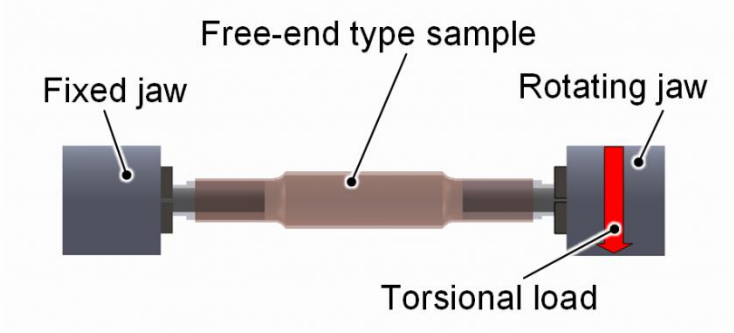

Fig. 3.6 Schematic diagram of the torsion test setup for SS-Cu-SS free-end type tubular joint

3.2.3.3 Compression test

Joint strength in compression is compared by applying an axially compressive load on the electromagnetically crimped Cu-SS tubular joint samples prepared for different surface combinations (smooth, knurled and threaded) at four different discharge energy levels. The compression test setup is the same as the pull-out tests setup, and the dimensions of the compression test samples are the same as the pull-out test sample as shown in Fig. 3.4, except an axially compressive load is applied instead of an axially tensile load. Finally, the test is performed at a constant compression speed of 0.5 mm/sec on a universal testing machine (UTM). It is ensured that the sample during compression testing is free from structural instabilities like buckling. The compression test sample during testing is assumed as a cylindrical beam fixed at both ends leading to its effective length factor being 0.5 [125]. The length of the sample is 124 mm, which can be observed from Fig. 3.4 (b). From the given information, the slenderness ratio is calculated as 14.8:1, which indicates the sample to be within the safe limit for buckling as per Rosato et al. [126].

3.2.3.4 Sample preparation for characterisation of EMC crimped joints

Samples are cut transversely in the form of a ring in the crimping zone using a wire electric discharge machine to characterise the tubular joint, as shown in Fig. 3.7 (a-b), and to avoid any microstructural changes; proper coolants are used. Mounting of obtained samples is done using phenolic powder for ease of handling. In the end, mounted samples are grind under water-cooling using Silicon carbide papers of grit sizes 80-1500 one after another, followed by Al_2O_3 abrasive polishing.

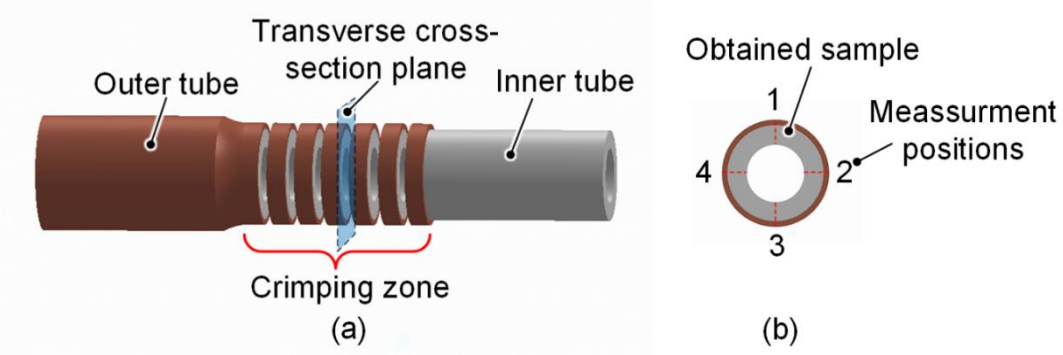

Fig. 3.7 Schematic of (a) cutting pattern for a joined sample and (b) obtained sample for characterisation of the joint

3.3 Results and discussion

Successfully crimped Cu-SS tubular joints for three different surface profiles at six different discharge energies. Crimped samples for three different surface profiles at 6.2 kJ discharge energy are shown in Fig. 3.8. Experiments are repeated at the same discharge energy to show the repeatability of the results.

3.3.1 Mechanical Pull-out testing

This study uses pull-out strength comparisons for threaded, knurled and smooth-surfaced crimped samples for discharge energies from 3.4 kJ to 6.2 kJ. A maximum pull-out load of 2.3 kN is obtained for the smooth-surfaced sample at 6.2 kJ of discharge energy which has drastically increased up to 8.3 kN and 8.2 kN (more than 3.5 times) in the case of the threaded and knurled sample respectively. The pull-out test is also performed for the parent copper tube, and the pull-out strength/failure load value of 8.34 kN is obtained.

Fig. 3.8 Crimped samples for three different surface profiles prepared at 6.2 kJ of different discharge energy levels

Table 3.5 Variation of failure modes with crimping parameters in pull-out test (showing maximum pull-out load in kN)

Energy	4.4 kJ			5.0 kJ			5.5 kJ			6.2 kJ		
Surface profile	TP	KP	SP	TP	KP	SP	TP	KP	SP	TP	KP	SP
Pull-out test results	× (7.00)	× (4.40)	× (1.84)	✓ (8.34)	✓ (8.29)	× (2.04)	✓ (8.35)	✓ (8.21)	× (2.28)	✓ (8.35)	✓ (8.24)	× (2.57)

threaded Profile (TP), knurled Profile (KP), smooth Profile (SP), detachment failure mode/Joint failure (×), crack failure mode/parent tube failure (✓)

Two different failure modes are observed during the pull-out test, reported by Weddeling et al. [38].

- Separation/detachment failure mode (joint failure): Joint strength is lower than the tensile strength of the base copper tube, which leads to detachment of the two joining partners. This failure occurs for all discharge energies for a smooth surface and lowers discharge energies (up to 4.4 kJ) for knurled and threaded surfaces, as shown in Fig. 3.9 (a-c).
- Crack failure mode (tube failure): Joint strength is higher than the tensile strength of the base copper tube. This failure occurs at higher discharge energy (for the threaded and knurled surface at 5.0 kJ or above), as shown in Fig. 3.10 (a-b), due to a fracture in the base copper tube.

Various samples and their failure modes with their maximum pull-out load are shown in Table 3.5.

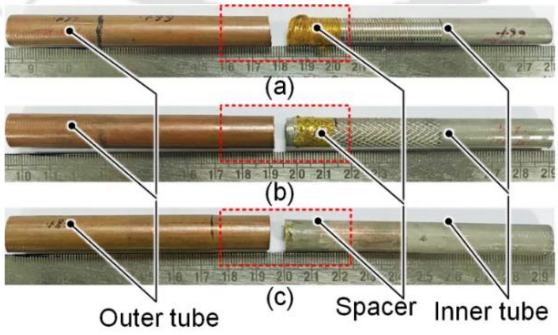

Fig. 3.9 Separation failure (Joint failure) in (a) threaded, (b) knurled and (c) smooth-surfaced sample

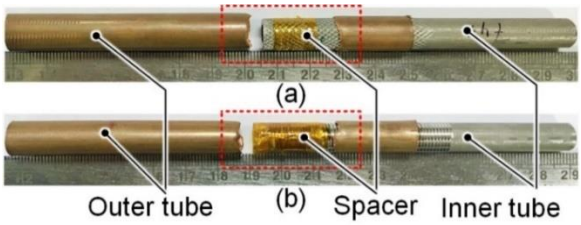

Fig. 3.10 Crack failure (Tube failure) in (a) threaded and (b) knurled surfaced samples due to weaker tube (copper) failure

The maximum pull-out load variation including the repeatability analysis is shown in Fig. 3.11. The pull-out load-extension plots for all the six different energy levels for threaded, knurled and smooth surfaces are shown in Fig. 3.12 (a), (b) and (c), respectively. Fig. 3.12 indicates an increase in pull-out load on increment in discharge energy for all three surface profiles. This can be explained as follows: increment of discharge energy leads to an increment in the radial deformation of the tubes and subsequent elastic recovery. This increases interference pressure, and hence pull-out load also increases. Weddeling et al. also suggested crack failure at higher discharge energies [38]. Furthermore, two significant pull-out load values are observed for the smooth surface, as shown in Fig. 3.11 (c), which are,

- The pull-out load at which the first relative motion between the two joining parts begin and
- The maximum pull-out load

The pull-out load, which has led to the initial relative motion between the two joining parts, can be critical in the early recognition of failure initiation so that steps can be taken before joint failure. These two pull-out load values are significantly different for smooth-surfaced samples due to the fretting and seizing effects as reported by Kleiner et al. [57].

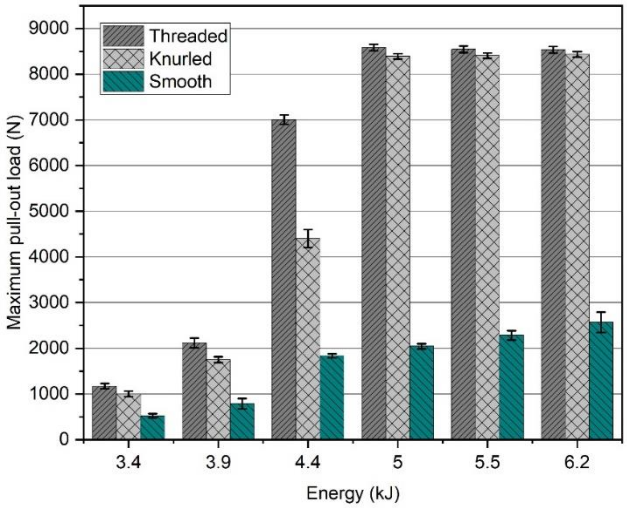

Fig. 3.11 Variation of maximum pull-out load with discharge energy for three different surface profiled samples

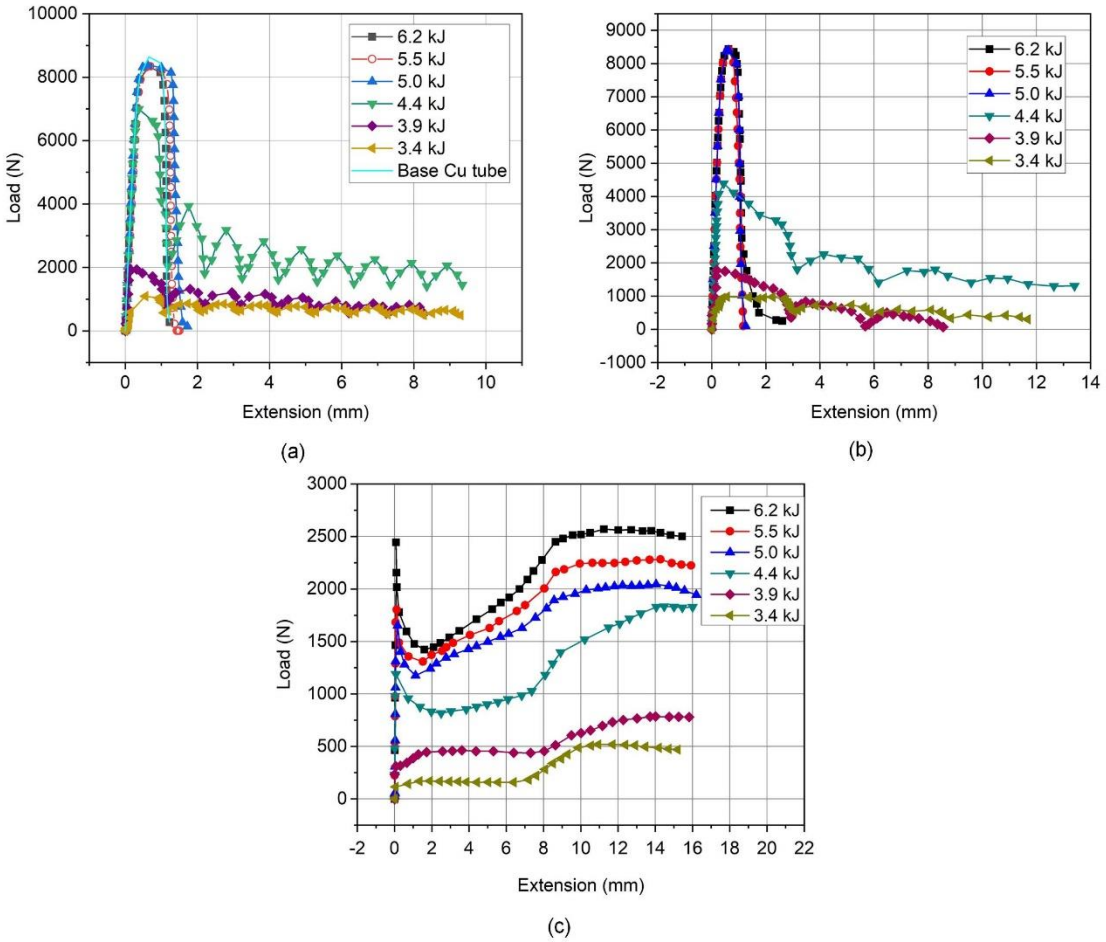

Fig. 3.12 Pull-out load-extension plot at six different discharge energies for (a) threaded, (b) knurled and (c) smooth-surfaced samples

A little variation of the results in the three repeated experiments for each case ensures the repeatability of our study as shown in Fig. 3.11. Fig. 3.12 further shows that the pull-out load-extension curve has followed a smooth pattern for a smooth surface and a repetitive cyclic pattern for the threaded and knurled surface. The wear mechanism and surface profile are responsible for the entire repetitive cycle pattern. Two-body abrasion wear mechanism is involved here, which offers resistance to the movement between Cu and SS tube. The resistance increases when a particular point in the outer tube crosses through the crests of the thread/knurl, and resistance decreases; hence, a release of load occurs when a particular one passes through the troughs of the thread/knurl. However, no zig-zag pattern is observed for threaded and knurled samples at discharge energy of 5.0 kJ or above because, in this case, failure occurs due to crack of the copper tube before initiating any relative motion between joining partners.

3.3.2 Compression test

This test comprises of compressive strength comparison for threaded, knurled, and smooth-surfaced EMC crimped samples for discharge energy ranging from 4.4 kJ to 6.2 kJ. Threaded surfaced samples at 5.5 kJ and 6.2 kJ have provided the maximum compressive strength of 8.6 kN among all. Two different failure modes are observed during this experiment,

- Sliding failure mode (joint failure): Here, joint strength is lower than the buckling resistance of the copper tube. This failure occurs at lower discharge energy (for all three surfaces up to 4.4 kJ) due to wear (Fig. 3.13).
- Buckling failure mode (tube failure): Here, joint strength exceeds the buckling resistance of the copper tube. This failure occurs at higher discharge energy (for threaded samples at 5 kJ or higher and knurled samples at 6.2 kJ) when the copper tube starts to buckle (Fig. 3.14).

Variation of maximum compressive load with discharge energy including the repeatability analysis is shown in Fig. 15. Load-extension plot for the threaded, knurled and smooth-surfaced sample at 5.5 kJ of discharge energy is shown in Fig. 3.16. Variation of failure modes and maximum compressive load with crimping parameters is shown in Table 3.6.

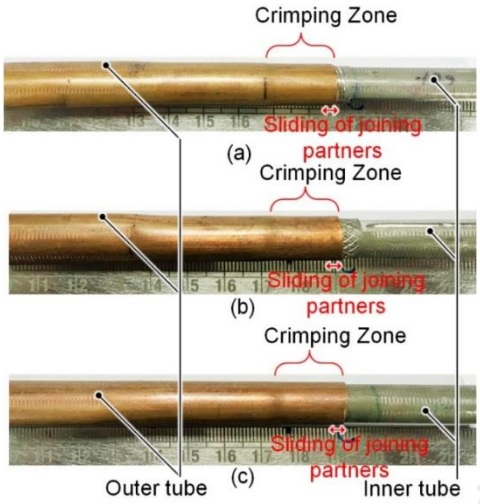

Fig. 3.13 Sliding failure during compression test in (a) Threaded-surfaced sample at 4.4 kJ, (b) Knurled surfaced sample at 5.5 kJ and (c) Smooth-surfaced sample at 6.2 kJ of discharge energy

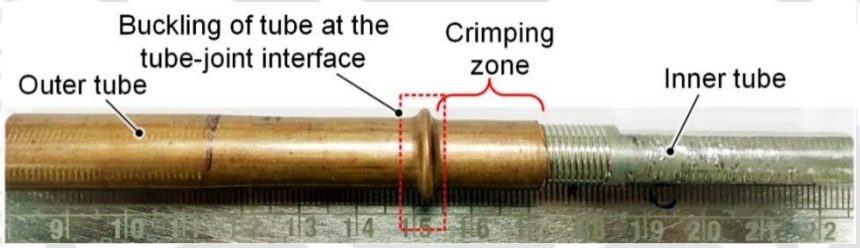

Fig. 3.14 Buckling failure in a threaded-surfaced sample at discharge energy of 5.0 kJ

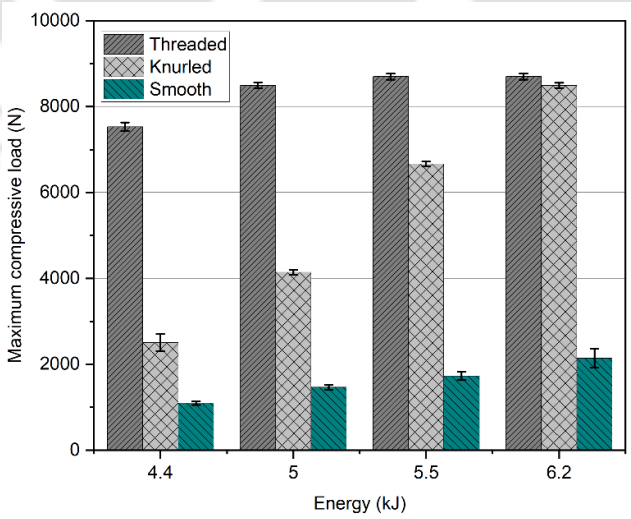

Fig. 3.15 Variation of maximum compressive load with discharge energy for three different surface profiled samples

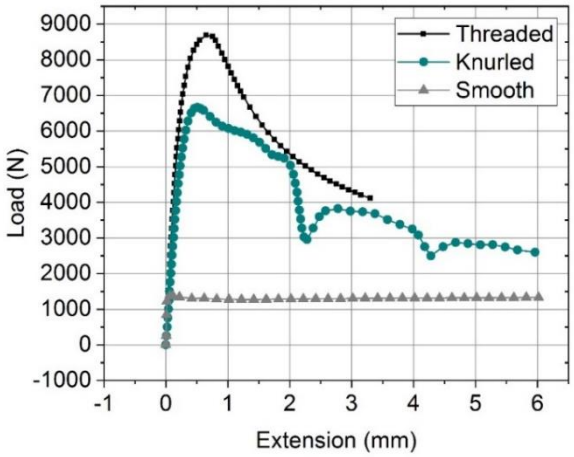

Fig. 3.16 Load-extension curve obtained during compression test for threaded, knurled and smooth-surfaced samples prepared at discharge energy of 5.5 kJ

Table 3.6 Variation of failure modes with crimping parameters in the compression test showing maximum compressive load in kN

Energy / Test	4.4 kJ			5.0 kJ			5.5 kJ			6.2 kJ		
	TP	KP	SP	TP	KP	SP	TP	KP	SP	TP	KP	SP
Compression test	× (7.53)	× (2.51)	× (1.1)	✓ (8.49)	× (4.14)	× (1.47)	✓ (8.69)	× (6.66)	× (1.73)	✓ (8.69)	✓ (8.49)	× (2.14)

threaded profile (TP), knurled profile (KP), smooth Profile (SP), sliding failure mode (×), buckling failure mode (✓)

3.3.3 Torsion test

This test comprises of torsional strength comparisons for threaded, knurled, and smooth-surfaced EMC crimped free-end type samples for discharge energy ranging from 4.4 kJ to 6.2 kJ. Knurled surfaced samples at 5.5 kJ and 6.2 kJ have provided the maximum torsional resistance of 32.25 Nm among all. Three failure modes are observed during this experiment.

- Sliding failure mode (joint failure): Here, joint strength is lower than the torsional resistance of the copper tube. This failure occurs at lower discharge energy (for all three surfaces up to 4.4 kJ) as well as at higher discharge energy (for threaded and smooth surfaces) due to wear (Fig. 3.17 (a-b)).

- Buckling failure mode with a crack (tube failure): Here, joint strength exceeds the torsional resistance of the copper tube. This failure occurs at higher discharge energy (for the knurled surface at 5.5 kJ or above) when after maintaining maximum torque for good angular displacement due to internal support of the SS 304 tube, the copper tube starts to buckle, followed by a transverse crack propagation (Fig. 3.18).
- Buckling failure mode without any crack (tube failure): This is a combination of the above two-failure mode and is observed for the knurled surface at 5.0 kJ when after buckling of the copper tube, the joint starts to fail before any crack propagation (Fig. 3.19).

Variation of maximum torsional resistance with discharge energy including the repeatability analysis is shown in Fig. 3.20. The torque-twisting angle plot for all three surfaces at 6.2 kJ of discharge energy is shown in Fig. 3.21. The representation of failure modes and torsional strength with crimping parameters is shown in Table 3.7.

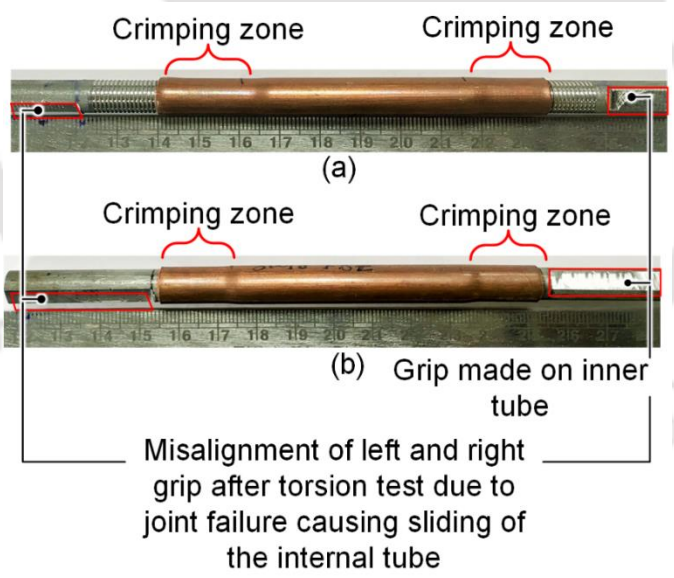

Fig. 3.17 Sliding failure in (a) threaded and (b) smooth-surfaced SS-Cu-SS fixed-end type joint prepared at 6.2 kJ of discharge energy

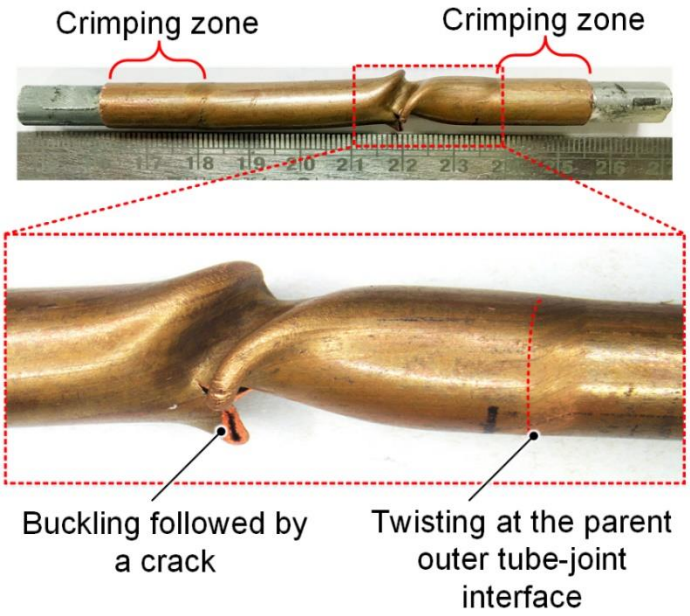

Fig. 3.18 Failure due to buckling of parent copper tube followed by crack propagation for the knurled-surfaced sample prepared at 6.2 kJ of discharge energy

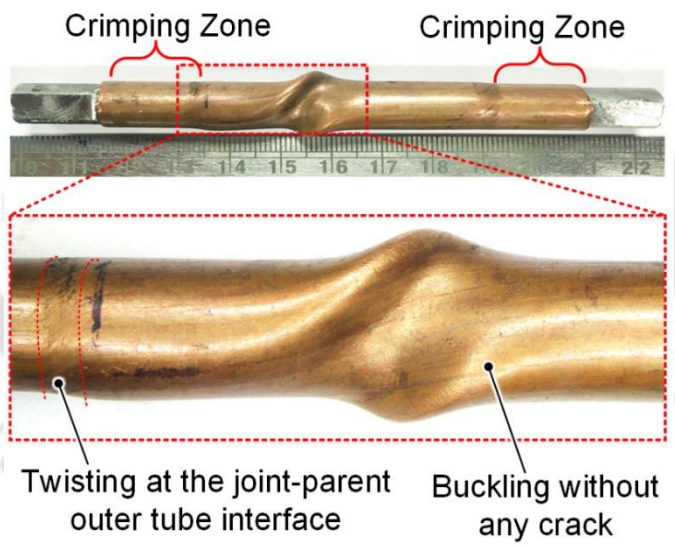

Fig. 3.19 Failure due to buckling in parent copper without any crack for the knurled-surfaced sample prepared at 5.0 kJ of discharge energy

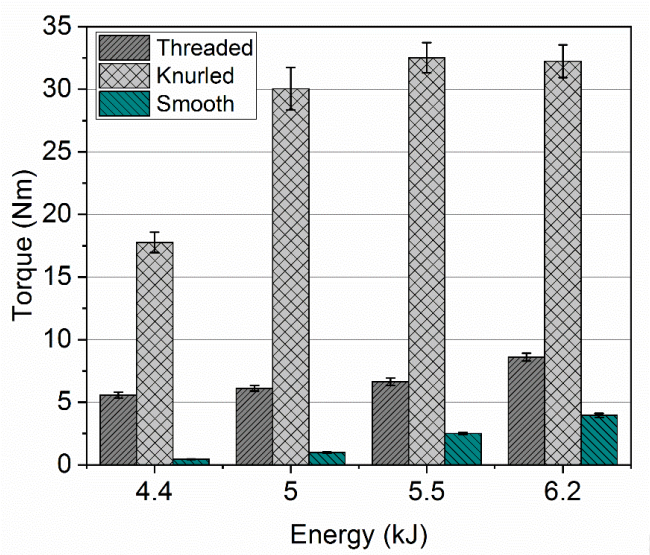

Fig. 3.20 Variation of maximum torque with discharge energy for three different surface profiled samples

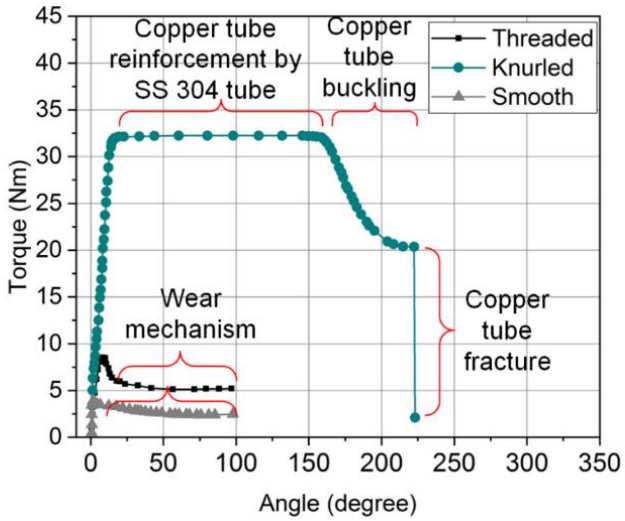

Fig. 3.21 Torque-twisting angle plot for threaded, knurled and smooth-surfaced fixed-end type sample prepared at 6.2 kJ of discharge energy

Table 3.7 Representation of failure modes with crimping parameters for torsion test (showing maximum torque in Nm)

Energy / Test	4.4 kJ			5.0 kJ			5.5 kJ			6.2 kJ		
Surface profile	TP	KP	SP	TP	KP	SP	TP	KP	SP	TP	KP	SP
Sliding failure mode (joint failure)	✓ (5.6)	✓ (17.8)	✓ (0.5)	✓ (6.1)		✓ (1.0)	✓ (6.6)		✓ (2.5)	✓ (8.6)		✓ (4.0)
Buckling failure mode with a crack (tube failure)								✓ (32.5)			✓ (32.3)	
Buckling failure mode without any crack (tube failure)					✓ (30)							

threaded profile (TP), knurled profile (KP), smooth Profile (SP), yes (✓)

3.3.4 Macrostructural and deformation analysis

Samples prepared for characterisation are photographed using an optical microscope on lower and higher magnifications, and to calculate the deformation, the outer diameters of all the crimped samples are measured using the NIS elements-microscope imaging software. The increased discharge energy adds more plastic deformation to the outer copper tube. Hence, the outer diameter and thickness of the copper tube in the crimping zone decrease with the increase of discharge energy. Variations of the outer diameter of the crimped sample and thickness of the outer tube with discharge energy for all the samples are shown in Fig. 3.22 and Fig. 3.23, respectively, where the initial outer diameter and thickness of the copper tube are 12.7 mm and 0.9 mm respectively.

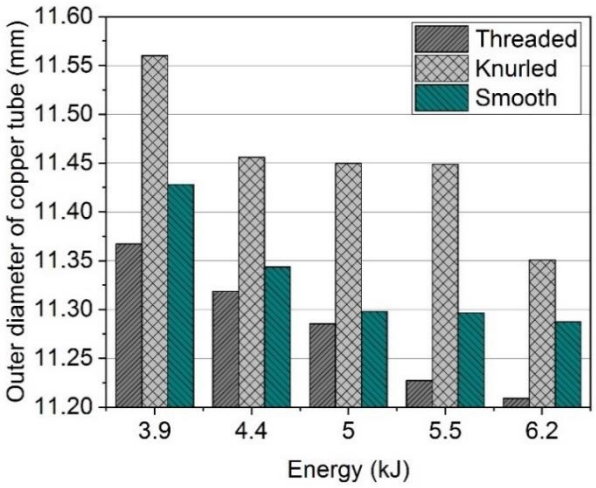

Fig. 3.22 Variation of the outer diameter of the tubular joint with discharge energy for threaded, knurled and smooth-surfaced samples after crimping

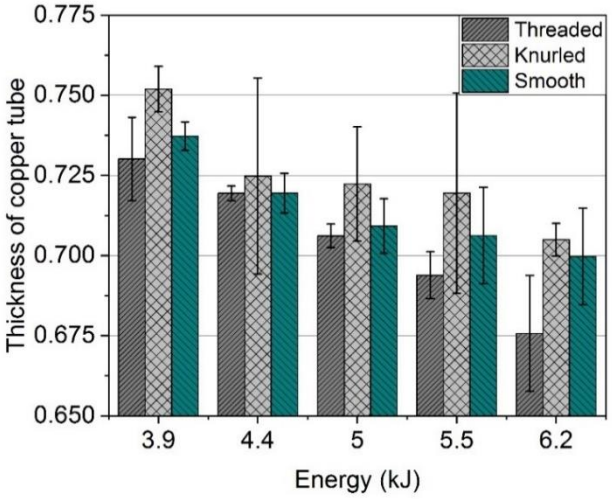

Fig. 3.23 Variation of the thickness of the outer (copper) tube after crimping in the crimping zone with discharge energy for threaded, knurled and smooth-surfaced sample

Higher magnification (400×) images of crimped samples at 6.2 kJ of discharge energy for all the surface profiles are shown in Fig. 3.24. At higher discharge energies, a negligible gap is observed for smooth-surfaced samples (Fig. 3.24 (d)), whereas; gaps can be seen in the threaded and knurled sample, indicating possibilities of more filling in the thread/knurl depths as shown in Fig. 3.24 (a-c). The threaded-surfaced sample shows a lower gap between the outer and inner tube on the crest side than on the root side in a particular transverse cross-section, as shown in Fig. 3.24 (a-b). Montages of the higher magnification images of the threaded, knurled and smooth-surfaced sample are shown in Fig. 3.25 (a), (b), and (c), respectively, for a zoomed-out cross-sectional view of the sample. Since the joint fails in the base copper tube (undeformed zone), which indicates that the

strength of the joint (in the crimping zone) is equal to or greater than the strength of the base copper, so increasing the filling of the outer tube by crimping at higher discharge energies will not be productive in terms of joint strength as the base copper tube strength limits maximum achievable strength.

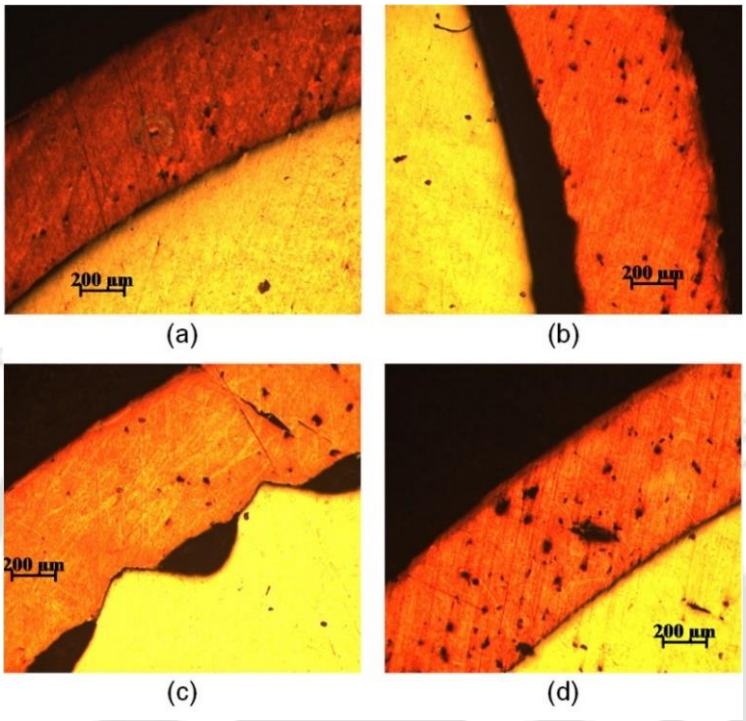

Fig. 3.24 Higher magnification (400×) macrographic image of Cu-SS tubular joint interface prepared at 6.2 kJ of discharge energy for (a) threaded (crest side), (b) threaded (root side), (c) knurled and (d) smooth-surfaced sample

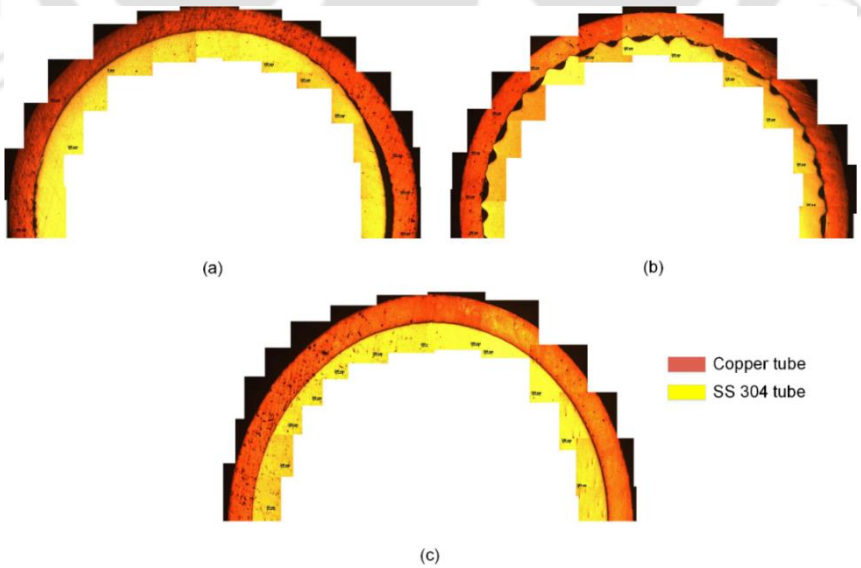

Fig. 3.25 Higher magnification (400×) macrographic image profile of Cu-SS tubular joint cross-section prepared at 6.2 kJ for (a) threaded, (b) knurled and (c) smooth-surfaced sample

3.3.5 Interface analysis

Microstructural and energy discharge dispersive X-ray spectroscopy (EDS) analysis is performed to understand the Cu-SS joint interface behaviour. Prepared samples at 6.2 kJ of discharge energy for characterisation are etched with a chemical solution (100 ml ethanol, 25 mm hydrochloric acid and 5 gm ferric chloride), and microstructural images are taken on an optical microscope at lower (100 ×) and higher (500 ×) magnification. The impact welding phenomenon is different from conventional welding phenomena like fusion welding, which goes through atomic diffusion due to the melting of the joining material leading to a straight joining interface. As documented in the literature [127], in impact welding wavy interface pattern is produced, which is not observed in the current electromagnetic crimping process, as shown in Fig. 3.26, Fig. 3.27 and Fig. 3.29. A gap between Cu and SS 304 material is observed at the interface. As discussed in the previous section, a threaded surfaced sample shows a lower gap in the trough side than the crest side, as shown in Fig. 3.26 (a) and (b). A gap in the range of 7-8 µm and 120-150 µm is observed in the crest and root sides, respectively, in the case of the threaded surfaced sample. A gap of 9-10 µm is observed in the contact zones of the knurled surfaced sample. At the same time, the smooth-surfaced sample has shown lower gaps in the range of 4-7 µm.

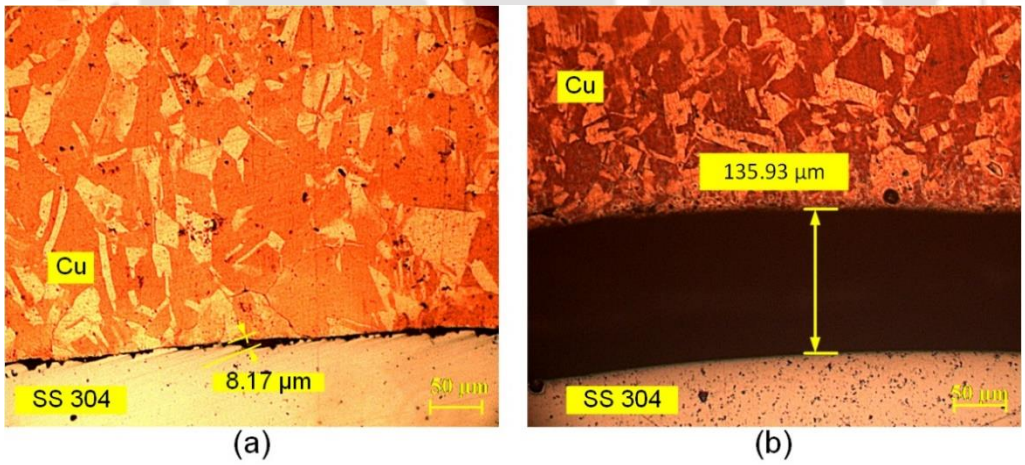

Fig. 3.26 Microstructural image of the threaded-surfaced sample at 500× magnification on (a) crest side and (b) root side

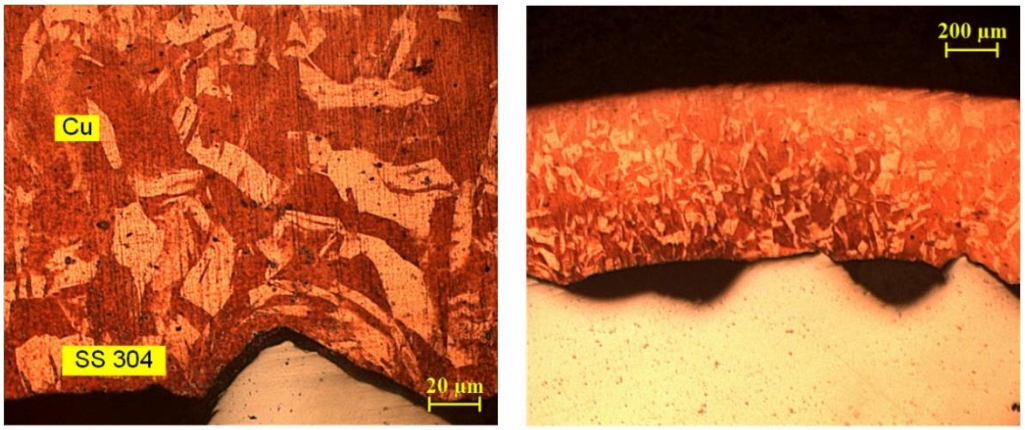

Fig. 3.27 Microstructural image of the knurled-surfaced sample at 6.2 kJ of discharge energy at (a) 500× and (b) 100× magnification

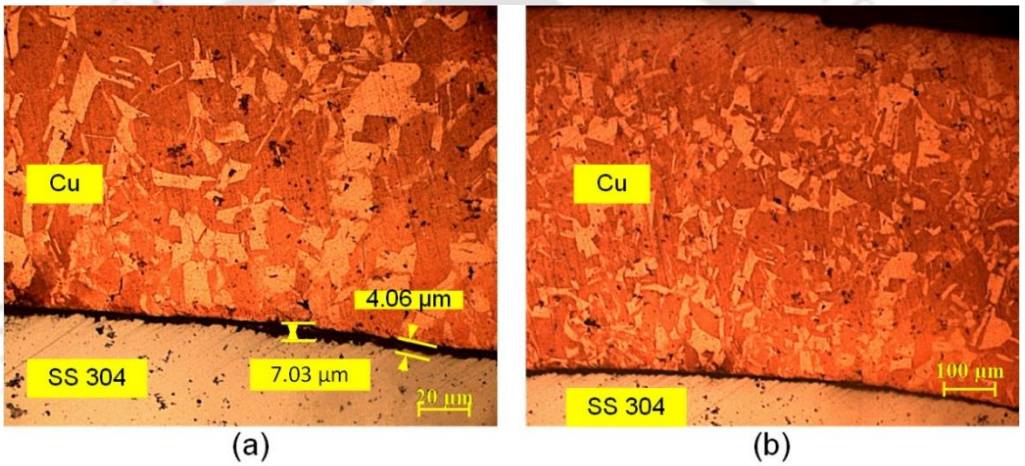

Fig. 3.28 Microstructural image of the smooth-surfaced sample at 6.2 kJ of discharge energy at (a) 500 and (b) 100× magnification

Furthermore, EDS elemental mapping is also performed to clarify any elemental diffusion and metallic bond formation possibilities. EDS elemental mapping distribution for a smooth-surfaced sample at 6.2 kJ of discharge energy for Cu-Fe, Cu and Fe is shown in Fig. 3.27 (a), (b) and (c), respectively. Any overlapped zone between Cu and Fe would have been an indication of diffusion [44]. No elemental overlapped area is observed in Fig. 3.29.

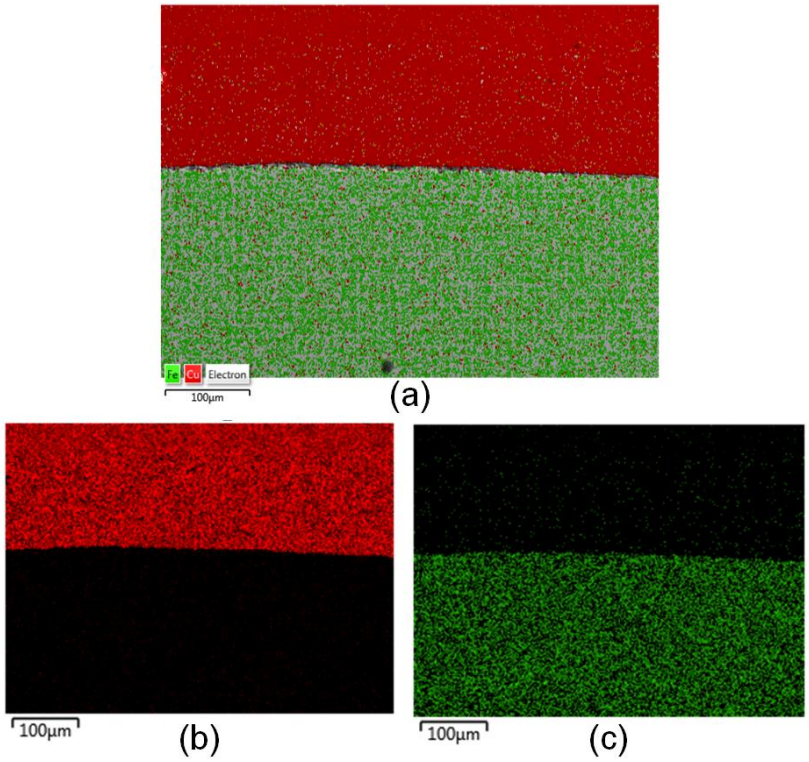

Fig. 3.29 EDS elemental mapping demonstrating (a) Cu-Fe distribution, (b) Cu distribution and (c) Fe distribution at the Cu-SS interface of a smooth-surfaced sample prepared at 6.2 kJ of discharge energy

3.3.6 Micro-hardness test

Vicker's micro-hardness test is performed on transversely cut samples throughout the thickness of the Cu-SS tubular joint at measurement positions, as shown in Fig. 3.7 (b). The test is repeated for better accuracy. The hardness value of 96.17 HV and 174.31 HV is observed for the base copper and stainless tube. A comparative plot for micro-hardness values, measured at every 200 µm from the joint interface in either direction for all the samples at 6.2 kJ of discharge energy is shown in Fig. 3.30. The maximum micro-hardness value of copper and stainless steel near the interface is 128.13 HV and 255.84 HV. This is increased due to the high strain rate of plastic deformation during EMC. This increment significantly depends on the surface profile as well (Fig. 3.30). Micro-hardness increases over the base material hardness for the outer copper tube are 33.08% for knurled surface, 29.73% for threaded surface and 18.60% for the smooth surface, as shown in Fig. 3.30. A micro-hardness increment is observed with an increase in discharge energy causing higher deformation, as shown in Fig. 3.31. Similar trends are observed in the Cu-SS interaction in the sheet joint by Kore et al. [51].

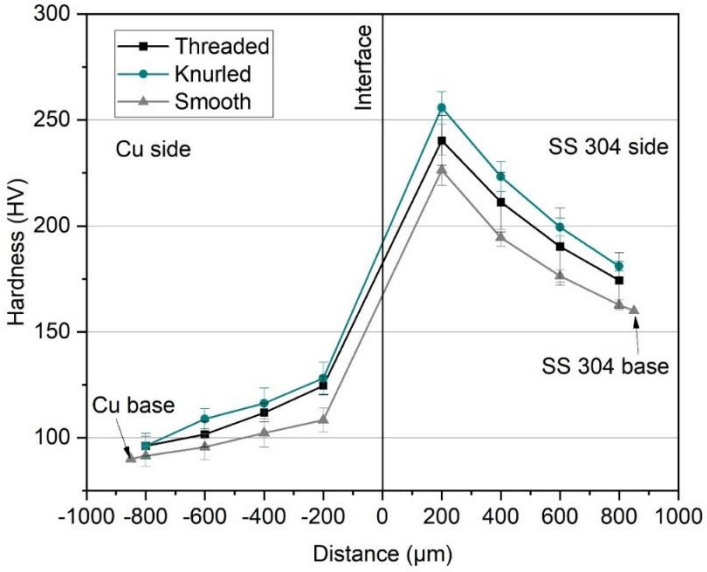

Fig. 3.30 Vicker's micro-hardness variation for 6.2 kJ of discharge energy across the cross-section of Cu-SS tubular joint interface using a load of 100 gm and a dwell time of 20 s

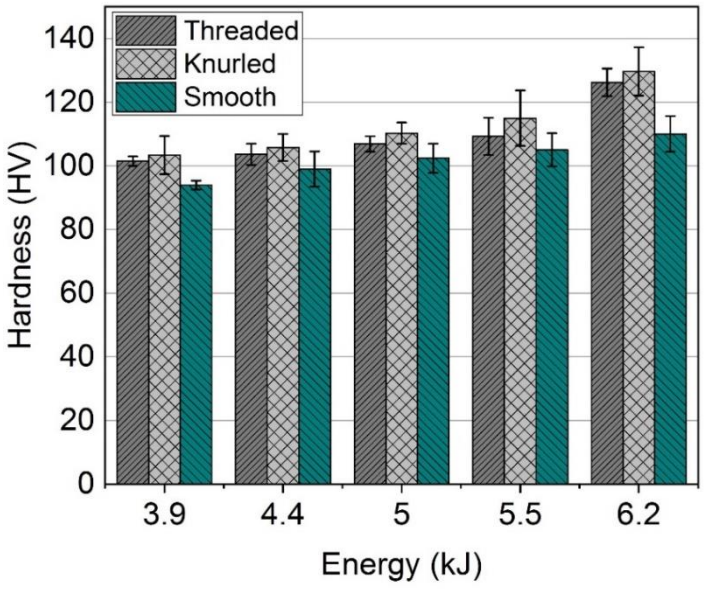

Fig. 3.31 Variation of micro-hardness for the copper tube at 200 μm from the interface in the crimping zone with discharge energy for threaded, knurled and smooth-surfaced sample

3.3.7 Surface Roughness

Surface roughness also impacts subsurface and surface stresses, structural integrity and wear behaviour of the parts. Abdulhadi et al. [128] have observed that parts having a surface roughness value of more than 3.114 μm tends to reduce hardness. In the case of tube-rod crimping, Kumar et al. have noticed the inner surface texture of the rod can affect the outer surface roughness of the joint in the case of the tube having a thickness of 0.5

mm [73]. Therefore, surface roughness is also analysed on the outer surface of the copper tube in the crimping zone for all three surfaces at higher discharge energy levels (5.0 kJ – 6.2 kJ) using a non-contact computerised surface profilometer with a precision of ±50 nm. The focal length of the optical profiler is 4.7 mm, and the maximum area captured by the non-contact profiler was 0.825 mm × 0.825 mm. For each surface profile, R_a (average roughness) values are measured at three different locations, and the average is taken for better accuracy, as shown in Table 3.6. Threaded surface profiles are observed to have the highest surface roughness among the three surfaces. A 3D fringe pattern for surface roughness for all three surfaces at 6.2 kJ discharge energy is shown in Fig. 3.32. Surface roughness is also being used as an indicator of joint performance. The higher surface roughness of the outer tube surface in the crimping zone indicates higher outer tube deformation leading to higher interference pressure build-up and higher joint performance. The trends can be seen in Table 3.8. It further indicates that higher discharge energy leads to higher surface roughness, verifying our statement.

Table 3.8 Average surface roughness (R_a) in µm in the crimped zone for threaded, knurled and smooth-surfaced samples prepared at higher discharge energy levels (5.0 kJ – 6.2 kJ)

Surface / Energy (kJ)	Threaded	Knurled	Smooth
6.2	2.734	0.966	0.705
5.5	2.512	0.943	0.674
5.0	2.441	0.936	0.591

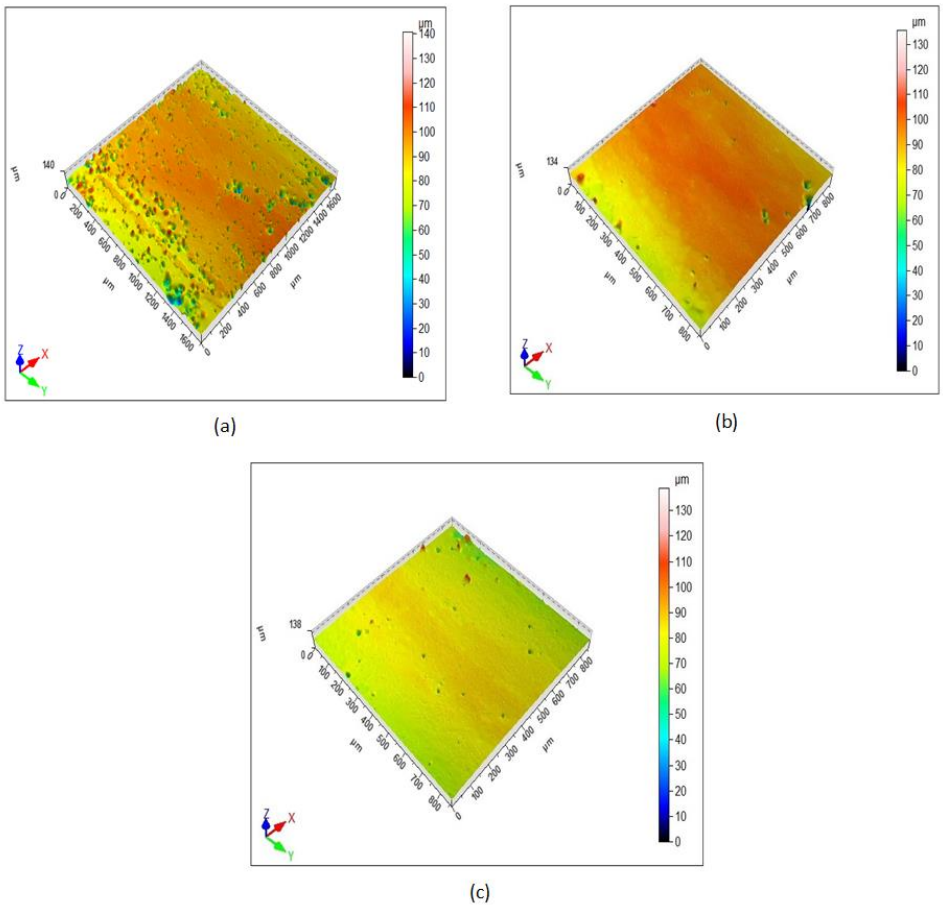

Fig. 3.32 3D fringe pattern for (a) threaded, (b) knurled and (c) smooth-surfaced sample prepared at 6.2 kJ of discharge energy

3.4 Conclusions

This chapter has shown the feasibility of a successful interference-fit tubular joint formation between Cu and SS tubes by the EMC technique. Contrary to conventional joining methods and high-energy EMW, it is possible to successfully create a Cu-SS tubular joint having higher joint strength than the base copper tube without any metallic bond formation. From the results, the following conclusions can be drawn:

- Pull-out strength is significantly increased by 2 times for threaded/knurled surfaced joint than the smooth-surfaced joint at 6.2 kJ of discharge energy.
- Compressive strength has also increased by 3.1 times for threaded surfaced joint compared to the smooth-surfaced joint at 6.2 kJ of discharge energy.
- Therefore, the pull-out and compression test conclude the threaded surfaced joint to be better suited among all three surface profiles for handling axial loading because the axial strength of the threaded surfaced joint is greater than equal to the axial strength of the knurled and smooth-surfaced joint.

- However, the torsion test suggested knurled surfaced joint to be a better surface profile for handling torsional resistance. Torsional strength is increased by 7 times after using a knurled outer surface profile of the inner tube for EMC crimped joints at 6.2 kJ of discharge energy.
- Therefore, knurled surfaced joint prepared at 6.2 kJ of discharge energy is the most versatile joint as per all three destructive testings. So knurled surface should be preferred for versatile loading applications.
- Macrostructuctal and deformation analysis has revealed that increasing discharge energy to increase the filling of outer tube material in the thread/knurl will not contribute towards strength once the maximum strength of the joint, which is the strength of the base copper tube, is reached.
- Interface analysis has revealed the absence of any atomic diffusion and metallic bond formation. Therefore, the strength is contributed purely by the interference-fit joining.
- Micro-hardness increment across the Cu-SS interface is observed due to deformation of the crimping layer and their work hardening. Knurled surfaced joints have shown the highest micro-hardness increment among all.

Surface roughness analysis has indicated a higher R_a value on the outer surface of the copper tube for threaded joint as compared to the other two types of surfaces. Surface roughness increases with an increase in discharge energy, indicating an increase in joint performance.

4 Finite Element Modelling of Smooth-Surfaced EMC Joints

4.1 Introduction

In previous chapter 3, the EMC technique is experimentally investigated for an improved Cu-SS tube-to-tube joining to obtain joints with higher strength than the base Cu tube failure strength. However, numerical prediction of the strength of an electromagnetically crimped joint can be of great use and can save a lot of time and resources. In the author's knowledge, numerical predictions of pull-out and compressive strength of electromagnetically crimped joints have not been reported yet. Therefore, this chapter presents a finite element modelling technique to investigate EMC joint and joint strength. This chapter explores a novel finite element model that has been developed to predict the pull-out and compressive strength of the smooth-surfaced Cu-SS tube-to-tube joint, joined using the EMC technique. Numerical simulations are performed using the electromagnetic (EM) module of LS-Dyna ™, which uses a combination of the finite element method and boundary element method (BEM). The work is performed in two parts, where the first part discusses a detailed numerical simulation of the EMC process, and in the second part, a model has been developed to simulate destructive testing for strength prediction. The model is validated with experimentally observed radial deformation and thinning of the outer tube during electromagnetic crimping, pull-out and compression strength. The effect of the slit of the field shaper on Lorentz force distribution is also studied, and It is observed that the slit of the field shaper leads to non-uniformity in Lorentz force distribution along the circumference, causing uneven radial deformation.

4.2 Methodology

4.2.1 Process parameters

EMC experiments are performed on an electromagnetic forming machine with circuit parameters, as shown in Table 3.1. The detailed dimension of the working setup is shown in Fig 3.1. The experiments are performed at five different discharge energy values: 3.9 kJ, 4.4 kJ, 5 kJ, 5.5 kJ and 6.2 kJ. Discharge current waveforms are measured with the help of an oscilloscope and a Rogowski coil, shown in Fig. 3.2. Smooth-surfaced profile is considered for the outer surface of the inner SS tube.

4.2.2 Finite Element Modelling

A finite element model is developed using the electromagnetic module of LS-Dyna ™, which involves a combination of the finite element method (FEM) and boundary element method (BEM) to solve the multi-physics problem of electromagnetic crimping as discussed by L'Eplattenier et al. [129]. The combination allows studying the motion of the conductor without the necessity of remeshing the surrounding air in the simulation model. The BEM efficiently solves the Maxwell equation for regions with no eddy current. The diffusion part is solved using FEM, and the induction part is solved using BEM. The BEM technique computes the interaction between different conductors through the electromagnetic field in the air surrounding. It removes the problems of meshing associated with the complex air region involving complicated conductor geometries [130, 131].

Furthermore, the BEM technique eliminates remeshing issues while using an air mesh around a moving conductor. During the first step, the magnetic field is evaluated by the electromagnetic solver to calculate the Lorentz force at each node that acts as input load to the mechanical solver at each time step which further computes the deformation of the workpiece and updates the deformed geometry in the electromagnetic solver that impacts the computation of magnetic field leading to modification of the structural deformation. This iteration continues until the end time is reached, as shown in the flow chart in Fig. 4.1. The measured damped sinusoidal current that flows through the solenoid coil after the discharge of the capacitor bank is applied as an input load. It has been stated that the majority of the workpiece deformation occurs during the first half of the current time cycle. Therefore, only the first half of the current-time waveform is applied to the finite element model as an input load [19].

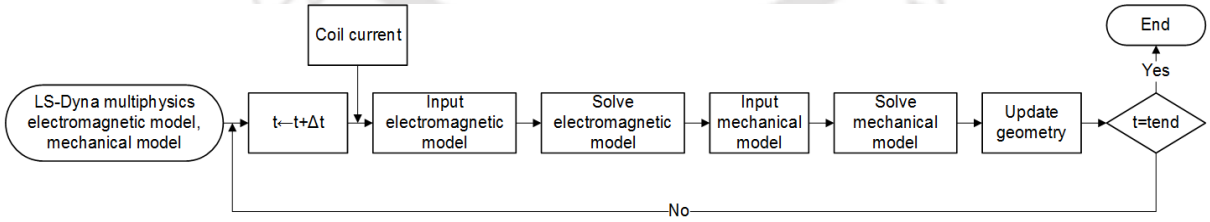

Fig. 4.1 Flow chart of the coupled simulation in LS Dyna

Furthermore, these are some assumptions/conditions considered for the simulation model, such as,

- The distribution of current through the coil cross-section is assumed to be uniform
- Permeability and conductance of the material is assumed to be constant and isotropic throughout the simulation period

- Joule heating loss is not considered in this simulation model
- The solenoid coil and field shaper is constrained to restrict any movement. The free ends of both tubes are constrained in all directions to replicate the nylon fixture holding the tubes during the experiment.

Since only hexahedral elements can be used for the electromagnetic module of LS-Dyna ™, geometries with complications are meshed in Hypermesh software and imported to LS-Dyna ™ software for computing. Tubes are modelled with general-purpose eight-node linear brick elements (C3D8R). Solenoid coil and field shaper are modelled with four-node rigid elements (R3D4). Total 47348 numbers of elements are used in the simulation model. Fine mesh is used to describe the inner SS 304 tube compared to the copper coil, and field shaper and even finer mesh is used for the outer copper tube, which is our main geometry of interest. 10 layers of elements through the thickness of the outer copper tube and 3 layers of elements through the thickness of the inner tube have been used. Meshed model for the analysis in the LS-Dyna ™ Simulation model is shown in Fig. 4.2.

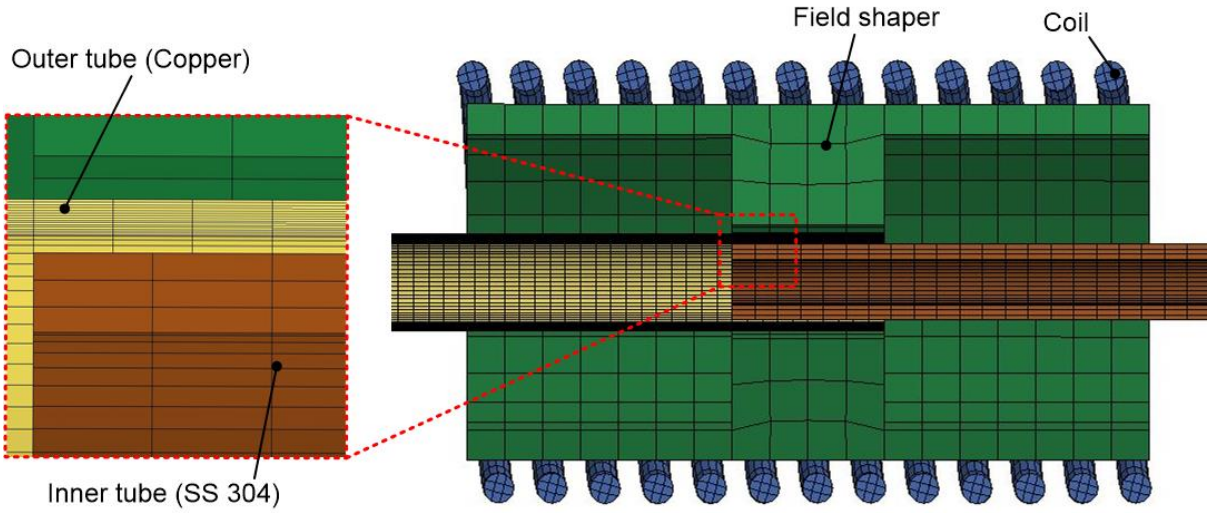

Fig. 4.2 Sectional view of the simulation model showing meshing of parts for electromagnetic and mechanical analysis

Johnson-cook (J-C) material model is used for both the workpiece material, which is a recommended material model for high temperature and high strain-rate process [19]. J-C model can be described as:

$$\sigma_y = (A + B\varepsilon^n)\left(1 + C\, ln\left(\frac{\dot{\varepsilon}}{\dot{\varepsilon}_o}\right)\right)\left(1 - \left(\frac{T - T_r}{T_m - T_r}\right)^m\right), \quad (4.1)$$

where, σ_y represents equivalent plastic stress. ε, $\dot{\varepsilon}$ and $\dot{\varepsilon}_0$ represents equivalent plastic strain, equivalent plastic strain rate and reference equivalent plastic strain rate,

respectively. *A, B, C, n* and *m* are material constants, whereas *T*, T_r and T_m represent absolute temperature, room temperature and melting temperature, respectively. Parameters of the J-C material model for Cu and SS 304 are shown in Table 4.1. Properties of the materials are considered to be isotropic for this simulation.

The shock wave equation of state (EOS) is defined in the J-C material model to construct the pressure-volume relationship during shock compression of solid analysis. Linear polynomial EOS used in the J-C material model can be described as,

$$P_1 = c_o + c_1\mu + c_2\mu^2 + c_3\mu^3 + E_o(c_4 + c_5\mu + c_6\mu^2), \quad (4.2)$$

where P_1 denotes pressure, c_o, c_1, c_2, c_3, c_6, c_4, c_5 and c_6 are the constants of EOS, $\mu = \frac{\rho}{\rho_0} - 1$ denotes compression factor where $\frac{\rho}{\rho_0}$ being the ratio of current density to the initial density and E_o represents specific internal energy. Constants of EOS for copper are shown in Table 4.2. Deformation of the outer tube in the crimping zone of the interference fit joint prepared by EMC in the numerical simulation model using LS-Dyna ™ at 5.5 kJ of discharge energy for three different time values are shown in Fig. 4.3. Results calculated from the numerical simulation model must be converged with mesh refinement and time step refinement. Therefore, a convergence study is performed for different time steps and mesh size values and converged results are obtained.

Table 4.1 Constants of J-C material model for Cu and SS 304 [19, 132]

Material	A(MPa)	B(MPa)	n	C	T_m(K)	m
Copper	90	292	0.31	0.025	1331	1.09
SS 304	350	275	0.36	0.022	1723	1

Table 4.2 Constants of linear polynomial EOS of copper [132]

Materials	c_o	c_1(N/m²)	c_2(N/m²)	c_3	c_4	c_5	c_6	E_o
Copper	0	140 e⁹	2.8 e⁹	1.96	0.47	0	0	0

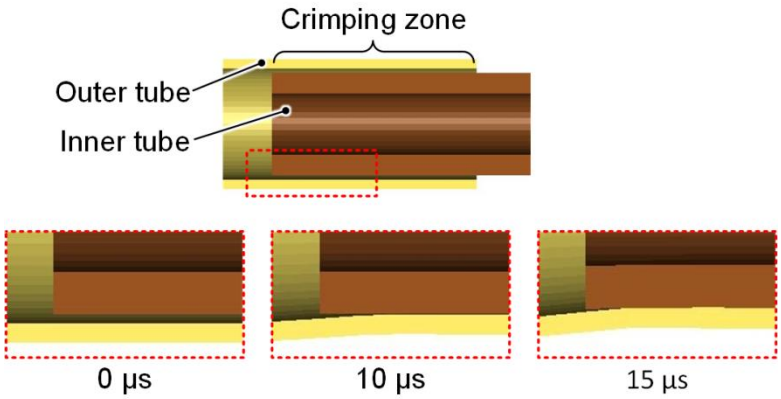

Fig. 4.3 Deformation stages of EMC crimped joint at three different times at 5.5 kJ of discharge energy observed in the simulation model

4.3 Results and discussion

A Mesh convergence study has been performed at four different mesh sizes, and the results are measured at four different nodes on the outer tube in the crimping zone selected at equal node intervals along the tube length and averaged. Variation of impact velocity and effective plastic strain with time at 3.9 kJ of discharge energy for four different mesh sizes of the outer tube (0.5 mm, 1 mm, 2 mm, and 3 mm) in the crimping zone of the outer tube is shown in Fig. 4.4. Results are observed to be converged, and hence further reduction of mesh size does not affect the results.

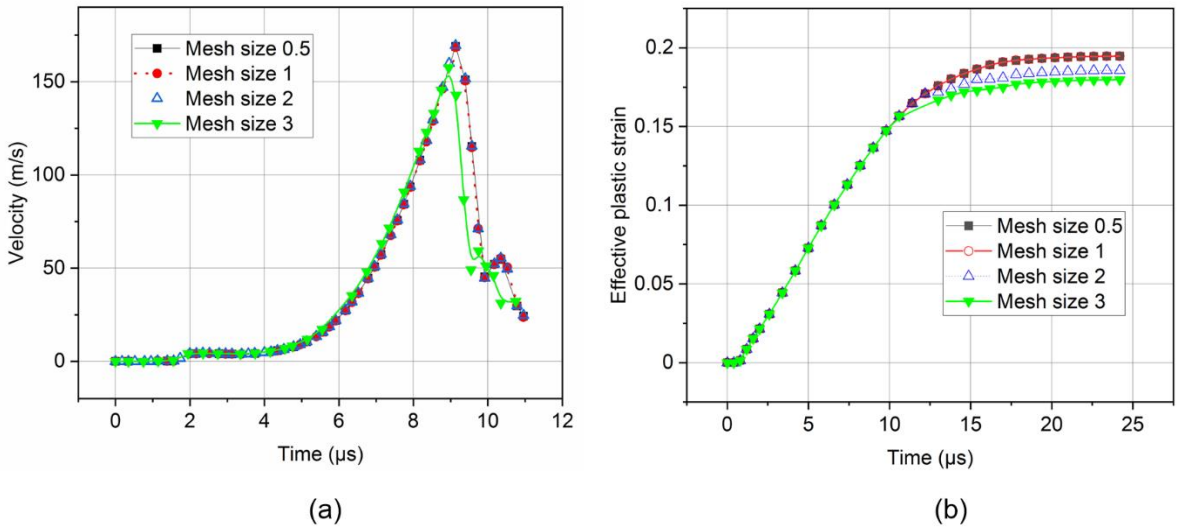

Fig. 4.4 Variation of (a) impact velocity and (b) effective plastic strain with time for different mesh sizes at 3.9 kJ of discharge energy during simulation

4.3.1 Effect of discharge energy

Fig. 4.5 shows the selected nodes on the outer tube along the length from the free end of the outer tube tip in the crimping zone for measurement of the magnetic field, radial displacement, velocity and effective plastic strain in the simulated model.

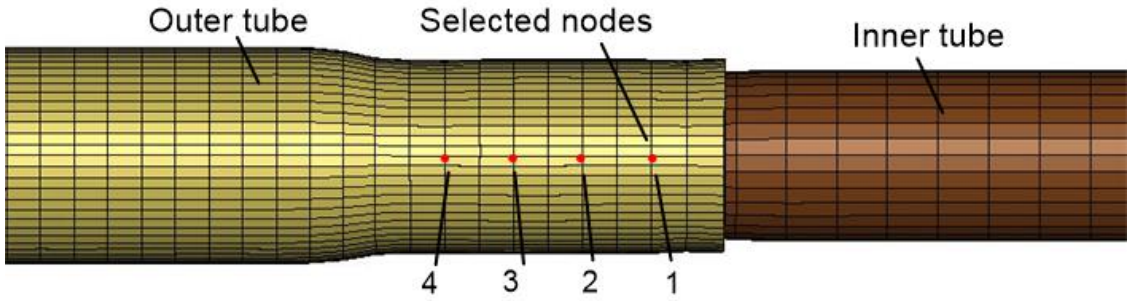

Fig. 4.5 Selected nodes for measurement of parameters in the coupled simulation model

4.3.1.1 Magnetic field

Fig. 4.6 (a) shows the variation of the magnetic field with time for five discharge energy values. The magnetic field is observed to be proportional to the discharge energy, and the maximum magnetic field of 18 T observed at 6.2 kJ of discharge energy in the simulation model.

4.3.1.2 Radial displacement

Fig. 4.6 (b) shows the variation of radial displacement with time during the crimping process for various discharge energy in the simulation model. Maximum radial displacement is found to be 0.96 mm at 6.2 kJ of discharge energies. The radial deformation is proportional to the magnetic flux density. So an increase in magnetic flux density due to an increase in discharge energy leads to an increase in radial deformation.

4.3.1.3 Impact velocity

Fig. 4.6 (c) shows the variation of impact velocity of the outer tube in the crimping zone for various discharge energy values in the simulation model. Impact velocity is observed to be proportional to the discharge energy and therefore, maximum velocity is observed at 6.2 kJ of discharge energy.

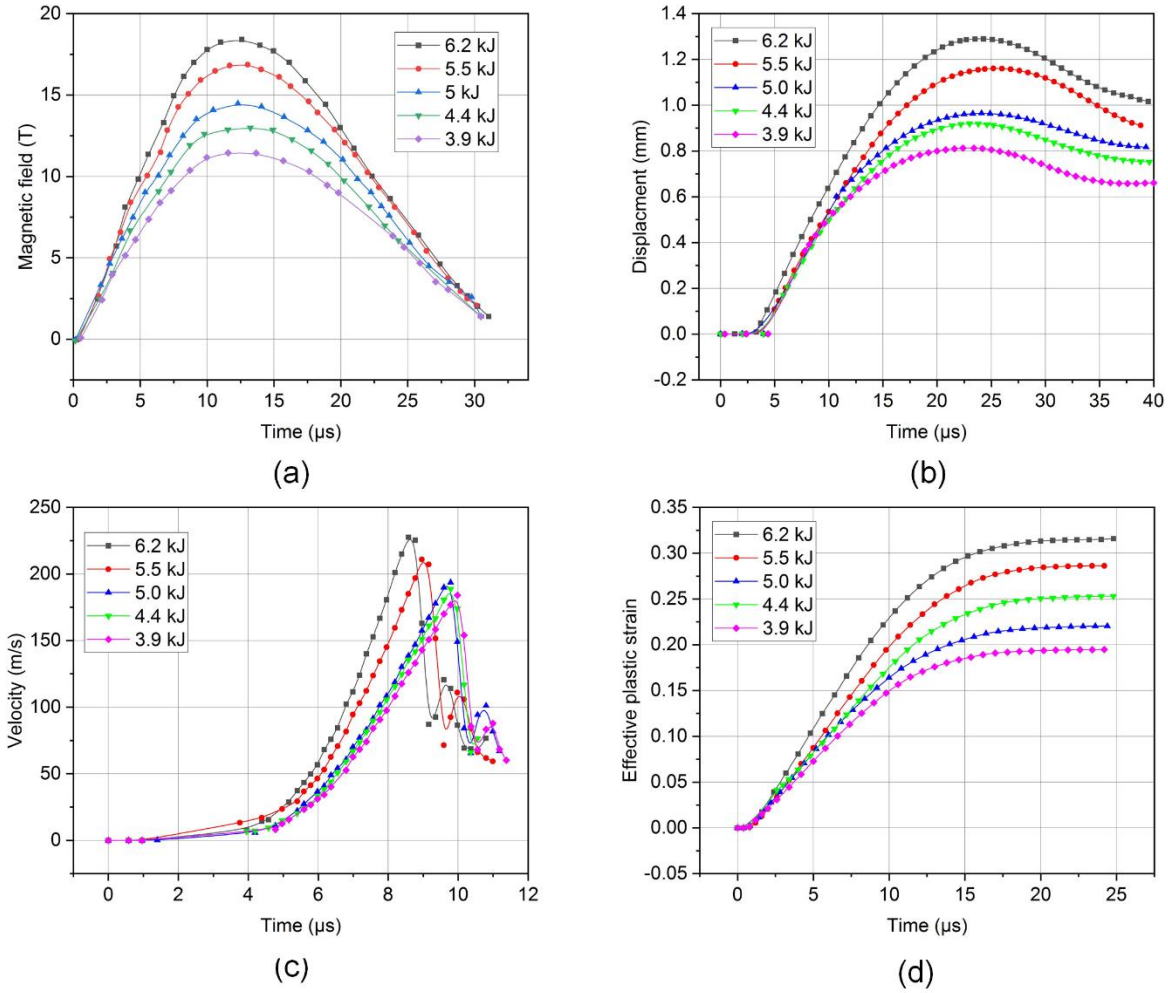

Fig. 4.6 Variation of (a) magnetic field, (b) displacement, (c) velocity and (d) effective plastic strain in the outer tube with time in the crimping zone in the coupled simulation model

4.3.1.4 Effective plastic strain

A minimum effective plastic strain must be achieved to facilitate the crimping of the outer tube onto the inner tube. An increase in the discharge energy value increases the impact velocity of the outer tube in the crimping zone, leading to higher effective plastic strain. A maximum effective plastic strain of 0.31 is observed at the discharge energy of 6.2 kJ, as shown in Fig. 4.6 (d). The development of effective plastic strain along the outer tube length from A to B with time observed at 5.5 kJ of discharge energy in the simulation model is shown in Fig. 4.7. The length AB is along the axis of the tube and represents the overlapped length of the crimped joint. With the passage of time, the element 20532, nearest to the outer tube tip, experiences maximum effective plastic strain, and it collides with the inner tube wall first, leading to an increase of effective plastic strain with time and eventually becoming stagnant. An effective plastic strain of the element 20530 and 20528 keeps increasing and eventually slows down after colliding with the inner tube wall.

The minimum effective plastic strain is observed for element 20522, which is farthest from the outer tube tip.

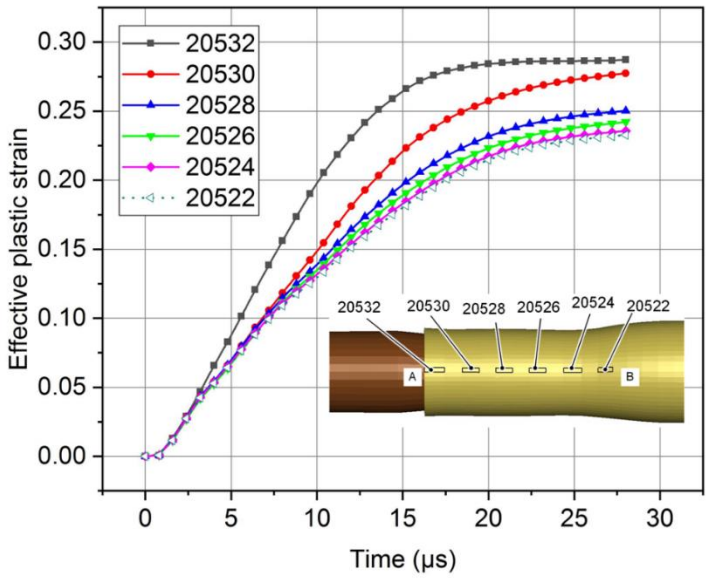

Fig. 4.7 Effective plastic strain variation along the axis of the outer tube in the crimping zone at 5.5 kJ of discharge energy in the coupled simulation model

4.3.2 Effect of field shaper slit

The slit is one of the main features of the field shaper, which leads the induced eddy current from the outer surface to the inner surface of the field shaper and maintains the continuity of eddy current flow. This section discusses the effect of the field shaper slit on the final output of the electromagnetic crimping process. Since the magnetic field is disrupted in the region close to the field shaper slit, it reduces the Lorentz force. Fig. 4.8 shows the distribution of the Lorentz force vector along the circumferential direction of the outer copper tube in the crimping zone, which is radially inward. It can be observed from the figure that the Lorentz force vector is uniform throughout the circumference of the tube except in the region close to the field shaper slit where the distribution is scattered (Fig. 4.8 & Fig. 4.9). The value of Lorentz force acting on the outer tube in the crimping zone is observed to be lower in the region close to the slit compared to the other region by 30%. This leads to the lower radial deformation of the outer tube in the region close to the slit throughout the crimping zone.

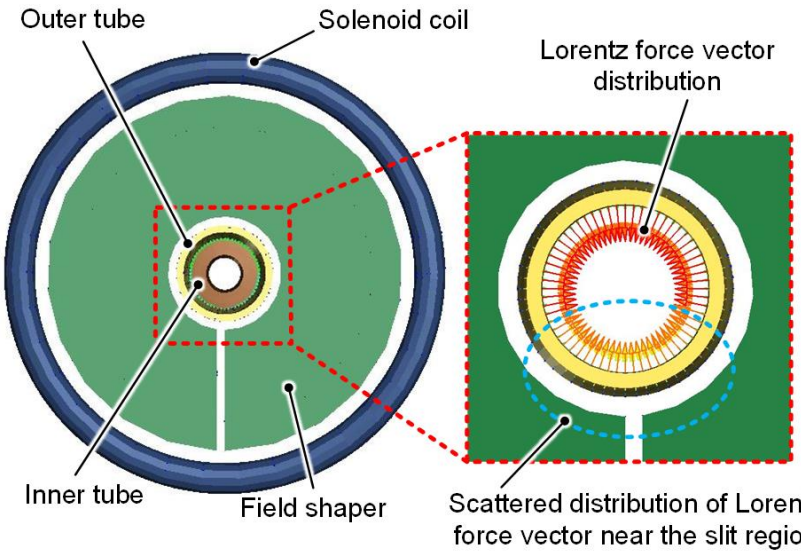

Fig. 4.8 Distribution of Lorentz force vector in the outer tube along the circumference in the crimping zone in the simulation at 5.5 kJ of discharge energy

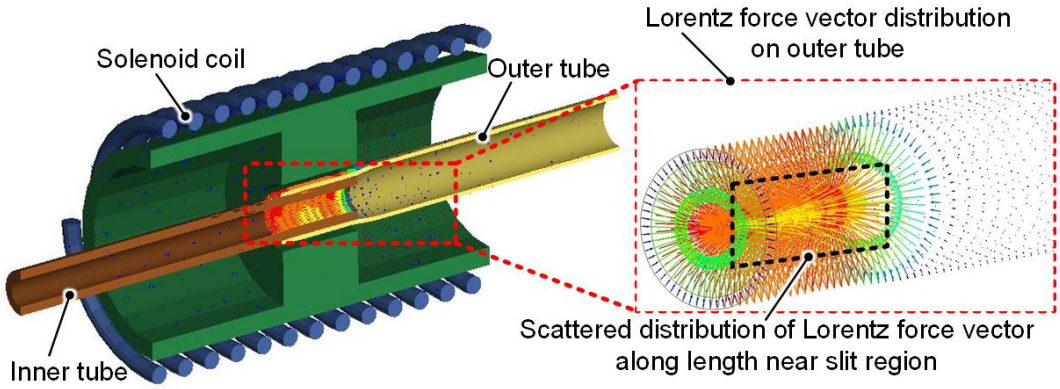

Fig. 4.9 Distribution of Lorentz force vector in the outer tube along the axis of the outer tube in the crimping zone in the simulation at 5.5 kJ of discharge energy

The effective plastic strain of the outer tube is represented along the path CD (C is near to the slit region and D is opposite to the slit region) for every node in the interval of 30° as shown in Fig. 4.10. With the increase of Lorentz force, effective plastic strain increases from C to D. This variant Lorentz force leads to uneven radial deformation along the circumference. Circumferential and radial strain reduce near the slit region, leading to a reduction in equivalent plastic strain. Also, due to Poisson's effect, there is a reduction in axial strain. Reduction in axial strain in the region close to the slit compared to other regions causes bending of the tube, and the impact can be significant if the deformation length is significant. So for longer overlapped lengths, stepwise joining along the length is recommended. Fig. 4.11 shows the uneven deformation of the copper tube along the

circumference in the region closed, opposite to the slit observed experimentally and in the numerically obtained EMC sample at 5.5 kJ of discharge energy. There is an uneven reduction of the diameter along the circumferential direction in the crimping zone. To understand this phenomenon, one angular parameter is considered. This angle is measured between the axial tangents to the crimped and non-crimped portions at the axial junction of these two portions. Simulation and experimental results are in good agreement. The shape of the experimentally and numerically obtained crimped sample is also compared by fitting half portion of the samples onto each other, and radial deformation is compared in terms of angles at 5.5 kJ of discharge energy as shown in Fig. 4.12. Good agreement is observed.

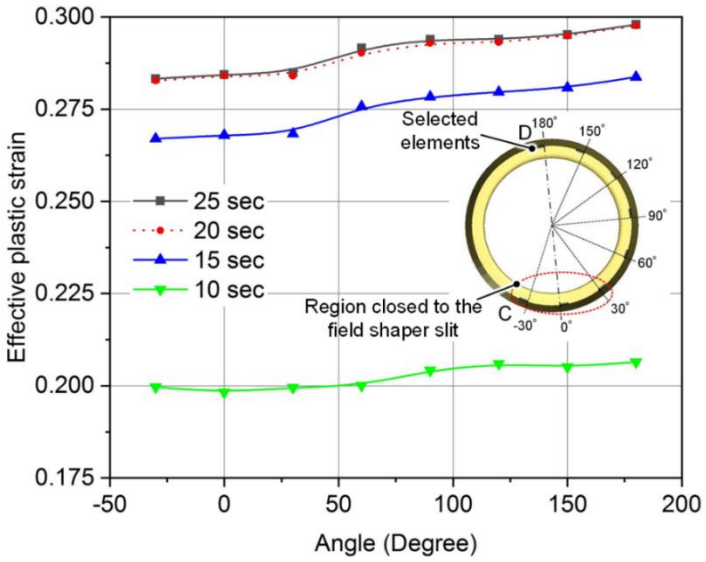

Fig. 4.10 Variation of the effective plastic strain of outer tube in the slit region along the circumference in the simulation at 5.5 kJ of discharge energy

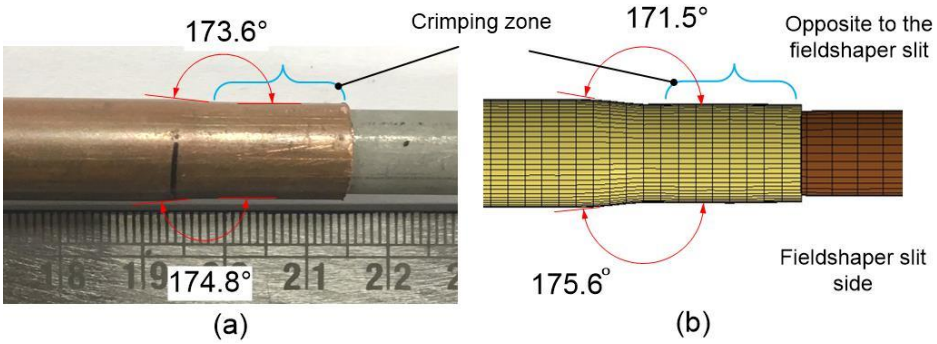

Fig. 4.11 Uneven radial deformation of the copper tube in the region near and opposite to the field shaper slit along with the circumference in (a) experiment (b) simulation at 5.5 kJ of discharge energy

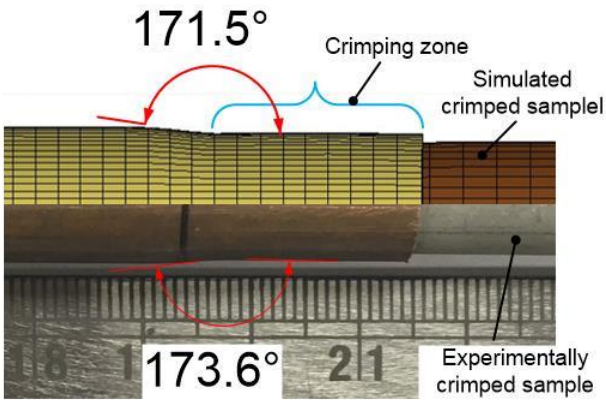

Fig. 4.12 Comparison of radial deformation of the electromagnetically crimped sample in the simulation and experiment at 5.5 kJ of discharge energy

4.3.3 Outer diameter and thickness

Fig. 4.13 (a-b) shows the variation of the outer diameter and thickness of the outer tube in the crimping zone with discharge energy, respectively, for simulation and experiment. The outer diameter and thickness of the copper tube averaged along the length in the crimping zone are measured experimentally with the help of a low magnification optical microscope and compared with the simulation results as shown in Table 4.3. Deformation increases with an increase in discharge energy, and the minimum value of outer diameter and thickness are observed at 6.2 kJ of discharge energy. Experimentally calculated values align with the simulated results with an error of 1-4.4 %. It is observed that the experimentally observed values of outer diameter and thickness of the outer tube in the crimping zone are higher than the simulated values, and this is probably due to the assumption that the current is uniformly distributed in the cross-section of the solenoid coil and the skin effect of the coil is neglected. Therefore, this might contribute to an increase in Lorenz force in simulation, leading to an increase in deformation. A sectional view of the sample is also compared by fitting the experimentally observed sample on to numerically obtained sample at 5.5 kJ of discharge energy, as shown in Fig. 4.14. From observations, no change in the diameter of the SS 304 (internal) tube is observed as SS 304 tube only goes through elastic deformation during the electromagnetic crimping process.

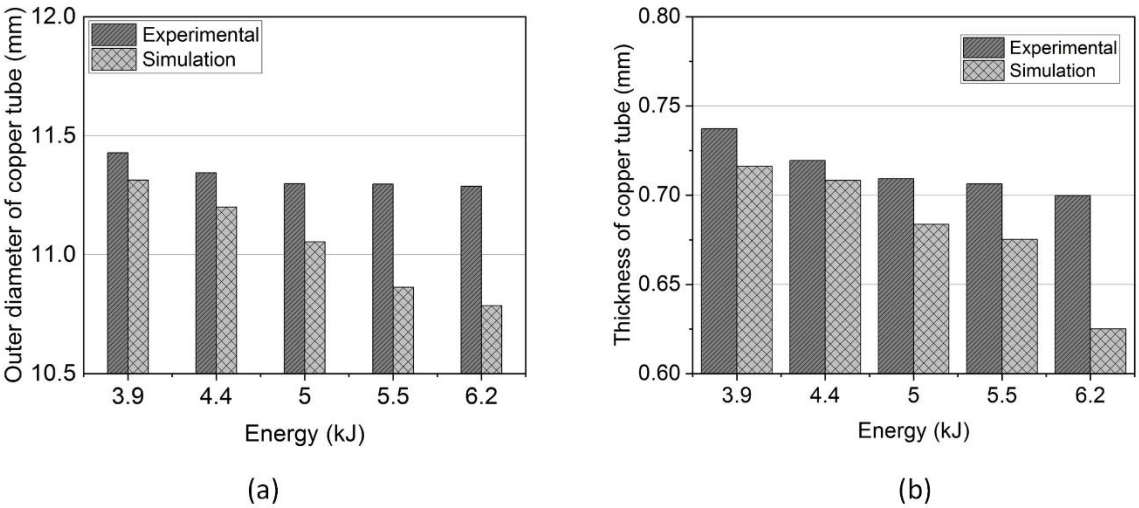

Fig. 4.13 Comparison of (a) outer diameter and (b) thickness of the outer tube in the crimping zone for various discharge energy values in the case of experiment and simulation

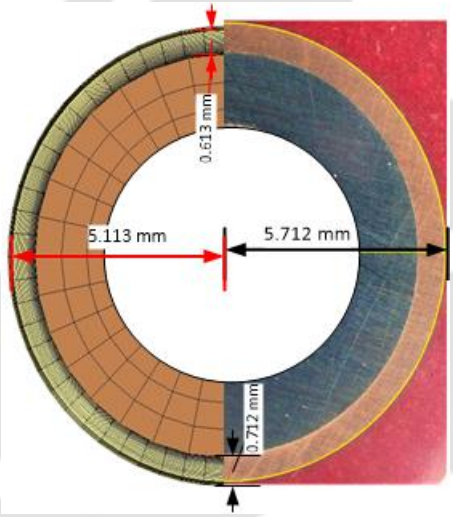

Fig. 4.14 Comparison of the shape of the electromagnetically crimped sample in the simulation and experiment at 5.5 kJ of discharge energy

Table 4.3 Comparison of outer diameter and thickness of copper tube for experiment and simulation

Energy in kJ	Outer diameter (mm)	Outer diameter (mm)	% error	Thickness (mm)	Thickness (mm)	% error
	(Experimental)	(Simulation)		(Experimental)	(Simulation)	
3.9	11.628	11.510	1.01%	0.737	0.716	2.86%
4.4	11.544	11.397	1.27%	0.720	0.708	1.56%
5.0	11.498	11.250	2.16%	0.709	0.684	3.6%
5.5	11.425	11.226	1.74%	0.712	0.613	4.4%
6.2	11.308	11.185	1.08%	0.700	0.625	10.66 %

Fig. 4.15 shows the tube thickness distribution along the length of the outer tube in the crimping zone at 5.5 kJ of discharge energy for simulation and experiment. Maximum variation of thickness along the length in the crimping zone is observed to be 2 % for experiment and 1% for simulation, which ensures the uniform radial deformation of the tube in the crimping zone along the length.

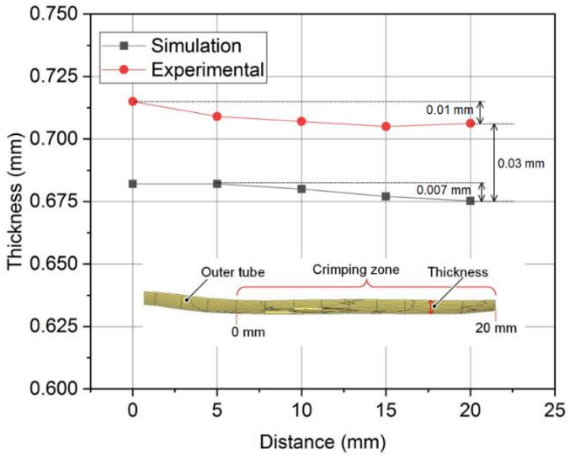

Fig. 4.15 Variation of the thickness of the outer tube along the length in the crimping zone at 5.5 kJ of discharge energy

4.3.4 Strength prediction and validation of predicted results

A simulated model is developed to predict the pull-out and compressive strength of an EMC crimped joint. A Dynain ASCII file is obtained at the end of the first simulation, which includes new nodal locations and new preloaded stresses and strains from the first simulation. Dynain ASCII file contains nodes, elements, stresses and strains of the tubes crimped in the first FEM model. These commands are merged into a single deck, and the second simulation is performed to predict the strength of the Cu-SS tubular joint during destructive pull-out and compression testing. Boundary conditions are applied on the Cu-SS composite tube as per the experimental condition for the pull-out test described in Fig. 4.16. Piecewise linear plasticity material model, which is an elastoplastic material model, is used during the pull-out and compression testing simulation. The model utilises input in the form of true stress vs effective plastic strain curves. This model is widely used for crash testing, drop testing and other rate-dependent phenomena. It is one of the simplest material models for tensile testing [133]. Boundary conditions are implied as per the real-life experimental conditions. On the one end of the joint, translational constraints are used in the x, y and z-direction for set nodes of the end, while on the other end, translational constraints are implemented in the x and z direction using the SPC_SET keyword input deck in LS-Dyna ™. A prescribed motion of 0.5 mm/sec in the y-direction is implemented on the end, which is not constrained in the y-direction using the PRESCRIBED_MOTION_SET keyword input deck in LS-Dyna ™ as shown in Fig 4.16.

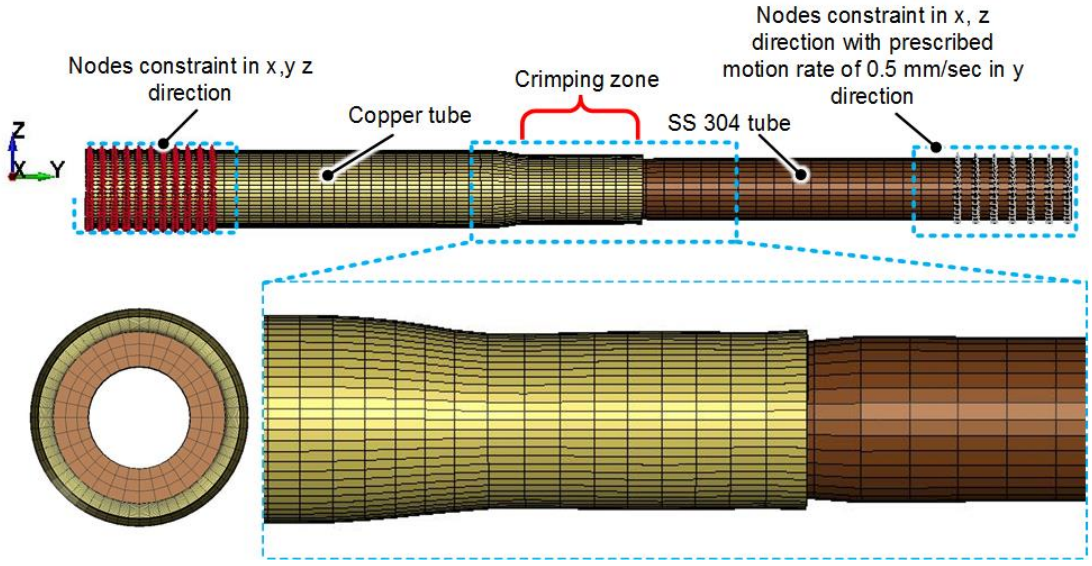

Fig. 4.16 Boundary conditions applied on the EMC crimped joint in the simulation model for prediction of strength

Modelling the contact between inner surface of outer tube and outer surface of inner tube is an important part of this simulation model. Explicit general contact algorithm has been implemented in the simulation model which automatically defines all the surfaces. CONTACT_AUTOMATIC_SURFACE_TO_SURFACE contact type of LS-Dyna ™ is used which is very efficient and robust and looks in both directions at the contact surface pair [36]. Friction coefficient is a very important part in defining contact, so it must be chosen very wisely. It's difficult to calculate the actual value of the friction coefficient between both the surfaces in contact. So, the simulation model is calibrated as per the experimentally obtained results. Four values of friction coefficient (0.1, 0.2, 0.3, and 0.4) are tried. For friction coefficient 0.3, simulation results become closest to the experimentally observed result. Hence, we have chosen friction coefficient 0.3 in the simulation model for all the discharge energies.

We have simulated in LS-Dyna ™ up to the point when longitudinal stress / pull-out load starts reducing due to the beginning of joint failure (considerable relative motion between the tubes) in both Pull out and Compressive tests. Longitudinal stress is observed from the simulation results and multiplied with the original cross-sectional area to obtain the pull-out load. Similar steps are repeated for compressive testing. Simulated results are validated with experimentally observed results. A schematic diagram of the pull-out test performed for experimental observation is shown in Fig. 3.4. The pull-out test is carried out at the pull-out rate of 0.5 mm/sec on a universal testing machine (UTM).

Fig. 4.17 (a-b) shows the comparison of numerically predicted and experimentally observed pull-out and compressive strength values of EMC crimped joint at various discharge energy values, respectively. Pull-out and compressive strength is observed to be proportional to the discharge energy as an increase in discharge energy leads to an increase in the radial deformation and subsequent elastic recovery, which further leads to an increase in interference pressure at the interface in the crimping zone. Therefore, pull-out and compressive strength increase. Calculated and experimentally observed results are in good agreement with an error of 1.45%-6.23% for pull-out strength and with an error of 1.4%-10.8% for compressive strength, as shown in Table 4.4. The maximum strength is achieved at 6.2 kJ of discharge energy.

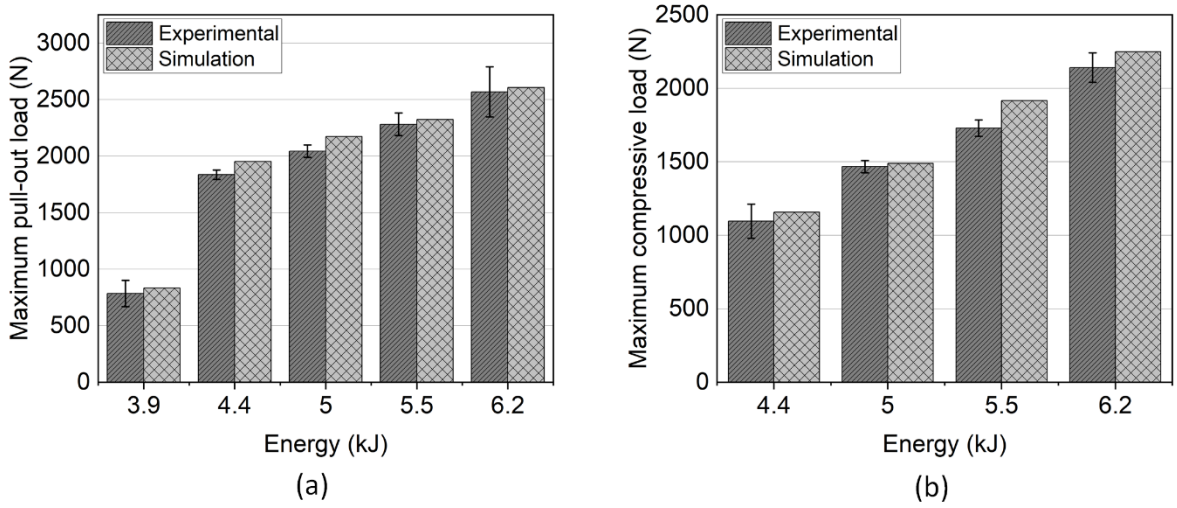

Fig. 4.17 Comparison of (a) maximum pull-out load and (b) maximum compressive load at various discharge energy values for simulation and experiment

Table 4.4 Comparison of maximum pull-out and the compressive load of smooth-surfaced samples for experiment and simulation at various discharge energy

Energy in kJ	Maximum pull-out load (Experimental) (N)	Maximum pull-out load (Simulation) (N)	% error	Maximum compressive load (Experimental) (N)	Maximum compressive load (Simulation) (N)	% error
3.9	785.17	834.09	6.23%			
4.4	1836.38	1952.11	6.3%	1096.02	1156.38	5.51%
5	2044.53	2172.64	6.27%	1467.93	1489.02	1.44%
5.5	2282.08	2323.44	1.81%	1729.24	1916.08	10.8%
6.2	2569.32	2606.71	1.45%	2141.38	2248.06	4.98%

The experimentally observed pull-out load vs extension curve is also compared with the numerically obtained curve, as shown in Fig. 4.18. Pull-out load is observed to be increasing with an extension until it reaches the maximum value in both the experiment and simulation. It can be said that the joint strength obtained is lower than the base copper tube strength. This causes the sliding failure of the joints during pull-out and compressive testing, where both the joining partners start to have a relative axial motion with respect

to each other after reaching the maximum strength value. Fig. 4.19 shows that the EMC crimped samples failed through sliding failure mode at the discharge energy of 5.5 kJ during the pull-out test in the experiment and simulation.

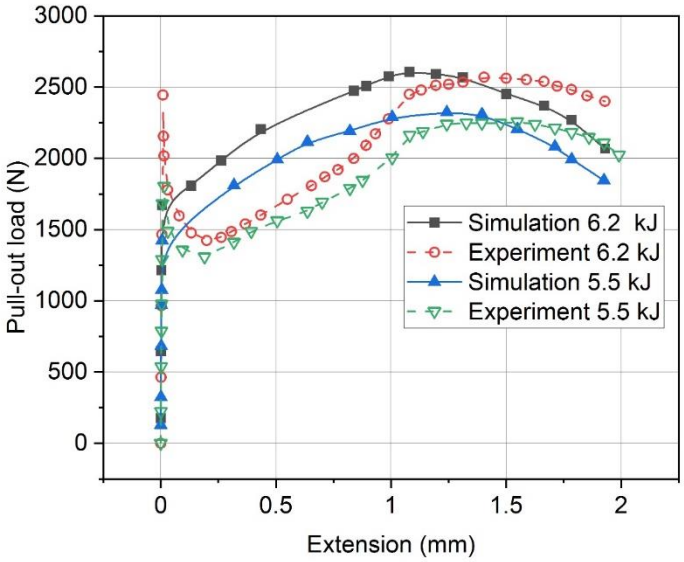

Fig. 4.18 Comparison of pull-out load vs extension curve at 5.5 kJ and 6.2 kJ of discharge energy for simulation and experiment

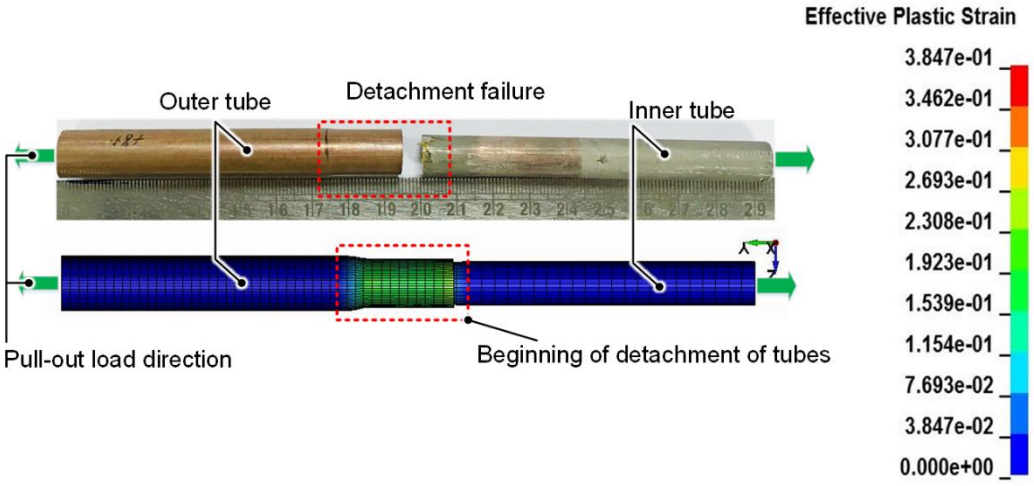

Fig. 4.19 Sliding failure of EMC crimped joint at 5.5 kJ of discharge energy in experiment and simulation

4.4 Conclusions

Numerical simulation for the EMC process has been performed using finite element software LS-Dyna ™ and validated with the experimental results in the following aspects (i) the outer diameter of the copper tube, (ii) thickness of the copper tube after electromagnetic crimping, and (iii) strength of the EMC Cu-SS joint tested by (a) Pull out test, (b) Compression test.

1. Distribution of thickness along the length of the outer tube in the crimping zone has shown a variation of 1-3 % in the numerical simulation and experimental measurement. There is uniform deformation throughout the crimping length during the electromagnetic crimping process. The little variation is probably due to little higher radial deformation close to the free end of the copper tube in the overlapped zone due to inertia. Effective plastic strain shows a consistent trend along the length.
2. Uneven radial deformation of the outer tube in the crimping zone in the circumferential direction is observed due to uneven Lorentz force distribution in the circumferential direction, which is caused by the presence of slit in the field shaper. The value of effective plastic strain of the copper tube is reduced by 11.5 % in the slit side compared to the area opposite to the slit. This observation is consistent in both simulation and experiment.
3. Strength prediction by finite element analysis using LS-Dyna ™ shows good agreement with experimental results. Pull-out and compressive strength observed in simulation has shown an error of 1-4 % compared with the experimental results.
4. Joints are failed through a sliding failure mechanism, which leads to relative motion between the Cu and SS 304 tubes in the axial direction during the pull-out and compression test. A similar mechanism is obtained in the experiment as well as simulation.

5 Electromagnetic Crimping on Threaded Surface

5.1 Introduction

In chapter 3, an experimental investigation is performed, and an improved Cu-SS tube-to-tube joint with a strength higher than the base Cu tube failure strength is achieved in the case of threaded and knurled surfaced joints and considering manufacturing complexities of knurls, threaded surfaced joints are observed to be most suited for axial strength. The work has been further extended in chapter 4, which presents an initial finite element model using LS-DYNA™ EM module to simulate the smooth surfaced Cu-SS tube-to-tube joining by EMC technique along with strength prediction of the joint. The FEM results are validated with experimental results and have shown good agreement. However, the proposed FEM model cannot predict the strength and analyse deformation behaviour for the threaded/knurled surfaced joint, as the LS-DYNA™ EM module can only use brick meshing or hexahedral elements in the model, which creates complexities while meshing geometries with surface profiles (threads and knurls). Furthermore, a more elaborated experimental investigation is needed for quicker industrial adaption of the EMC technique, which can be further expedited by developing FEM models around it. Therefore, this chapter provides an approach to improve the knowledge about EMC tubular joining. It focuses on three central aspects during the formation of the Cu-SS electromagnetically crimped threaded surfaced tube-to-tube (EMCT3) joint: (1) Developing a FEM model for predicting the deformation and strength of an EMCT3 joint along with its experimental validation; (2) Expressing the effect of pitch and discharge energy on the deformation and strength of an EMCT3 joint in an empirical relation; and (3) Performing ANOVA analysis to address the relative contribution of different process parameters. Previously developed FEM models for smooth surfaces are incapable of predicting the strength of the EMCT3 joint. Therefore, a non-coupled multi-step FEM model is developed in this work. Simulation is performed for different combinations of discharge energy and pitch of thread values. A good agreement is observed between simulated and experimental results. The experimental investigation includes pull-out testing. The pull-out testing results in crack failure mode and detachment failure mode for EMCT3 joint based on higher and lower joint strength, respectively, as compared to the base Cu tube strength. Furthermore, from the experimental data, an empirical relation is

developed using LAR and bisquare method for deformation and joint strength as a function of discharge energy and pitch.

5.2 Methodology

5.2.1 Process parameters

As per the previous chapter 4, it has been concluded that among three surface profiles (threaded, knurled and smooth) for the outer surface of the inner tube during EMC, the threaded surface is most suitable to obtain Cu-SS tube-to-tube joint with maximum pull-out and compressive strength where the specification of the thread in use is ISO M10 ×1. ISO metric threads are general-purpose threads with the thread angle of 60°. In order to further optimise the joint, four different pitch values of ISO M10 threads (0.75 mm, 1 mm, 1.25 mm and 1.5 mm) and four different thread angle values are used for the outer surface of the target tube, as shown in Fig. 2 (b). Electromagnetic crimping experiments are performed at three discharge energy values: 3.4kJ, 3.9 kJ, and 4.4 kJ. A Rogowski coil and an oscilloscope are used to measure the current waveforms at three discharge energy values.

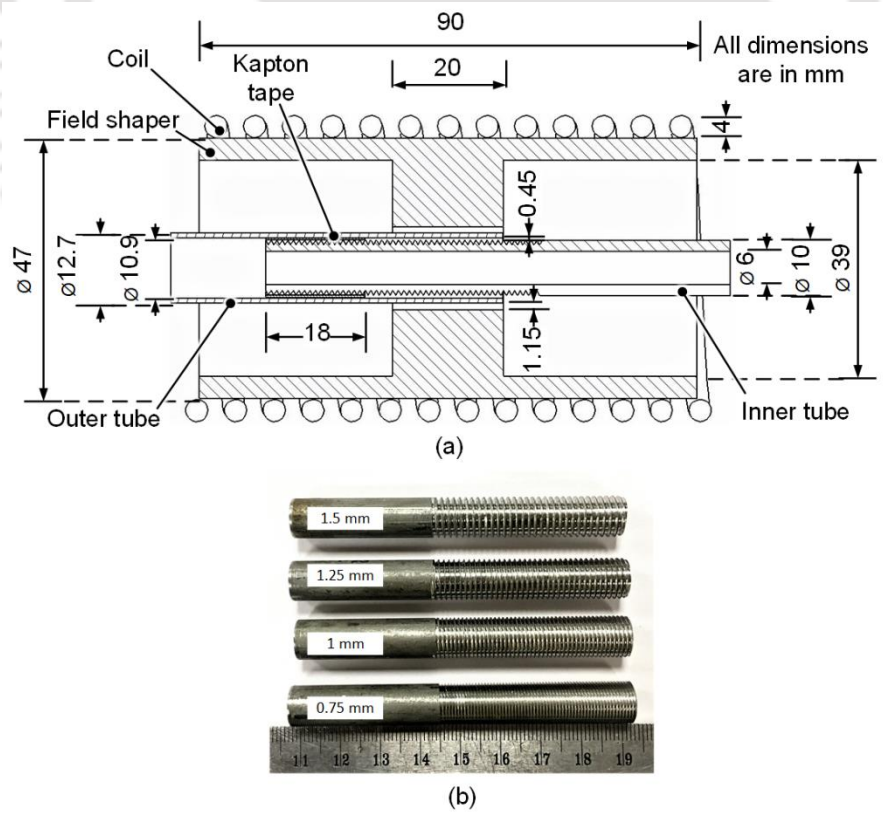

Fig. 5.1 (a) Detailed Dimensioning of various components (b) Images of ISO M10 threaded surfaced SS 304 inner tube with the various pitch size

Electromagnetic crimping is performed at three discharge energy levels for four-pitch combinations. Three energy levels are decided based on the previously obtained results. All these twelve sets of experiments are repeated thrice to ensure repeatability. The pull-out test is performed at a constant pulling-out speed of 0.5 mm/sec on the UTM machine as discussed in section 3.2.3.1.

5.2.2 Sample preparation for characterisation of EMCT3 joints

Samples are cut transversely in a ring in the crimping zone using a wire electric discharge machine to characterise the tubular joint, as shown in Fig. 5.2 (a-b). To avoid any microstructural changes, proper coolants are used. Mounting of obtained samples is done using phenolic powder for ease of handling. In the end, mounted samples are grind under water-cooling using Silicon carbide papers of grit sizes 80-1500 one after another, followed by Al_2O_3 abrasive polishing.

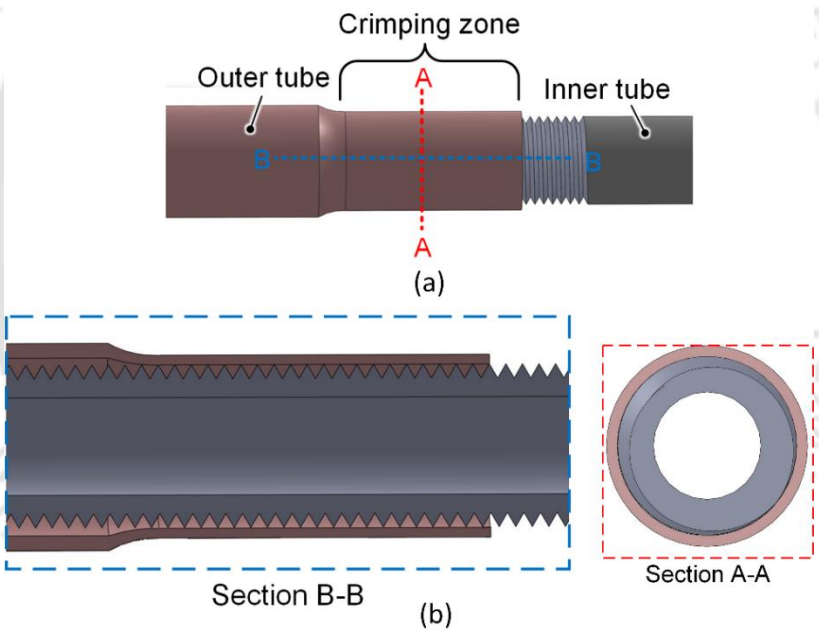

Fig. 5.2 Schematic of (a) cutting pattern for a joined sample and (b) sectional views of the inner (SS) and outer (Cu) tubes

5.2.3 Numerical simulation for destructive testing

A non-coupled multi-step FEM simulation model has been developed to create an EMCT3 joint and perform destructive testing on created joints. The model is simulated by combining ANSYS Maxwell and ANSYS explicit dynamics software packages. The simulation divides the EMCT3 joining problem into two parts (electromagnetic and mechanical). ANSYS Maxwell solves the electromagnetic part while ANSYS explicit dynamics solve the mechanical part, as shown in Fig. 5.3. A multi-step technique (Fig. 5.3)

is used for successful numerical modelling of destructive testing of the Cu-SS joint in the mechanical part.

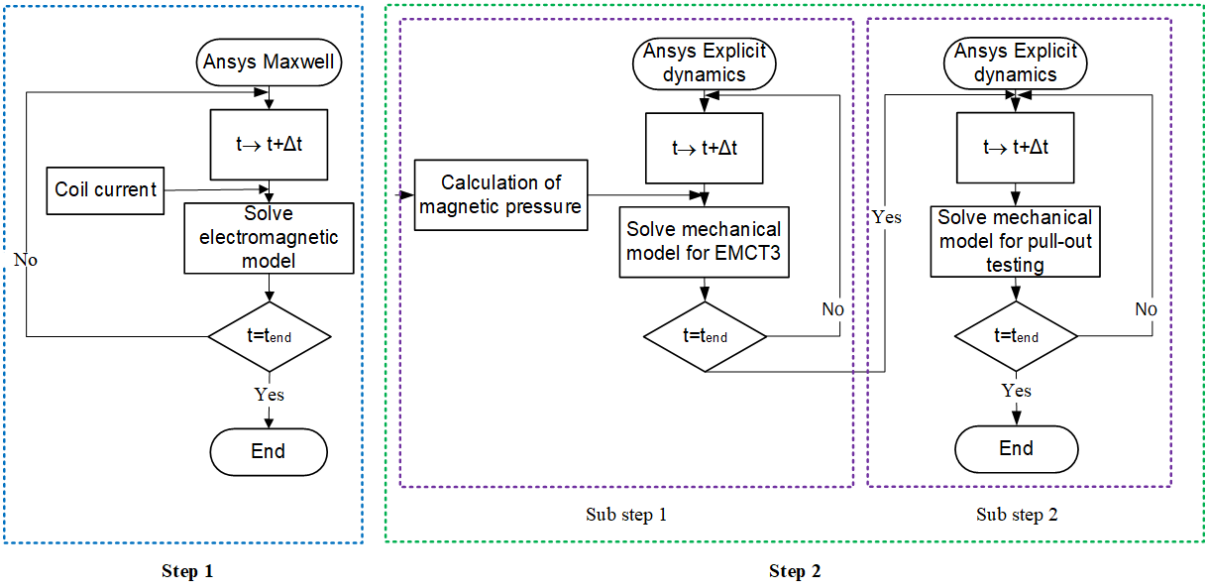

Fig. 5.3 Flow chart for the non-coupled multi-step simulation model

5.2.3.1 Electromagnetic analysis using ANSYS Maxwell

The measured current is used as an input to the ANSYS Maxwell to calculate the magnetic field. Input current curves are shown in Fig. 5.4 (a). At the input terminal of the coil, the current is applied, as shown in Fig. 5.4 (b). The end time for the simulation is 3×10^{-5} s. The following assumptions are made in this simulation model:

1) The skin and proximity effects are considered during the current distribution in the tool coil.

2) The electrical properties of the material, such as conductance and permeability, are assumed to be constant throughout the time period.

3) Joule heating loss has not been considered.

A three-dimensional electromagnetic field model is established (Fig. 5.4 (b)), where the coil, field shaper, Cu tube and SS tube are sealed in air. As discussed, there is a ring current load in the coil, which generates a magnetic field for EMCT3 joining. In the analysis, a vacuum box is considered surrounding the coil-tube model in such a way that its dimension is sufficient enough so that the magnetic field decays to zero in the far-field. As shown in Fig. 5.4 (c), the coil, field shaper, Cu tube and SS tube are divided into a meshed model using the adaptive meshing technique. The current density for the Cu tube at 15 μs after discharge is shown in Fig. 5.4 (d). A ring current is induced on the surface of the Cu

tube in the crimping zone of the field shaper, but the current density is low outside the working area of the field shaper. The magnetic field at the surface of the Cu tube is calculated, and the magnetic pressure is calculated from the magnetic field, which is further used as an input to the ANSYS explicit dynamics to calculate structural deformation.

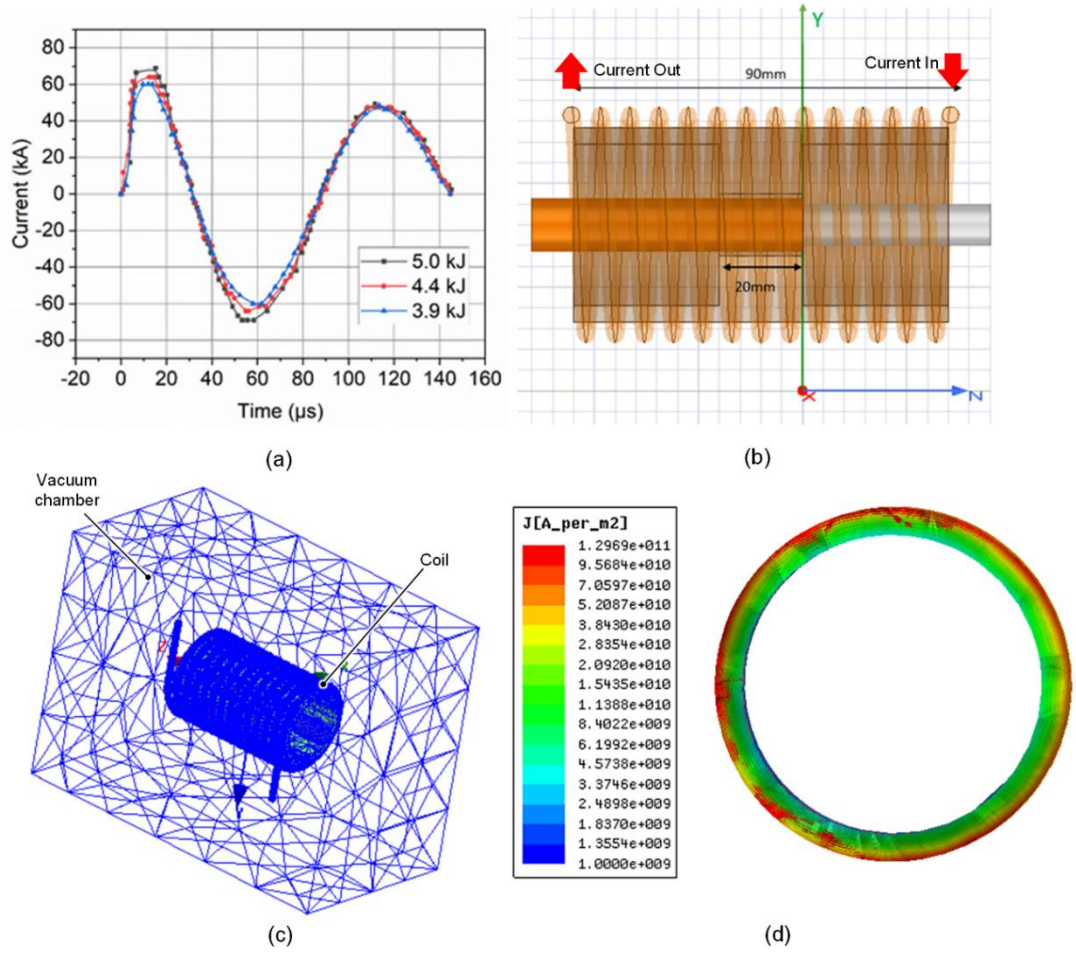

Fig. 5.4 Simulation model for electromagnetic field analysis (a) current curve, (b) ANSYS Maxwell model, (c) mesh cluster showing the vacuum enclosed model and (d) current density for 5.0 kJ at 15 μs showing induced current at the Cu tube surface in the middle of the crimping zone

5.2.3.2 Structural deformation analysis using ANSYS Explicit Dynamics

The schematic of the model developed in ANSYS Explicit Dynamics is shown in 5.5 (a). The ends of the tubes are fixed using boundary conditions in ANSYS to replicate the experimental setup. The front and sectional views are shown in Fig. 5.5 (b) and (c),

respectively. The pressure data obtained from Maxwell is used here as input. The equivalent pressure is applied uniformly along the circumference in the crimping zone.

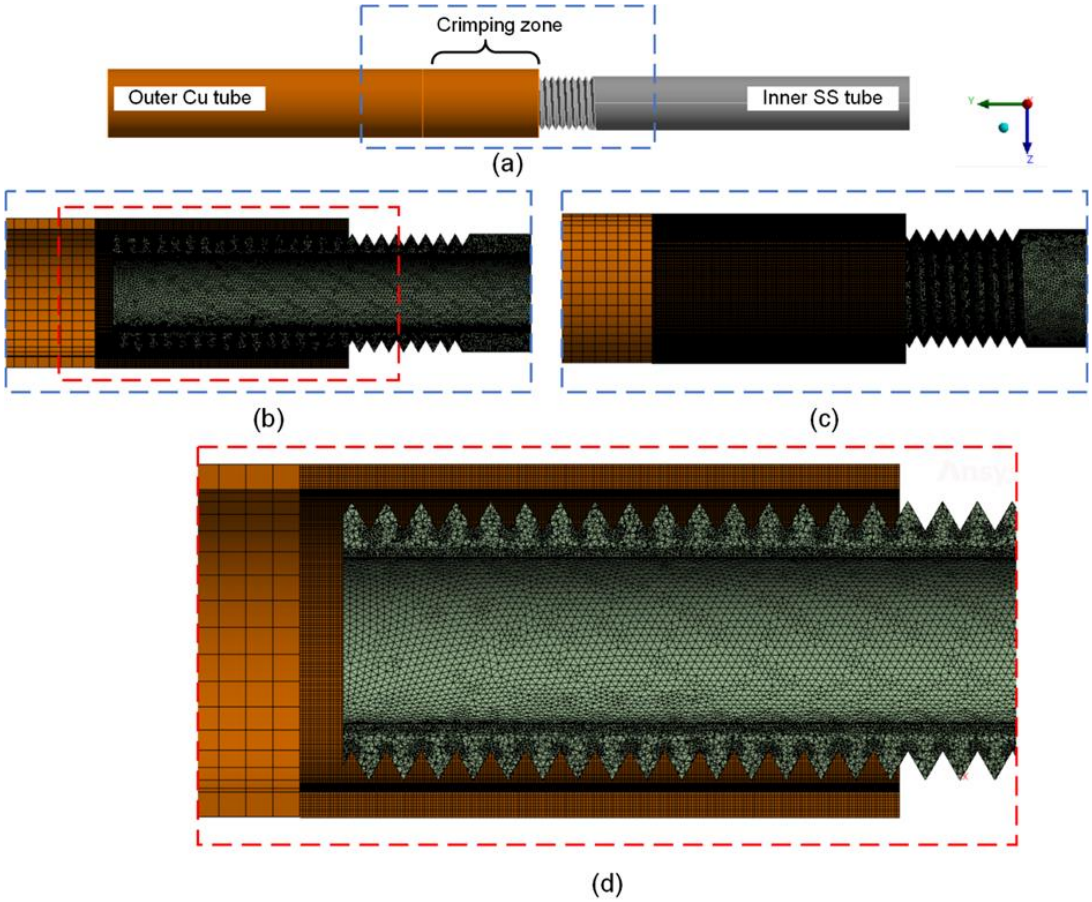

Fig. 5.5 (a) 3D Cu-SS tube-to-tube assembly, (b) front sectional view of the meshed model, (c) back sectional view of the meshed model and (d) zoomed view of the meshing

The Johnson-Cook (J-C) material model is used for all the workpiece, a recommended material model for high temperature and high strain-rate processes [132]. J-C model has already been discussed in section 4.2.3.

5.2.3.3 Strength prediction for EMCT3 joints

Numerical prediction of the strength of an electromagnetically crimped joint can be of great use and can save a lot of time and resources. It can provide a complete idea of creating a structural joint along with the strength of that joint, eliminating the necessity of initial experimentation for designing the structural joint. Section 4.3.4 have also proposed a novel FEM model for strength prediction of an electromagnetically crimped smooth-surfaced tube-to-tube joint using the LS-Dyna ™ EM module. However, the EM module has limitations of using only brick meshing in the model, which creates complexities while meshing threaded geometries. Therefore, the LS-Dyna ™ EM module cannot be used for

the strength prediction of EMCT3 joints. Hence, a different methodology is required. Therefore, we have developed a non-coupled multi-step simulation model in two steps, as discussed in the flow chart in Fig. 5.3. During strength prediction simulation, the second step of calculating mechanical deformation, as discussed in the previous section, is performed in two sub-steps. Electromagnetic crimping due to the magnetic pressure is performed in the first sub-step, and destructive testing of the EMCT3 joint is performed in the second sub-step. The mechanical solver in Ansys explicit dynamics uses a transient dynamic equilibrium equation to compute deformation at each time step during the second step. Boundary conditions are implied as per the real-life destructive testing experimental conditions, as shown in Fig. 5.6. On the one end of the joint, translational constraints are used in the x, y, and z directions for set nodes of the end, while on the other end, translational constraints are implemented in the x and z directions. A 0.5 mm/sec pull-out speed is applied on the end in the y-direction. Modelling the contact between the outer and inner surfaces of the inner and outer tubes, respectively, is an essential part of this simulation model. The simulation model has implemented an explicit general contact algorithm, which automatically defines all the surfaces. The friction coefficient is essential for defining contact, so it must be chosen wisely. It is difficult to calculate the actual value of the friction coefficient between both the surfaces in contact. So, the simulation model is calibrated as per the experimentally obtained results. For friction coefficient 0.35, simulation results become closest to the experimentally observed result. Hence, we have chosen a friction coefficient of 0.35 in the simulation model for all the discharge energies.

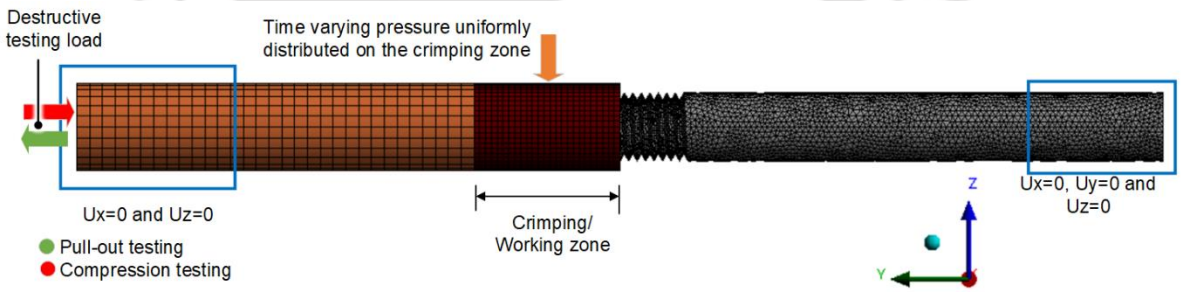

Fig. 5.6 Representation of boundary conditions for strength prediction simulation as per experimental conditions

5.3 Results and Discussion

It is observed that the magnetic field (H) follows the same pattern as the input discharge current and reaches maxima when the current reaches maxima at 1.4×10^{-5} s during Maxwell simulation. The solution converges at a mesh with 5000 elements. Timestep

refinement is automatically controlled as per the refined mesh by ANSYS Maxwell, and the optimum time step is chosen. The magnetic field data is converted to corresponding magnetic pressure by using the equation (2.14). The maximum magnetic field and corresponding maximum pressure variation along the axis of the Cu-SS EMCT3 joint are plotted in Fig. 5.7 (a) and (b).

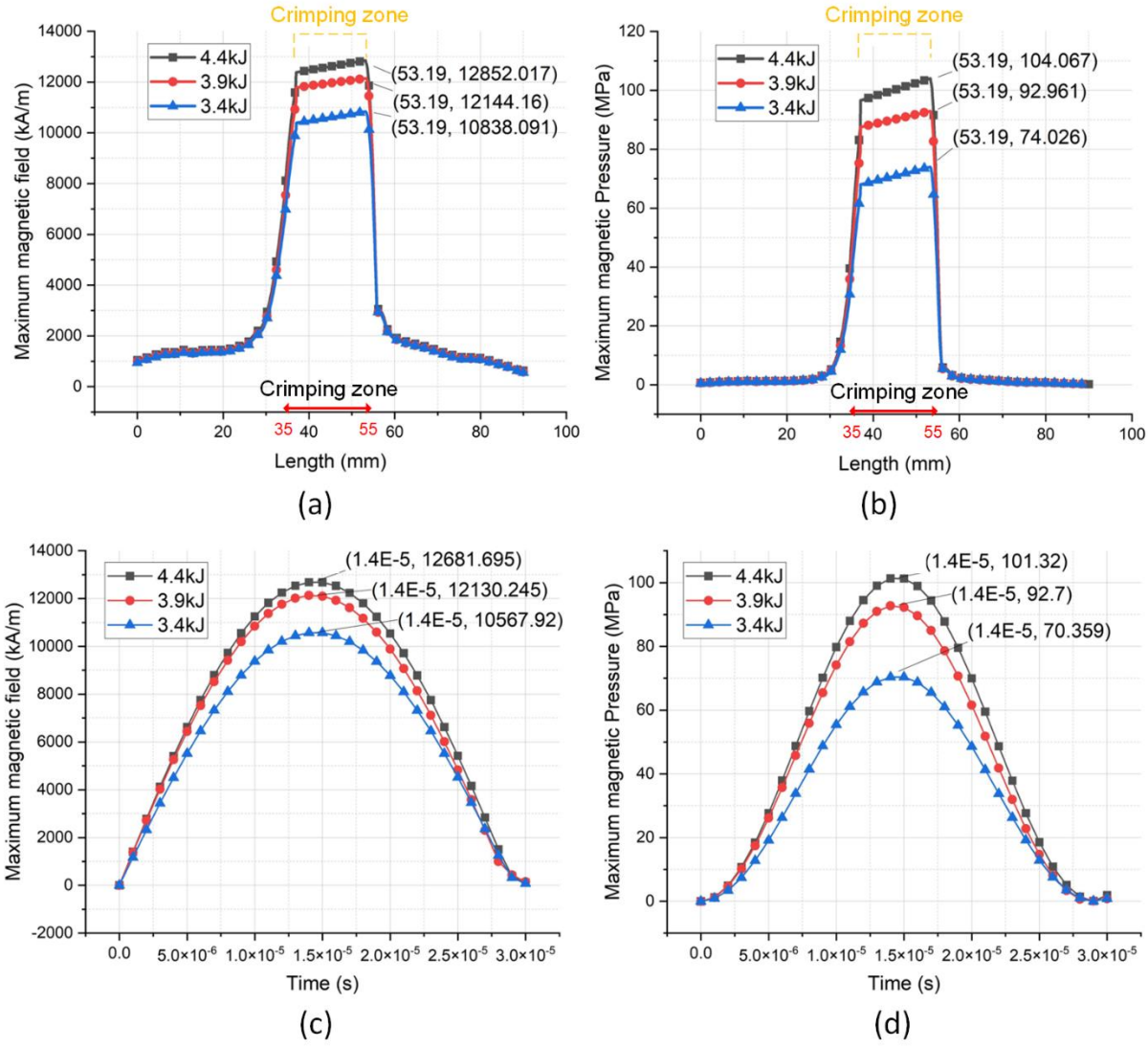

Fig. 5.7 (a) Maximum magnetic field and (b) maximum magnetic pressure variation at the time of maxima ($1.4 \times 10^{-5} s$) along the axis of Cu-SS EMCT3 joint and (c) magnetic field and corresponding (d) magnetic pressure variation with time, average out over the crimping zone

The maximum pressure is observed between 35 mm and 55 mm (crimping zone) due to the magnetic field concentration in the working zone caused by the field shaper. The variation of the magnetic field and the corresponding magnetic pressure with time, averaged out for the crimping zone, is shown in Fig. 5.7 (c) and (d). This time-varying

pressure data for the crimping zone is given as input in ANSYS explicit dynamics. Convergence analysis is also performed for Explicit dynamics to use suitable mesh and time step size for getting accurate results. Experiments are performed at three discharge energies (3.4 kJ, 3.9 kJ, and 4.4 kJ) and repeated thrice to ensure repeatability of the results. Experimentally obtained EMCT3 samples for four-thread pitch sizes at 3.9 kJ discharge energy are shown in Fig. 5.8.

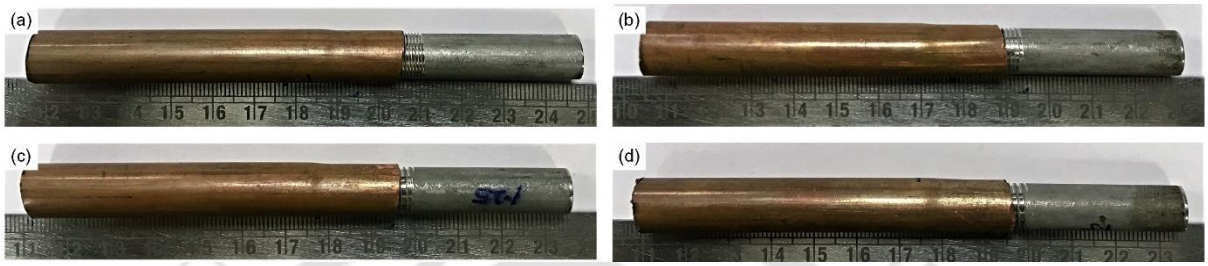

Fig. 5.8 EMC crimped samples at 3.9 kJ of discharge energy for four different pitches (a) 0.75 mm, (b) 1 mm, (c) 1.25 mm, and (d) 1.5 mm

5.3.1 Experimental validation of FEM simulation for predicting deformation and strength of EMCT3 joint

5.3.1.1 Deformation analysis for EMCT3 joint

The deformation analysis is done for different combinations of pitches of thread and different discharge energies, i.e., for combinations of discharge energies 3.4 kJ, 3.9 kJ and 4.4 kJ with pitches of the thread 0.75 mm, 1 mm, 1.25 mm and 1.5 mm. The height of the outer tube material, which deforms into the thread, is measured as h_c, as shown in Fig. 5.9. Dimensions of the various threads are shown in Table 5.1. With increasing discharge energy, the amount of deformation of the outer tube also increases. The maximum deformation is observed at a discharge energy of 4.4 kJ. No permanent deformation is observed in the inner SS tube as it only undergoes elastic deformation during the crimping process. The amount of material of the outer tube entering the thread is also found to be increasing with the pitch of the thread. The deformation is averaged over the crimping zone length to calculate h_c.

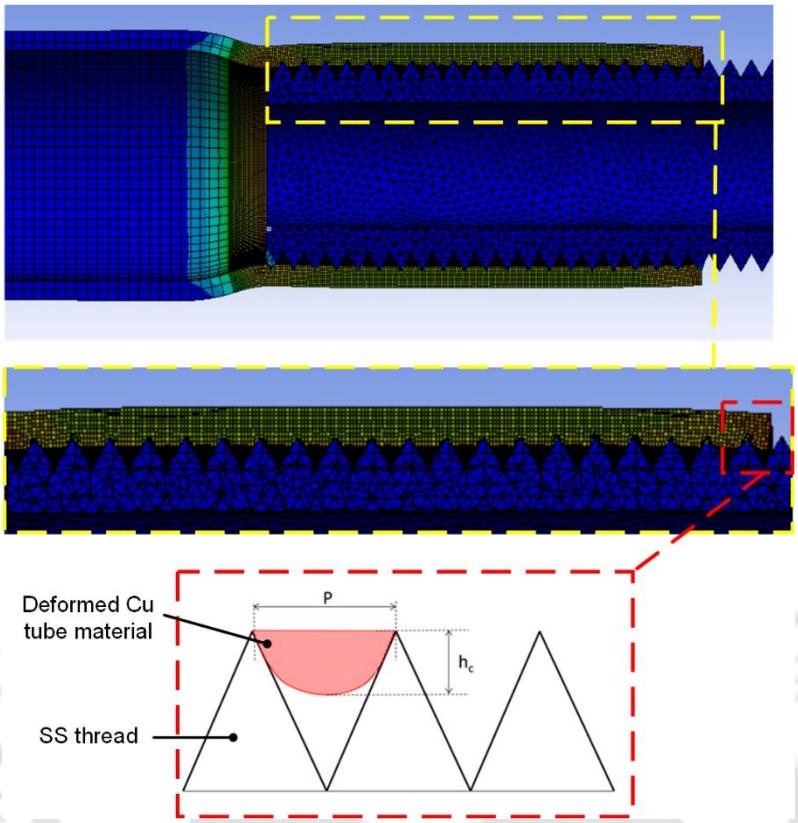

Fig. 5.9 Sectional view of simulated Cu-SS crimped sample showcasing deformation of Cu tube material in between SS threads to calculate deformation height h_c

Table 5.1 Dimensions of the thread at various pitch

Pitch	h_t (mm)	P (mm)
0.75	0.6495	0.75
1	0.866	1
1.25	1.0825	1.25
1.5	1.299	1.5

5.3.1.2 Experimental validation of deformation analysis of EMCT3 joint

The deformation is measured in the crimping zone for section B-B, as shown in Fig. 5.2. The outer diameter of the outer tube and its average thickness over length is studied experimentally using an optical microscope with 10 × magnification. Deformation increases proportionally with the discharge energy and the pitch of the thread. Fig. 5.10 shows the comparison of values obtained from experimental observation and simulation. Three repetitions are made for each observation. The experiment and simulation values

are in good agreement for all pitch and discharge energy combinations. Furthermore, the sectional view is compared by fitting half portions onto each other, and no deformation in the SS 304 tube is observed, along with an overestimation of results in simulation, as shown in Fig. 5.11 and Fig. 5.12.

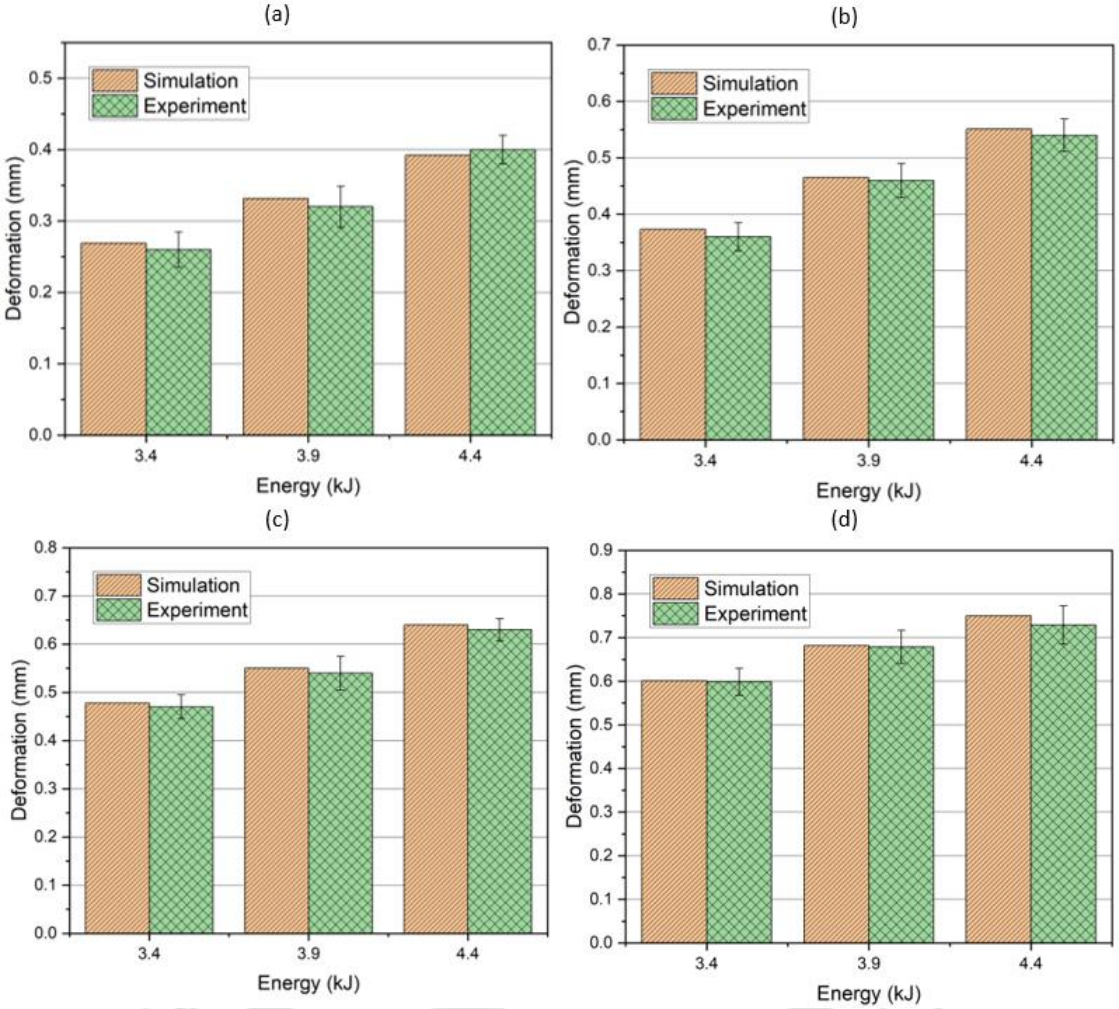

Fig. 5.10 Experiment and Simulation values of h_c for a pitch of thread (a) 0.75mm (b) 1 mm (c) 1.25mm (d) 1.5mm

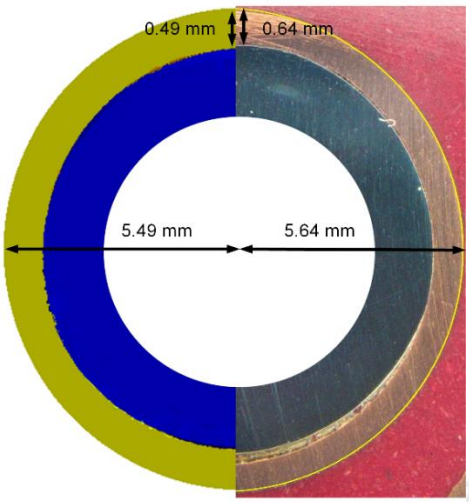

Fig. 5.11 Comparison of the experimentally obtained transverse cross-section of the EMCT3 joint sample with the simulated sample in the crimping zone at 4.4 kJ of discharge energy and 1 mm of pitch

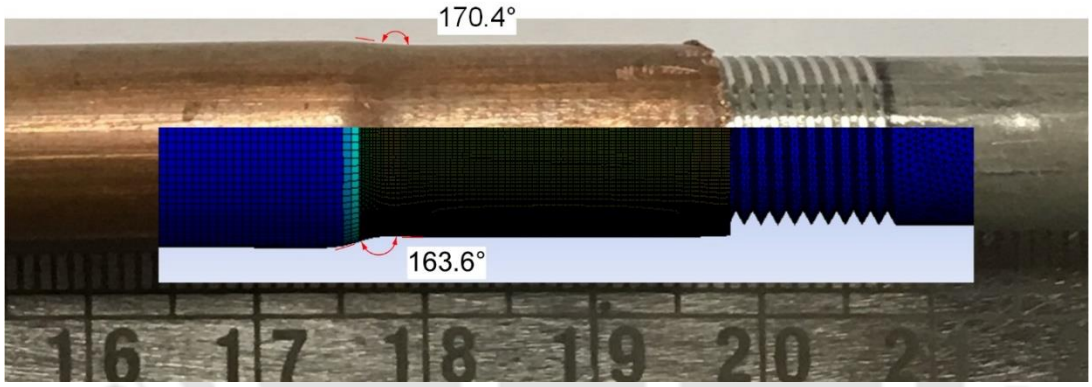

Fig. 5.12 Comparison of radial deformation of experimentally obtained EMCT3 joint sample with the simulated sample at 4.4 kJ of discharge energy and 1 mm of pitch

The validations showcase the credibility of the non-coupled simulation model for the EMCT3 joint.

5.3.1.3 Strength prediction, along with experimental validation of EMCT3 joint

Experiments and strength prediction simulations are performed. Table 5.2 summarises the maximum pull-out strength values of the EMCT3 joint experimentally. Fig. 5.13 compare numerically predicted and experimentally observed pull-out strength values of the EMCT3 joint at various pitch values for 3.9 kJ and 4.4 kJ of discharge energy. Calculated and experimentally observed results are in good agreement with an error of 1.15%–9.2% for pull-out strength. The maximum strength is achieved at 4.4 kJ of discharge energy. Fig. 5.14 and 5.15 show the EMCT3 samples for 1 mm pitch at 3.9 kJ and 4.4 kJ. Two different failure modes are obtained in simulation as well as experiment, detachment failure mode and crack failure mode.

Table 5.2 Maximum pull-out load variation with discharge energy and pitch of the thread in the experiment

Pitch (mm) Energy (kJ)	0.75	1	1.25	1.5
3.4	2.5 kN	1 kN	0.7 kN	1.2 kN
3.9	5 kN	8 kN	5.7 kN	6 kN
4.4	8 kN	8.3 kN	8.37 kN	6.9 kN

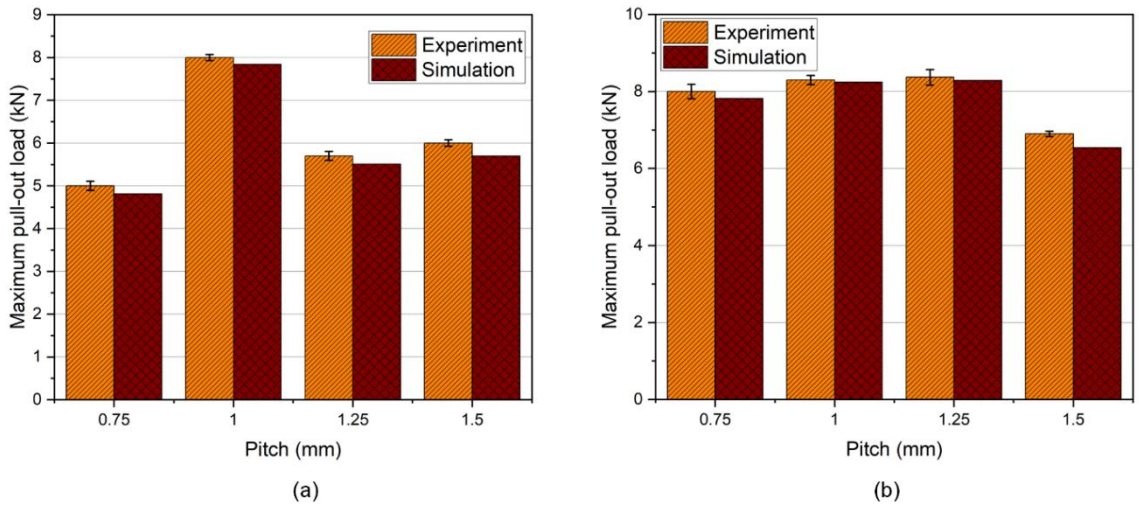

Fig. 5.13 Comparison of experimental and simulation values of the maximum pull-out test at (a) 3.9 kJ and (b) 4.4 kJ of discharge energies for all the pitches

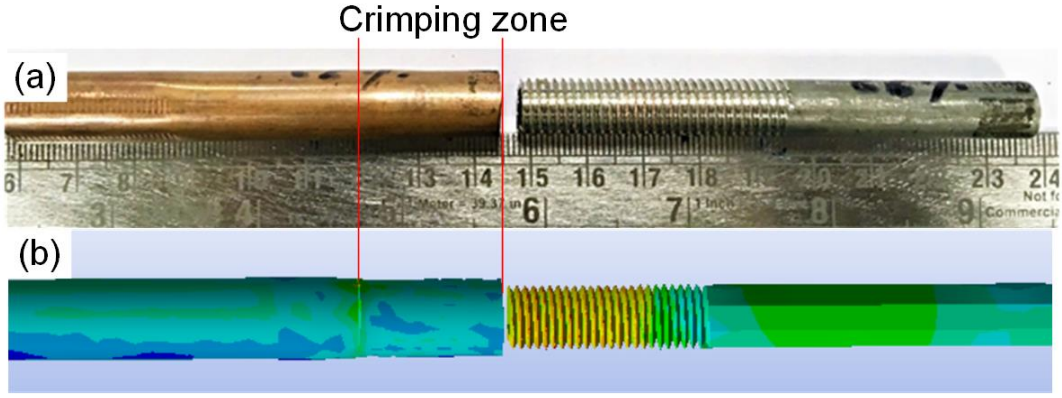

Fig. 5.14 Detachment failure mode in (a) experiment and (b) simulation for 1 mm threaded pitch for 3.9 kJ of discharge energy

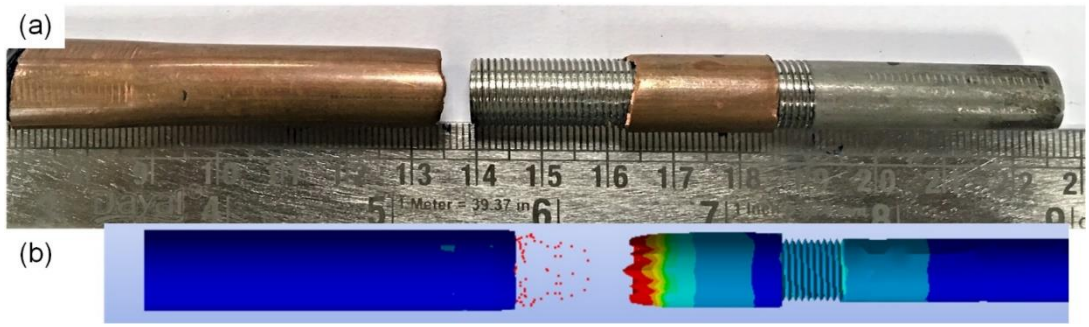

Fig. 5.15 Crack failure mode in (a) experimental and (b) simulation for 1 mm threaded pitch for 4.4 kJ of discharge energy

The pull-out load vs extension graphs for 3.4 kJ, 3.9 kJ and 4.4 kJ for four pitch values (0.75 mm, 1 mm, 1.25 mm and 1.5 mm) are shown in Fig. 5.16. At 3.4 kJ of discharge energy, the maximum pull-out strength of 2.5 kN is achieved for a pitch size of 0.75 mm among pitches. At 3.9 kJ of discharge energy, the maximum pull-out strength of 8 kN is achieved for a pitch size of 1 mm. However, at 4.4 kJ of discharge energy, maximum pull-out strength of 8.37 kN is achieved for a pitch size of 1.25 mm, with samples of 1 mm and 1.25 mm pitch failing through base copper tube failure. i.e. the joint strength is obtained to be higher than the base tube strength.

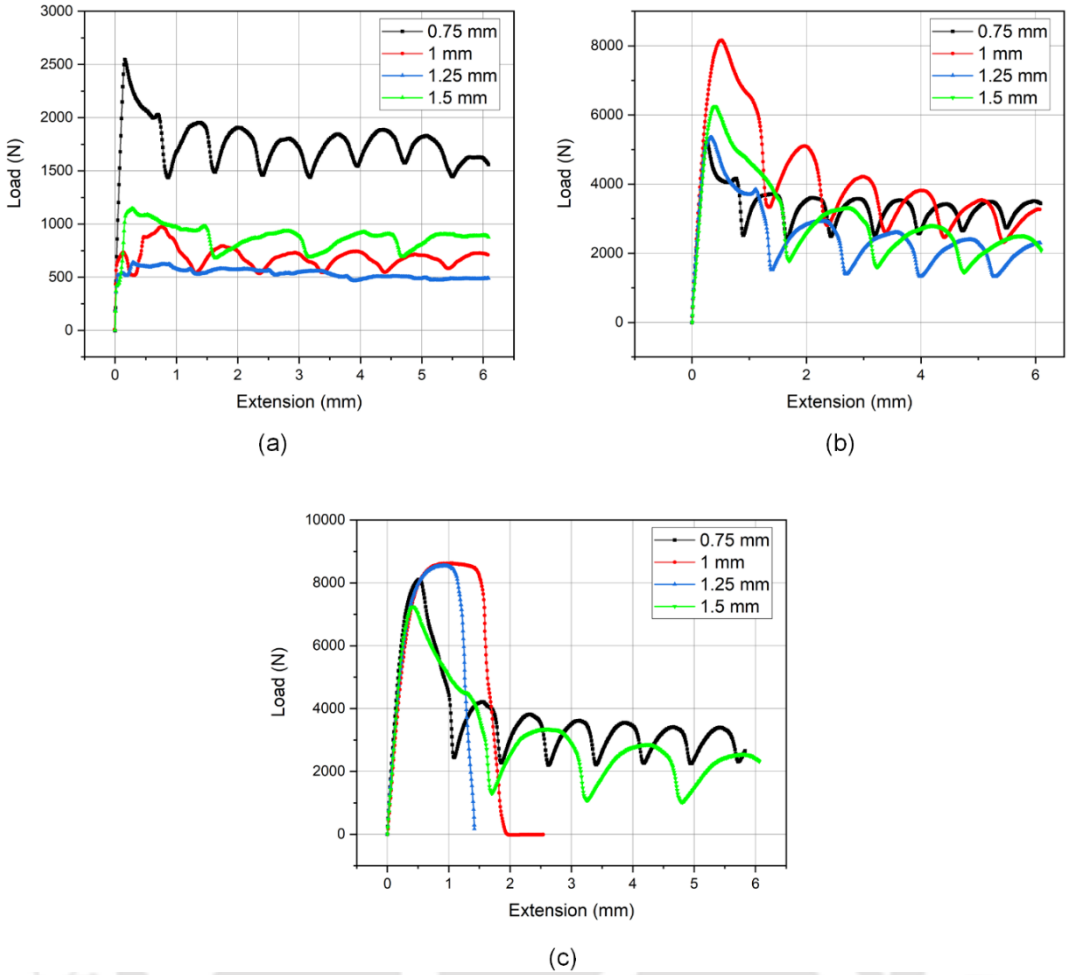

Fig. 5.16 Pull-out load vs extension plot (experimental) at (a) 3.4 kJ, (b) 3.9 kJ and (c) 4.4 kJ of discharge energy for thread profiles of different pitch

Fig. 5.17 indicates that for a particular pitch, the pull-out strength of the EMC crimped joint increases with an increase in discharge energy, which can be explained as follows: increment of discharge energy leads to increment in the radial deformation of the tubes. This increases interference pressure, and hence pull-out load also increases. Therefore, at every pitch, maximum strength is achieved at maximum energy in the experiment. Two different failure modes are observed during the pull-out test.

- Separation/detachment failure mode (joint failure): Joint strength is lower than the tensile strength of the base copper tube, which leads to detachment of the two joining partners. This failure occurs for all discharge energies except for 4.4 kJ of discharge energy with 1 mm and 1.25 mm pitch, as shown in Fig. 5.19
- Crack failure mode (tube failure): Joint strength is higher than the tensile strength of the base copper tube. This failure occurs for 4.4 kJ of discharge energy with 1

mm and 1.25 mm pitch.), as shown in Fig. 5.20 (a-b), due to a fracture in the base copper tube.

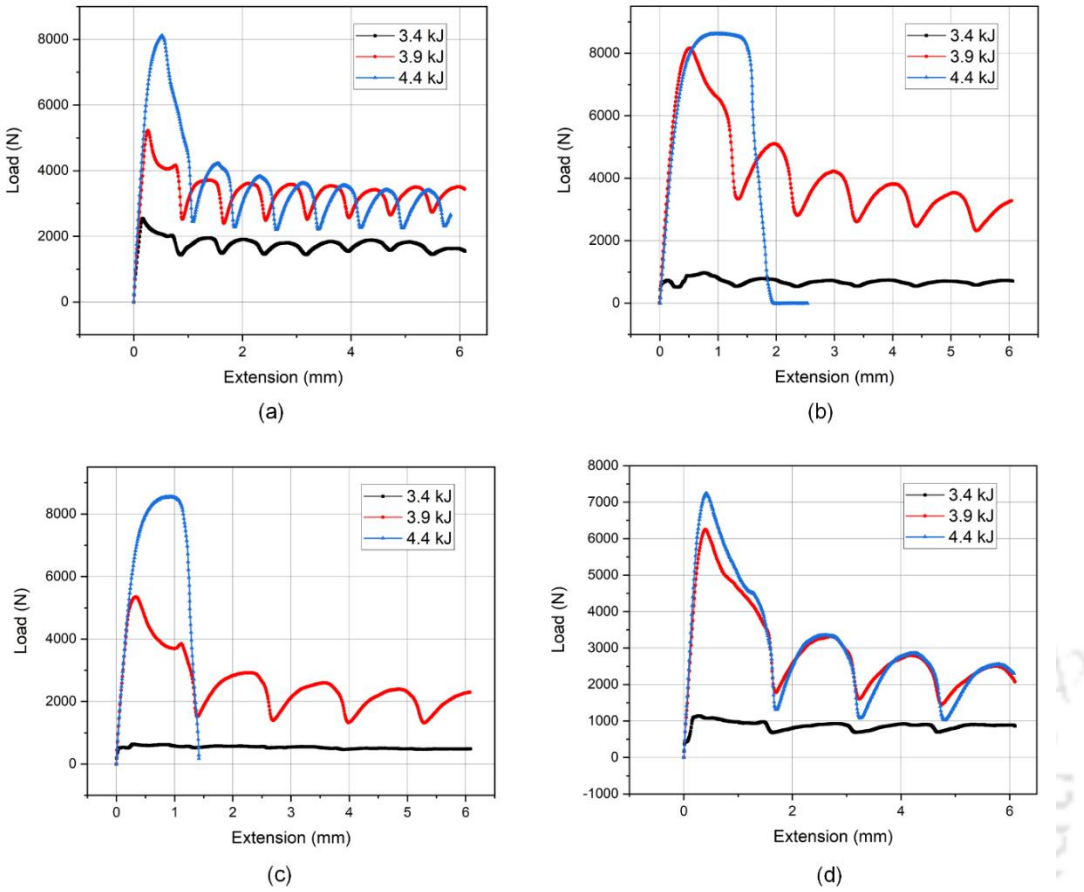

Fig. 5.17 Pull-out load vs extension plot (experimental) at (a) 0.75 mm, (b) 1 mm, (c) 1.25 mm and (d) 1.5 mm of pitch for three different discharge energies

Fig. 5.18 Separation failure mode

Fig. 5.19 Crack failure mode obtained for samples at 4.4 kJ of discharge energy for the pitch of (a) 1 mm and (b) 1.25 mm

Fig. 5.17 further show that the pull-out load-extension curve has followed a repetitive cyclic pattern for the threaded surface. This is because there is an increase of pull-out load in the separation mode due to the sticking of the outer copper tube onto the crest and root of the threads on the inner SS tube, followed by a release of the load due to the wear mechanism. However, no zig-zag pattern is observed for samples at discharge energy of 4.0 kJ with the pitch of 1 mm and 1.25 mm, as shown in Fig. 5.17 (b-c), because in this case, failure occurs due to a crack of the copper tube before initiation of any relative motion between joining partners.

5.3.1.4 Expressing the effect of pitch and discharge energy on deformation and strength of EMCT3 joint in empirical relations

Deriving Empirical relations from experimental data of deformation

An empirical relation is developed in MATLAB Curve fitting using the experimental data to predict the probability and distribution of the outcome (deformation and strength) when the process parameters vary in a range which has been further validated by varying the process parameters in a range and obtaining its results through numerical simulations and comparing it with predicted results from the empirical relations. Two different curve fitting methods are used. In the Bisquare method, a weighted sum of squares of the differences between fitted and experimental values are minimised, whereas, in the LAR method, the absolute differences between fitted and experimental values are minimised. The distance of the data point from the fitted line determines the weight of the point. Points closer to the line get the full weight, and those away from the line get reduced weight. Zero weight is given to points that are farther from the line than expected [134]. When a simple empirical model is required, polynomials are often preferred. Polynomial fits provide reasonable flexibility for less complex data, making the fitting process simple. They do have a disadvantage of unstable high-degree fits. Also, they can provide a good fit within the data range, but they may diverge wildly outside that range.

Here, the prediction is made only inside the range of the upper and lower bounds of pitch (0.75-1.5 mm) and discharge energies (3.4 kJ-44 kJ) used in the experiment. If the deformation is denoted by h_c, the pitch is denoted by P, and the discharge energy is denoted by E; the empirical relation can be expressed in the form,

$$h_c = a_{00} + a_{10}P + a_{01}E + a_{20}P^2 + a_{11}PE + a_{02}E^2 + a_{30}P^3 + a_{21}P^2E + a_{12}PE^2 \quad (5.1)$$

The coefficients (with 95% confidence bounds) derived using the bisquare method are shown in Table 5.3. The curve fitted using the Bisquare method is shown in Fig. 5.20. The black dots represent the experimental data points. The coefficients (with 95% confidence bounds) derived using the LAR method are shown in Table 5.4. The curve fitted using the LAR method is shown in Fig. 5.21. The black dots represent the experimental data points.

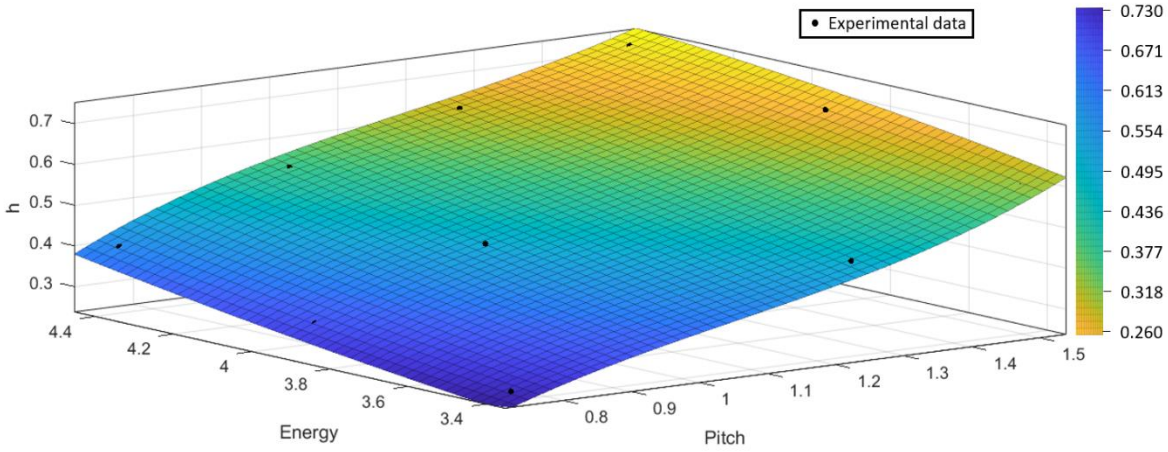

Fig. 5.20 Obtained solution surface through curve fitting using bisquare method

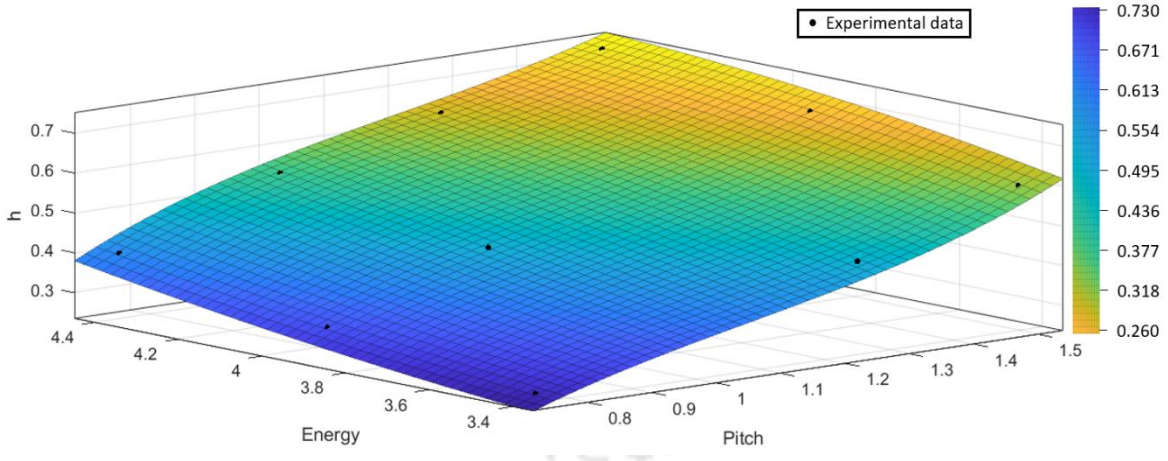

Fig. 5.21 Obtained solution surface through curve fitting using LAR method

Table 5.3 Coefficients of empirical relation fitted using bisquare method

a_{00}	a_{01}	a_{02}	a_{10}	a_{11}	a_{12}	a_{20}	a_{21}	a_{30}
1.168	-0.8989	0.09493	-0.7936	1.306	-0.0889	-1.17	-0.2807	0.6659

Table 5.4 Coefficients of empirical relation fitted using LAR method

a_{00}	a_{01}	a_{02}	a_{10}	a_{11}	a_{12}	a_{20}	a_{21}	a_{30}
1.947	-1.265	0.14	-1.673	1.673	-0.133	-1.023	-0.2874	0.6293

Validation of the obtained empirical relation with simulation

The L_2 error norm of the developed relations is calculated using the equation:

$$L_2\text{error} = \frac{\sum_{i=1}^{N}\left(h_{c_{s_i}} - h_{c_{e_i}}\right)^2}{\sum_{i=1}^{N} h_{c_{e_i}}^2}, \tag{5.2}$$

where i denotes a particular combination of discharge energy and pitch, $h_{c_{s_i}}$ is h_c from simulation for ith case, $h_{c_{e_i}}$ is h_c from empirical relation for the ith case. The L_2 error norm for the Bisquare method is calculated to be 8.77×10^{-5} and the L_2 error norm for the LAR method is calculated to be 1.2074×10^{-4}. This error is calculated over the 30 combinations of pitch and discharge energies, i.e. for combinations of discharge energies 3.4 kJ, 3.65 kJ, 3.9 kJ, 4.15 kJ, and 4.4 kJ with pitches of the thread 0.75mm, 1mm, 1.15mm, 1.25mm, 1.4mm and 1.5mm. The deformation predicted by the empirical relations is validated using simulations for the above combination of six pitches and five discharge energies, including two new intermediate pitches (1.15 mm and 1.4 mm) and two new intermediate discharge energies (3.65 kJ and 4.15 kJ). Considering the lower error norm of the Bisquare method as compared to the LAR method, empirical relation obtained from the Bisquare method is preferred. Fig. 5.22 shows the variation of h_c with discharge energy for different pitches, and Fig. 5.23 shows the variation of h_c with the pitch of the thread for different discharge energies. The markers represent the simulation data, and the lines represent the predicted values by the empirical relation. Both Fig. 5.22 and Fig. 5.23 perfectly match the empirical relation derived from experimental data and the numerical simulations using ANSYS Maxwell and ANSYS explicit dynamics. There is also a consistent match between empirically predicted deformation and numerically simulated deformations for the discharge energies of 3.65 kJ and 4.15 kJ and pitches of 1.15 mm and 1.4 mm. These data sets are not used while deriving the empirical relations from experimental results. Therefore, the empirical relation is proven to be successful in predicting h_c within the range of discharge energies.

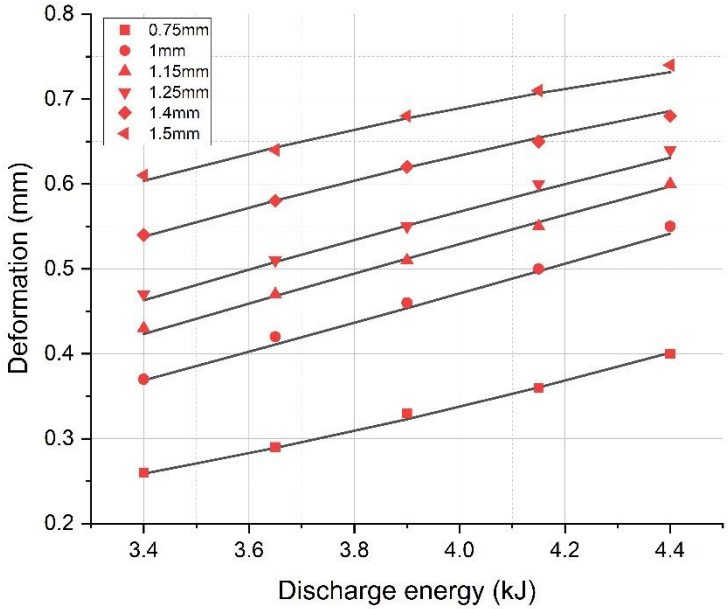

Fig. 5.22 Deformation vs discharge energy for different pitches

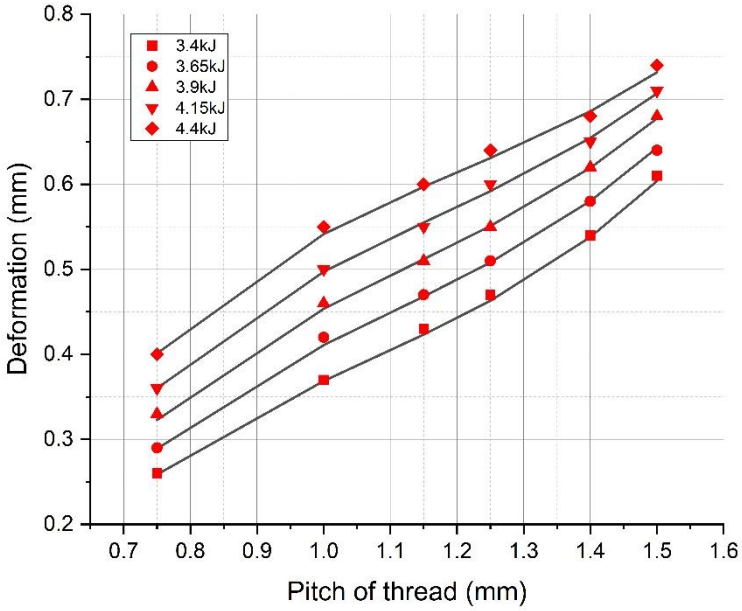

Fig. 5.23 Deformation vs pitch of thread for different discharge energies

Deriving Empirical relations from experimental data of pull-out strength

Here, the prediction is made only inside the range of the upper and lower bounds of pitch (0.75-1.5 mm) and discharge energies (3.4 kJ-44 kJ) used in the experiment. If the

Maximum pull-out load is denoted by L_{max}, the pitch is denoted by P, and the discharge energy is denoted by E; the empirical relation can be expressed in the form,

$$L_{max} = b_{00} + b_{10}P + b_{01}E + b_{20}P^2 + b_{11}PE + b_{02}E^2. \quad (5.3)$$

The coefficients (with 95% confidence bounds) derived using the bisquare method are shown in Table 5.5. The curve fitted using the Bisquare method is shown in Fig. 5.24. The black dots represent the experimental data points. The coefficients (with 95% confidence bounds) derived using LAR method are shown in Table 5.6. The curve fitted using the LAR method is shown in Fig. 5.25. The black dots represent the experimental data points.

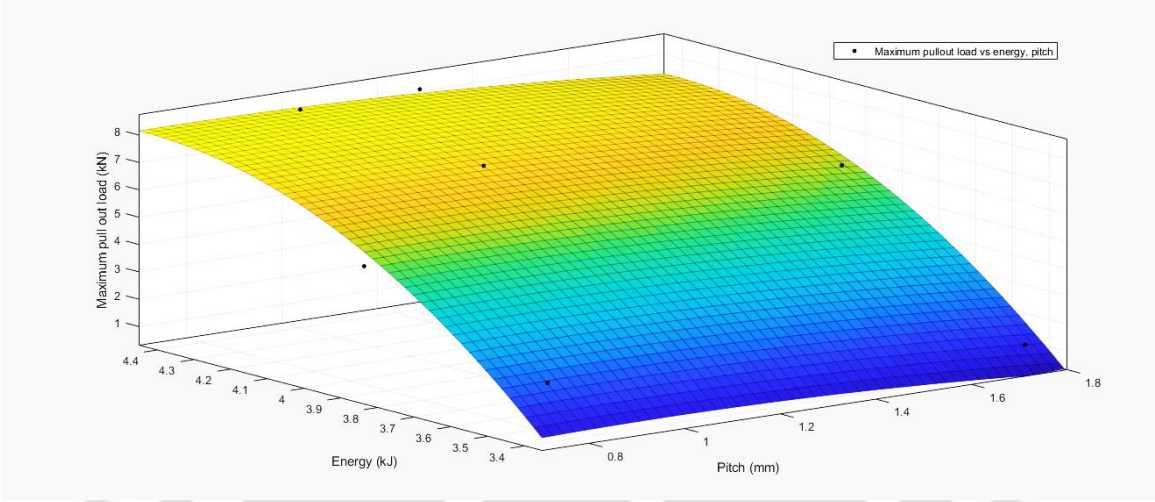

Fig. 5.24 Obtained solution surface through curve fitting using bisquare method

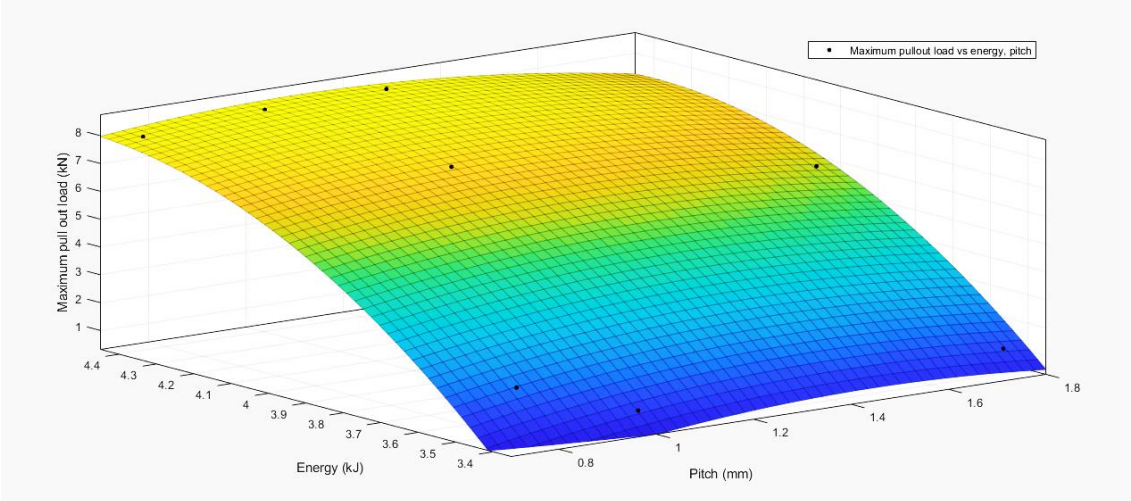

Fig. 5.25 Obtained solution surface through curve fitting using LAR method

Table 5.5 Coefficients of empirical relation fitted using bisquare method

b_{00}	b_{01}	b_{02}	b_{10}	b_{11}	b_{20}
-115.3	55.2	-6.197	2.418	-0.2414	-0.8572

Table 5.6 Coefficients of empirical relation fitted using LAR method

b_{00}	b_{01}	b_{02}	b_{10}	b_{11}	b_{20}
-125.3	56.78	-6.159	11.67	-1.437	-2.371

5.3.1.5 Effect of thread angle on deformation height (h_c)

All previous analysis has been performed considering the thread angle of 60° for the threaded surface profile of the inner SS304 tube. The only discussed variables are the discharge energy and the pitch. So, for further analysis of the EMCT3 joint, the effect of the thread angle on the deformation height (h_c) produced is also discussed. Five different thread angles (45°, 52.5°, 60°, 67.5° and 75°) are selected. Table 5.7 shows the process parameters under consideration.

Table 5.7 Parameters of the process

Discharge Energy	Pitch of Thread	Thread Angle
3.4kJ	0.75mm	45°
3.9kJ	1mm	52.5°
4.4kJ	1.25mm	60°
	1.5mm	67.5°
		75°

Simulations are run for the three variables' 48 combinations (3×4×4 (cases for 60° are already discussed in section 5.3.1.1)). The deformation is plotted against the thread angle for different discharge energies while keeping the pitch of the thread constant. The results are plotted in Fig. 5.26. For a particular thread pitch and specific discharge energy, the deformation height increases with the thread angle at first, reaches a maximum, and then decreases. This trend is followed for all selected discharge energies for a constant pitch. The thread with the highest angle (75°) has a lower thread depth to be filled by the deformed outer Cu tube. The thread depth increases with a decrease in thread angle, and

therefore an increment in deformation height is observed with a decrease in thread angle. However, threads with lower angles have a steeper slope because hypotenuses increase with a decrease in thread angle, due to which the friction resistance towards the deformation of the outer Cu tube onto the thread also increases, which restricts further deformation. Furthermore, threads below 60° have a depth more than the thickness of the outer Cu tube beyond that point, force-fit joining transitions into form-fit joining, which requires a higher amount of discharge energy and; hence at particular discharge energy, there is a further decrement in deformation height.

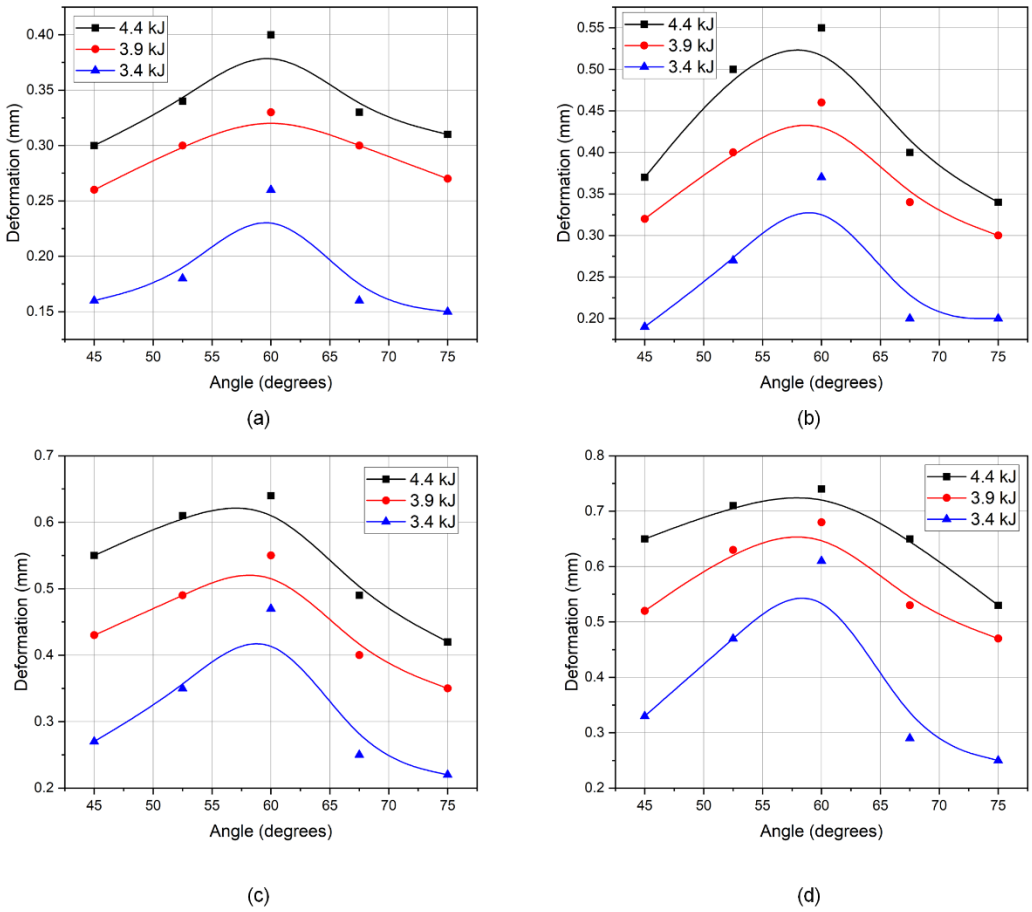

Fig. 5.26 Variation of deformation height with thread angle for (a) 0.75mm, (b) 1mm, (c) 1.25mm and (d) 1.5mm of thread pitch values

Fig. 5.27 showcases the variation of maximum pull-out load with thread angle at a constant pitch of 1 mm in simulation and experiment. It is observed that at lower discharge energy (3.4 kJ), the EMCT3 joint with the highest thread angle provides the maximum strength as the thread with the highest angle (75°) has a lower thread depth to be filled by the deformed outer Cu tube leading to higher surface contact between the two workpieces causing higher strength. After that, the highest strength is observed for the lowest thread

angle (45°), which offers higher resistance to the relative movement between two workpieces as threads with lower angles have a steeper slope due to which the component of frictional force towards the axial direction is higher, causing higher pull-out strength. However, when the discharge energy is further increased to 3.9 kJ, the maximum strength obtained is shifted from the thread angle of 75° to 67.5°. This can be well explained by two contradicting physical phenomena using Fig 5.28: 1) the component of frictional force in the axial direction, which contributes toward the pullout strength of the EMCT3 joint, increases with an increase in thread angle (Fig. 5.28 (a)). Hence pull-out strength should increase with the increase in thread angle. 2) On the other hand, with the decrease in thread angle, the depth of the thread increases, which provides an opportunity for more interference fit. Furthermore, as the base (pitch) is the same in Fig. 5.28 (b), the hypotenuses increase with a decrease in thread angle, leading to higher contact length, which causes higher frictional force and hence higher pull-out strength. As a combined result of these two opposite contributing factors, intermediate thread angles (60° or 67.5 °) provide the best performance at higher discharge energies.

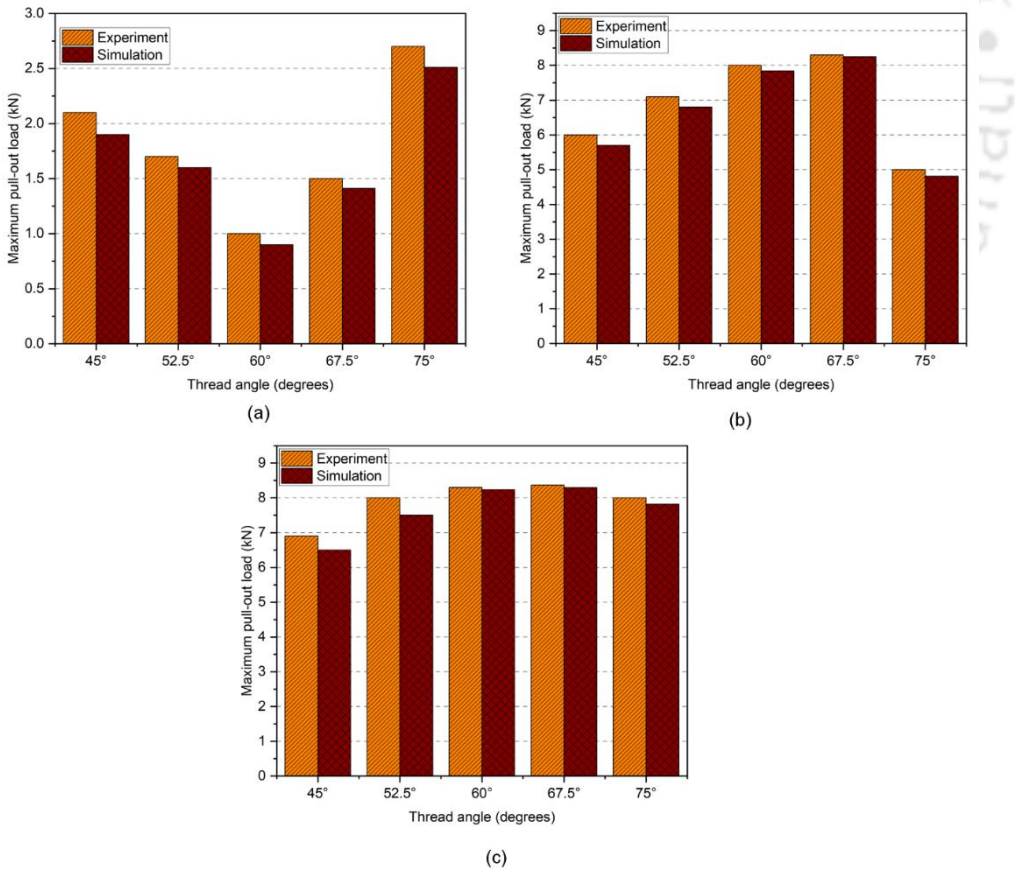

Fig. 5.27 Comparison of maximum pull-out load results obtained from experiment and simulations for five different thread angles and at 1 mm of thread pitch at (a) 3.4 kJ and (b) 3.9 kJ and (c) 4.4 kJ of discharge energies

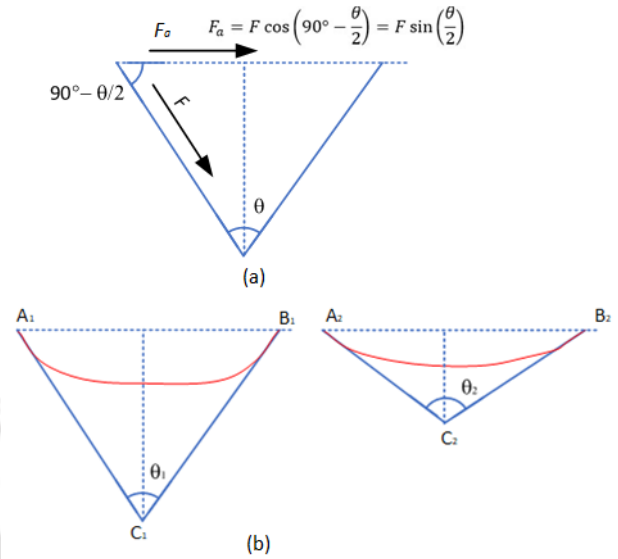

Fig. 5.28 Image showcasing (a) dependency of the axial component of the frictional force on the thread angle and (b) variation of contact length due to variation in thread angle

5.3.1.6 ANOVA analysis to address the relative contribution of different process parameters on the pull-out strength of the EMCT3 joint

The pull strength testing is performed experimentally for all three variables' 48 combinations (3×4×4 (cases for 60° are already discussed in section 5.3.1.3)), and a statistical approach is used to clarify the relative effects of different processes parameters on the pull-out strength of the EMCT3 joint. Hence a three-factor Analysis of variance (ANOVA) method is used on the obtained dataset to investigate the effect of multiple parameters, namely pitch, thread angle and discharge energy, on the strength using the ANOVA module in the Minitab software. It is a statistical tool to split the aggregate variability present inside a dataset into random and systematic factors. A list of influencing factors and their corresponding levels affecting the responses are shown in Table 5.8. The influencing factors are 3 discharge energy values (3.4 kJ, 3.9 kJ and 4.4 kJ), 4 different pitches (0.75 mm, 1 mm, 1.25 mm and 1.5 mm) and 5 different thread angles (45°, 52.5°, 60°, 67.5° and 75°). Table 5.9 comprises the degrees of freedom (DF), contribution %, the sum of squares (SS), the sum of mean squares (MS), Fisher (F) value and pre-set confidence (P) value. Error represents the consideration of trials.

Table 5.8 Influencing factors and levels affecting the EMCT3 joining process

Symbols	Factors	Levels				
		1	2	3	4	5
A	Discharge energy (A)	3.4 kJ	3.9 kJ	4.4 kJ		
B	Pitch of the thread (B)	0.75 mm	1 mm	1.25 mm	1.5 mm	
C	Angle of the thread (C)	45°	52.5°	60°	67.5°	75°

Table 5.9 Analysis of Variance for Transformed Response

Source	DF	Contribution %	SS	MS	F-Value	P-Value
Discharge Energy	2	32.99%	2.8925	1.44625	128.17	0.000
Pitch of the thread	3	41.35%	3.6251	1.20838	107.09	0.000
Thread angle	4	19.22%	1.6847	0.42118	37.33	0.000
Error	50	6.44%	0.5642	0.01128		
Total	59	100.00%				

The significance of the influence of the factors can be determined by comparing the F-value with the corresponding critical F-value at a 99% confidence level. All the obtained F-values are higher than their corresponding critical F-value, which implies that both the factors and their interplay significantly affect the response, i.e. the joint strength of the Cu-SS tubular Joint. Their corresponding p-values can further clarify it as all p-values are smaller than 0.05 satisfying the 95% confidence level. The contribution % of factors A, B, and C are calculated to be 32.99%, 41.35%, and 19.22 %, respectively. Hence it can be shown that the pitch of the thread has a more significant impact on the response variable (pull-out strength of EMCT3 joint) than the discharge energy and thread angle.

5.4 Conclusions

- A non-coupled multi-step simulation model is developed using Ansys Maxwell and Ansys explicit dynamics to predict the deformation and joint strength of an EMCT3 joint. The simulations are done for multiple combinations of discharge energies and pitches of the thread. The calculated deformation of the tube is in good agreement with the experiments. The predicted strengths have shown an error of 1–9% compared with the experimental results.
- EMCT3 joint samples are failed through the separation failure mechanism, leading to relative motion between the Cu and SS 304 tubes in the axial direction during pull-out test samples at low energies. This behaviour is observed in both experiments and simulations. However, simulation of higher energy samples (4.4 kJ for 1 mm and 1.25 pitch) show base Cu tube crack failure mode leading to tube failure instead of joint showcasing joint strength to be higher than the base Cu tube strength, and the same has been validated through experimental results.
- An empirical relation is developed from the experimental data by curve fitting using the bisquare and LAR methods. Bisquare method has a lesser L_2error norm, so it is preferred as the predicting relation. These empirically obtained deformations also closely match with the FEM-simulated deformations. The empirically predicted deformation values are further validated with FEM simulations for intermediate pitches and discharge energies, which have not been considered in deriving the empirical relation.
- Three factor ANOVA method shows that the pitch of the thread contributes more to the strength of the EMCT3 joint than the pitch of the thread and discharge energy.

6 Electromagnetically Assisted Adhesive Joining (EAAJ)

6.1 Introduction

Chapters 3, 4 and 5 propose the various aspects of an improved multi-material Cu-SS tube-to-tube joint created using the EMC technique with the experimental and numerical investigation. The produced joints have good strength in the case of smooth surfaced joints, but joint strength increases to the base Cu tube failure strength with the use of a threaded surface for the outer surface of the inner SS tube. However, EMC tubular joints can only be used for structural applications as the absence of metallurgical bonding leads to a lack of leak tightness and makes them unfit for piping applications. EMW joints are recommended for such purposes, as demonstrated by Patra et al. [44], but that requires a heavy initial investment in terms of large capacitor banks to accelerate the flyer workpiece to a velocity higher than the critical velocity (velocity of the impact of flyer workpiece onto target workpiece leading to the formation of a metallic bond between two workpieces). Hybrid joining techniques can be developed to counter such disadvantages to achieve leak-tight tubular joints with higher strength at lower discharge energy levels and lower initial investment while keeping all the benefits of multi-material unconventional joining.

Therefore, an alternative approach can be employed to join different tubular components using adhesives, and in recent years the applications of adhesives have significantly increased, as discussed by Amancio et al. [135] and Petrie et al. [136]. Joining with adhesives has its advantages and disadvantages. Adhesive joints do not require any additional components; they are easy to assemble and lead to a lightweight structure, as talked about by Martinsen et al. [137] and Silva et al. [138]. However, Gallio et al. say that an adhesive joint may lead to durability issues and lower joint strength [139]. These demerits can be overcome by combining adhesive joining with another joining technique (mechanical fastening/conventional/non-conventual joining) to generate a hybrid joint, leading to combining the benefits of multiple methods while overcoming their drawbacks, as discussed vividly by Silva et al. [138] and Ufferman et al. [140].

Furthermore, Meschut et al. [141] and Silva et al. [138] have also concluded that multi-material, multi-method hybrid joints can have the advantages of two different materials and two different methods. Mechanical clamping is employed along with adhesive joining by Silva et al. [138]. The author has observed that mechanical fasteners provide the

necessary clamping force during the adhesives' curing process and restrict the parts from moving. At the same time, the adhesives contribute to the joint and mechanical fastener's shear strength and increase the energy absorption before the joint's complete failure during destructive testing, as said by Slvial et al. [138] and Ufferman et al. et al. [140]. Multiple experiments have shown that adding adhesives into conventional interference-fit joints significantly improves joint strength. Gallio et al. [142] and Kawamura et al. [142] point out that the strength of such joints is the summation of resistance due to adhesives and interference pressure. Dragoni et al. have also compared the static strength of a tightened joint bonded with or without adhesive and observed that strength increases with clamping force and applying strong anaerobic adhesive [144]. Corigliano et al. [145] have investigated the effect of contact pressure on the shear strength of an anaerobic adhesive layer of finite thickness and surface area. The analysis discusses two-component, high strength, steel pressed, and bonded joint joined with weak and strong anaerobic adhesive (Loctite 243 and Loctite 638). Authors have observed a 10 times increment in shear strength with 1000 MPa and zero pressure conditions with the Loctite 638 adhesive. Ragni et al. [146] have discussed the shear strength measurement in hybrid interfaces of press-fitted cylindrical components bonded with strong adhesives (Loctite 638 and Loctite 648).

Furthermore, the authors have validated the applicability of the constitutive model describing the interface behaviour by combining the cohesive and a pure friction law. Castagnetti et al. [147] have further analysed the experimental responses of a pressure-reinforced adhesively bonded interface up to complete failure. The authors have used two types of adhesives (Loctite 243 and Loctite 638) and the nominal contact pressure as two different parameters for this investigation. Castagnetti et al. discuss a steady increment in shear strength with an increment in clamping pressure in a clamped adhesive friction joint. Authors have emphasised using strong anaerobic adhesives instead of weak anaerobic adhesives to maximise the strength increment with clamping pressure.

Furthermore, a micro-scale finite-element simulation model is developed to explain the macroscopic behaviour [148]. Castagnetti et al. [149] have also designed an experimental campaign including three different variables distributed over two levels to investigate a micro-mechanical model proposed by Dragoni et al. [150], which explains the shear strength provided by an anaerobic adhesive as a function of intimate properties of adhesive adherents at the interface. Dragoni et al. [150] have analysed the static strength

of an anaerobic adhesive-supplemented friction joint and observed that friction strength is proportional to the clamping force, whereas the adhesive strength is independent of the clamping force. Croccolo et al.have investigated the effect of the ratio of coupling length and coupling diameter (engagement ratio) on the response of an anaerobic adhesive in a press-fitted specimen and observed the shear strength of the joint to be negligibly dependent on the engagement ratio [151]. Croccolo et al. [152] have further investigated the effect of coupling techniques and interference levels on the shear strength of an anaerobic Loctite 648 adhesive in a press-fitted adhesively joined shaft-hub assembly made of 42CrMo4 tempered steel and 16CrNi4Pb hardened steel. Authors have observed that the adhesive significantly enhances shear strength when clearance is induced to avoid adhesive stripping during assembling [152].

In this chapter, a novel hybrid joining technique has been successfully developed, combining EMC techniques with adhesive joining, which has been named in this work as electromagnetically assisted adhesive joining (EAAJ). Successful smooth-surfaced Cu-SS tubular joints are created and compared with EMC joints to demonstrate the improvements achieved over EMC with the application of adhesives. An acrylic-based anaerobic adhesive is used in this process. Destructive testings (pull-out and compression) are performed, and improvements in the strength with adhesive are highlighted. A two-factor ANOVA analysis is also performed to calculate the contribution of adhesives and discharge energy over pull-out and the compressive strength of the joint. Micro-hardness and macrostructure are analysed for various discharge energy values. Furthermore, one experimental setup has been developed to analyse improvement in air leak tightness due to adhesives.

6.2 Working Principle

The basic working setup of the EAAJ process is a modification over the EMC working setup, as shown in Fig. 6.1. The current curve is shown in Fig. 6.2 after measuring with the help of a Rogowski coil and an oscilloscope. Therefore in one hand, magnetic field interaction leads to high Lorentz force generation, which results in plastic deformation. This plastic deformation leads to interference pressure build-up between tubes which contributes to developing joint strength.

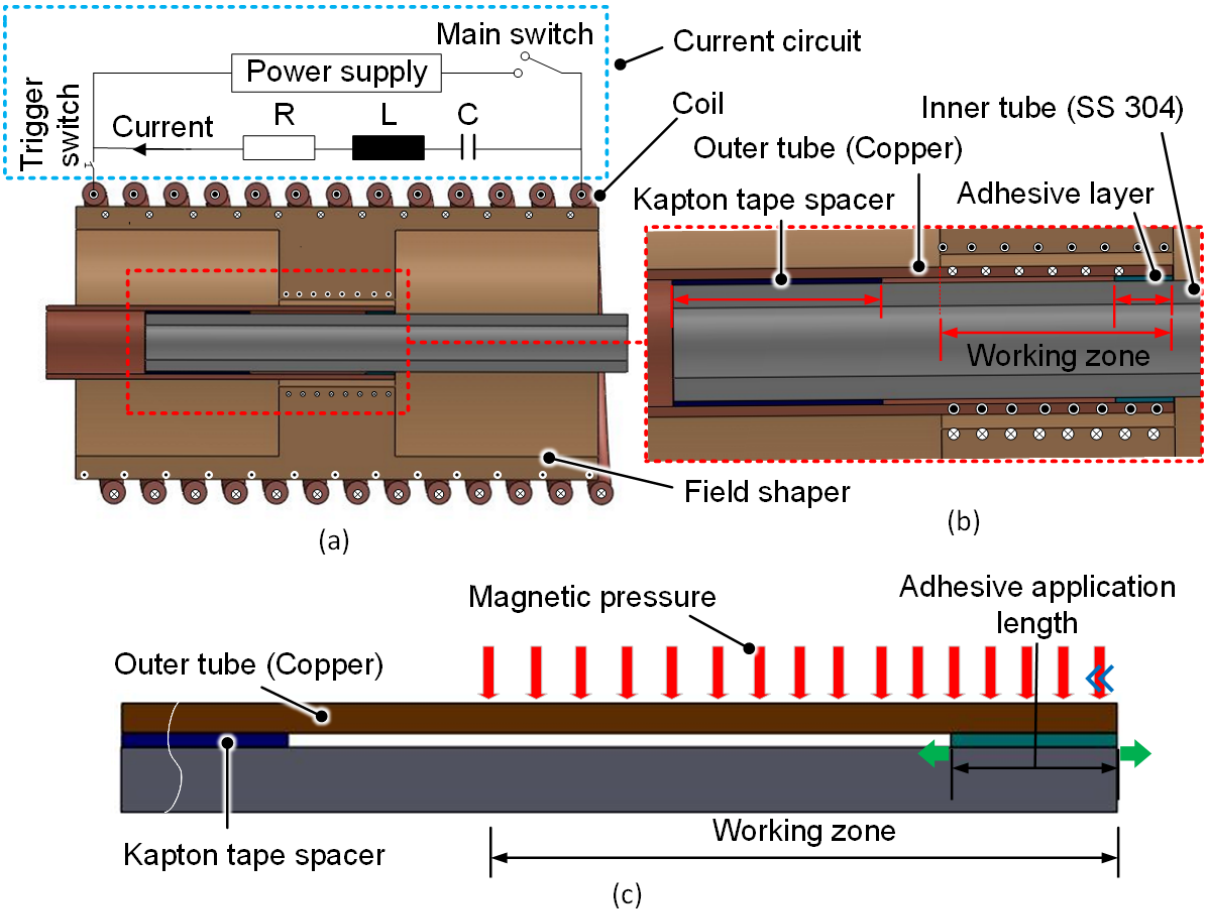

Fig. 6.1. Pictorial representation of the experimental setup demonstrating (a) the placements of various components on setup, (b) Zoomed view showing the details and (c) mechanism of EAAJ indicating the flow of adhesives

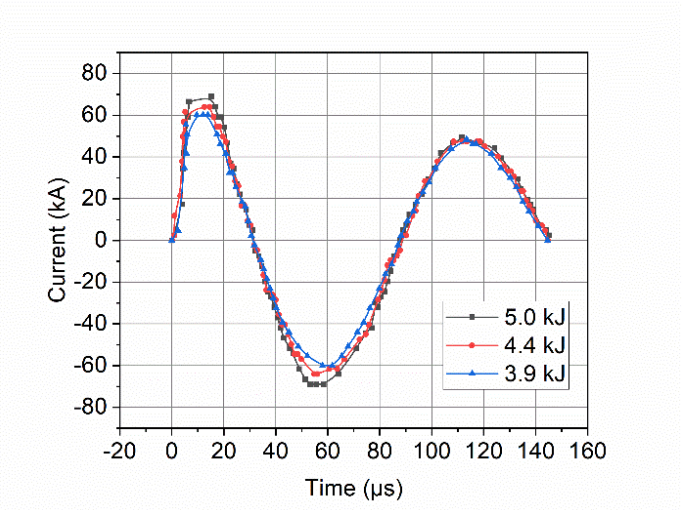

Fig. 6.2. The first pulse of the current waveform in the coil for three discharge energy values observed through an oscilloscope

On the other hand, adhesive joining occurs which is based on developing an intermolecular bond between the workpiece and the polymeric adhesive itself. Adhesive goes through chemical and physical reactions for bond formation. It gets strongly affected by the quality of the surface. In this case, the adhesive is applied between the outer and inner tubes; the Interference condition creates a confined situation between tubes for the anaerobic adhesive to cure effectively. Therefore, in this case, electromagnetic crimping plays a significant role in facilitating the curing process of the anaerobic adhesive effectively. However, applying adhesives in the entire working zone can significantly reduce the plastic deformation of the outer tube due to the dampening effect of the highly viscous adhesive between the outer and inner tube. The radial velocity of the outer tube reduces significantly due to this dampening effect, causing less deformation leading to lower residual stress and, eventually, lower joint strength. Therefore, the adhesive has only been applied to a smaller portion of the working zone to enhance adhesive strength and leak tightness without significantly reducing the interference-fit joint strength. Section 4.2.2 observes that electromagnetic forming is initiated from the free end of the outer tube and moves towards the working zone (closed-end), squeezing the adhesives in between tubes in the longitudinal and circumferential direction, as shown in Fig. 6.1 (c). Circumferential movement of adhesives may lead to non-uniformity in the circumferential deformation in the working zone, while the longitudinal movement of adhesives shifts the adhesive application length inward without any significant loss of adhesives due to squeezing. This is further discussed in section 6.4.4.

6.3 Materials and Methods

6.3.1. Formation of the electromagnetically assisted adhesive tube-to-tube joining between Cu and SS tubes

6.3.1.1 Geometry and Materials of the Constituent Cu and SS tubes and Loctite 638 adhesives

A Cu tube is used as an outer tube, and SS 304 tube is used as an inner tube. Dimensions of the workpiece, mechanical properties and chemical percentage are the same as discussed in section 3.2.2. An acrylic-based anaerobic structural adhesive, Loctite 638, is selected for this experiment based on its high-temperature resistance, small particle size and low viscosity. Properties of the adhesive are shown in Table 6.1. It cures quickly in the absence of air after getting in contact with the metal.

Table 6.1 Properties of Loctite 638 adhesive used [153]

Adhesives	Loctite 638
Technology	Acrylic
Chemical type	Urethane methacrylate
Appearance (uncured)	Green liquid
Fluorescence	Positive under UV light
Components	One component- requires no mixing
Viscosity	High
Cure	Anaerobic
Secondary cure	Activator
Application	Retaining
Strength	High

6.3.1.2 Experimental Set up for the formation of joint

Electromagnetically assisted adhesive joining is carried out on an electromagnetic forming (EMF) machine.

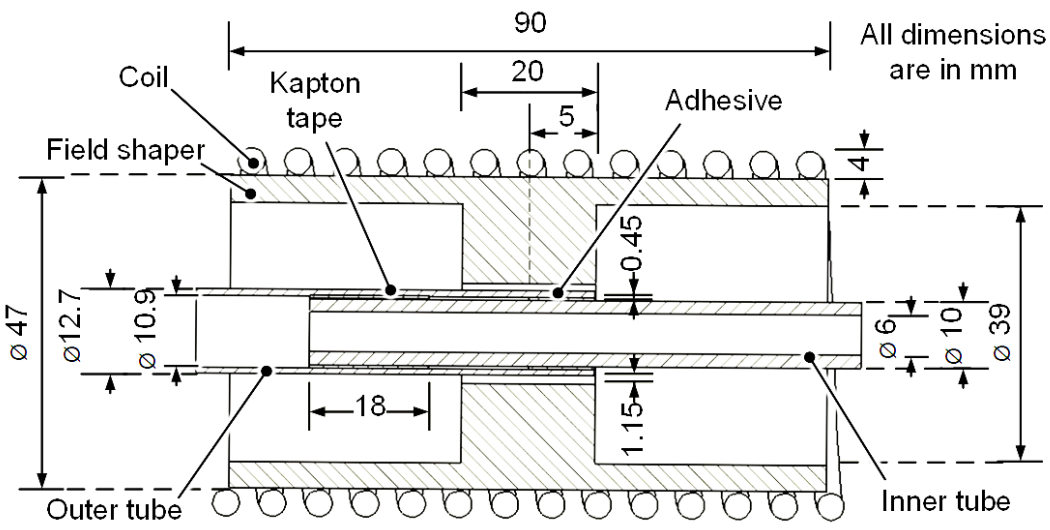

Fig. 6.3 Schematic diagram showing the dimensions of various parts in the EAAJ setup

The coil setup is provisional, and it gets replaced after every 50 experiments. The smaller coil has lower inductance loss; therefore, it works better due to lower losses on a smaller electromagnetic forming setup of 10 kJ.

The detailed description of the dimensions of various components in this process is demonstrated in Fig. 6.3. The adhesive is applied in the gap between the outer tube and

the inner tube in the overlapped zone. The adhesive application length in the overlapped area is 5 mm from the free end of the outer copper tube.

6.3.1.3 Preparation of Surface and Application of adhesives

Quality of the surface plays a vital role in deciding the strength of an adhesive joint. Therefore, mechanical abrasion with various silicon carbide papers having grit size 80 is used to remove any surface layer from the tubes. After the initial surface preparation, tubes are cleaned in methyl alcohol to remove any dirt. A high-temperature resistant Kapton tape is used as a spacer (see Fig. 6.1) between the tubes applied on the SS tube at a distance of 5 mm from the working zone to avoid any effect on the deformation process. A piece of masking tape is applied at the edge of the bonding area, and then adhesive (Loctite 638) is deposited along that edge which is removed after the adhesive application before joint formation and processing. After the deposition, copper and stainless-steel tubes are placed coaxially, followed by co-axial placing with the coil and field-shaper using Polytetrafluoroethylene (PTFE) fixtures. The overlapped length between the outer and inner tube, also known as the working zone, is 20 mm. At the same time, the adhesive is applied only up to a length of 5 mm from the free end of the copper tube in the working zone.

6.3.1.4 Other process parameters

After a few minutes of anaerobic adhesive settling, EMC is performed at 3 different discharge energy values (3.9 kJ, 4.4 kJ and 5.0 kJ). Since the adhesive is still in a semi-solid/liquid state initially, a movement of the incompressible adhesive is observed in longitudinal and circumferential direction due to the impact of the outer tube onto the inner tube, causing non-uniformity in deformation in the adhesive application area. Specified discharge energy values are decided after the initial screening and represent 62%, 66% and 70% of the capacitor charging, respectively. The range of discharge energy is selected for this analysis is based on the range of pull-out strength being offered by the EMC Cu-SS tubular joint. After 5.0 kJ, the rate of increment of pull-out strength with increment in discharge energy is observed to be reduced. Although an increment in discharge energy will increase the strength, only three values are used to compare EAAJ and EMC for simplicity. Samples are cured for 72 hours in the absence of air at room temperature. Experiments are also performed without adhesives as electromagnetic crimping to analyse the benefits of the improved hybrid joining method over the electromagnetic crimping process.

6.3.2 Experimental analysis of strength, hardness and leak-tightness for the electromagnetically assisted adhesive tube-to-tube joint

6.3.2.1 Strength testing: (i) pull-out test, (ii) compression test, microhardness and deformation analysis

Two destructive tests evaluate the joint strength of Cu-SS tubular adhesive joints, viz, (i) Pull out test and (ii) Compression test. The procedures are discussed in section 3.2.3.1 and section 3.2.3.3, respectively. Furthermore, microhardness and deformation analysis is performed as per section 3.2.3.4.

6.3.2.2 Leak testing setup

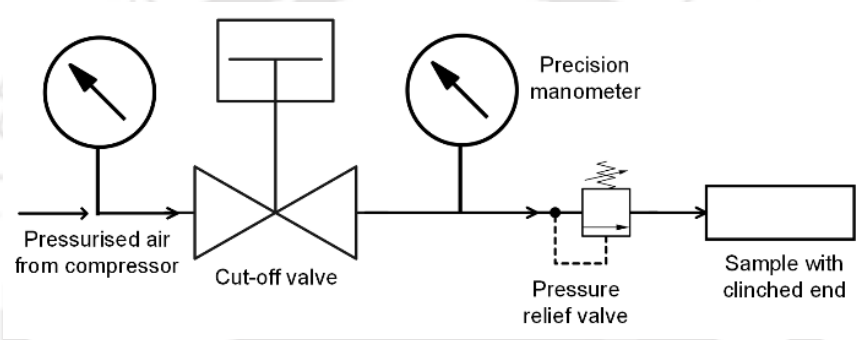

Fig. 6.4 Schematic diagram of the air leak test setup

An air leak testing setup has been developed to check the leak tightness of joined samples. A schematic of the leak testing setup is shown in Fig. 6.4. The setup comprises of a cut-off valve, a precision manometer, a pressure relief valve and one tubular connection leading to clinched hybrid joint samples. The outer Cu tube end is clinched and then brazed so that the other end can be closed and leakage in the tube joining region can be identified. Total 18 {2 processes (EAAJ and EMC) × 3 discharge energy × 3 repeatitions} samples are prepared, including three repetitions to ensure repeatability of the results. The leak test is performed at 8 bar air pressure. Non-destructive leak tightness inspection has been carried out.

Initially, samples are inspected by the bubble test. Samples are submerged inside water in the tank, and pressurised air is passed to the clinched sample. Any present leakage will lead to the escape of pressurised air resulting in bubble formation, as discussed by Kalpakjain et al. [154]. This test can help to determine the location of the leak, but the test only gives qualitative results. Therefore, after the initial inspection, an air pressure decay test is performed. In this method, samples are pressurised until a threshold value of

pressure is reached, and then the supply of pressurised air is cut off so that the only way the air can get out is through leaks (if present). The presence of any leak will lead to a reduction of the air pressure in the system. This air pressure decay test offers a quantitative measurement of leakage. An energy equivalent measure of leak rate Q (in Watt) can be calculated as

$$Q = \frac{\Delta p.V}{t}, \tag{6.1}$$

where Δp represents the pressure drop across the elapsed time t, V represents the pressurised air volume. Calculated Q for EAAJ as well as EMC crimped joint is compared with industry standards.

6.4 Results and Discussion

Electromagnetically assisted adhesive joining is performed for 3 discharge energy values. Zoomed 5× view of the successfully joined samples at 4.4 kJ discharge energy by EAAJ and EMC method are shown in Fig. 6.5. A clear difference in the outer surface profile in the working zone is observed. EAAJ samples have a curved profile in the adhesive zone due to the non-uniform distribution of adhesive and a smooth profile in the non-adhesive zone. However, a smooth profile can be seen in the ECM samples due to uniform deformation across the crimping zone/working zone.

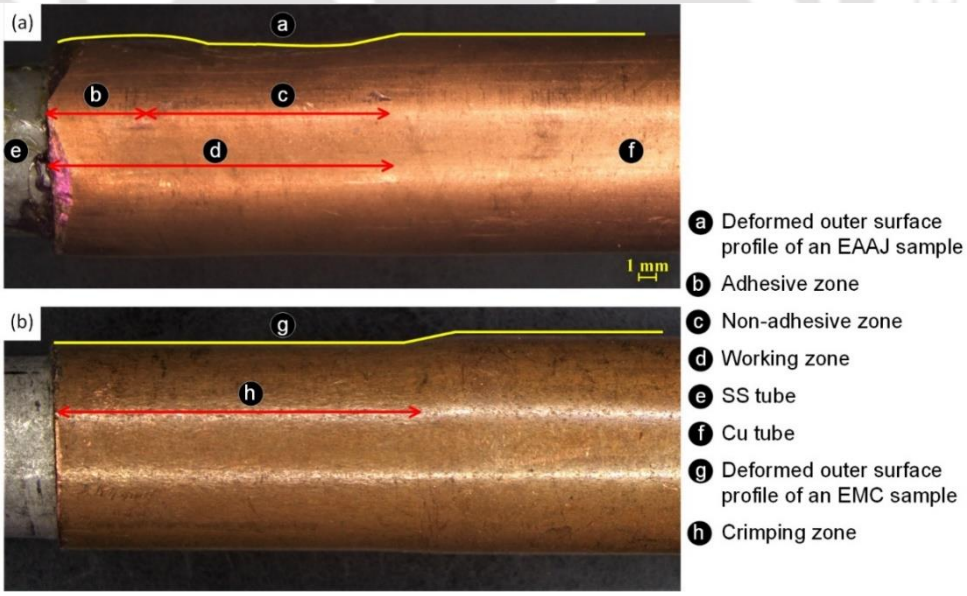

Fig. 6.5 Cu-SS tube-to-tube joined sample at 4.4 kJ of discharge energy by (a) EAAJ and (b) EMC method

6.4.1 Pull-out testing results

6.4.1.1 Pull-out load variation and failure mode analysis

The pull-out load vs displacement curve and maximum Pull-out load without failure for EAAJ and EMC joints for three different discharge energies are shown in Fig. 6.6 (a) and (b), respectively. It can be observed from Fig. 6.6 (a) that a maximum pull-out load of 2.1 kN is obtained for an EMC joint at 5.0 kJ of discharge energy which is increased by 2.6 times to 5.3 kN with the use of adhesive in the case of hybrid EAAJ joint. Two factors contribute to the improvement of strength in EAAJ; Here, in addition to the attained strength due to interference pressure resulting from electromagnetic crimping, strength is also provided by structural adhesive.

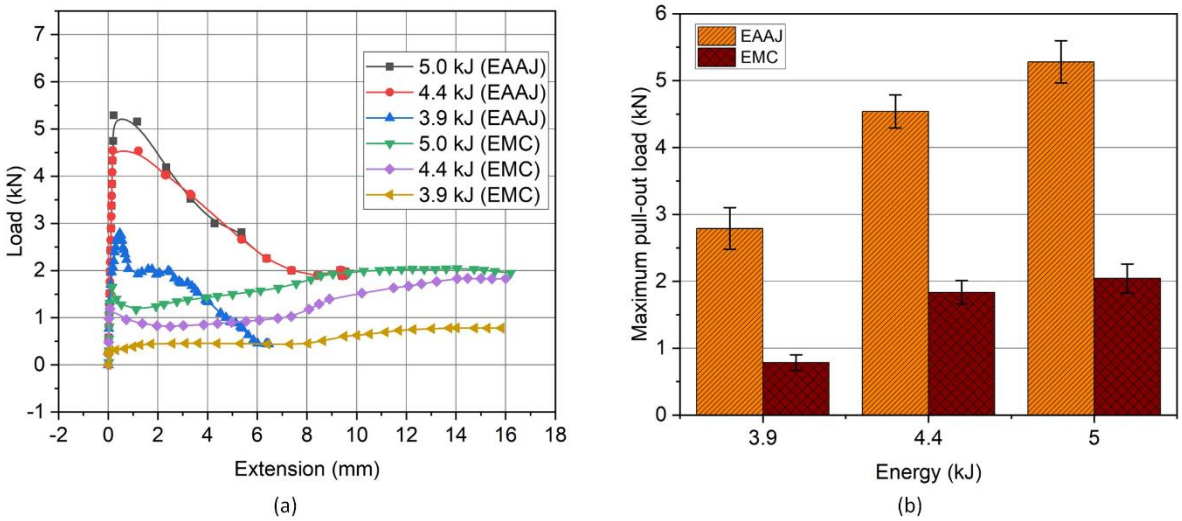

Fig. 6.6 (a) Pull-out load vs extension plot and (b) maximum pull-out load comparison for with and without adhesive joint at three different discharge energy values

Two significant load values can be observed during the pull-out test for EMC joint samples in Fig. 6.6 (a). The first load value represents the point where the relative motion between two joining components is initiated, and the second is the maximum pull-out load. The first load can be critical in taking precautions before complete joint failure by early identification of failure initiation. These two pull-out load values can be the same (in EAAJ) or different (in EMC) for the tubular joints. The values are different in the smooth-surfaced EM-crimped tubular joint due to the fretting and seizing effect, as discussed by Kleiner et al. [57].

Furthermore, Fig. 6.6 (a) has the following observations:

(a) There are two peaks in the EMC graphs (green, purple and yellow) as there is a drop in the pull-out load due to relative motion in EMC.

(b) There is lesser deformation in EAAJ (black, red and blue) for the same pull-out load due to the dampening effect provided by the adhesives.

(c) To overcome this dampening effect, significant force is required with EAAJ, which is evident by higher peaks in the load-extension graph for EAAJ.

(d) There is second peak in the graphs for EMC due to the presence of Kapton tube spacers which restricts the relative axial motion of the Cu tube. For EAAJ, the load attained in the first peak is high enough to overcome this restriction of the Kapton tube.

It can also be observed from Fig. 6.6 (b) that an increase in discharge energy leads to increased joint strength due to the enhancement of interference pressure resulting from increased radial deformation and subsequent elastic recovery. In EAAJ joints, failure is restrained by two resistive forces. One resistive force is between adhesive and adherents (Cu and SS tubes) due to adhesion. Another resistive force is due to the interference pressure created by electromagnetic crimping. Adhesive joining is observed to be failed by a combination of adhesive and cohesive failure, which is evident in the failed samples at 4.4 kJ of discharge energy, as shown by Fig. 6.7. Adhesive failure is the failure at the interface between adhesive and adherend, leading to a complete adhesive layer removal from the adherend surface [155]. At the same time, a cohesive failure is the failure of the adhesive layer, which results in sticking an adhesive layer on to the substrate surface [156]. All the tests are performed thrice to ensure repeatability. If the discharge energy is further increased, it will increase the pull-out strength until it reaches the failure strength of the parent copper tube, as discussed in section 3.3.1.

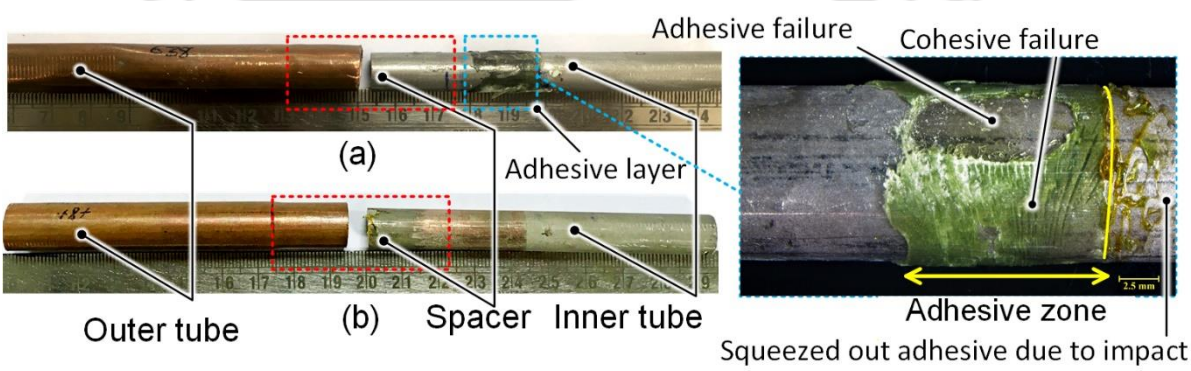

Fig. 6.7 Sliding failure sample at 4.4 kJ of discharge energy for (a) EAAJ sample, (b) EMC sample

6.4.1.2 Statistical analysis

It is observed that both factors (discharge energy and application of adhesives) considerably affect the pull-out strength of the tubular joint. Therefore, to analyse and

interpret the relative effects correctly, a statistical approach is necessary. Hence a two-factor analysis of variance (ANOVA) method is implemented to investigate the significance of both factors using the ANOVA module of Minitab software. Table 6.2 shows the list of influencing factors and their corresponding levels affecting the responses, and the maximum pull-out load value at their corresponding factors are shown in Table 6.3. The results of the two-factor ANOVA analysis are shown in Table 10. The Table comprises the degrees of freedom (DF), contribution %, the sum of squares (SS), the sum of mean squares (MS), Fisher (F) value and pre-set confidence (P) value. A "×" symbol represents the effect of the interplay between two factors, and error represents the consideration of trials in Table 6.4. The significance of the influence of the factors can be determined by comparing the F-value with the corresponding critical F-value at a 99% confidence level.

Table 6.2 Influencing factors and levels affecting the Cu-SS tube-to-tube joining process

Symbols	Factors	Levels		
		Low (1)	Medium (2)	High (3)
A	Type of process	EAAJ	EMC	
B	Discharge energy	3.9 kJ	4.4 kJ	5.0 kJ

Table 6.3 Maximum pull-out load values in kN at both influencing factors (type of process and discharge energy) for three repetitions

Discharge energy	3.9 kJ		4.4 kJ		5.0 kJ	
Trials	EAAJ	EMC	EAAJ	EMC	EAAJ	EMC
1	2.98	0.76	4.46	1.94	5.54	1.99
2	2.52	0.81	4.32	1.78	5.23	2.13
3	2.87	0.77	4.84	1.79	5.07	2.01

All the obtained F-values are higher than their corresponding critical F-value, which implies that both the factors and their interplay significantly affect the response, i.e. the joint strength of the Cu-SS tubular Joint. Their corresponding p-values can further clarify

it as all p-values are smaller than 0.01satisfying the 99% confidence level. The contribution % of factor A (type of process) and factor B (discharge energy) are calculated to be 59.17% and 33.10 %, respectively. Simultaneously, the interplay of the type of process and discharge energy has a 7.33% contribution. Hence it can be shown that the type of the process (with or without adhesive) has a lot more significant effect over the response variable (pull-out strength) than the discharge energy or interplay between the type of process and discharge energy.

Table 6.4 Analysis of Variance for Transformed Response

Source	DF	Contribution	SS	MS	F-Value	P-Value
Type of process	1	59.17%	0.567	0.566779	1832.39	1.72×10^{-14}
Energy	2	33.10%	0.317086	0.158543	512.57	2.40×10^{-12}
Type of process × Energy	2	7.33%	0.070250	0.035125	113.56	1.60×10^{-8}
Error	12	0.39%	0.003712	0.000309		
Total	17	100.00%				

6.4.2 Compression testing results

6.4.2.1 Compressive load variation and failure mode analysis

This test comprises the compressive strength comparison for EAAJ and EMC joints at three discharge energy values. Maximum compressive load of 1.5 kN is achieved at 5.0 kJ of discharge energy for an EMC crimped Cu-SS tubular joint, which is increased by 3.5 times up to 5.2 kN with the application of adhesive in the hybrid joining technique as shown in the load-compression graph (Fig. 6.8 (a)). Comparison of maximum compressive loads for both the EMC and EAAJ joints is shown in Fig. 6.8 (b). Improvement in strength in EAAJ samples compared to EMC is provided by additional adhesive strength between adhesive and adherends.

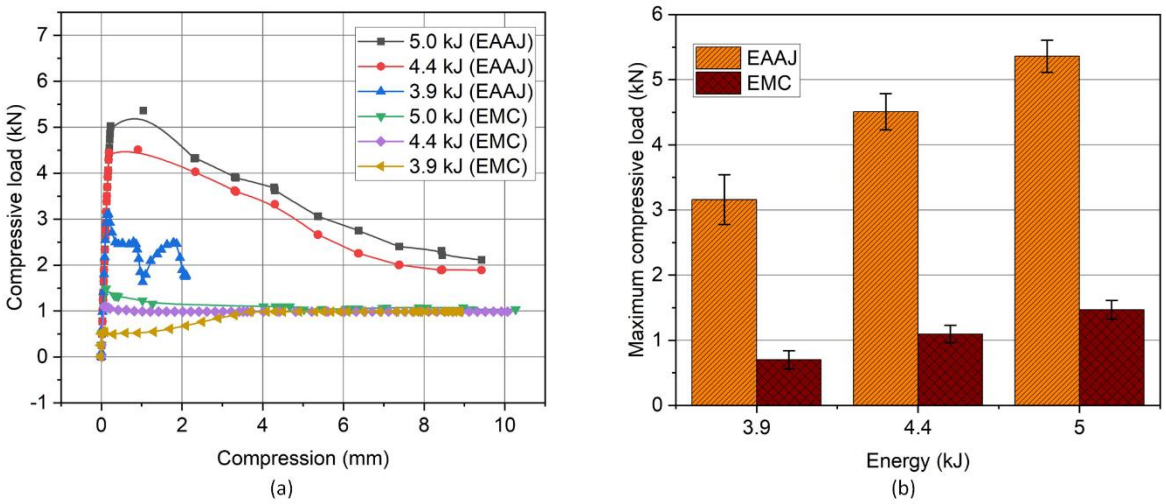

Fig. 6.8 (a) Compressive load vs compression plot and (b) maximum compressive load comparison plot for EAAJ and EMC joint at three different discharge energy values

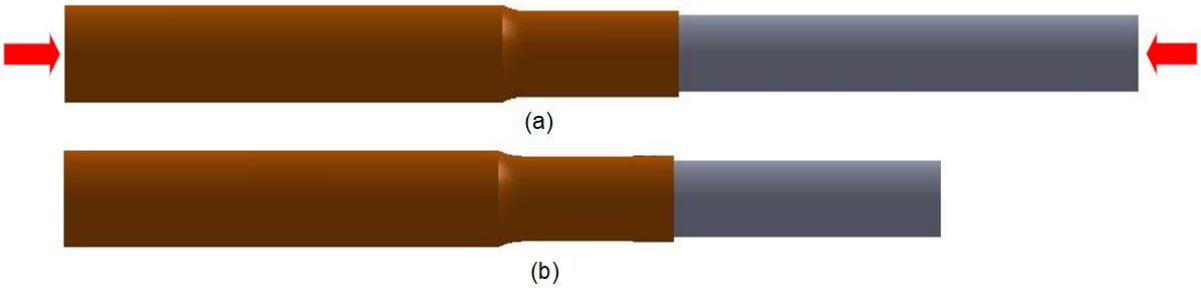

Fig.6.9 Sliding failure behavior being demonstrated by compression test sample (a) before the test and (b) after test

An increment in strength in EMC and EAAJ samples with discharge energy can also be observed by Fig. 6.8 (b), which can be explained by an increment in interference stress due to higher plastic deformation of the outer tube with an increase in the discharge energy. Both types of samples are failed by the sliding failure method demonstrated by the relative motion of Cu and SS tube into each other, as shown in Fig. 6.9. Results can be interpreted like the pull-out test results. An increase in the discharge energy will increase the compressive strength until it reaches up to the buckling strength of the parent copper tube, as discussed in section 3.2.3.3. All the tests are performed thrice to ensure repeatability.

4.2.2 Statistical analysis

A two-factor analysis of variance (ANOVA) method is also performed to investigate the significance of multiple factors (the type of process and discharge energy) on the compressive strength. Table 6.5 shows the response values (maximum compressive load) at both factors for three repetitions. Results of the statistical analysis are tabulated in Table 6.6. Symbols can be interpreted as discussed in section 6.4.1. Compressive strength is

observed to be contributed by 87.57% by the type of the process and by 11.38% by the discharge energy, as shown in Table 6.6. The results clarify that factor A (type of process) is more significant over the response variable (compressive strength) than the discharge energy or interplay between the type of process and discharge energy.

Table 6.5 Maximum compressive load values in kN at both influencing factors (type of process and discharge energy) for three repetitions

Discharge energy / Trials	3.9 kJ		4.4 kJ		5.0 kJ	
	EAAJ	EMC	EAAJ	EMC	EAAJ	EMC
1	3.21	0.74	4.63	1.12	5.04	1.50
2	3.44	0.75	4.55	1.18	5.48	1.47
3	2.83	0.62	4.35	0.98	5.56	1.43

Table 6.6 Analysis of Variance for Transformed Response

Source	DF	Contribution	SS	MS	F-Value	P-Value
Type of process	1	87.57%	4.870	4.870	1711.37	2.58×10^{-14}
Energy	2	11.38%	0.633	0.316	111.22	1.80×10^{-8}
Type of process × Energy	2	0.43%	0.024	0.012	4.19	4.18×10^{-2}
Error	12	0.61%	0.034	0.003		
Total	17	100.00%				

6.4.4 Deformation analysis

Transversely and longitudinally cut samples are photographed using an optical microscope at a lower resolution, and dimensional measurements are taken using NIS imaging software. Variation of outer diameter and thickness of the Cu tube with discharge energy for EAAJ and EMC are shown in Fig. 6.10 (a) and (b), respectively. Deformation values obtained in different zones of the EAAJ sample are tabulated in Table 6.7, whereas, Cu-SS interface 5.0 kJ of discharge energy for EAAJ and EMC sample is shown in Fig. 6.11. Various zones of the EAAJ and EMC

sample in the longitudinal direction are shown in Fig. 6.12. Outer diameter and thickness value is significantly higher in the case of EAAJ samples than in EMC samples because adhesives restrict the deformation in the case of EAAJ. The adhesive in between tubes acts as a dampener during the deformation process. It slows the impact velocity of the outer tube leading to a significant reduction in deformation, as shown in Fig. 6.11. A reduction in adhesive layer thickness is observed with an increase in discharge energy due to higher magnetic pressure, which further contributes to increasing the joint strength.

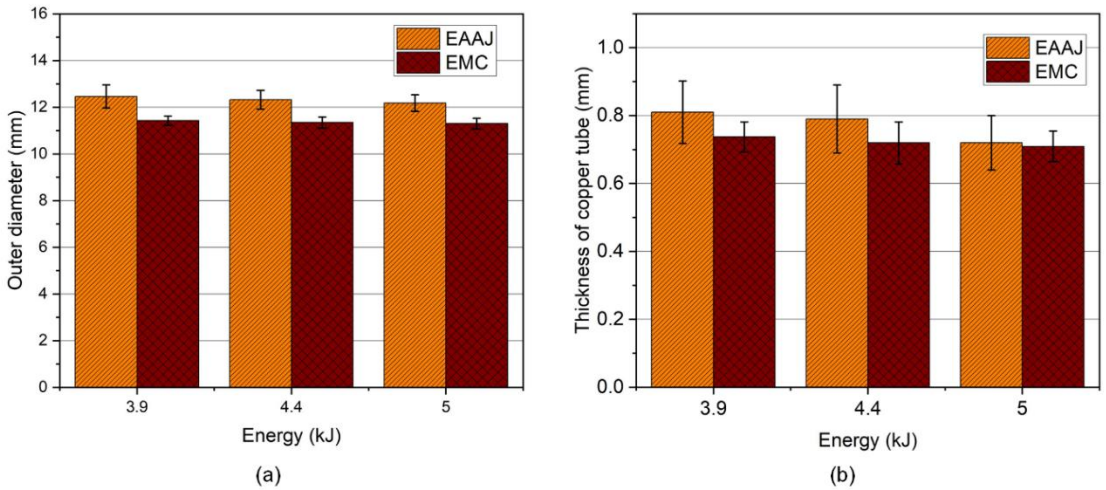

Fig. 6.10 Variation of (a) outer diameter and (b) thickness of copper tube with discharge energy for two processes in the working zone (for EAAJ measurements are taken in the adhesive zone)

Table 6.7 Results obtained from deformation analysis for EAAJ samples

Discharge energy (kJ)	Outer diameter in the adhesive zone (mm)	Outer diameter in the non-adhesive zone (mm)	The thickness of the adhesives layer (mm)
3.9	12.46	12.13	0.31
4.4	12.32	12.04	0.27
5.0	12.18	11.93	0.20

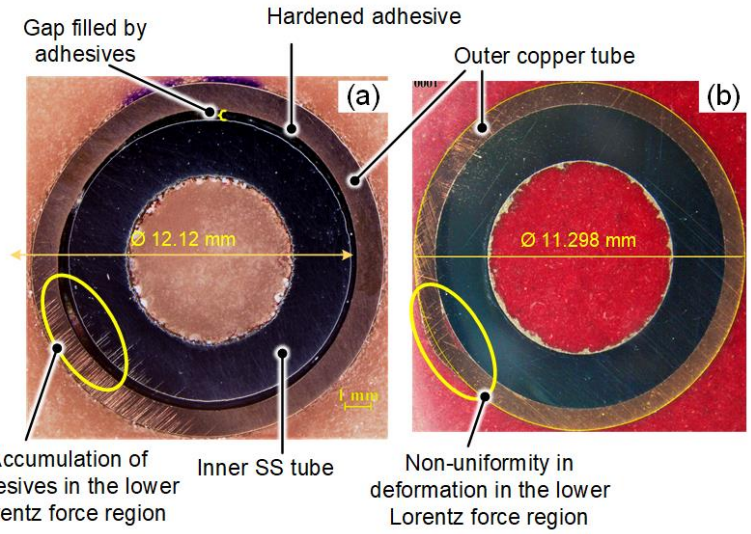

Fig. 6.11 Cu-SS interface at 5.0 kJ of discharge energy for (a) EAAJ and (b) EMC

Furthermore, Fig. 6.11 also shows the effect of the slit of the field shaper; as discussed in section 4.3.2, the slit creates a non-uniformity in the Lorentz force in the circumferential direction leading to non-uniformity in the radial deformation. In EAAJ, the impact of the outer tube displaces the adhesive in between tubes in the longitudinal and circumferential direction. Therefore, adhesive moves in the circumferential direction from the higher Lorentz force region to the lower Lorentz force region, as shown in Fig. 6.11. Longitudinal movement of adhesives can be observed in Fig. 6.12 as the adhesive particles close to the free end of the Cu tube gets drifted away to the outside. Furthermore, the adhesive particles at the interface between the non-adhesive zone get drifted towards the non-adhesive zone as the deformation of the Cu tube begins at the free end and proceeds towards the working zone, as discussed in section 4.2.2. Simultaneously, in the EMC samples, a uniform deformation is observed along the crimping zone, as shown in Fig. 6.12 (b). The length of the crimping zone in EMC is observed to be more than the length of the working zone in the EAAJ sample, which the lower impact velocity can justify in EAAJ samples due to adhesive dampening.

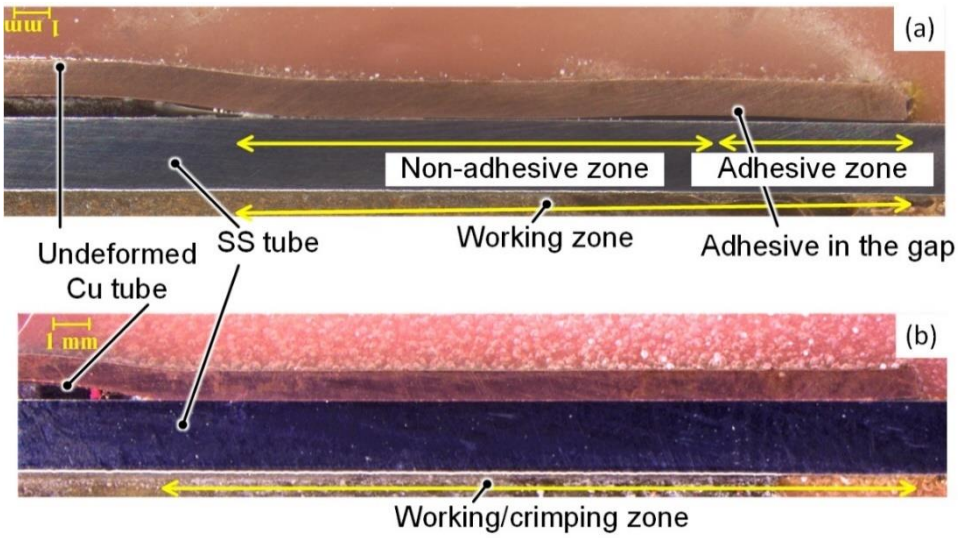

Fig. 6.12 Axially cut Cu-SS interface at 5.0 kJ of discharge energy for (a) EAAJ sample showcasing non-adhesive and adhesive regions, (b) EMC sample showcasing crimping zone

6.4.3 Micro-hardness analysis

A transverse cut sample and an axially cut sample is used for Vicker's micro-hardness analysis. For a transverse cut sample, measurements are taken at an interval of 200 µm throughout the Cu-SS tubular joint sample thickness for both processes (EAAJ and EMC). The hardness value of the parent copper and SS tube is 96.17 HV and 174.31 HV, respectively. Micro-hardness variation at every 200 µm from the non-adhesive zone interface at 5.0 kJ of discharge energy for both samples is shown in Fig. 6.13. The maximum value of hardness is observed near the interface. An increment in microhardness near the interface in both processes is observed due to the high strain rate plastic deformation leading to strain hardening. A lower microhardness value is observed in EAAJ (non-adhesive zone) than in EMC, with a decrement of 4%.

Furthermore, hardness measurements are also taken along the length in the working zone in the Cu tube near the Cu-SS interface at different positions of importance in the base Cu tube, non-adhesive zone and adhesive zone, as shown in Fig. 6.14. In the EAAJ sample, the adhesive zone has a lower hardness value than the non-adhesive zone due to the lower deformation of the Cu tube. At the same time, the EMC sample has a uniform hardness variation with the length due to uniform deformation in the crimping zone. However, crimping initiates at the free end of the Cu tube and move towards the crimping zone leading to higher deformation at the free end, as discussed in section 4.2.2. Therefore, hardness tends to increase with length from the closed end to the free end of the Cu tube in the crimping zone.

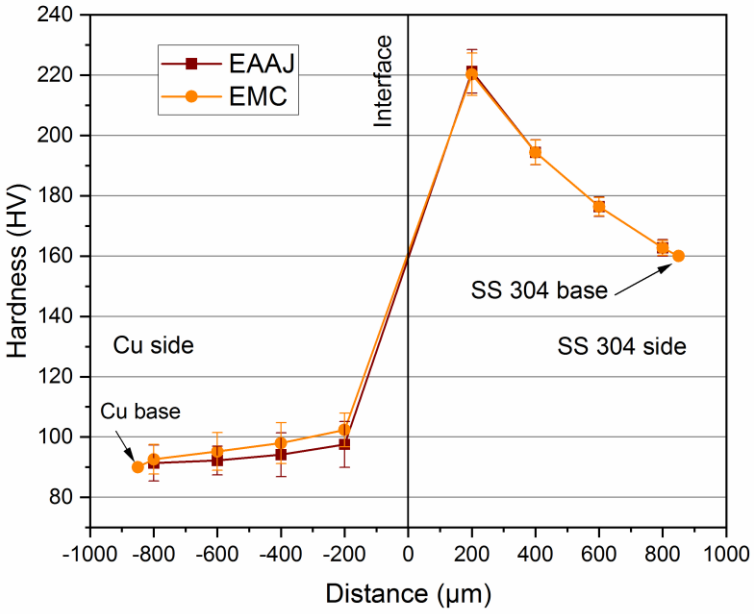

Fig. 6.13 Micro-hardness variation at 5.0 kJ of discharge energy across the interface at 100 gm load with 20 s of dwell time

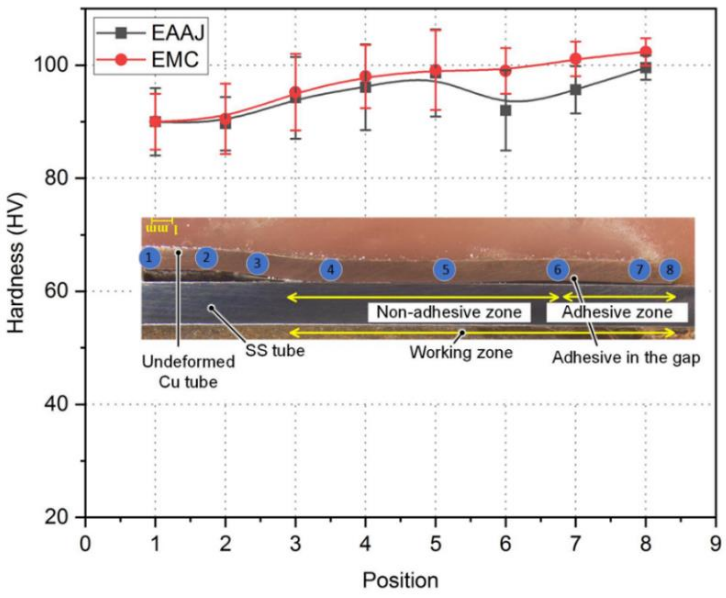

Fig. 6.14 Variation of micro-hardness of Cu tube along the length in the working zone for both processes (EAAJ and EMC) at 5.0 kJ of discharge energy

6.4.5 Leak test results

A leak test is performed as described in section 6.3.4.3. The results are quantified and presented with air pressure decay rate. EAAJ leak test sample at 3.4 kJ of discharge energy is shown in Fig. 6.15. Initial visual inspections are performed with the bubble test to identify

the leaking location. EMC crimped samples have shown multiple leaking regions at the joint interface leading to a large bubble formation due to voids between the Cu-SS interface in the crimping zone. However, EAAJ samples have shown a significant decrement in bubble formation. Testing is performed thrice to ensure repeatability of the results. Leak test results for both processes at three different discharge energy values are shown in Table 6.8. A very substantial improvement in the air leak-tightness can be observed in EAAJ samples compared to EMC samples. A maximum air leak rate of 8.35×10^{-9} mbarl/s is obtained at 5.5 kJ of discharge energy for the EAAJ joint, which is 1000 times leak-tight than the EMC sample same discharge energy. This is due to adhesives acting as a sealing material to fill any gap between the Cu-SS interface in the overlapped region. An increment in leak tightness with an increment in discharge energy can also be observed in Table 6.8 because an increase in discharge energy leads to an increase in deformation resulting in higher residual stress, which creates a higher interference fit, contributing to higher leak tightness. Here 4.4 kJ can be considered as a lower limiting discharge energy value to have a proper leak tightness.

Fig. 6.15 Electromagnetically assisted adhesive Cu-SS joint sample at 3.4 kJ of discharge energy for leak test

Table 6.8 Air leak rate in mbarl/sec at three different discharge energy for two different processes at three repetitions of experiments

Discharge Energy (kJ)	Joining method	Experiment 1	Experiment 2	Experiment 3
3.9	EAAJ	2.14×10^{-8}	1.86×10^{-8}	2.12×10^{-8}
	EMC	4.76×10^{-5}	6.32×10^{-5}	5.48×10^{-5}
4.4	EAAJ	1.52×10^{-8}	8.58×10^{-9}	1.84×10^{-8}
	EMC	1.24×10^{-6}	9.82×10^{-7}	8.08×10^{-7}
5.0	EAAJ	9.22×10^{-9}	8.64×10^{-9}	8.35×10^{-9}
	EMC	1.38×10^{-6}	9.77×10^{-7}	9.43×10^{-7}

6.5. Conclusions

In this chapter, an attempt has been made to investigate the novel hybrid joining process, EAAJ experimentally, and its benefits over the EMC joining of Cu tube to SS tube. The main points can be concluded as,

- Pull-out and compressive strength have increased with an increase in discharge energy in both joining processes. An increase in discharge energy leads to increased radial deformation resulting in higher residual stress. Hence we have better joint strength due to higher interference pressure.
- Pull-out strength has shown a significant increment by an average of 2.5 times in EAAJ compared to EMC at different discharge energy ranges.
- The statistical analysis has calculated that the type of process contributes by 59.17% and discharge energy contributes by 33.10 % to the pull-out strength of the Cu-SS tube-to-tube Joint.
- Compressive strength has also shown a significant increment by 3.4 times in EAAJ compared to EMC at different discharge energy ranges.
- The statistical analysis has calculated that the type of process contributes by 87.57% and discharge energy contributes by 11.38 % to the pull-out strength of the Cu-SS tube-to-tube Joint.
- Therefore, pull-out and compressive strength results conclude that EAAJ is better suited than EMC for creating a Cu-SS tube-to-tube joint with higher joint strength.
- Micro-hardness increment across the Cu-SS interface is observed due to the deformation of the crimping layer and work hardening. EAAJ samples tend to have a lower micro-hardness value (in the non-adhesive zone) than EMC samples.
- Lower deformation is observed in EAAJ compared to EMC due to the dampening of impact velocity by adhesives in the overlapped region.
- Leak test results have shown a significant improvement in the case of EAAJ joints compared to EMC joints. With the application of adhesives, leak tightness is improved by 1000 times.

7 Effect of Process Parameters on the Joint Strength and Leak Tightness in EAAJ

7.1 Introduction

In previous chapter 6, a novel hybrid joining technique, EAAJ, is developed to overcome the shortcomings of a traditional EMC joint. An increment in pull-out and compressive strength by 2 to 3 times is observed, along with an improvement in leak tightness by 1000 times in the case of the EAAJ joint compared to EMC joint. This chapter focuses on further improving and optimising the various aspects of the EAAJ process using the obtained information from the EMC process in chapters 3, 4 and 5. Therefore, the current chapter mainly focuses on performing a detailed experimental investigation to study the effect of various process parameters (discharge energy, adhesive application length, types of adhesives and curing time) on EAAJ joint characteristics leading to optimization of the process. Pull-out and compression test is performed to investigate the joint strength and joint failure behaviour. Statistical analysis is performed to study the contribution of different parameters on joint strength. Micro-hardness and deformation analysis are also performed to characterise the Cu-SS hybrid tube-to-tube joint. Furthermore, an air leak testing setup has been developed, and the leak tightness of the hybrid joint is measured with an air pressure decay test.

7.2 Preparation of Electromagnetically Assisted Adhesive Cu-Ss Tube-To-Tube Joining Process

7.2.1 Tube and adhesive materials

The working principle of the EAAJ process is already discussed in section 6.2. Cu and SS tubes are selected here as outer and inner tubes based on their applicability in air compressor tubular parts. Three adhesives (Loctite 638, Loctite 567 and Loctite SI 596) are used. Loctite 638 is an acrylic-based green coloured one component structural adhesive with a urethane methacrylate chemical type. It is designed for the cylindrical bonding part. It is an anaerobic adhesive which implies that it cures in the absence of air when confined between metal surfaces in the closed fitting. This adhesive works with active metals like Cu and passive substrates like SS. Loctite 567 is also an acrylic-based one-off-white paste adhesive with a chemical type of methacrylate ester. It is purposed as a thread sealing adhesive. It has robust curing performance, and this adhesive as well works for both active

and passive substrates. This adhesive further offers high-temperature performance and a suitable industrial plant fluid power system. Loctite 596 is a silicon-based one component red coloured smooth flowable paste adhesive with a chemical type of acetoxy silicone. This adhesive is used as a sealant to repair and assemble heating elements in electrical appliances, boilers, ovens, industrial furnaces, and high-temperature ducting. It cures when exposed to moisture in the presence of air to form a flexible, tough, oil-resistant silicon rubber bond [153]. A detailed description of the properties of adhesives is shown in Table 7.1.

Table 7.1 Properties of adhesives used in the experiment [153]

Adhesives	Loctite 638	Loctite 567	Loctite SI 596
Technology	Acrylic	Acrylic	Silicon
Chemical type	Urethane methacrylate	Methacrylate ester	Acetoxy silicone
Appearance (uncured)	Green liquid	Off-white paste	Red smooth flowable paste
Fluorescence	Positive under UV light	NA	NA
Components	One component-requires no mixing	One component-requires no mixing	One component-requires no mixing
Viscosity	High	High	High
Cure	Anaerobic	Anaerobic	Room temperature vulcanising (RVT)
Secondary cure	Activator	Activator	Activator
Application	Retaining	Thread sealing	Gasket sealing
Strength	High	Low	Low

7.2.2 Process parameters

Adhesives are kept between outer and inner tubes before the overlapped/working zone deformation process, filling any gap between tubes after the deformation process. Anaerobic adhesives get cured with time without air in the confined space. Joule's heating loss leading to an increase in the temperature of various components involved during the EAAJ process does not affect the adhesives properties or the strength of the adhesive joint as the rise in temperature is not significant (30° -50 °). As per the adhesive databook, only after a temperature rises in the range of ≥ 150°, an adhesive joint's initial strength starts reducing significantly [153].

All the EAAJ joints are created with a Cu tube as an outer tube and an SS tube as an inner tube. Although for such tube-to-tube adhesive joining process, adhesion is proved to be higher if the surfaces to be joined are plain, and higher adhesion leads to higher joint strength compared to joints without adhesives which has also been explored in chapter 6, where an increment in joint strength by 2.5 times is observed in EAAJ joints (with adhesives) compared to EMC joints (without adhesives). However, in the case of EAAJ, overall joint strength is contributed by two factors; strength due to electromagnetic crimping and strength due to adhesive joining. Therefore, a significant amount of electromagnetic crimping-induced strength is also necessary, along with the strength due to adhesives. Especially higher "Pull Out", and "Compressive" strength of the joint is mainly contributed by strength due to crimping, not by strength due to adhesive. Here the strength in the case of EMC joints (without adhesives) is four times lower in the case of smooth-surfaced joints compared to threaded/knurled surfaced joints, as discussed in chapter 3. Therefore, the grooved outer surface of the inner tube is recommended in the case of EAAJ joints despite lower adhesion compared to smooth-surfaced EAAJ joints. The intention behind choosing a grooved surface for the inner SS tube while creating a Cu-SS tube-to-tube joint using EAAJ is to retain the higher joint strength provided by the threaded/knurled surfaced Cu-SS electromagnetically crimped tube-to-tube joint even at the cost of lower adhesive strength contribution while making the joint leak-tight due to adhesives. A threaded outer surfaced inner SS tube is used in this work. The SS tube has an ISO metric M10×1 threaded profile on the outer surface to increase the surface area of contact, leading to improved interference strength of the joint. The threaded surface with one pitch is selected based on the experimental work performed in chapters 3 and 5. We have performed EMC and EAAJ experiments, and the threaded surfaced joint is observed

to be best suited to achieve higher joint strength for pull-out strength and ease of manufacturing. Furthermore, after trial and error, 1 mm standard pitch is best suited to achieve higher joint strength among different pitches in this outer tube-inner tube configuration, as discussed in chapter 5 in detail. The initial radial gap between the field shaper and the outer tube is 1.15 mm. Cu and SS tubes are placed co-axially with field shaper and coil with polytetrafluoroethylene (PTFE) fixtures beside Kapton tape as tube spacer, as shown in Fig. 6.1. Overlapped length or working length is also kept constant as 20 mm. The stand-off distance, the initial radial gap between the flyer tube (Cu) and the target tube (SS), is chosen as 0.45 mm for the tube dimensions. This gap is required to accelerate the flyer tube under electromagnetic pressure. Also, a high-temperature resistant Kapton tape spacer is applied between tubes at a distance of 5 mm from the working zone to keep the tubes co-axial. As discussed, three different adhesives (Loctite 638, Loctite 567 and Loctite SI 596) are used. As shown in Fig. 7.1, the application length of the adhesive has been varied as a critical parameter in our analysis. Four different adhesive application lengths (20mm, 15mm, 10mm and 5mm) are used. Experiments are performed at three discharge energy values (3.9 kJ, 4.4 kJ and 5.0 kJ).

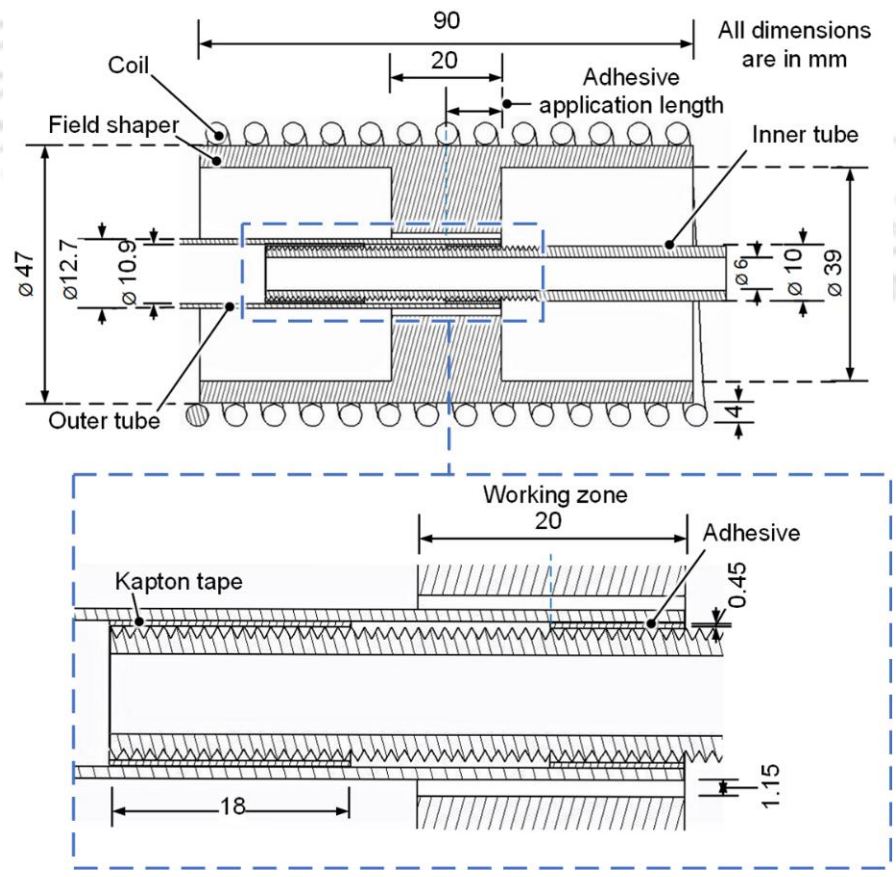

Fig. 7.1 Schematic diagram showing the dimensions of various parts in the EAAJ setup

7.2.3 Experimental procedure

7.2.3.1 Surface preparation

The quality of the surface of the workpiece is critical for an adhesive joint, as discussed in detail by Fritzsche et al. [127]. Mechanical abrasion technique is used with the help of a rotary sander with 100 grid SIC sandpaper to remove any surface layers/contaminations on the inner surface of the Cu (outer) tube and the outer surface of the SS (inner) tube. Abrasion of the surface increases the surface energy of the workpiece surface in contact with the atmosphere. When the surface energy exceeds the value of adhesives' surface energy, an adhesive becomes favourable to wet the application's surface, Kowalski et al. [128]. After the abrasion of substrates, workpieces are cleaned with methyl alcohol to remove any residual dirt. To understand the impact of abrasion, surface roughness is measured at the outer surface of the inner tube using a non-contact computerised optical surface profilometer with a precision of ±50 nm. Fig. 7.2 shows the surface roughness values before and after the grinding process. The average surface roughness (R_a) value before and after abrasion is observed to be 0.35 µm and 1.44 µm, respectively. After abrasion, the average surface roughness value and waviness both have increased. As we understand, surface roughness and waviness are small-scale and large-scale deviation measurements. In cases where big abrasive particles are used compared to the original surface finish, it may cause deeper grooves or scratches, which could be considered as a more significant deviation from the surface and hence increases the waviness, which causes the drastic deterioration in the surface finish, which helps in adhesive joining [157, 158].

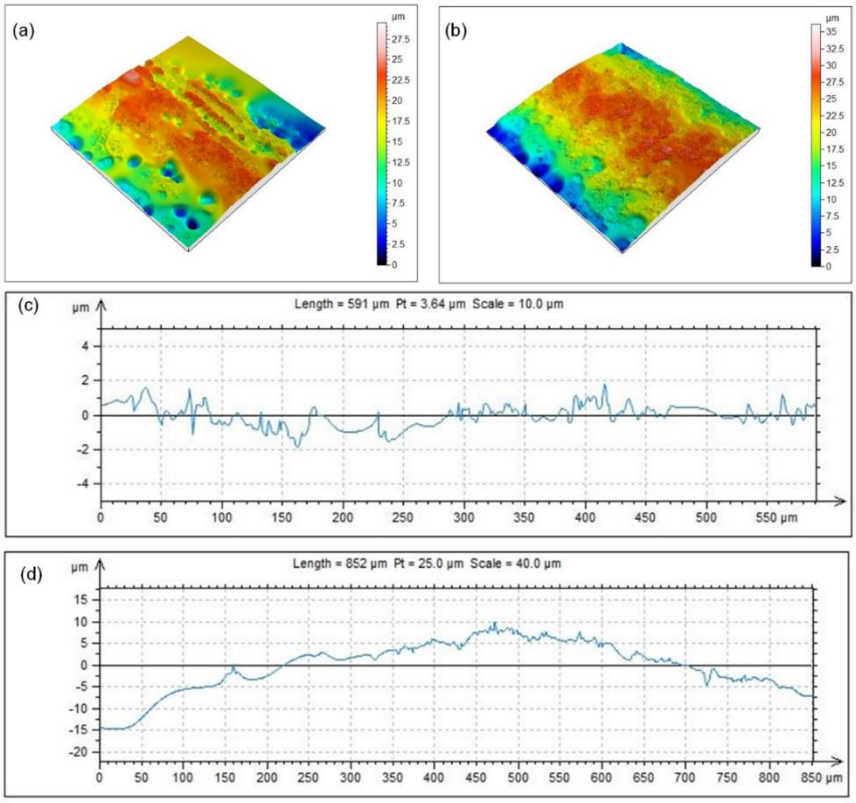

Fig. 7.2 Three-dimensional surface topology (a) before grinding, (b) after grinding and surface roughness variation with the length (c) before grinding, (d) after grinding

7.2.3.2 Adhesive application

A rotating spindle with jaws of a mini lathe machine is used to hold the inner SS tube and rotate at a constant speed while applying adhesives to ensure its uniform application on the surface. A masking tape is applied at the edge of the adhesive application area/edge of the working zone to ensure proper adhesive deposition. After using adhesives, tubes are placed co-axially with the help of the Kapton tube and nylon fixtures. Electromagnetic forming is performed immediately to create a Cu-SS tube-to-tube hybrid joint.

7.2.4 Testing methods

7.2.4.1 Mechanical pull-out testing

Mechanical pull-out testing is performed on a UTM (Universally tensile testing) machine where one of the joints is fixed, and the other end is pulled out at a constant speed of 0.5 mm/sec. The setup is shown in Fig. 3.4.

7.2.4.2 Leak test

A leakage implies an escape of liquid or gas from a pressurised or evacuated system through an imperfection such as a hole or a crack. For a Cu-SS tube-to-tube hybrid joint to be used as a medium to transport the fluid, the joint needs to be leakproof up to a certain

degree based on its application. Therefore, as the name implies, leak testing is a technique to detect leaks to verify manufacturing defects and improve their integrity. To check the leak tightness of the Cu-SS hybrid joint, one end of the joint is subjected to the flow of compressive air, and the other end is closed by mechanical clinching followed by brazing, as shown in Fig. 5. converting this into a pressurised closed system. This section discusses two basic air leak testing techniques, the air bubble test and the air pressure decay test. In the bubble test, the pressurised system is submerged inside the water; any crack presence would lead to a flow of pressurised air resulting in numerous bubble formations [159], as shown in Fig. 7.3. This test gives some qualitative idea about the leak location but does not produce any quantitative information about the leak rate. Therefore, the first test is only recommended as an initial inspection. The second test is called the air pressure decay test and is often used in manufacturing production lines, says Loosveld et al. [160]. In this test, a specimen is pressurised by supplying a compressive airflow, as shown in Fig 7.4, until a threshold pressure is reached; in the current analysis, it is taken as 8 MPa in this case. The flow is then cut off, and the drop in system pressure is measured over a certain period. A schematic diagram of the air leak rate testing setup is shown in Fig. 7.5. It contains air compressors, cut-off valves, precision manometers, pressure relief valves, and connection lines. The presence of any leak will lead to a drop in air pressure over the period, the rate of which can be measured quantitatively with the help of a precision manometer as represented by the equation 6.1, as also discussed by Loosveld et al. [160]. The leak test is repeated three times for better accuracy. Thus, samples are inspected with the bubble test and then processed through an air pressure decay test to calculate the leakage rate.

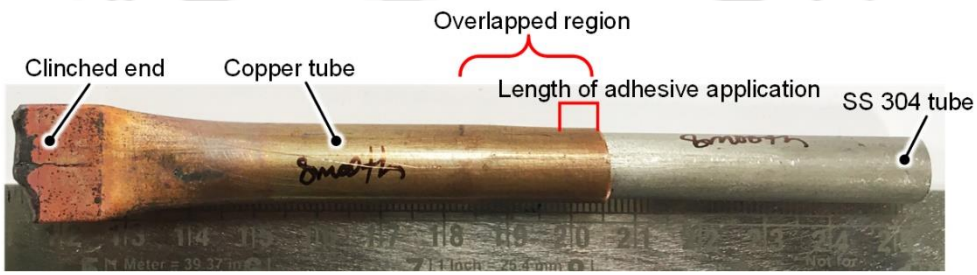

Fig. 7.3 Air leak test sample

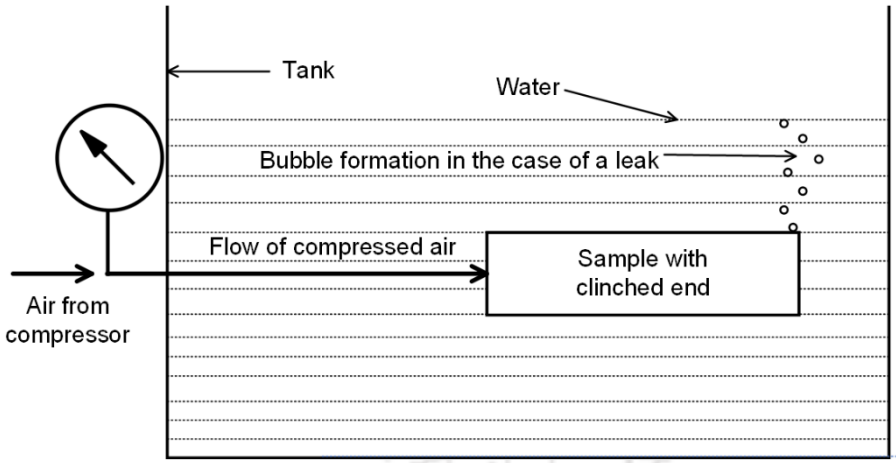

Fig. 7.4 Schematic diagram of the air bubble test

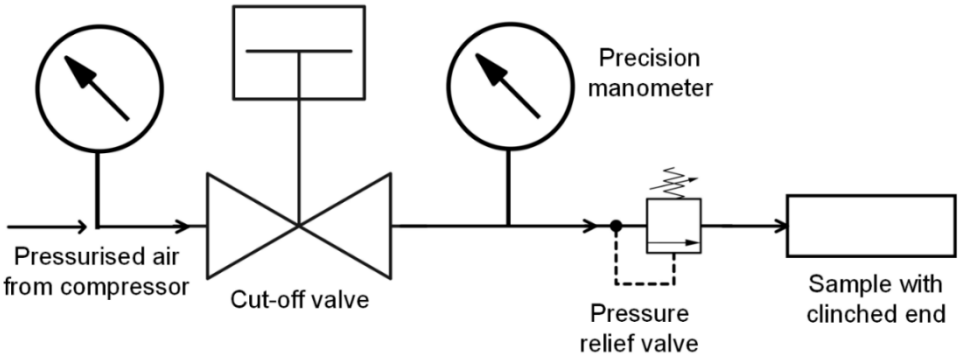

Fig. 7.5 Schematic diagram of the air pressure decay test

7.2.3 Characterisation of the hybrid joint

In the crimped region, samples are cut throughout the thickness in a ring shape with the wire electric discharge machine to analyses further the Cu-SS hybrid joint as discussed in section 3.2.3.4.

7.3 Results and Discussions

7.3.1 Mechanical pull-out test and compression test

EAAJ samples for pull-out testing are shown in Fig. 7.6. Tests are repeated for better accuracy. The pull-out test is performed for EAAJ samples of three adhesives (638, 567, and SI 596) and four adhesive application lengths (5mm, 10mm, 15mm, 20mm) for three different discharge energy values (3.9 kJ, 4.4 kJ, and 6.2 kJ). Maximum pull-out strength values are demonstrated in Fig. 7.7 (a), (b), and (c). Here the curing time is considered as 96 hours. A maximum pull-out load of 7000 N is observed at 5.0 kJ of discharge energy for adhesive 638 samples with 5 mm of adhesive application length.

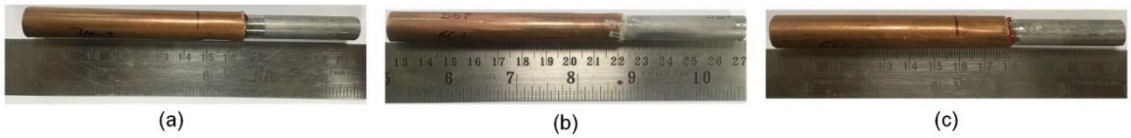

Fig. 7.6 EAAJ samples at 5.0 kJ of discharge energy for three different adhesives (a) adhesive 638, (b) adhesive 567, and (c) adhesive SI 596

From Fig. 7.7 (a), (b), and (c), it can be concluded that the adhesive 638 is most suitable among three adhesives (638, 567, and SI 596) to achieve a joint with higher joint strength. A significant increment in pull-out strength is observed even at lower discharge energy (3.9 kJ) with proper adhesive application length, as shown in Fig. 7.7 (a). These results act as a guideline to proceed further for experimentation. Two factors affect the strength of an EAAJ joint; strength due to interference stress caused by electromagnetic crimping and strength due to adhesion. Since the depth of the M10×1 thread being used is 0.86 mm, which is relatively higher than the particle size of adhesives being used, and as lower gaps are required for stronger adhesion. Therefore, the contribution of adhesion in the overall joint strength is not significant, and the strength due to electromagnetic crimping dominates the overall joint strength. As already discussed in section 2.4, the threaded joint is selected for its high strength due to electromagnetic crimping despite poor adhesion strength to achieve a joint of high overall strength (due to electromagnetic crimping) and leak tightness (due to adhesion).

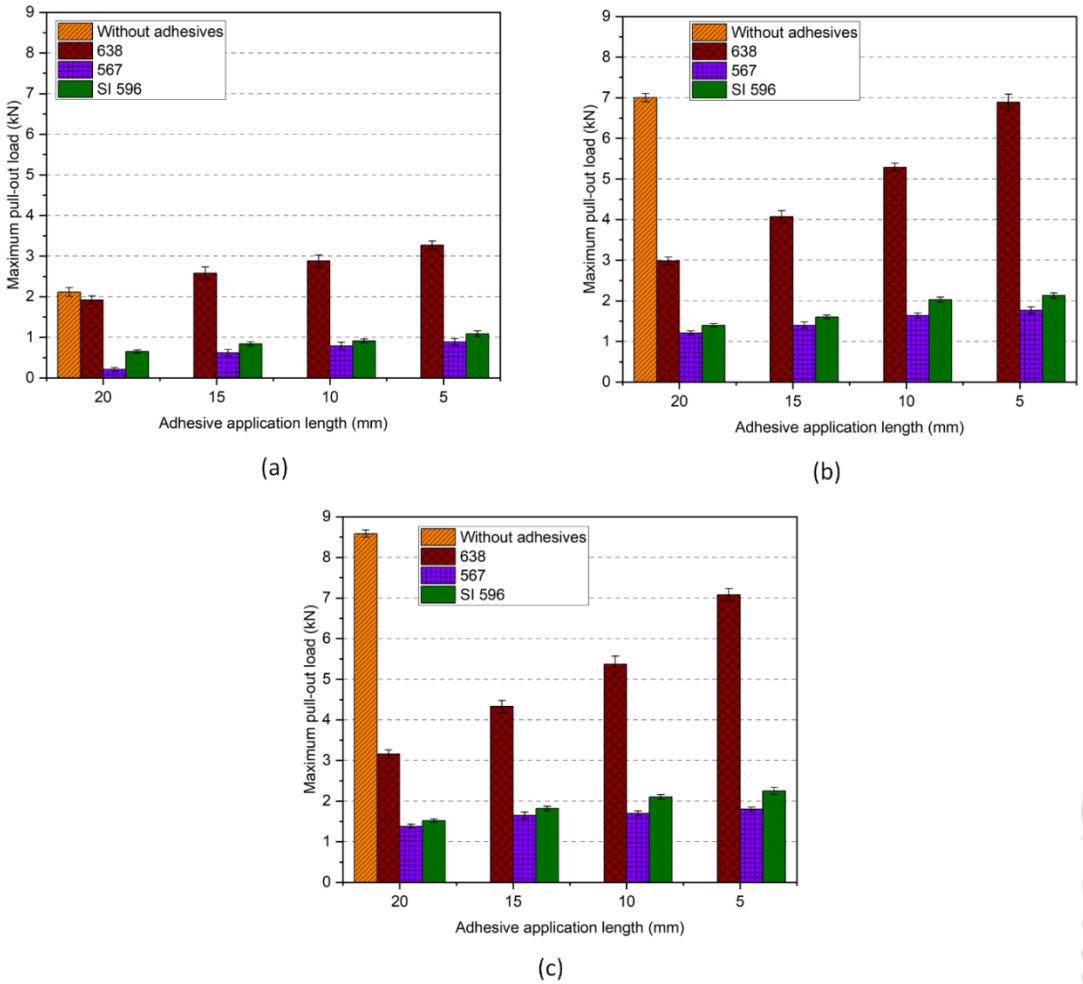

Fig. 7.7 Variation of pull-out load with the adhesive application length for three adhesives at (a) 3.9 kJ, (b) 4.4 kJ and (c) 5.0 kJ of discharge energy

7.3.1.1 Effect of adhesive application length

Adhesive application length is the length of the application of adhesive in the working zone. It is observed that the increase in adhesive application length leads to a decrease in joint strength, as shown in Fig. 7.7 (a), (b) and (c). As initially, the air having a viscosity of 0.018 cP is between the outer and inner tube (in joints with no adhesives), which gets replaced by adhesives (in joints with adhesives) having dynamic viscosity in the range of 1.9 cP to 73 cP [145]. Therefore, adhesives with much higher viscosity create a dampening effect to significantly reduce the impact velocity, leading to lower interference stress build-up resulting in lower joint strength. The velocity with which the outer tube impacts the inner tube after getting accelerated due to Lorentz force is called impact velocity. Furthermore, dampening of the outer tube impact also results in lower outer tube deformation causing lower interference stress and eventually lower joint strength. Therefore, It can be concluded that in the case of EAAJ, maximum strength is achieved at

5mm of adhesive application length. It can also be observed from Fig. 7.7 (c) that maximum strength is achieved at 5.0 kJ of discharge energy in the case of joining without adhesives (EMC) which is the base copper tube failure strength. It indicates that joint strength exceeds the base copper tube strength at this point leading to failure of the tube. However, adding adhesives in creating a threaded surfaced Cu-SS joint only reduces the strength due to lower interference stress caused by adhesive dampening. Therefore, joint without adhesive has higher strength.

7.3.1.2 Failure mode

This section discusses the joint failure mechanism observed during the pull-out and compressive testing of EAAJ samples. The load vs displacement curve for pull-out and compression testing is shown in Fig. 7.8 (a) and (b), respectively and a similar trend is observed in both graphs. The pull-out/compressive load increases until it reaches its maxima leading to the initiation of relative motion between parts. A repetitive cyclic pattern can be observed after reaching the maximum load in samples at 4.4 kJ and 5.0 kJ during pull-out and compression test as there is an increase of pull-out/compressive load due to sticking of the outer copper tube onto the crest and root of the inner SS tube threads, followed by a release of the load due to constant wear mechanism. However, the wear rate may vary as the material properties depend on the type of loading (pull-out/compression). Croccolo et al. [161] have also talked about decreasing interference stress and occurring of peeling stress on adhesive, leading to lower joint performance, whereas in compression, actual interference increases, leading to overestimation of the joint performance. A similar trend can be observed in Fig. 7.18 (a) and (b). A different rate of repetitive motion can be observed in pull-out and compression test results due to different wear rates. The motion is initiated when the load required to sustain the tubes together is more than the load provided by frictional resistance due to interference pressure and adhesive strength, so a crack is initiated in the adhesive structure, and relative movement begins. Therefore, the sliding failure mechanism of the joint is observed in the EAAJ of Cu-SS tubes, as shown in Fig. 7.9. This also implies that the base copper tube strength is higher than the joint strength. After carefully examining the failed sample, a combination of adhesive and cohesive failure mode is observed. Here the adhesive failure is the failure of the interface leading to a complete adhesive layer removal from the adherend surface, as discussed by Renart et al. [162]. Simultaneously, cohesive failure is the adhesive layer's failure, leading to an adhesive layer sticking on the substrate

surface [8], as shown in Fig. 7.10. Zoomed views of the failed samples after the pull-out test are shown in Fig. 7.11, and a combination of both failure modes (cohesive and adhesive) can be seen in samples. Here, the outer copper tube and inner SS 304 tube are considered substrate 1 and substrate 2. Two different adhesive failure modes can be seen for samples at 3.9 kJ and 4.4 kJ considered as adhesive failure 1 and adhesive failure 2. In adhesive failure 1, removal of the adhesive layer is from the surface of substrate 2, and in adhesive failure 2, removal of the adhesive layer is from the surface of substrate 1.

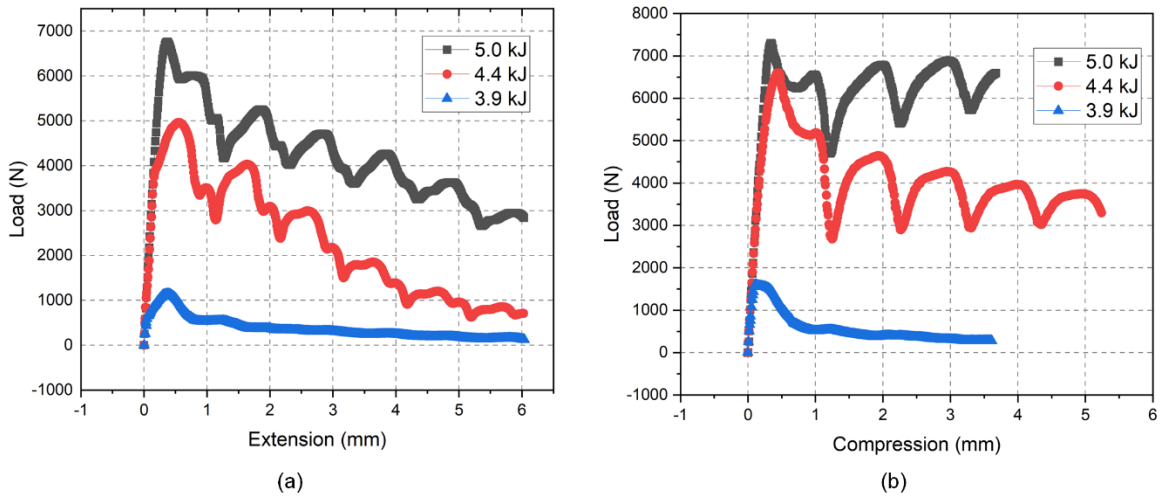

Fig. 7.8 (a) Pull-out load vs extension and (b) Compressive load vs compression plot for adhesive 638 samples with 5 mm of adhesive application length

A combination of cohesive and two adhesive failure modes (adhesive failure 1 and adhesive failure 2) is observed for the sample at 4.4 kJ of discharge energy, and a combination of cohesive and adhesive (adhesive failure 1) failure mode is observed for 5.0 kJ of discharge energy. An increase in discharge energy leads to an increase in residual stress resulting in higher pressure during curing, resulting in improved adhesive joint quality, which reflects in the transition of joint failure mode from complete adhesive failure mode to a combination of adhesive and cohesive failure mode. The area occupied by cohesive failure in the adhesive zone increases with an increase in energy and contributes to strength.

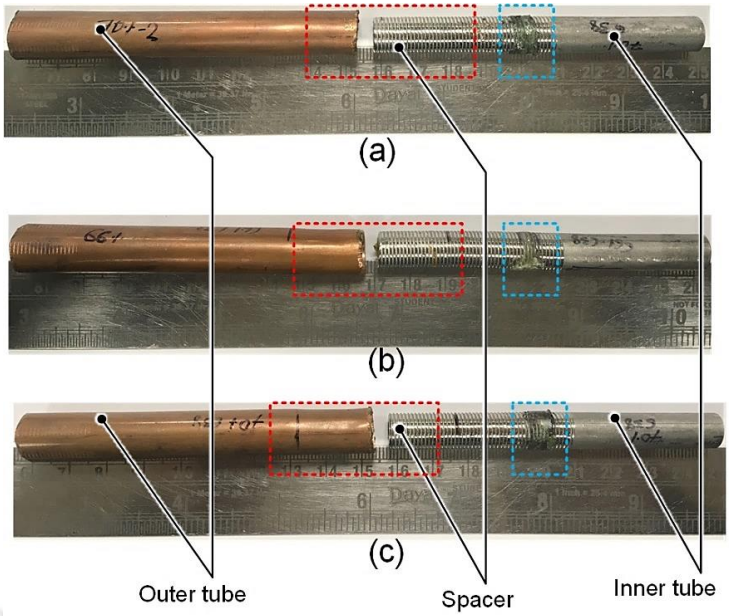

Fig. 7.9 EAAJ samples for adhesive 638 at 5 mm of adhesive application length after pull-out testing at (a) 3.9 kJ, (b) 4.4 kJ and (c) 5.0 kJ of discharge energy demonstrating the sliding failure

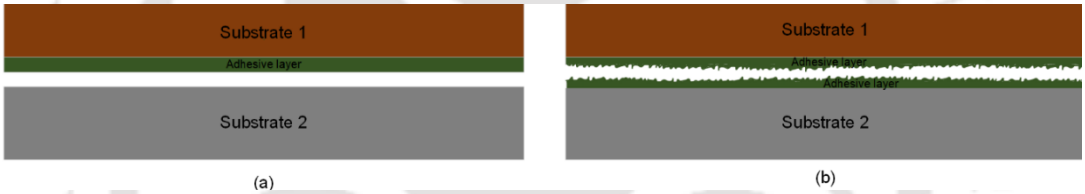

Fig. 7.10 Representation of (a) adhesive and (b) cohesive failure mode of an adhesive joint

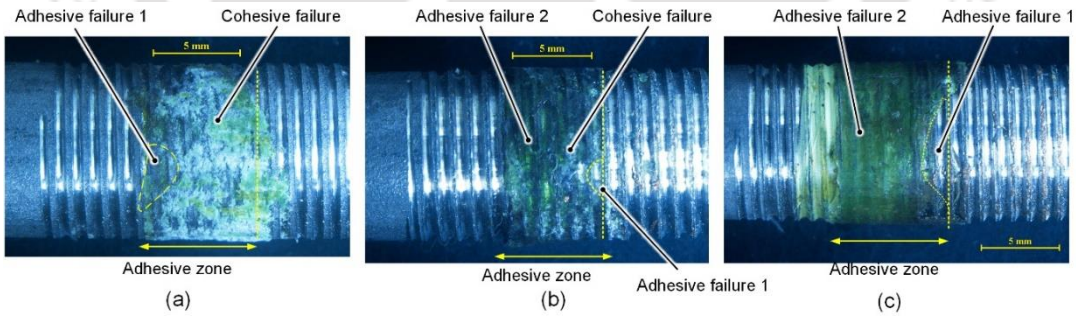

Fig. 7.11 Zoomed view of EAAJ substrate 2 after the pull-out test for (a) 5.0 kJ, (b) 4.4 kJ and (c) 3.9 kJ

7.3.1.3 Effect of discharge energy

From Fig. 7.12 (a) and (b), It can be observed that the strength is increasing with the increase in discharge energy, and the maximum value of 7 kN and 7.2 kN is obtained at 5.0 kJ of discharge energy at 5 mm of adhesive application length for Loctite 638 adhesive using EAAJ technique for pull-out and compressive test respectively which is around 90% of the base copper tube strength. Higher strength at higher discharge energy is due to an

increment in the radial deformation and subsequent elastic recovery of the tubes with an increment of discharge energy leading to increased interference pressure causing increased strength. Furthermore, maximum pull-out and compressive load values of 8.34 kN and 8.56 kN (base copper tube strength) are obtained during threaded surfaced EMC (without adhesives) at 5.0 kJ of discharge energy, the reasoning behind higher strength in EMC joints has been explained in sections 2.4 and 3.1. However, samples at lower discharge energy (3.9 kJ), having lower tube deformation and interference pressure shows a significant contribution of adhesion strength in Fig. 7.12 (a) and (b), where the strength of an EAAJ joint with 638 adhesive is higher than the strength of an EMC (without adhesive) joint. Since the lower contribution of interference stress towards overall joint strength gets further reduced by adhesive damping and the strength due to adhesion in the case of 638 adhesive is higher than the reduction leading to EAAJ joints with 638 adhesives at 3.9 kJ of discharge energy to have higher strength than the EMC (without adhesive) joint.

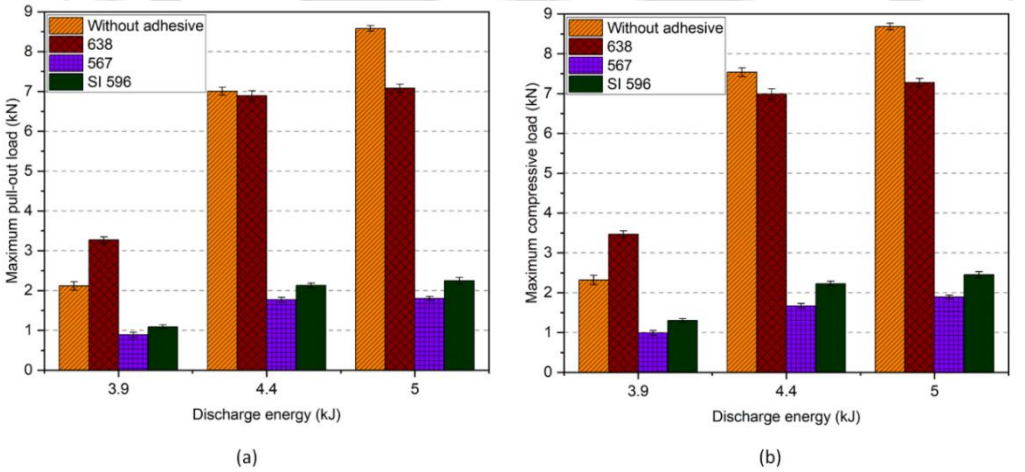

Fig. 7.12 Variation of (a) maximum pull-out load and (b) maximum compressive load with discharge energy across three adhesives for 5mm adhesive application length

7.3.1.4 Effect of curing time

Curing time is an essential parameter in deciding the strength of an adhesive joint. Curing is a chemical process during which adhesive crystallises completely. After this, the adhesive attains its final form and build-up strength. As the name suggests, the curing time is the time required for an adhesive to cure. Four different values of curing time are used in this experiment (24 hours, 48 hours, 96 hours and 120 hours). Pull-out and compressive tests are performed at each value to analyse the effect of curing time on the strength of the joint when other parameters are constant. In Fig. 7.13, we can see the effect of curing time on (a) Maximum pull out load and (b) Maximum compressive load for

different discharge energies. The line, representing the variation, has been obtained through curve fitting.

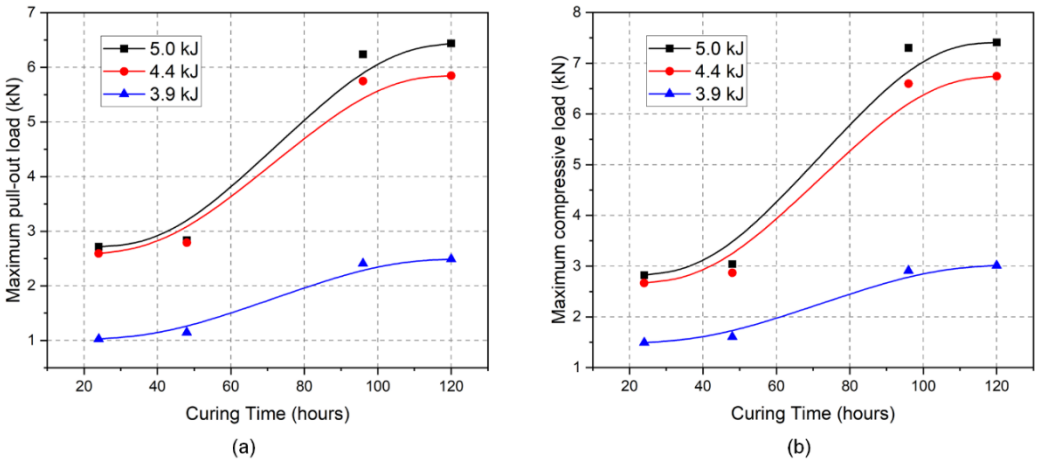

Fig. 7.13 Variation of (a) maximum pull-out load and (b) maximum compressive load with curing time at three discharge energy values

From Fig. 7.13, an increment in pull-out and compressive strength with an increase in curing time can be seen; as with the passage of time during the curing process, adhesive starts to settle better, which leads to an increment in cohesive and adhesive bond strength, but beyond a point, any further increment in curing time does not contribute much to curing of adhesives, and therefore, constant strength is obtained. Four days (96 hours) of curing time is observed to be ideal for optimum strength. Therefore, four days of curing is used for all the variations of the other three parameters.

7.3.1.5 Statistical analysis of pull-out test results

During the experimentation, it is observed that there are three factors (type of adhesives, adhesive application length, and discharge energy) affecting the pull-out strength of the threaded surfaced Cu-SS tube-to-tube EAAJ joints. Therefore, to understand the amount of contribution being made by each factor, a statistical analysis is necessary. Hence a three-factor analysis of variance (ANOVA) is used to investigate the significance of all the factors with the ANOVA module of Minitab software. A list of influencing factors and their corresponding levels are shown in Table 7.2.

Table 7.2 Influencing factors and levels affecting the Cu-SS tube-to-tube joining process

Symbols	Factors	Levels			
		1	2	3	4
A	Type of Adhesives	Loctite 638 (A_1)	Loctite 567 (A_2)	Loctite SI 596 (A_3)	
B	Adhesive application length	20 mm	15 mm	10 mm	5 mm
C	Discharge energy	3.9 kJ	4.4 kJ	5.0 kJ	

Table 7.3 Variation of maximum pull-out load (in kN) at three discharge energy values with four adhesive application lengths for three different adhesives

Discharge energy	Adhesive application length	20 mm			15 mm			10 mm			5 mm		
	Adhesives / Trial	A_1	A_2	A_3	A_1	A_2	A_3	A_1	A_2	A_3	A_1	A_2	A_3
3.9 kJ	1	1.92	0.21	0.65	2.58	0.62	0.84	2.88	0.79	0.91	3.27	0.89	1.09
	2	2.14	0.25	0.66	2.33	0.68	0.87	2.91	0.81	0.92	3.32	0.93	1.14
	3	1.94	0.27	0.58	2.59	0.59	0.83	2.73	0.71	0.9	3.01	0.88	1.12
4.4 kJ	1	2.98	1.21	1.40	4.07	1.40	1.60	5.29	1.64	2.03	6.89	1.77	2.13
	2	3.11	1.18	1.37	3.94	1.33	1.65	5.14	1.58	2.08	6.54	1.73	2.14
	3	2.91	1.13	1.41	3.99	1.36	1.63	5.17	1.52	1.95	6.97	1.68	2.11
5.0 kJ	1	3.16	1.38	1.52	4.33	1.65	1.82	5.37	1.7	2.10	7.08	1.8	2.25
	2	3.22	1.34	1.55	4.29	1.63	1.87	5.42	1.72	2.16	6.97	1.88	2.28
	3	3.07	1.41	1.56	4.10	1.57	1.79	5.23	1.76	2.13	7.10	1.84	2.31

Furthermore, responses (maximum pull-out load) corresponding to their influencing factors with three repetitions are shown in Table 7.3. The results of the three-factor ANOVA analysis are shown in Table 6, which comprises the degrees of freedom (DF), contribution %, the sum of squares (SS), the sum of mean squares (MS), Fisher (F) value, and pre-set confidence (P) value. A "×" symbol represents the effect of the interplay between two factors, and error represents the consideration of trials. The significance of the influence of the factors can be determined by comparing the F-value with the corresponding critical F-value at a 99% confidence level. All the obtained F-values are higher than their corresponding critical F-value, which implies that both the factors and their interplay significantly affect the response, i.e., the joint strength of the Cu-SS tubular joint. Their corresponding p-values further clarify it, and all the p-values are smaller than 0.01, which satisfies the 99% confidence level. The contribution of factor A (type of adhesives), factor B (adhesive application length) and factor C (discharge energy) is calculated to be 64.40 %, 9.94 %, and 21.45 %, respectively. Simultaneously, the interplay between all factors also contributes to the response. Hence it can be seen that the type of adhesive has a lot more significant effect over the response variable (pull-out strength) than the discharge energy and adhesive application length.

Table 7.4 Analysis of Variance for Transformed Response

Source	DF	Contribution	SS	MS	F-Value	P-Value
A	2	64.40%	17.1497	8.57485	15506.22	0.000
B	3	9.94%	2.6483	0.88278	1596.37	0.000
C	2	21.45%	5.7132	2.85658	5165.66	0.000
A×B	6	2.34%	0.6243	0.10405	188.16	0.000
B×C	6	0.22%	0.0587	0.00978	17.68	0.000
A×C	4	0.28%	0.0745	0.01863	33.69	0.000
A×B×C	12	1.21%	0.3231	0.02692	48.69	0.000
Error	72	0.15%	0.0398	0.00055		
Total	107	100.00%				

7.3.2 Leak test

After identifying the presence and location of the leak through the bubble test (Fig. 7.4), an air pressure decay test (Fig. 7.5) is performed to quantify the amount of leakage for both EMC samples (electromagnetically crimped samples without adhesives) and EAAJ samples (electromagnetically crimped joint in the presence of adhesives). The observed leak rates for EAAJ and EMC samples created with 5 kJ discharge energies are 3.01×10^{-8} mbarl/sec and 4.28×10^{-5} mbarl/sec, respectively. Therefore, an improvement of around 1000 times in leak tightness is observed with Loctite 638 adhesives in the case of EAAJ samples compared to EMC samples. Adhesive acts as a sealing material and fills any gap between the Cu-SS interface in the overlapped region, leading to massive improvement in the leak tightness.

7.3.2.1 Effect of discharge energy

The results from the air pressure decay test at three different discharge energy values for 5 mm of adhesive application length are shown in Table. 7.7. A significant improvement in the air leak-tightness can be observed in electromagnetically assisted adhesive joining samples with an increase in discharge energy. Higher energy leads to higher deformation resulting in improved joint tightness, i.e. lower leak rate. A minimum air leak rate of 2.64×10^{-8} mbarl/s is obtained at 5.0 kJ of discharge energy for EAAJ. Testing is performed thrice to ensure repeatability of the result.

Table 7.7 Air leak rate in mbarl/sec at three different discharge energies for adhesive 638 samples at 5mm of adhesive application length

Energy Trial	3.9 kJ	4.4 kJ	5.0 kJ
1	1.09×10^{-7}	5.48×10^{-8}	2.64×10^{-8}
2	1.45×10^{-7}	4.99×10^{-8}	2.87×10^{-8}
3	2.11×10^{-7}	5.12×10^{-8}	3.01×10^{-8}

7.3.2.2 Effect of adhesive application length

Leak tests are also performed with different adhesive application lengths, and results are shown in Fig. 7.14. It is observed that the leak rate increases (leak tightness decreases) as adhesive application length increases, reaches its maxima and then decreases. This variation in air leak rate in an EAAJ joint is due to the combined effect of two factors: 1)

tightness of the joint contributed by interference stress and 2) gap filling between tubes at the interface by adhesion.

Initially, at particular discharge energy, a sample with 5 mm of adhesive application length shows the low leak rate (high leak tightness) as maximum interference stress is observed at this adhesive application length due to low adhesive dampening leading to higher joint tightness along with stronger adhesion. However, as we increase the adhesive application length to 10 mm /15 mm, adhesive dampening of the outer tube velocity drastically increases, leading to lower interference pressure and lower joint tightness, causing a higher leak rate (lower leak tightness). Furthermore, at 20 mm of adhesive application length, the leak rate again decreases (leak tightness increases) as, at this point, the entire working zone is filled with adhesives, filling the gaps between parts leading to higher adhesion despite lower joint tightness due to adhesive dampening. Here the contribution of adhesion towards leak tightness exceeds the contribution of joint tightness due to interference stress towards leak tightness. Furthermore, an increase in discharge energy leads to a lower air leak rate (higher leak tightness) as the increase in discharge energy increases the interference stress/outer tube deformation contributing to higher joint tightness and higher adhesion due to lower gaps between tubes, as shown in Fig. 7.14.

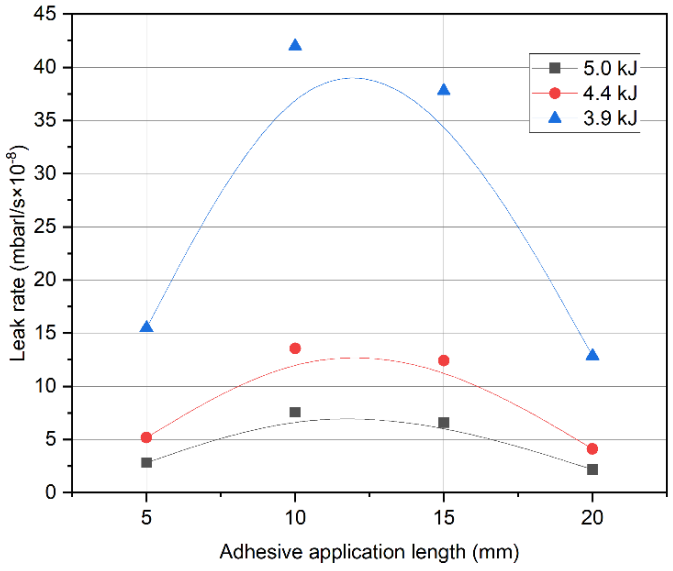

Fig. 7.14 Variation of leak rate with adhesive application length at three discharge energy values at 96 hours of curing time

7.3.2.3 Effect of curing time

As discussed in section 7.3.1.4, curing time is an essential parameter in deciding the characteristic of an adhesive joint. Therefore, the effect of curing time on leak tightness is

also studied. Four curing time values (24 hours, 48 hours, 96 hours and 120 hours) are observed, and the results are shown in Fig. 7.15. An increase in leak tightness can be observed with an increase in curing time; with time, adhesive starts to settle better, which leads to an increment in leak tightness, but beyond a point, any further increment does not contribute much to the curing of adhesives, and hence constant leak tightness is obtained. Four days (96 hours) of curing time is observed to be optimum for three anaerobic adhesives used in the experiment, which has also been stated by the adhesive company [145] and also, the effect of curing time is more significant at lower discharge energy and curing become redundant at higher discharge energy.

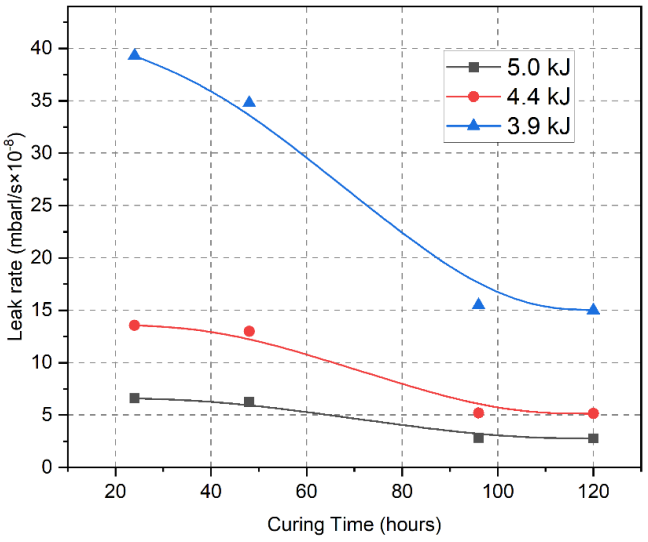

Fig. 7.15 Variation of leak rate with curing time for adhesive 638 with 5 mm of adhesive application length for three discharge energy

7.2.4 Statistical analysis

Furthermore, statistical analysis of the leak test results is also performed using a 3-way ANOVA method. A list of corresponding factors with their assisted levels considered for this study is tabulated in Table 7.8. The result of the four-way ANOVA analysis is shown in Table 7.9. The contribution % of factor C (discharge energy) and factor B (adhesive application length) and factor D (curing time) is calculated to be 51.54 %, 28.34 %, and 15.62 %, respectively. For an EAAJ Cu-SS tube-to-tube joint with Loctite 638 adhesive. Hence, discharge energy is most important, followed by adhesive application length and curing time.

Table 7.8 Influencing factors and levels affecting the leak tightness of Cu-SS tube-to-tube joint

Symbols	Factors	Levels			
		1	2	3	4
C	Discharge energy	3.9 kJ	4.4 kJ	5.0 kJ	
B	Adhesive application length	20 mm	15 mm	10 mm	5 mm
D	Curing time	24 h	48 h	96 h	120 h

Table 7.9 Analysis of Variance for Transformed Response for leak test results

Source	DF	Contribution	SS	MS	F-Value	P-Value
C	2	51.54%	20.676	10.3381	223.46	2.71×10^{-17}
B	3	28.34%	11.366	3.7888	81.90	1×10^{-15}
D	3	15.62%	6.267	2.0891	45.16	9.247×10^{-13}
Error	39	4.5%	1.804	0.0463		
Total	47	100.00%				

According to the chapters (4.1.5 and 4.2.4), a conclusion can be drawn that Loctite 638, 5 mm of adhesive application length at 5.0 kJ of discharge energy for 96 hours of curing time is the most suitable parameters to achieve Cu-SS hybrid adhesive joint with the best joint strength and least air leak rate.

7.2.5 Microhardness analysis

As discussed in section 7.2.3., the microhardness test is performed on the cross-section of the Cu-SS tube-to-tube joint. The Micro-hardness of the base copper and stainless-steel

tube is 96.17 HV and 174.31 HV, respectively. Fig. 7.16 demonstrates the variation of micro-hardness on the interval of every 200µm along with the thickness of the hybrid joint's cross-section at different discharge energies. The maximum micro-hardness value is obtained for Cu and SS at 5.0 kJ of discharge energy. The maximum hardness value is obtained near the joint interface, and it decreases with the distance from the interface. This variation is due to strain hardening during deformation. Furthermore, an increase in hardness value is observed with an increase in discharge energy due to the rise in plastic deformation leading to higher strain hardening, as shown in Fig. 7.16.

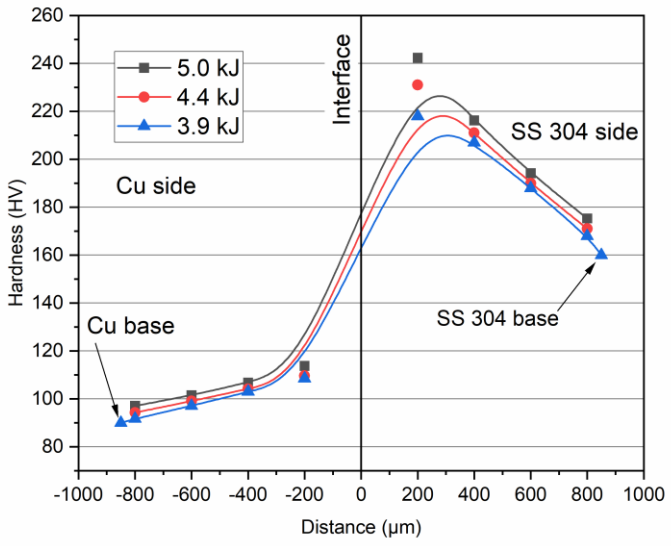

Fig. 7.16 Variation of micro-hardness with distance and discharge energy

7.2.6 Deformation analysis

Transversely cut and longitudinally cut EAAJ samples are studied for deformation analysis. Samples are prepared using WEDM (wire electric discharge machining), followed by moulding with phenolic powder and grinding using Sic paper of different grit sizes. The process is discussed in detail in section 3.2.3.4. Images are taken using a low-resolution optical microscope, as shown in Fig. 7.17 (a) and (b).

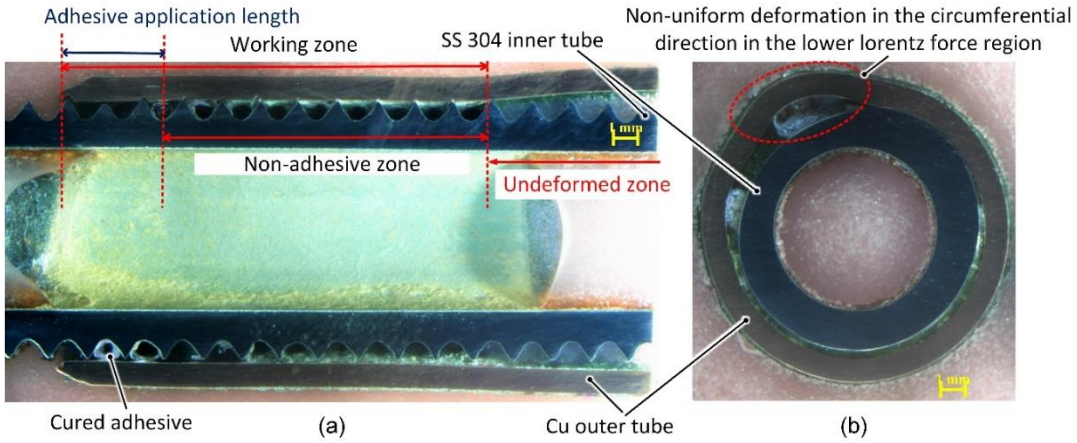

Fig. 7.17 Cu-SS interface for Loctite EAAJ sample at 5.0 kJ of discharge energy for (a) axial view and (b) circumferential view

A higher circumferential deformation is observed in the non-adhesive zone than the adhesive zone, as the adhesives act as a dampening material and reduce the deformation. Furthermore, a non-uniformity in deformation in the circumferential direction can be observed due to the slit of the field shaper used in the setup, as also discussed in section 4.3.2. The slit of the field shaper directs the induced eddy current from the outer surface to the inner surface of the field shaper, leading to intensification and concentration of magnetic field in the working zone but creating a lower Lorentz force region near the slit. This imbalance of Lorentz force regions in the circumferential direction causes a non-uniformity in radial deformation. Further, it leads to the drifting of adhesive particles from the higher Lorentz force region to the lower Lorentz force region, as shown in Fig. 7.18.

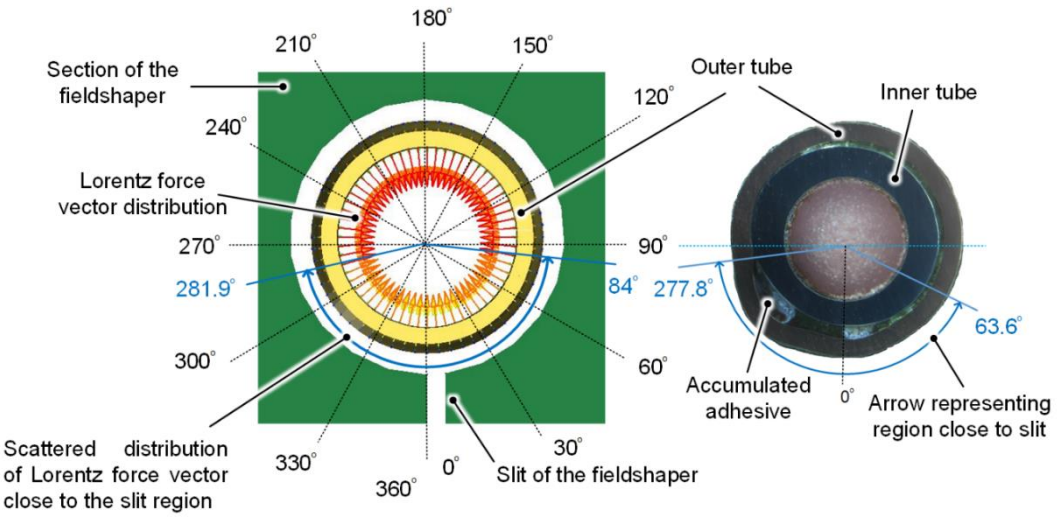

Fig. 7.18 (a) Representation of Lorentz force distribution in the working zone and (b) zoomed view showcasing the impact of the slit on the distribution along with (c) experimental image

Considering slit at 0°, accumulation of adhesive is observed from 277.8° to 63.6°.

7.3 Conclusions

The EAAJ joining of a Cu tube to an SS tube is performed in this chapter; an experimental investigation is studied. The main points can be concluded as,

- Adhesive 638, a structural anaerobic adhesive, is best suited for electromagnetic joining techniques as it has low viscosity and small particle size, which signifies that structural adhesive with lower viscosity is ideal for EAAJ joints.
- Lower adhesive overlap length is best suited to achieve good joint strength with leak tightness. Among four adhesive application overlap lengths, 5 mm is best suited and offers three times higher joint strength than joint with 20 mm adhesive application length.
- Pull-out and compressive strength has increased with an increase in discharge energies as an increase in discharge energy leads to an increase in radial deformation resulting in higher residual stress hence higher pull-out and compressive strength.
- The maximum pull-out load of 7000N is reached at 5.0 kJ of discharge energy with adhesive 638 and 5 mm of adhesive application length.
- The compressive test itself showed a significant value of 7200 N for adhesive 638 at 5mm of adhesive application length and 5.0 kJ of discharge energy which is 3.5 times the value for adhesive 567 or adhesive 596.
- From the perspective of pull out and compressive strength of EAAJ, (i) Loctite 638 is best suited as compared to adhesive 567 and adhesive 596, and (ii) the strength improves with reduction of adhesive application length.
- The three-way ANOVA analysis indicates that the contribution of type of adhesives, adhesive application length and discharge energies on the pull out strength performance in the joint strength of an EAAJ joint are 64.40 %, 9.94 %, and 21.45 %, respectively.
- Joint strength and leak tightness increase with an increase in curing time and gests stagnant after reaching a critical point. 96 hours is observed to be the critical curing time.
- Leak tightness increases with discharge energies. For higher discharge energies, variation of leak-tightness with the adhesive application length is reduced.

- A three-way ANOVA analysis indicates that the contribution % of discharge energy, adhesive application length, and curing time on an EAAJ joint leak tightness is calculated to be 51.54 %, 28.34 %, and 15.62 %, respectively.
- The microhardness value is observed to be increased with discharge energy, and the value near the interface is observed to be increased by 29% compared to the base material value.
- Deformation analysis indicates a non-uniformity of radial deformation leading to the accumulation of adhesive particles in a lower Lorentz force region.

8 Electromagnetic Welding of D9 Steel Tube to SS316LN End Plug

8.1 Introduction

Previous chapters have discussed the two variations of the joining of tubes by the EMF process; EMC and EAAJ. An improved Cu-SS tube-to-tube joint is proposed using the EMC technique, and the process is further improvised into the hybrid EAAJ technique. The chapters have discussed that multi-material Cu-SS joints with good joint strength and leak tightness can be obtained at lower discharge energy with a lower capacitor bank. However, if higher grades of leak tightness are required (for example, for nuclear applications in the range of 10^{-11} mbarl/sec(100 times the leak tightness offered by the EAAJ process)), which can not be obtained from the EAAJ process, then the electromagnetic welding (EMW) process which is based on high-velocity EMF to create a metallic bond, can be recommended. Therefore, to further widen the understanding of the joining of tubes by EMF, a detailed experimental and numerical investigation has been performed in this chapter 8. This chapter investigates the joining of the D9 steel tube to the SS316LN end plug using the EMW process. As established in the previous chapters, developing a FEM model helps to save time and resources and further guides in optimizing the process. Therefore, an axisymmetric Lagrangian (mesh-based) simulation model is developed and validated with an experimentally observed deformation value. An SPH (meshless) simulation model is also developed, and simulated interface morphology is compared with experimentally obtained microstructural morphology. To find the weldability window, SPH simulations are performed for different contact angles and contact velocities, considering waviness formation as the weldability criteria (the waviness formation at the interface has been an important characteristic of impact welding as discussed in section 2.3.1.). The effect of contact angle and contact velocity on amplitude and wavelength of waviness morphology is also studied. Furthermore, the helium burst test and argon gas pressure burst test at varying temperatures are also performed to establish the durability of the D9-SS 316LN tube-to-end plug sample. SEM analyses the interface morphology and the welding quality.

The D9-SS 316LN tube-to-end plug component is used as a fuel-clad end-plug joint in fire breeder reactor fuel pins. Initially, the fabrication is normally done using the traditional fusion welding approach [163-165]. Traditional procedures such as gas tungsten arc

welding (GTAW) are preferred to link clad tubes to the end plugs. However, these techniques have high heat input, resulting in a larger heat-affected zone (HAZ). As a result, methods like laser welding having higher energy density, have exhibited greater process control and smaller HAZ as an alternative to GTAW [165, 166]. Compared to thermal nuclear reactors, the materials must function at greater temperatures and in a harsher radiation environment to be employed in sodium-cooled fast reactors [167]. As a result, the outer tube material is titanium-modified SS316, known as alloy D9 (15 percent Cr-15 percent Ni-0.2 percent Ti).

However, due to the production of low melting point eutectics caused by impurities such as sulphur and phosphorous, fusion welding of austenitic stainless steel (ASS) causes hot cracking flaws [168, 169]. When phosphorous is specified as an alloying element, the defect rises, but the maximum sulphur concentration is limited to 0.0005 wt. percent in modified alloys. The Ti proportion of D9 steel makes ASS more prone to breaking [163]. Hot cracking tests in 316LN ASS have revealed that the total concentration of P and S must be kept below 0.03 wt% to avoid the negative effects of their segregation [163, 170, 171]. Noh et al. [172] discuss the traditional welding process causing residual stress and microstructural heterogeneity leading to brittle fracture and embrittlement.

A solid-state welding procedure can eliminate such problems when attaching a fuel-clad tube to an end-plug in a fuel pin assembly. Electromagnetic welding (EMW) is a solid-state welding technology that produces connections devoid of heat-impacted zones and hot fractures [38, 173]. It is appropriate for axis-symmetric components. It is a high-speed or impulse-forming technique that employs a transient alternating magnetic field to strike non-contact forces on a conductive workpiece without using working material. No filler material is utilised, and the contact-free force causes nearly minimal damage to the workpiece's surface [110, 174]. It is also one of the industry's most extensively utilised high-energy rate forming (HERF) processes [19, 36]. The process is discussed in detail in section 2.3.

8.2 Numerical Simulation Setup with Finite Element Lagrangian Model and Smoothed Particle Hydrodynamics (SPH)

We have simulated EMW using Lagrangian finite element analysis and smoothed particle hydrodynamics. Combining the ANSYS Maxwell and ANSYS explicit dynamics software programmes, a non-coupled finite element model is simulated. The simulation divides the

magnetic pulse welding problem into two parts (electromagnetic and mechanical). ANSYS Maxwell and ANSYS explicit dynamics solve the electromagnetic and mechanical part, respectively, as shown in Fig. 8.1. Dimensions of the various magnetic pulse welding setup components are shown in Fig 8.2. After that, we have used Smoothed Particle Hydrodynamics (SPH) in ANSYS Autodyne (Fig. 8.1) for successful numerical modelling of metal jet emission and interface welding morphology.

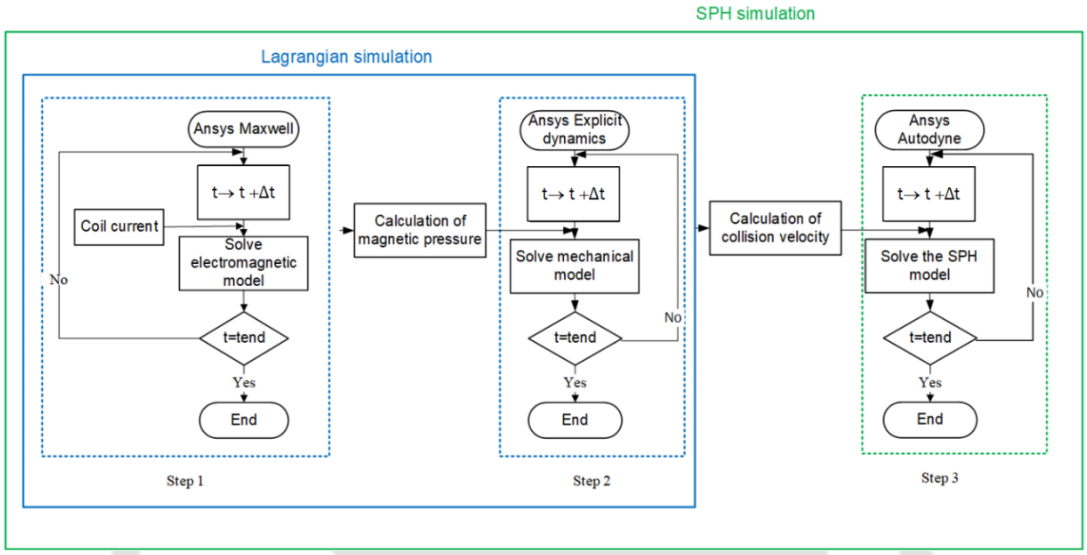

Fig. 8.1 Brief Flow Chart for Numerical Modelling for Electromagnetic analysis (ANSYS Maxwell), Structural deformation (ANSYS Explicit dynamics) and Welding morphology (ANSYS Autodyne)

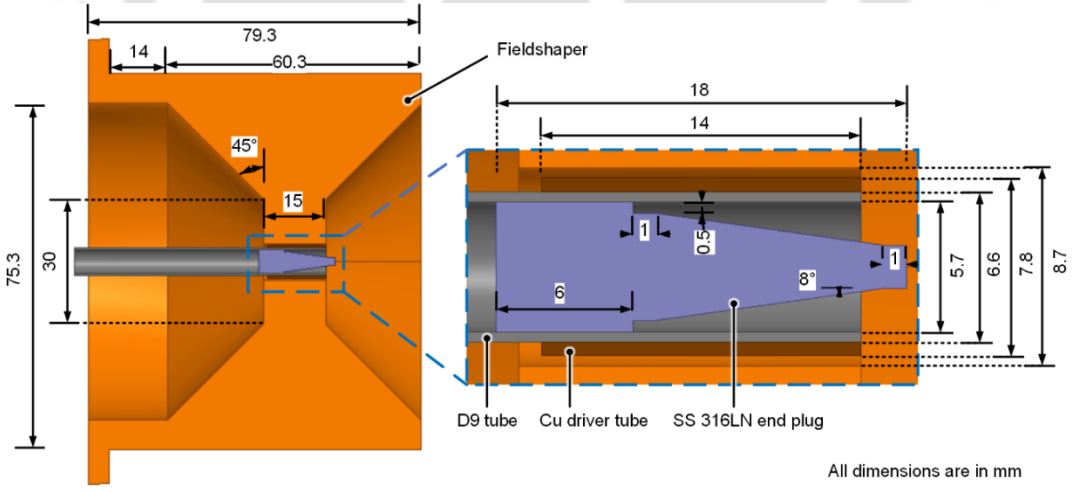

Fig. 8.2 Dimensions of various parts of the components of the magnetic pulse welding setup

8.2.1 Electromagnetic analysis using ANSYS Maxwell

During experiments, the current is monitored using an oscilloscope and utilised as an input to the ANSYS Maxwell to compute the magnetic field. Fig. 8.3 (a) shows the input

current curves. The coil, driver tube, flyer tube, end plug, and field shaper are all enclosed in air in a three-dimensional electromagnetic field model (Fig. 8.3 (b)).

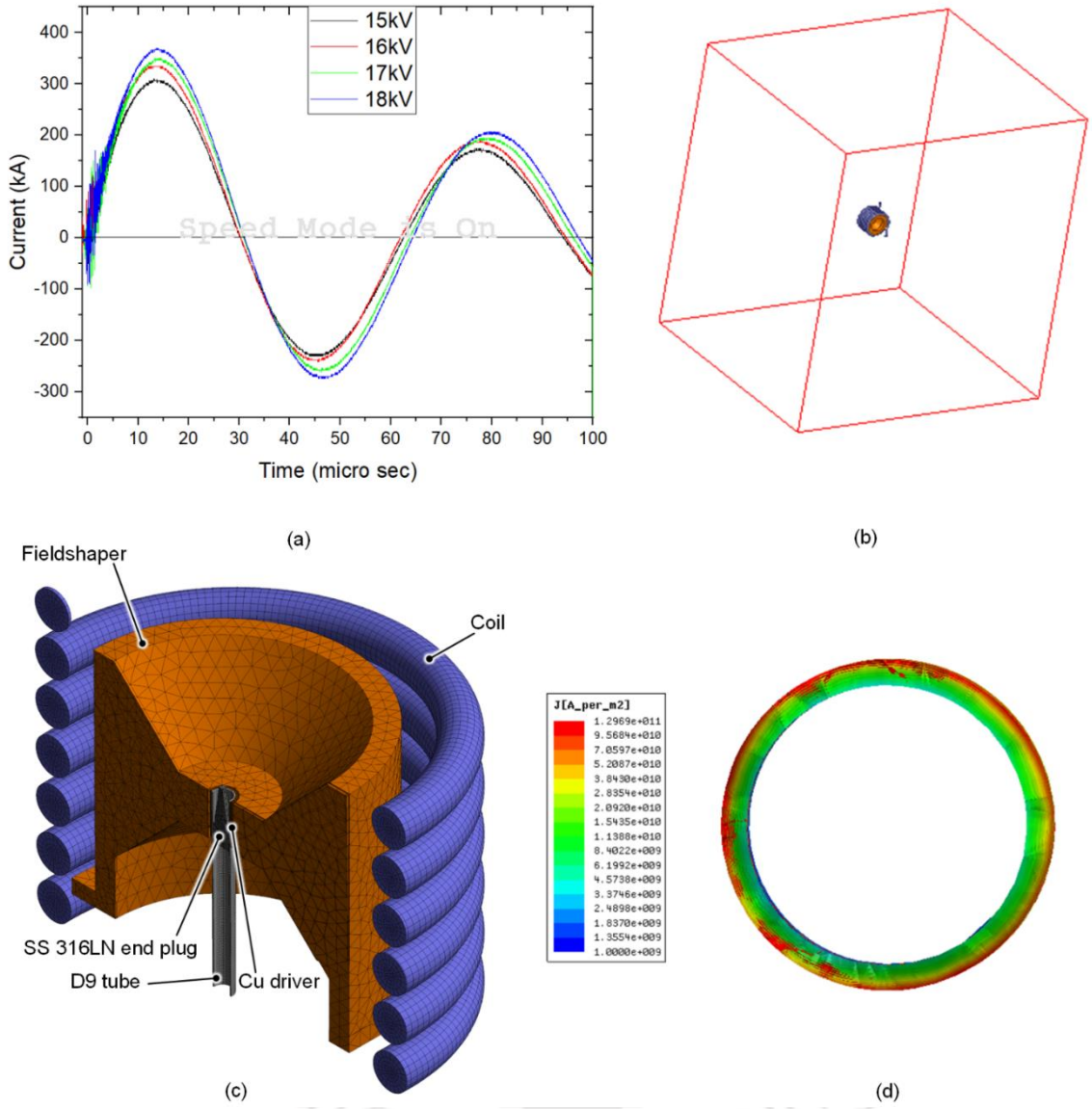

Fig. 8.3 Simulation model for electromagnetic field analysis (a) current curve, (b) ANSYS Maxwell model, (c) grid details showing the sectional view and (d) current density for 18 kV at 15 μs showing induced current at the Cu driver tube surface in the middle of the working zone

As previously stated, the coil has a ring current load that provides a magnetic field for EMW. A vacuum box is assumed to be surrounding the coil-tube model in such a way that its dimension is sufficient enough for the magnetic field to decrease to zero in the far field. The coil, driver tube, flyer tube, end plug and field-shaper are meshed into a hexahedral mesh model, as shown in Fig. 8.3 (c). Fig. 8.3 (d) shows the current density of induced current for the Cu driver tube at 15 μs. An induced current is observed on the outer surface

of the driver tube in the working zone of the field shaper. However, outside the working zone, a lower current density is observed. The magnetic field at the surface of the Cu driver tube is obtained to calculate the magnetic pressure, which is further to calculate structural deformation in the ANSYS explicit dynamics.

8.2.2 Structural deformation analysis using ANSYS Explicit Dynamics

ANSYS Explicit Dynamics is a multi-physics software capable of solving short-duration, structural problems with complex contact interactions with or without friction, including linear and non-linear buckling, fracture, fatigue and more. The problems may have nonlinearities in the geometry, such as large deformation and considerable strain, including rate-independent and rate-dependent plasticity. They make use of both linear and non-linear material models. Structural analysis having very small-time steps, such as high-speed impacts or explosions, can be performed efficiently using the Explicit Dynamics package. The physical problem domain, boundary conditions and loading are axisymmetric. Therefore, an axisymmetric simulation model is used for the mechanical part instead of a 3-D model to save time and cost. The conversion of a 3-D model into an axisymmetric model is shown in Fig. 4. The ANSYS explicit dynamics model schematic is shown in Fig. 8.4 (b). The linear meshing technique is used. Parameters of the J-C material model for Cu, D9 and SS 316LN are shown in Table 8.1. [175, 176]. Properties of the materials are considered to be isotropic for this simulation. The shock wave equation of state (EOS) is defined in the J-C material model to construct the pressure-volume relationship during shock compression of solid analysis. Linear polynomial EOS used in the J-C material model. Constants of EOS for copper are shown in Table 8.2.

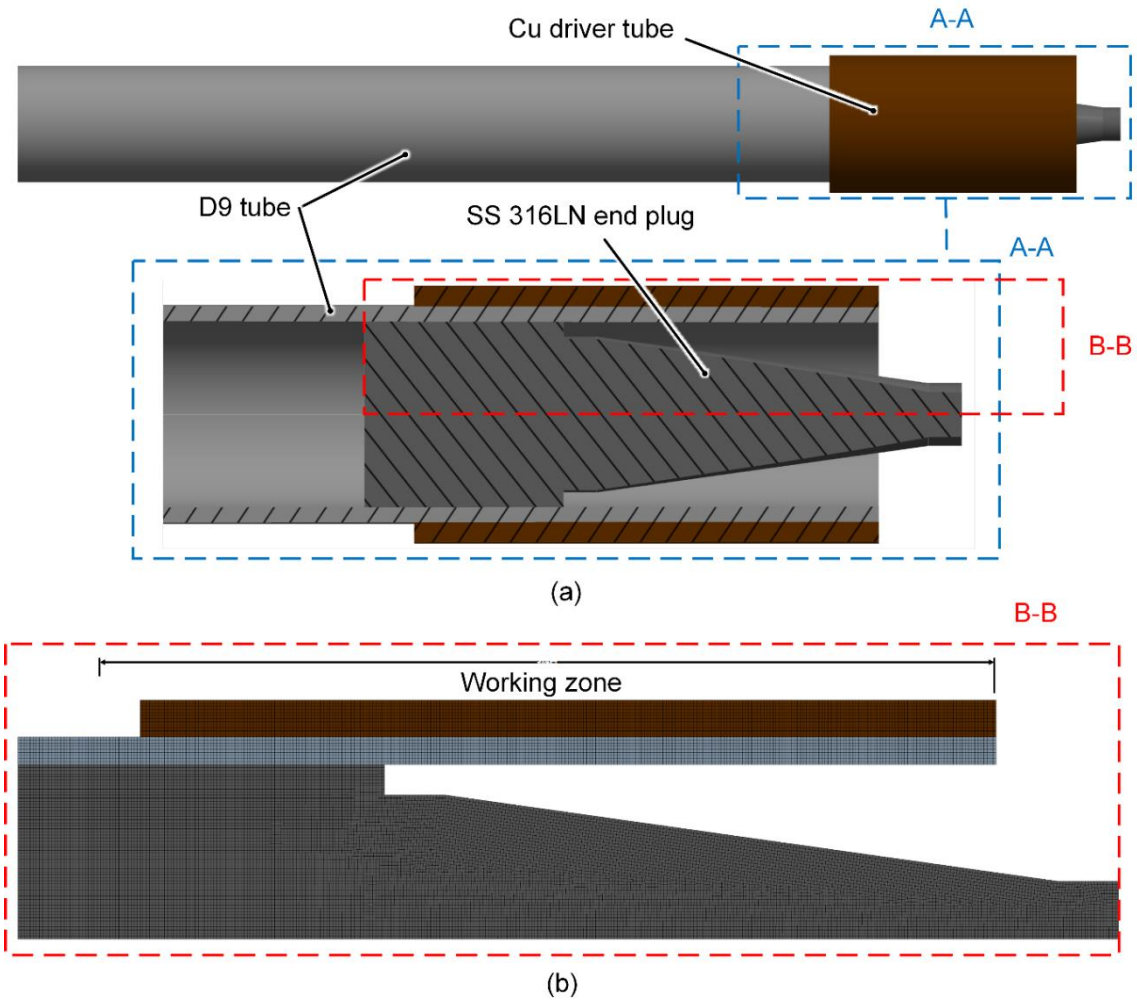

Fig. 8.4 (a) 3-D model showcasing the arrangement of components and (b) Axisymmetric meshed simulation model for ANSYS explicit dynamics

Table 8.1 Constants of J-C material model for Cu, D9 and SS 316LN [175, 176]

Material	A(MPa)	B(MPa)	n	C	T_m(K)	m
Copper	90	292	0.31	0.025	1331	1.09
D9	120	465	0.308	0.1	1449	0.75
SS 316LN	250	1143	0.67	0.0229	1440	1

Table 8.2 Constants of linear polynomial EOS of copper [132]

Materials	c_o	c_1(N/m²)	c_2(N/m²)	c_3	c_4	c_5	c_6	E_o
Copper	0	140×10^9	2.8×10^9	1.96	0.47	0	0	0

8.2.3 Fluid dynamics modelling of Welding morphology using Smoothed Particle Hydrodynamics in ANSYS Autodyne

SPH is a meshless approach in which a group of particles with a spatial position represent a continuous body. Relative attributes of neighbouring particles are summed up to calculate the physical attributes of individual particles. The smoothing length and number of neighbouring particles are determined by the kernel function, also known as the weighting function. The characteristics and deformation of adjacent particles are affected more than those of distant particles in this approach, and the function corresponds to the shape function in the classic Lagrangian finite element method. SPH is primarily utilised in fluid dynamics modelling by establishing a free surface between two interacting fluids, and mass conservation is enforced to mimic fluid motion. By addressing instabilities, solution accuracy and lack of consistency in material deformation, the SPH approach is expanded to solid mechanics applications. During impact welding, the wavy morphology and jetting phenomena may be anticipated using SPH.

An axisymmetric SPH simulation is performed using ANSYS Autodyne (Fig. 8.5) to study the waviness formation during EMW of the D9 tube on the SS 316LN end plug. The flow chart of the process is shown in Fig. 8.1. Fig. 8.5 represents the required geometry for SPH modelling of the welding morphology at the interface. The model considers the D9 tube and SS 316LN end plug inclined at an angle as per the design before the initial contact/impact. The contact velocity of the D9 tube is calculated from the Lagrangian model and used as an input to the SPH simulation model. Particle size of 5 µm is decided for both materials during SPH to study the interfacial morphology and jetting. Both components are assumed to be 3 mm from the point of contact, that has been observed to be sufficient for waviness generation as per experimental results. Room temperature is fixed as the initial temperature, replicating the experimental conditions.

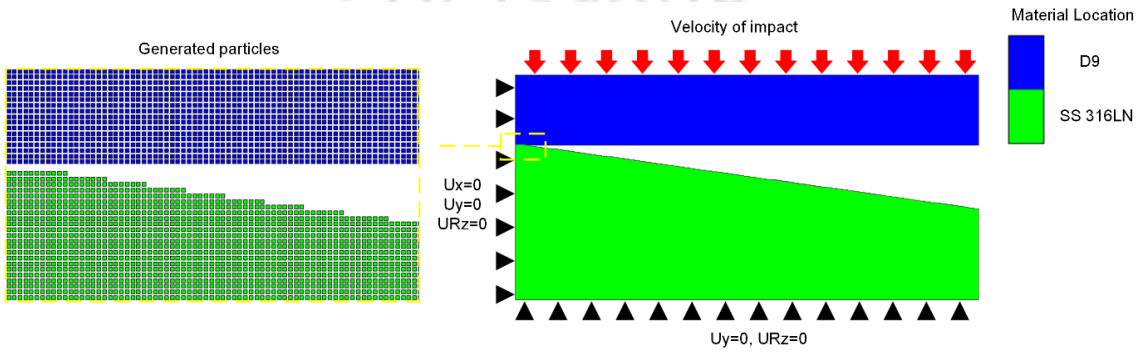

Fig. 8.5 Geometry used for the SPH numerical model

Furthermore, a constant value velocity is applied in the negative y-direction to the outer surface of the working zone. The only boundary condition is to fix the bottom edge of the end plug, constrain the left edge of the tube, and end plug vertically. The Johnson-Cook material model with the constants given in Table 8.1 is used to study the material deformation.

8.3 Experimental setup

For welding of the D9 tube to the SS316LN end-plug, an indigenously designed electromagnetic machine with a maximum charging energy of 70 kJ at a voltage of 25 kV is employed, as has been discussed by Kumar et al. [177-178]. The electromagnetic processing system consists of two capacitor sub-banks, each with a single trigatron type switch. To close the switch simultaneously with minimal jitter, a specially developed trigger generator is used. These operational characteristics of capacitor banks are determined by trial and error. The maximum current and short circuit frequency are 700 kA and 22 kHz, respectively. The minimal work thickness to be welded is constrained by this frequency as the skin depth should be smaller than the job thickness, which is highly dependent on the current frequency. A four-disc bitter coil has been constructed for this experiment [178]. The principal function of the coil is to conduct current and provide an appropriate magnetic field and pressure distribution. A bitter type coil is insufficient to meet the required magnetic field because it loses mechanical integrity at such high magnetic fields and fails catastrophically before achieving the requisite magnetic field. Using a multi-turn coil with a fine winding pitch to raise local field intensity is also difficult due to the increased coil inductance. Therefore, a disposable copper field shaper is used for the process along with the bitter type coil, which contributes to the mechanical integrity of the coil and further distributes and intensifies the magnetic field in the working zone as discussed in chapter 3 and 4. Fig. 8.6 demonstrates the electromagnetic manufacturing machine setup consisting of the bitter coil, a disposable field shaper and metallic fixtures to hold the workpiece axially.

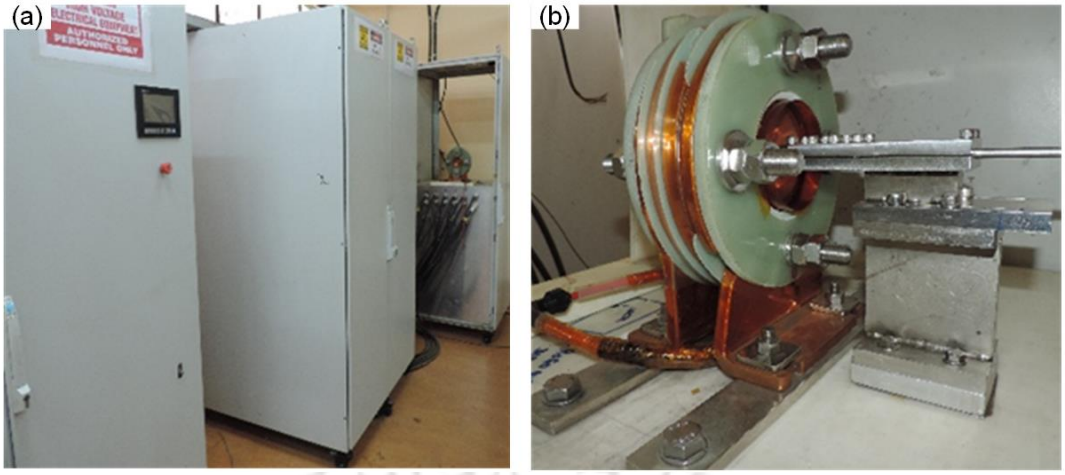

Fig. 8.6 Machine used: (a) 70kJ/25kV magnetic welding machine, (b) Welding tool consisting of Bitter coil with disposable copper field shaper and

The EMW generates an extremely strong magnetic field B_{max} of more than 40T and a rise time of less than 25 μs which results in a dynamic pressure of more than 640 MPa. The magnetic pressure exceeding the yield strength of the field shaper material leads to residual plastic deformation, accumulating in every successive pulse, causing the progression of deformation and further reducing field strength over the usage. Therefore, developing a mechanically robust field shaper with materials like Cu-Be, Cu-Ti, Cu-Cr-Zr, and Al-Sn alloys having relatively higher conductivity (greater than 15% IACS) is a necessity. However, these materials get to suffer from saw-effect at magnetic fields above 40 T (minimum required magnetic field for welding D9 steel tubes [179]) because of the melting of the field shaper material at sharp corners in the field shaper, caused by high eddy current density. Due to the saw-effect, the field shaper is not suitable for many shots, and the only option is to utilise disposable field shapers. Therefore, replaceable inserts made of Cu, Al, Nb, Ta, SS, C-W, and Ta are used with hybrid field shapers. However, arcing at the interface of the field shaper and the insert at the slit site affect these replaceable insert field shapers, making them unsuitable for use in an industrial machine as also discussed by Kulkarni et al. [180].

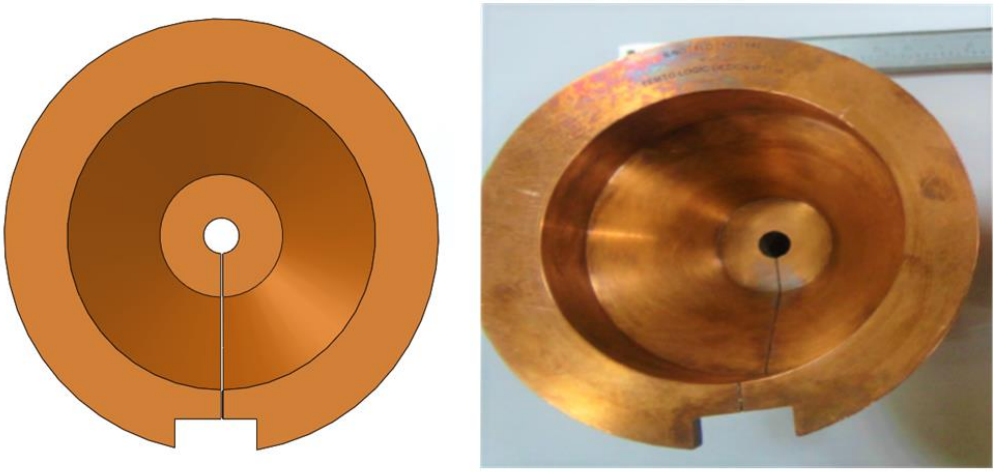

(a) (b)

Fig. 8.7 Copper field shaper (a) top view, (b) experimental sample

Furthermore, it has been observed that the slit in the field shaper leads to an asymmetrical force distribution on the clad tube in the working zone, as discussed in section 7.2.6, causing bending of the joint towards the slit side. This bending problem in the weld portion is mitigated by designing an innovative fixture as shown in Fig. 8.6 (b), which minimises the bending effect. This modification in the fixture has made all MP welded joints within acceptable dimensional tolerances. D9, which is used as a clad tube material, is a nuclear-grade austenitic stainless steel with broad applications in fuel pin cladding and other core components [163]. It has an operating temperature up to 923K. A tapered SS 316LN rod is used as an end plug. The chemical composition of D9 and SS 316LN is obtained using EDS (energy-dispersive X-ray spectroscopy) and compared with the standards as shown in Table 3. Here, as the D9 steel tube has poor electrical conductivity and high yield strength, the magnetic field induces a lower eddy current resulting in very low effective pressure for welding even at a higher magnetic field (50T). A high electrically conductive copper tube called 'driver' is used as a sleeve around the tube to address this problem. This driver translates Lorentz's forces effectively on the tube to be welded, and its thickness is chosen equal to that of magnetic skin depth [163]. The driver tube gets damaged after each welding shot. The geometry of the driver and the clad tube is kept constant throughout the experiment. The taper design of the end plug ensures its self-cleansing during impact, and it also resists the resulting stress wave. The geometry of the end plug is considered as one of the most critical factors for achieving a successful weld. Therefore, the taper angle and tapered length of the end plug are optimised for the D9 steel tube by trial and error. All angles between 6° to 9° have resulted in a proper weld, but 8° has produced the longest welding joint of 5 mm. Due to the high pulsed forces, the

driver and flyer accelerate towards the end plug and collide with a high velocity in the ranges of 300–500 m/s, resulting in a metallic bonding between the tube and the end plug. All trials are conducted in atmospheric conditions. Four discharge voltages are tried (15 kV, 16 kV, 17 kV and 18 kV). Process parameters are shown in Table 8.4. The stand-off distance between the tube and end plug increases gradually along the collision direction due to the taper angle, enabling it to attain an optimum collision velocity. The mechanical properties of the Cu and D9 tubes are shown in Table 8.5.

Table 8.3 Chemical composition of D9 tube and SS 316LN metallic plug

Element	C	Ni	Cr	Mo	Ti	Si	Mn	N	Fe
D9 tube	0.04	15.5	14.04	2.25	0.26	0.61	1.78	0.0037	Balance
SS316 LN	0.03	14	18	-	-	0.33	1.88	0.044	Balance

Table 8.4 Process parameters of the experiment

Discharge voltage (kV)	15	16	17	18
Current (kA)	310	334	354	374
Taper angle (degrees)	8°	8°	8°	8°

Table 8.5 Mechanical and electrical properties of driver and flyer material

Material	Yield strength (Mpa)	Ultimate tensile strength (MPa)	Elongation	Magnetic permeability	Electrical conductivity (MS/m)
Copper	70	210	60%	0.99	58.7
D9	550	770	20%	1.02	1.351

8.4 Results and discussions

8.4.1 Lagrangian Finite element model

The deformation pattern of the D9 tube over the SS 316LN end plug shows effective plastic strain in the working zone of the magnetic pulse welding joint in the numerical simulation model (Fig. 8.4 (b)) using ANSYS explicit dynamics at 18 kV of discharge voltage for four different time values is shown in Fig. 8.8. A convergence study is conducted for various mesh sizes to ensure convergence with mesh refinement.

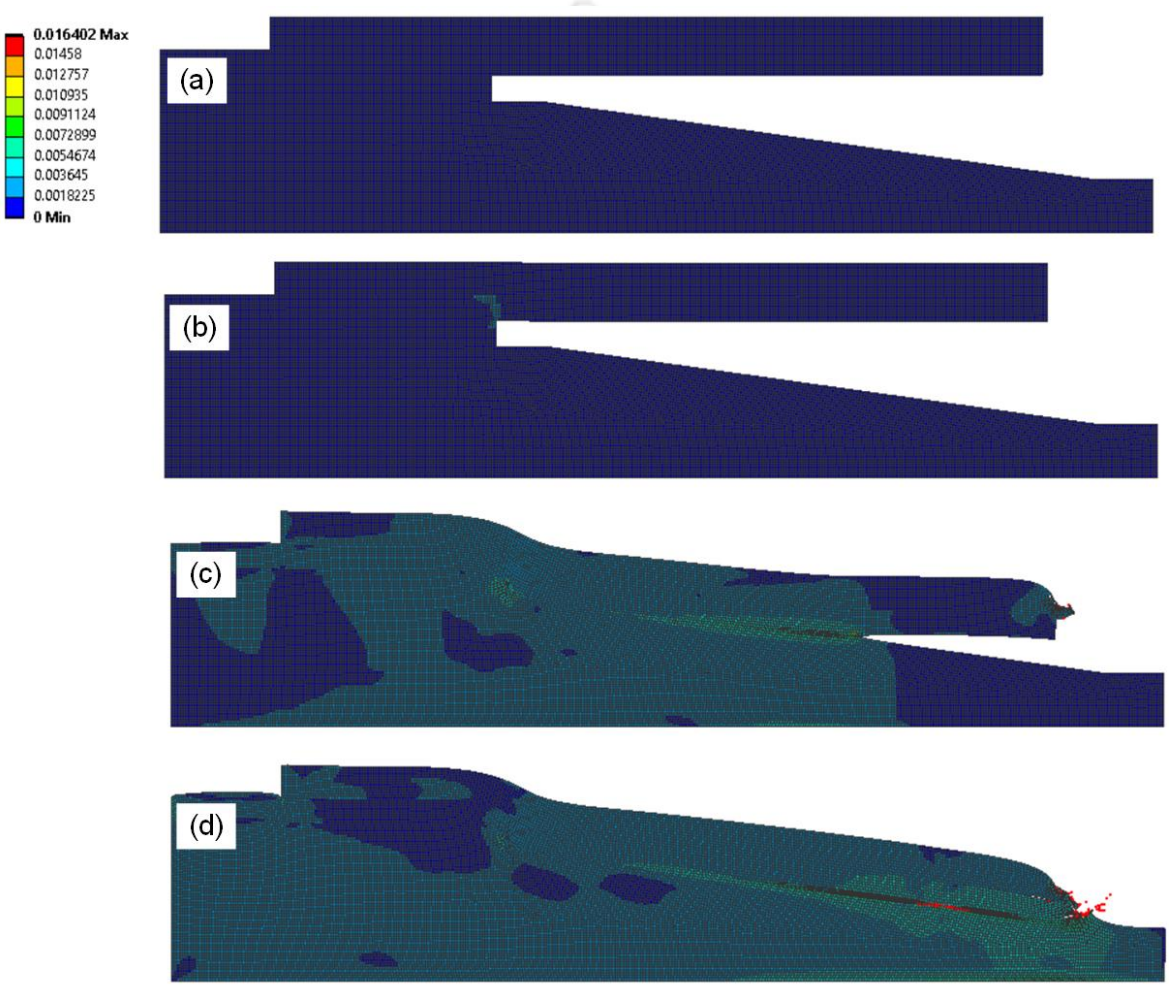

Fig. 8.8 Deformation stages showing the effective plastic strain fringe pattern of EMW joint at four different times (a) 0 µs, (b) 5 µs, (c) 10 µs and (d) 15 µs at 18 kV of discharge voltage

8.4.2 Experimental validation of Lagrangian simulation model

The outer diameter of the tube-to-end plug (D9-SS 316LN) joint is experimentally measured using an optical microscope of low magnification and compared with the results obtained from Lagrangian simulation. Fig. 8.9 shows the experimentally and numerically observed variations of the outer diameter (averaged circumferentially) of the

D9 tube-SS 316LN tube-to-end plug assembly after welding at four different locations (2mm, 5 mm, 9 mm and 12 mm) along the axis in the working zone for two different discharge voltages (18 kV and 17 kV). Deformation increases with an increase in discharge voltage, and the minimum value of outer diameter is observed at 18 kV of discharge voltage. Experimentally calculated values align with the simulated results with a 2-5.1 % error. It is observed that the experimental values of the outer diameter in the working zone are lower than the simulated values, and this is probably due to the assumption that the current is uniformly distributed in the cross-section of the solenoid coil leading to an increase in deformation due to the increased Lorentz force.

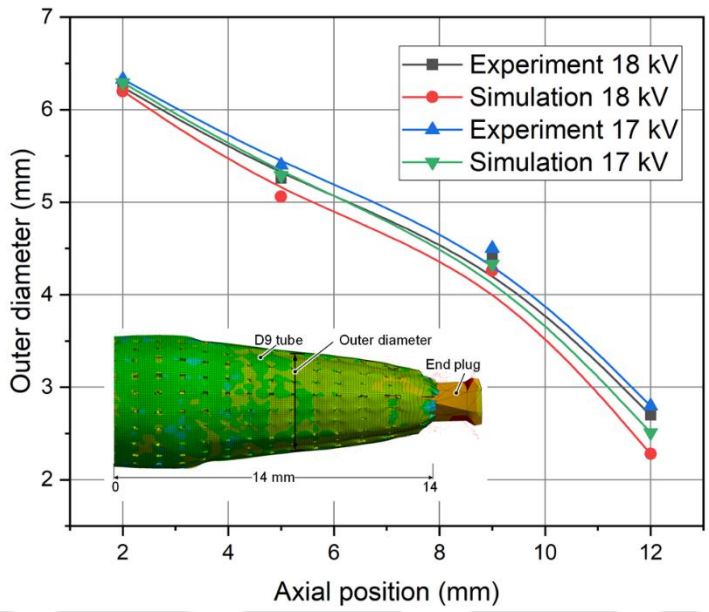

Fig. 8.9 Outer diameter comparison of the D9 tube-SS 316LN end plug joint in the working zone

8.4.3 SPH results along with experimental validation

As the particles in SPH are not connected, their relative movement facilitates to a model of metal jet emission, which mesh-based numerical approaches could not do. Jetting is thought to be a requirement for welding as it removes nascent oxides and impurities from the mating surfaces, allowing solid-state bonding to occur without substantial melting or long-range diffusion. The SPH approach accurately recreated metal jet emission during impact welding. The interface morphologies of the joint at different time frame during simulation is shown in Fig. 8.10. The initial input radially inward velocity is 540 m/s, and the initial angle is 8 degrees. A metal jet is released from the collision location when the flyer tube collides with the target end-plug.

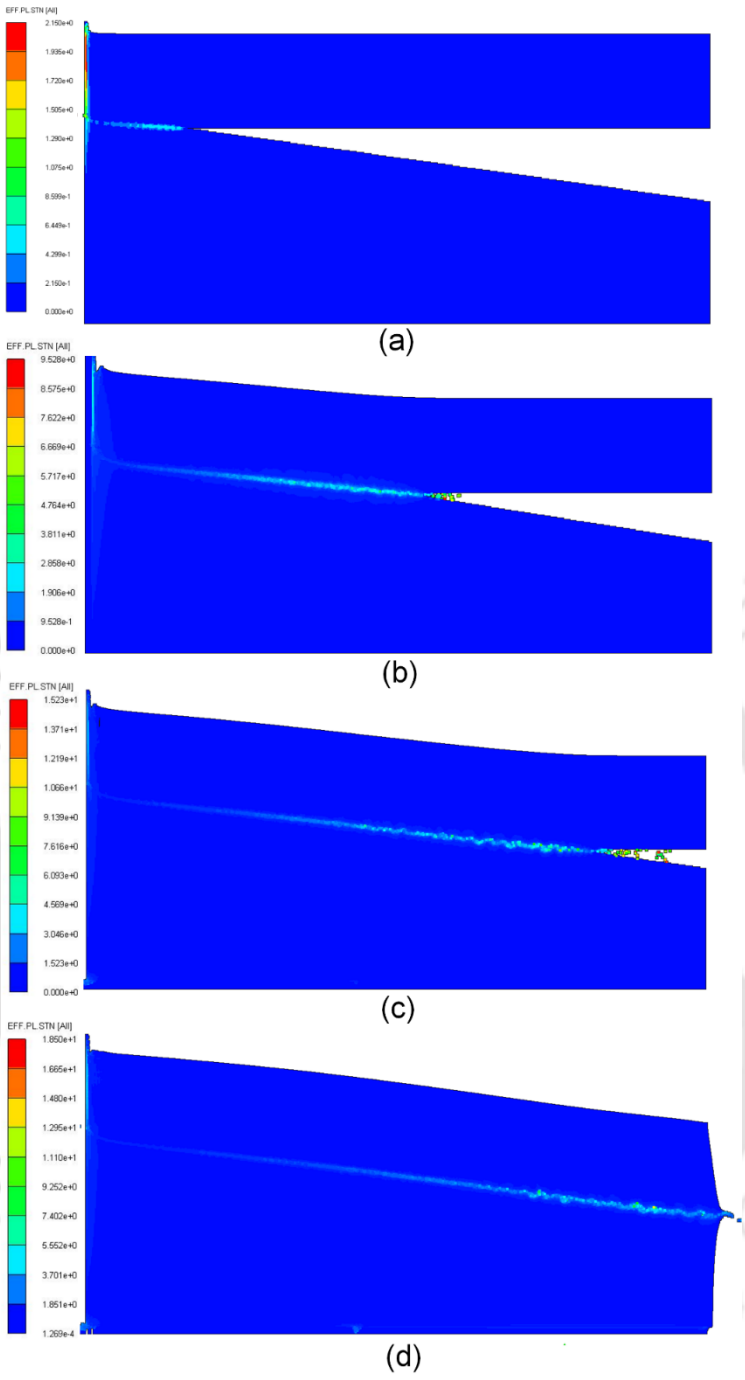

Fig. 8.10 SPH interface morphologies during simulation at (a) 0.12 μs, (b) 0.46 μs, (c) 0.64 μs and (d) 0.72 μs

The metal jet's velocity is estimated to be 1000–1200 m/s range. It is also discovered that the amount of expelled metal jet has increased with increasing impact velocity for a given collision angle. Fig. 8.11 shows the waviness as well as the jetting phenomenon. Fig. 8.11 illustrates that the jetting phenomena have removed around 10-15 μm layer (2-3 particles) from the surfaces of the D9 steel tube and SS 316LN end plug. The probable reason for same amount of surface material removal may be the same range of shear moduli of them.

The ejected materials during the simulation account for the deposited particles outside the welded zone as observed in the experiments.

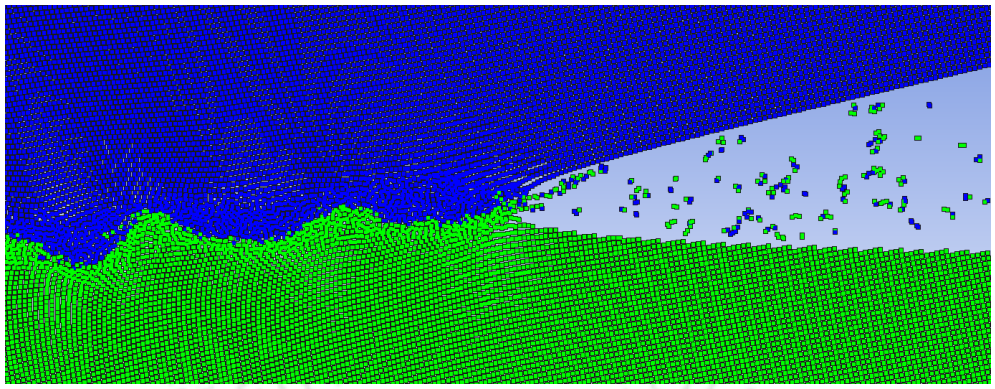

Fig. 8.11 Formation of wave structure and jetting during magnetic pulse welding simulation using SPH

Fig. 8.12 shows the field variables, effective plastic strain, pressure, and temperature after 1μs for the impact angle of 8 degrees. The effective plastic strain distribution (Fig. 8.12 (a)) shows high values, mainly in the range of 1 to 9, near the interface with a distance of 15-20 μm between both materials, while the rest of the workpieces remain elastic. Experiments show elongated grains at the interface, which are consistent with these high strain levels. Furthermore, such a common interfacial strain could be a source of kinematic instability. The pressure at the collision point is around 18 GPa, as shown in Fig. 8.12 (b). The anticipated temperature is strongly localised near the interface where significant plastic deformation develops, as seen in Fig. 8.12 (c). The thickness of this zone is around 30-55 μs. Predicting such a confined zone is critical since melting has long been thought to be undesirable for weld quality because of the intermetallic produced.

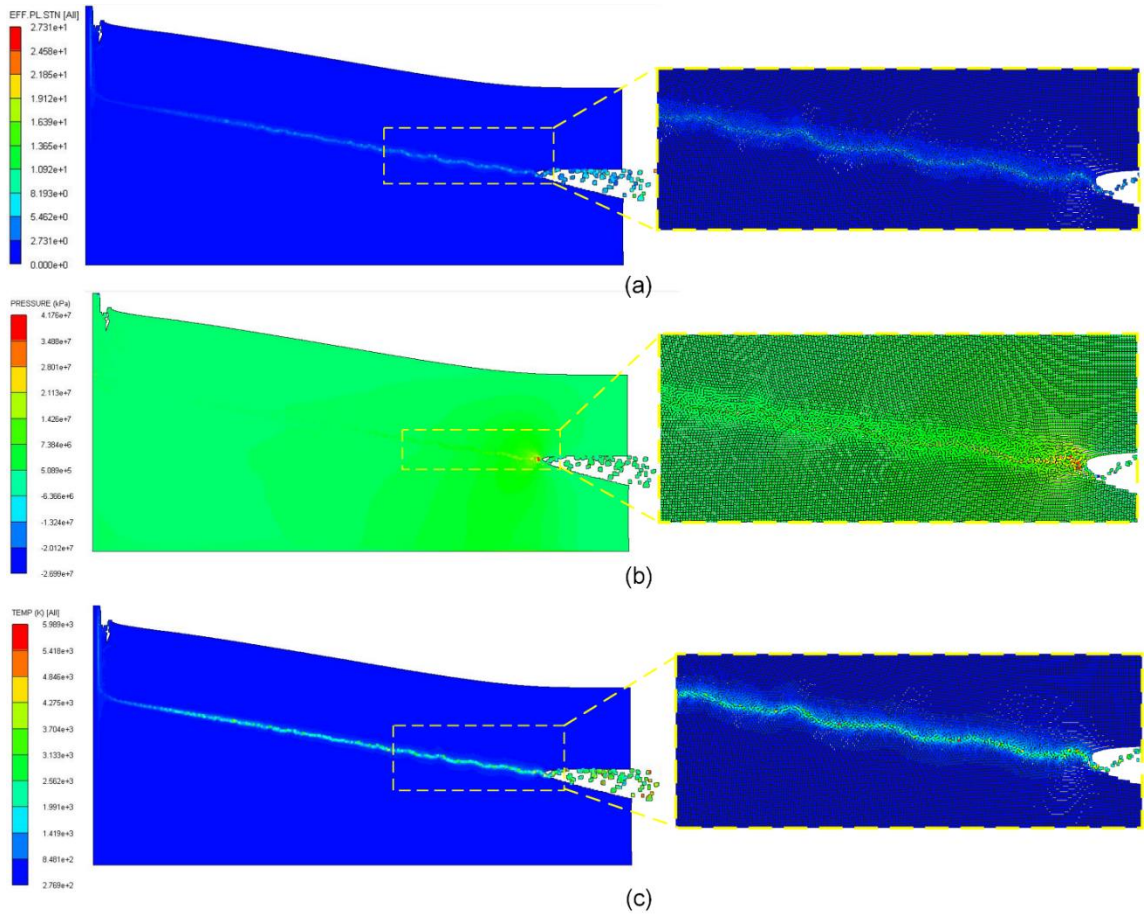

Fig. 8.12 Predicted field variables at 1 μs for impact angle 8 degrees (a) effective plastic strain, (b) pressure and (c) temperature

Fig. 8.13 (a) further confirms localised plastic deformation in the immediate vicinity of the D9-SS 316LN interface in the range of 55 μm while the rest of the workpiece remains elastic. The significant strain value obtained near the interface aligns with the deformed/equiaxed grains obtained near the interface in experimental samples. Fig. 8.13 (b) shows the stress localisation in the SS 316LN side. One of the most exciting aspects of impact welding is the formation of waves at the interface. Many theoretical and practical research have been devoted for solving the problem in the early history of impact welding, one of which have been proposed by Abrahamson et al. [181], where the authors proposes indentation mechanism. The process of waviness formation has been further explored by Bahrani et al. [182], and it is now an often-cited explanations for the mechanics of wave propagation during impact welding. Furthermore, Hunt et al. [183], Cowan et al. [184], Robinson et al. [185], have attempted to characterise the wave generation during impact welding qualitatively and quantitatively. Hay et al. [186] discusses that the material behaves like a fluid under specific types of impact.

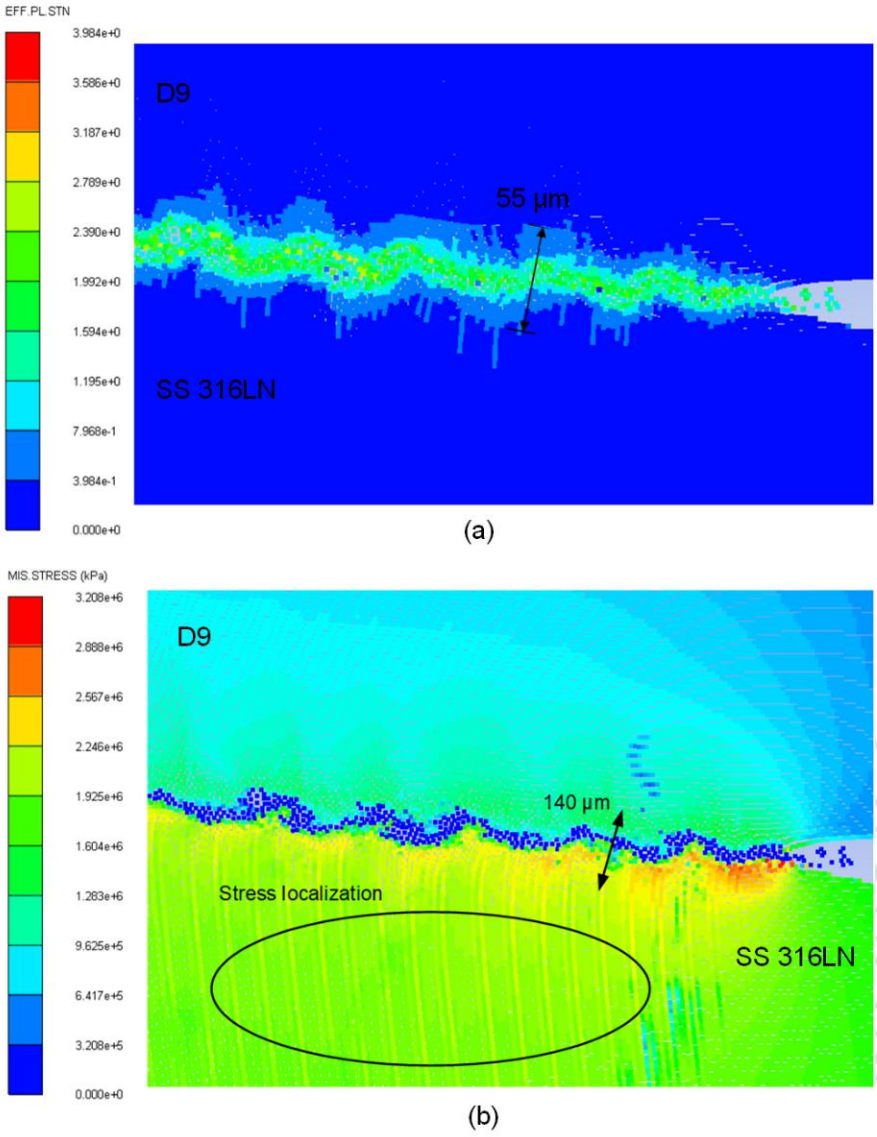

Fig. 8.13 Predicted (a) effective plastic strain and (b) von Mises stress fringe pattern at 3 µs for an impact velocity of 500 m/s and 8 impact angles of 8 degrees

We have used the hydrodynamic methodology to explain the material behaviour during high-velocity impact and in further elaborating the wave generation theory. However, Hay et al. remarked that a thorough explanation of the wave creation process using conventional hydrodynamic methodologies is difficult because of the unavailability of vortex formation models for all Reynolds values [186]. Calculating metal viscosity over the range of strain rates is also challenging. According to the data reported in the preceding sections, SPH simulation accurately reproduces the empirically obtained interface morphology (Fig. 8.14). More attention must be devoted to the movement of individual particles in the model to understand better the dynamics behind the generation of waves and vortex zones. Fig. 8.14 depicts a typical collision that results in the production of waves.

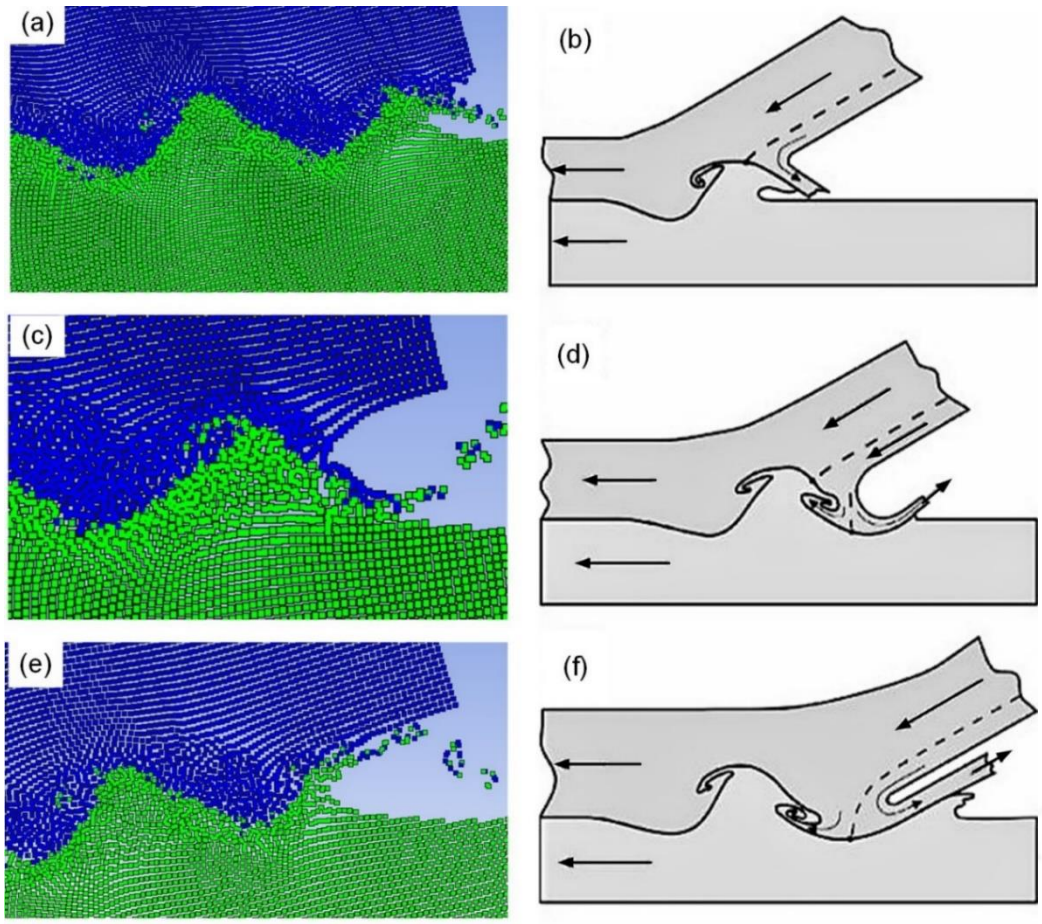

Fig. 8.14 Comparison of results of SPH simulation with the Bahrani-Black-Crossland wave formation model

The collision point, which moves from left to right, is connected to the model's reference system, which follows the material flow of D9 steel flyer tube. In the Bahrani-Black-Crossland model, the flyer tube material is divided into two jets, one (salient jet) flows towards left and the other (re-entrant jet) towards right. The jet from the flyer tube interacts with one previous protrusion on the target tube in Fig. 8.14 (a). The jet is diverted downwards, deforming the target tube and forming a depression there (Fig. 8.14 (c, e)), and, as a result, a new protrusion rapidly grows at the tube contact just at the right of the depression (Fig. 8.14 (e)). This protrusion creates some depression on the flyer tube and further diverts the material flow of the flyer tube, as shown in Fig. 8.14 (a). These successive generations of depression and protrusions on both the flyer and the target tube materials create a wavy interface in the MP welded joint. Fig. 8.15 and Fig. 8.16 compare waviness morphology obtained at 18 kV of discharge voltage during SPH simulation as well as experiment. A good agreement in simulation and experimental results is obtained with the values of amplitude and wavelength of interface waviness being in close proximity. The effect of contact angle and contact velocity on the amplitude and

wavelength of waviness morphology is also studied, as shown in Table 8.6. No waviness is observed below 400 m/s, above 800 m/s and below 8 degrees; hence no welding is happening at those parameters.

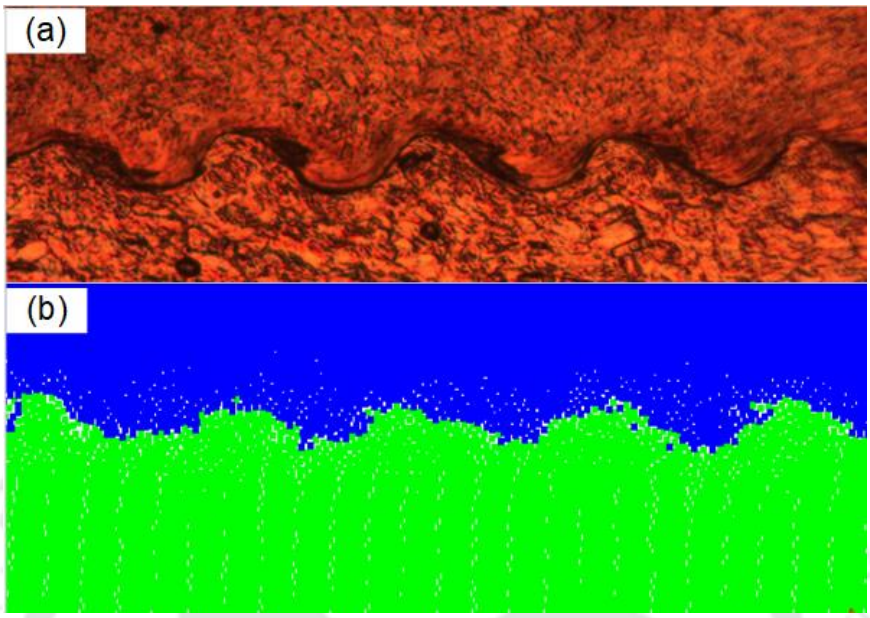

Fig. 8.15 Comparison of waviness morphology in (a) Experiments and (b) Simulation

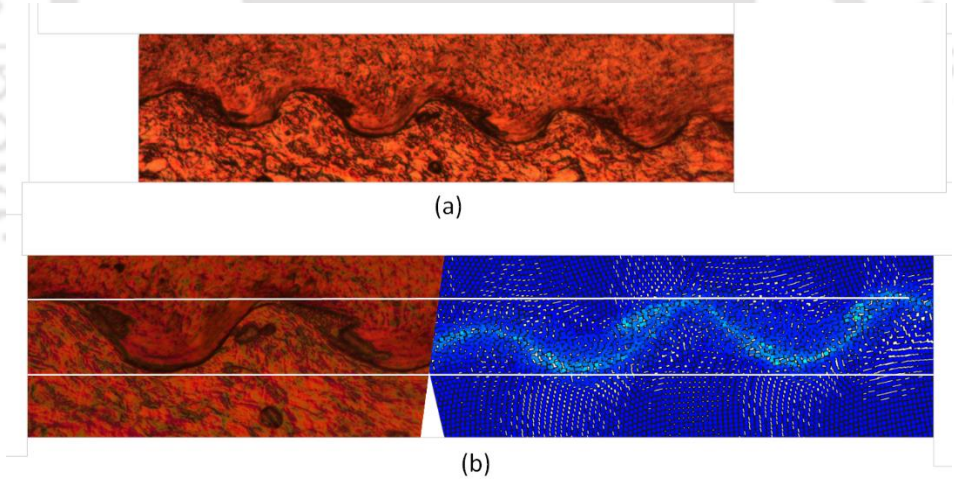

Fig. 8.16 (a) Optical micrograph showcasing waviness pattern of the welded interface in experiments (b) Comparison with SPH (zoomed view) at 8-degree, 18 kV discharge voltage

Table 8.6 Variation of Wavelength (λ) and Amplitude (A) of waviness morphology in μm with impact velocity and impact angle

Impact velocity / Impact angle	400 m/s	500 m/s	600 m/s	800 m/s
6 deg	λ = 100, A = 20	λ = 105, A = 30	λ = 115, A = 35	λ = 120, A = 40
8 deg	λ = 150, A = 40	λ = 160, A = 45	λ = 180, A =55	λ = 190, A = 60
10 deg	λ = 190, A = 45	λ = 215, A = 50	λ = 225, A = 60	λ = 235, A = 70
12 deg	λ = 205, A = 50	λ = 225, A = 65	λ = 235, A = 80	λ = 250, A =100

8.4.4 Hydraulic burst test

The strength of the tube-to-end plug junction has been analysed using a hydraulic pressure burst test at 300K. With the use of fluid, pressure is applied in all directions in this procedure. It is a destructive testing approach for estimating a part's pressure overload capability in pressurised settings [187]. To connect the joint to a hydraulic burst tester at one end, EMW samples are welded to a fixture tube (used to close the tube to the end plug joint) using inert tungsten gas (TIG) welding. At 300 K, three samples are subjected to a hydraulic burst test.

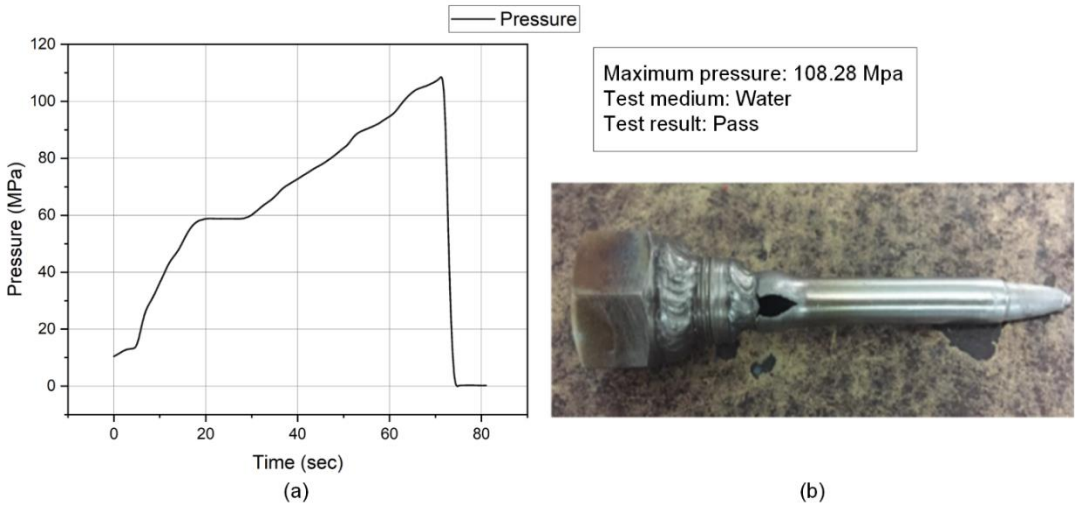

Fig. 8.17 (a) Pressure profile with time obtained from hydraulic burst test indicating the failure of the tube at 108 MPa and (b) Hydraulic burst sample failed at D9 tube near the TIG joint

At pressures reaching 105 MPa, all three samples rupture near 108 MPa (Fig 8.17 (a)) at the D9 steel tube near the TIG welded joint region between the D9 steel clad and the fixture

tube (used to close the tube-to-end plug joint). This means that EMW joints are more durable than the weakest parent metals. Based on the first principle of the thin cylinder, this measured rupture pressure reasonably fits the tube's rupture strength.

8.4.5 Micro-hardness test

The hardness variation across the joint interface is measured using a micro-hardness tester with a 250-gm load. As illustrated in Fig. 8.18, the average microhardness values on the D9 side and the SS 316LN side are 309 VHN and 280 VHN, respectively. A 3-5 percent increase in hardness is noted on both sides of the contact, which can be attributed to the strain hardening during the EMW process.

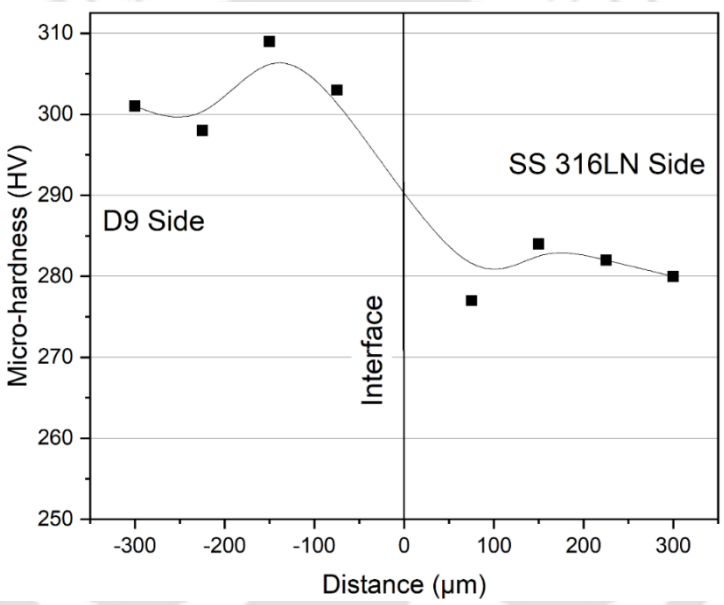

Fig. 8.18 Micro-hardness distribution near the bonding interface for the MP welded sample

8.4.6 X-ray computer tomography

X-ray computer tomography is a non-destructive technology for visualising several forms of three-dimensional data about a solid object, such as microstructure, flaws, and crystallography. Fig. 8.19 shows an X-ray tomography image of a D9-SS 316LN tube-to-end plug MP welded sample, demonstrating deformation of the D9 outer tube onto the tapered SS 316 LN end plug. The tomography used X-ray clearly distinguishes between a uniform welded region without any fracture and a non-uniform, irregular non-welded region with a gap along with the interface. The welding length is more than 5 mm from this tomography image. Fig. 8.20 shows the reconstructed voxel image of size 4 μm, which further confirms the non-uniformity at the D9-SS 316 LN interface at the beginning of the

working zone. However, uniformity can be seen in the latter half of the working length as the welding proceeds in the welding direction. `

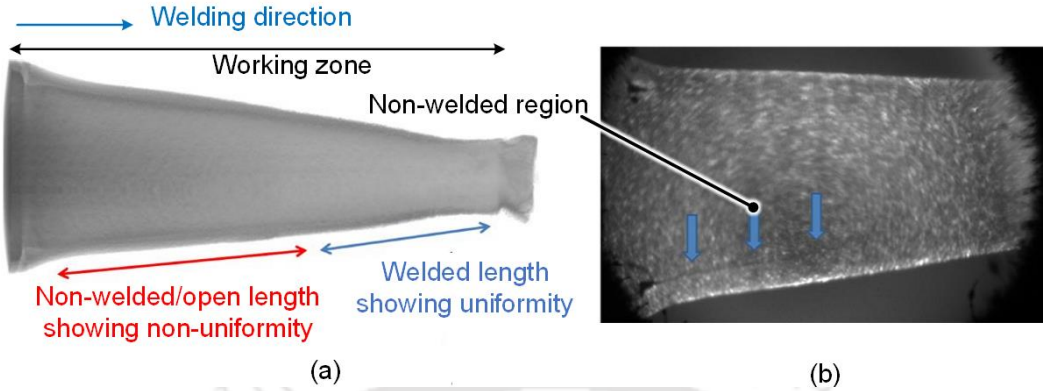

Fig. 8.19 (a) X-ray tomography of one of the samples and (b) high-resolution optical image indicating uniformity in the welded region

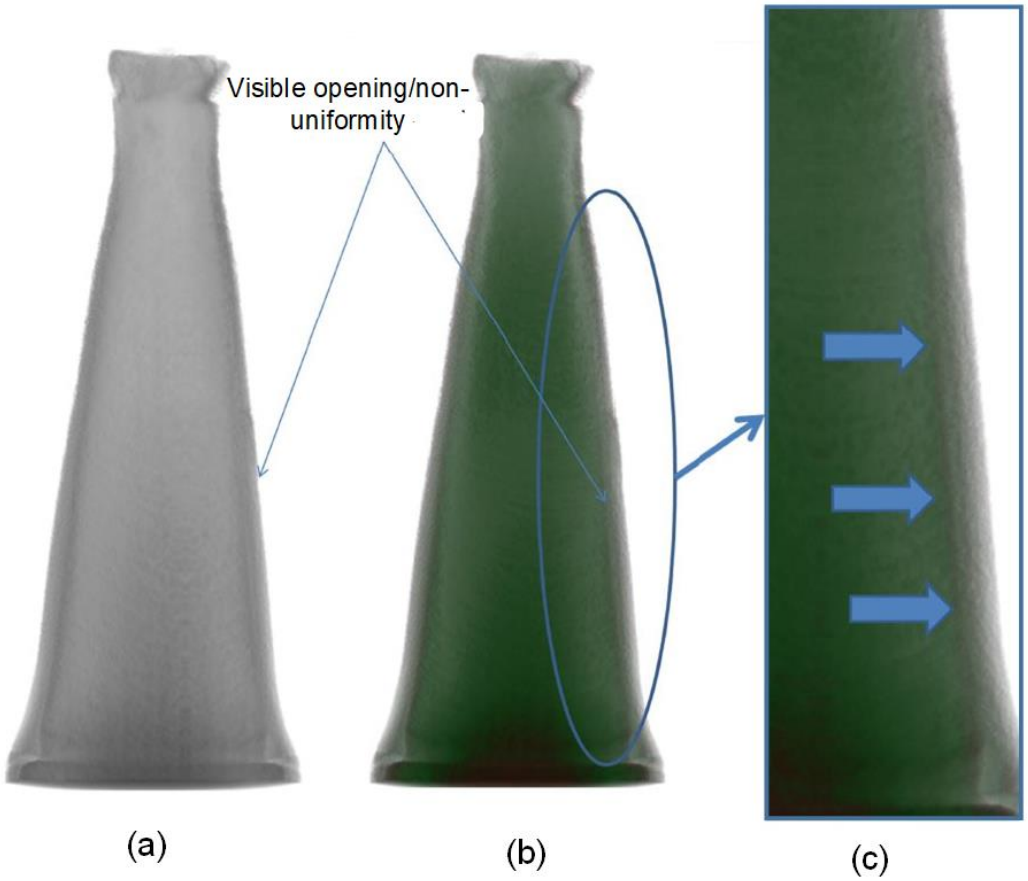

Fig. 8.20 (a) Half-cut sample micro-tomography, (b) reconstructed voxel (volume pixel) of the sample and (c) zoomed view showing opening/non-uniformity in welding at the D9-SS 316LN interface

8.4.7 Optical micrography and Scanning electron microscopy

The integrity of the EMW samples are checked in transverse and longitudinal directions using optical micrography (OM) and scanning electron microscopy. Samples are cut longitudinally and transversely using a WEDM (wire-cut electric discharge) machine to characterise the joint. During the cutting operation, adequate coolant is utilised to avoid any microstructural alterations. After that, silicon carbide (SiC) sheets having grit size in the range of 100-2000 in increasing order are used to ground the samples, followed by abrasive polishing. Fig. 8.21 show two optical micrographs of the D9-SS316 interface at 200 and 500 nm. Weld interface shows wavy morphology. These waviness patterns are caused by the jet from the flyer tube penetrating the target end plug surface at the point of impact. During high-velocity impact, Plastic deformation converts the grains to become semisolid near the interface leading to the hydrodynamic behaviour of metal [34]. Periodic and symmetric waves, comparable to explosive [188] and electromagnetic welding [189], have been shown in wavy morphologies, indicating good joint quality. The unwielded area shows no effect in grain morphologies. However, grains at the interface are severely distorted, mirroring the waviness phenomenon of the weld. Due to fluctuations in the magnetic field, the amplitude and wavelength of the waves alter gradually from the vertical centreline along with the interface EMW of sheets [34]. However, in this tube-to-end plug joining, the field shaper in the working zone produces a uniform magnetic field circumferentially, resulting in a series of homogenous waves with comparable amplitude and wavelength at the weld interface. The wavelength and amplitude are 32 and 73 meters, respectively. The intimate contact area and interlocks between two metal surfaces are increased by these wavy morphologies [34]. The deformation of the D9 tube causes grain refinement at the contact on the D9 side. The interface area is depicted in SEM pictures at various magnifications in Fig. 8.22. Kulkarni et al. [180] have conducted an EDS analysis of the experimental work to determine the composition at the interface area, which they discovered to be a combination of both metals.

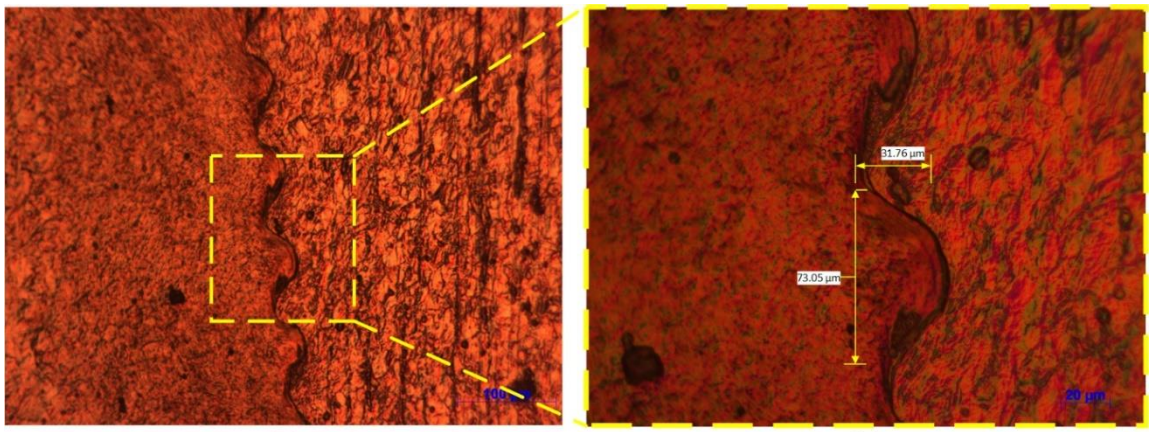

Fig. 8.21 Optical micrographs at (a) 200× and (b) zoomed view at 500× showcasing the waviness pattern at the interface

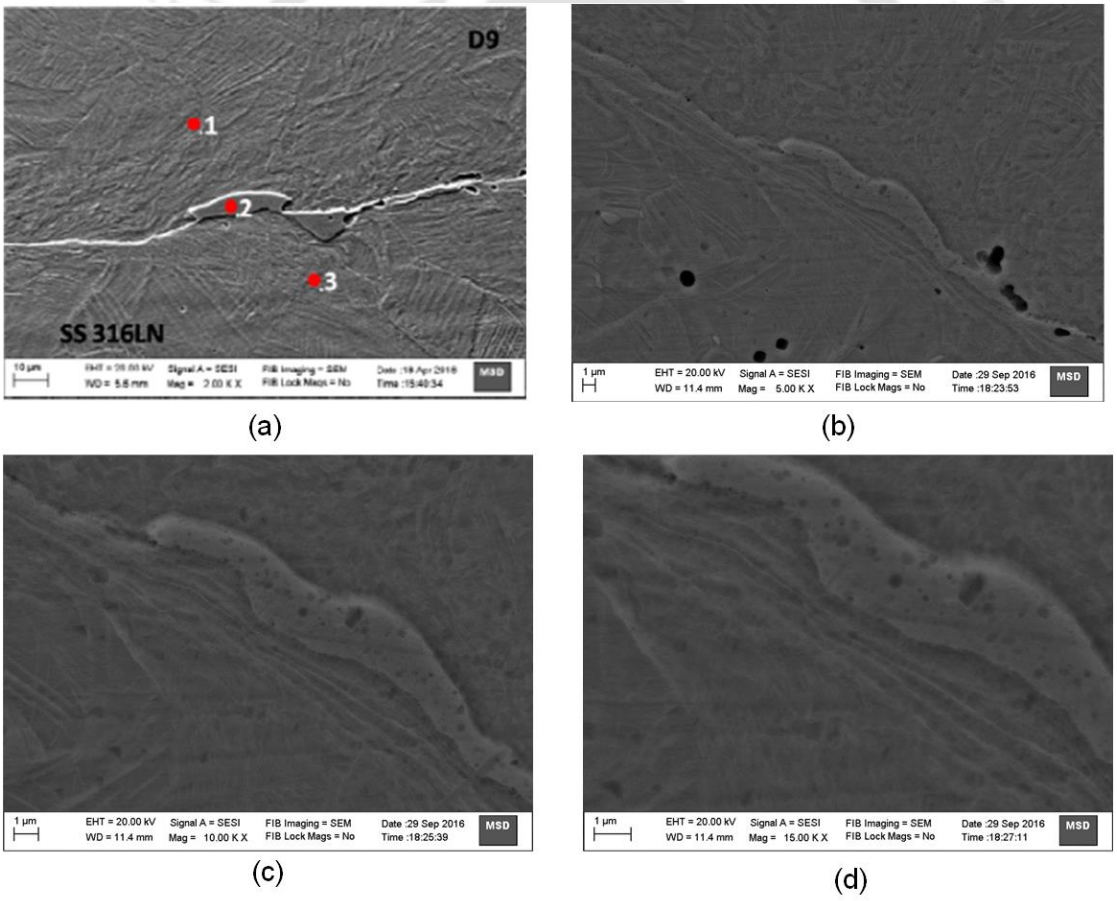

Fig. 8.22 SEM micrographs of the interface between SS 316LN and D9 at (a) 2.0K ×, (b) 5.0 K ×, (c) 10 K × and (d) 15.0 K ×

To analyse the composition or intermixing of materials at the interface in the welded sample, SEM-EDS analysis is also carried across the interface region. The composition in the diffusion zone is observed to be the mixture of both metals as shown in Fig. 8.23. It is

evident that, D9 and SS316LN only have two uncommon elements between them which is Mo and Ti, are present in D9 but absent in SS316LN. EDS measurement shows that that these two elements are present in the mixing zone/diffusion zone, however, no detectable transitions of Ti and Mo are observed in SS316 LN side.

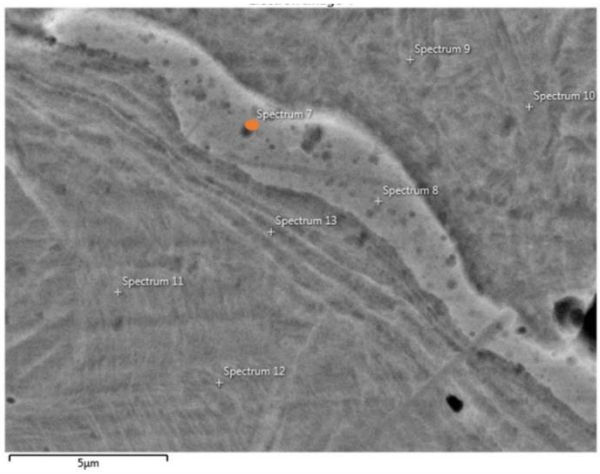

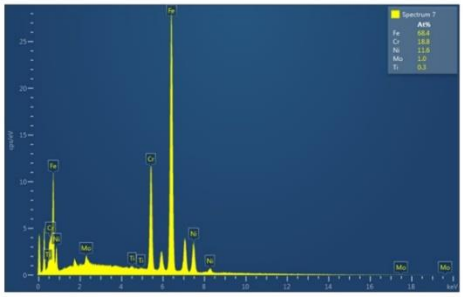

S. No.	Fe	Cr	Ni	Ti	Mo	Phase Identity
7	68.4	18.8	11.6	0.3	1.0	
8	68.8	18.9	11.3	0.2	0.8	

Fig. 8.23 EDS measurement in the D9-SS 316LN interface region showing composition at the interface

8.5 Conclusions

EMW process is used in this chapter to build a D9-SS 316LN tube-to-end plug junction. High-speed, flexible, and high-integrity weld joints are produced using a green and solid-state welding technique. The high-speed impact welding technique is being studied experimentally and simulated. Experimental procedures resulted in a leak-tight junction with wavy interface morphology and no defects. SPH simulation has recreated the same phenomenon. It is possible to draw the following conclusions.

- The Lagrangian mesh-based simulation indicates a good agreement of deformation with experimental results.
- The D9-SS316LN tube-to-end plug interface shows wavy morphology with narrow grain boundary-like bonding interfaces.
- The metal jet emission and weld interface morphology is reproduced successfully using the SPH method.
- The SPH simulation results are validated with the Bahrani-Black-Crossland wave formation mechanism.

- Hydraulic burst tests show failure in the base tube area near the TIG joint and not the EMW area, showcasing the excellent quality of the EMW joint.
- Samples show uniformity in the welded region in the working zone during X-ray tomography.
- OM and SEM analysis have been used to explore further the waviness morphology obtained in the SPH simulation.

Acknowledgement for Experimental work in Chapter 8

The experimental investigations in Chapter 8 have been performed by BARC Mumbai, India and IGCAR Kalpakkam, India. Therefore, we acknowledge the contribution made by Mrs Supriya Barje for the timely preparation of required engineering drawings. We also would like to thank the technical assistance rendered by Mr Rajesh Kakad for conducting the experiments and Dr R. Suresh Kumar, Head HTAS/SMD, IGCAR, for conducting a high pressure-temperature test. Mr.R. K. Rajawat, Head APPD & AD, BTDG, BARC and Dr R. Tewari, Head MSD, BARC, for the encouragement received during the development of this process.

9 Conclusions and Scope of Future Work

9.1 Conclusions

In this thesis, research work is carried out to provide an alternative and effective way to tackle problems being faced in the joining of tubes by EMF. The work carried out will be helpful in the faster industrial adaptation of EMF technology for the joining of tubes. Important conclusions and recommendations from the thesis work are summarised below.

- An improved multi-material Cu-SS tube-to-tube joining has been carried out using the EMC process. The integrity of the joints is studied through the various destructive and non-destructive processes, and the joints with strength higher than the base Cu tube failure strength are obtained at particular discharge energies for threaded and knurled surfaced joints. It has been further established that threaded surfaced joints are most suitable for axial strength considering the ease of manufacturing of threads compared to knurls.
- Furthermore, a strategy of developing FEM models to replicate the complete experimental investigation is adopted to save time and resources and assist in further optimisation of the joint for future works. A coupled FEM model produces results of pull-out and compression tests of smooth surfaced EMC crimped Cu-SS tube-to-tube joint within an error range of 5-7 %.
- Threaded surfaced joints are further investigated by varying the thread pitch and thread angle, and it is observed that in this case, optimum results are obtained with the thread having 60° thread angle and 1 mm thread pitch. The developed non-coupled FEM model produces pull-out strength results within an error range of 2-9 %. The FEM model is further validated by fitting into an empirical relationship.
- A novel hybrid joining technique is developed to overcome the shortcomings of an EMC tube-to-tube joint by combining the EMC process with adhesive joining named as EAAJ. A comparative experimental investigation is performed between EAAJ and EMC process for the smooth-surfaced Cu-SS tube-to-tube joint. An increment in pull-out and compressive strength by 2 to 3 times is observed, along with an improvement in leak tightness by 1000 times in the case of the EAAJ joint compared to EMC joint. Statistical Analysis further clarifies the picture and shows that type of process (EAAJ

and EMC) contributes by 87.57%, and discharge energy contributes by 11.38 % to the pull-out strength of the smooth-surfaced Cu-SS tube-to-tube Joint.

- A detailed experimental investigation further elaborates the EAAJ process to study the effect of various parameters (discharge energy, adhesive application length, types of adhesives and curing time) on EAAJ joint characteristics leading to the optimisation of the process. Adhesive 638, discharge energy of 5.0 kJ, adhesive application length of 5 mm (lowest adhesive application length (25 % of working length)) and curing time of 96 hours is observed to be best suited for highest joint strength and leak tightness. Furthermore, the three-way ANOVA analysis indicates that the contribution of type of adhesives, adhesive application length and discharge energies on the pull-out strength performance in the joint strength of an EAAJ joint are 64.40 %, 9.94 %, and 21.45 %, respectively. The contribution % of discharge energy, adhesive application length, and curing time on an EAAJ joint leak tightness are calculated to be 51.54 %, 28.34 %, and 15.62 %, respectively.
- Furthermore, the third type of EMJ process, namely EMW to join tubular components is also investigated. An SPH-based FEM model is developed for D9 tube-to-SS 316 LN end plug joining by the EMW process, which establishes a weldability window by considering waviness formation as the criteria. The taper angle of 8° and impact velocity of 500 m/s is observed to be optimum. The Lagrangian simulation is validated with experimental deformation results, and the SPH simulation is validated with microstructural results of waviness morphology.

Overall the current work proposes detailed experimental and numerical findings. The results obtained through developed numerical models agree with general findings in experiments that show the prediction capability of developed models. The present study concludes that the EMJ techniques are advantageous for creating multi-material tubular joints. Finally, by modifying the elements in this study, one can commercialise these applications of tube joining by EMF processes. The table below shows the discussed processes to be used depending upon the output requirement and available discharge energy.

Representation of different joining processes to be used depending on the required output

Available EM discharge energy	Required output			Processes to be used
	Joint strength	Leak tightness		
		Moderate ($10^{-8} - 10^{-9}$) (mbarl/sec)	High (10^{-11}) (mbarl/sec)	
Low (3.4 kJ-5.0 kJ)	✓			EMC
Low (3.4 kJ-5.0 kJ)	✓	✓		EAAJ
High (10 kJ-15 kJ)	✓		✓	EMW

9.2 Scope of Future work

Subsequent studies can be done in the current domain to widen the understanding further.

- An analytical methodology can be proposed for the current work to reduce the dependency on the software packages, and such an analytical model can be used in calculating other values like current amplitude and impact velocity before experimentation to predict the
- The present work in chapter 4 and 5 assumes the value of coefficient of friction and caliberate it with experimental output results which can be further improved by performing experimental investigations to calculate the value of coefficient of friction to further improve the simulation results.
- In the present study, the setup is designed based on the literature. However, various aspects of the experimental setup can still be improved. A field shaper which is an essential part of the setup and is used to intensify and concentrate the magnetic field in the working zone, have limitations, as discussed in section 4.3.2 and 7.2.6, due to the slit of the field shaper. Therefore, further investigation can be done to improve the shortcomings.

- Furthermore, in order to be adopted in the industry, understanding setup life is essential. Therefore, an investigation on the life and fatigue damage of disposable field shapers with prolonged application is needed.

List of Publications

- **International Journals**

- **Published / Accepted**

1. **Deepak Kumar**, Sachin D. Kore, Arup Nandy, (2021), "*Finite Element Modeling of Electromagnetic Crimping of Cu-SS Tube-to-Tube Joint along with Simulation of Destructive Testing for Strength Prediction of the Joint*", ASME Journal of Manufacturing Science and Engineering, Volume 143(4), 041004, https://doi.org/10.1115/1.4048431
2. **Deepak Kumar**, Sagar Pawar, Sachin D. Kore, Arup Nandy, (2020), *"Comparison of Coupled and Non-Coupled Finite Element Models for Joining of Cu-SS Tubes by Electromagnetic Forming*", Procedia Manufacturing, Volume 47, 673-677, https://doi.org/10.1016/j.promfg.2020.04.208
3. **Deepak Kumar**, Sachin D. Kore, Arup Nandy, (2020), *"An Interference-Fit Joining of Cu-Ss Composite Tubes by Electromagnetic Crimping for Different Surface Profiles"*, Welding in the World, Volume 65, 1031–1050. https://doi.org/10.1007/s40194-021-01081-8
4. **Deepak Kumar**, Sachin D. Kore, Arup Nandy, (2021), *"Experimental Investigation of Cu-SS Electromagnetically Assisted Adhesive Tube-to-Tube Joining: Its Advantages Over Electromagnetic Crimping"*, International Journal of Adhesion and Adhesives, Volume 109, 102908, https://doi.org/10.1016/j.ijadhadh.2021.102908
5. M. R. Kulkarni, Tanmay Kolge, **Deepak Kumar**, S. D. Kore, Archana Sharma, Voona Srikanth, Arijit Laik, Gopa Chakraborty, Shaju Albert, (2022), "*Magnetic Pulse Welding of D9 Steel Tube to SS316LN End Plug"*, Transaction of Indian Institute of Metals, Volume 75, 171-182, https://doi.org/10.1007/s12666-021-02413-4
6. **Deepak Kumar**, Sachin D. Kore, Arup Nandy, (2022), *"A Study on the Effect of Process Parameters on the Joint Strength and Leak Tightness in Electromagnetically Assisted Adhesive Cu-SS Tube-to-Tube Joining Through Statistical Analysis",* International Journal of Adhesion and Adhesives, Volume 116, 103136, https://doi.org/10.1016/j.ijadhadh.2022.103136

- **Communicated / Under Review**

7. M. R. Kulkarni, **Deepak Kumar**, Arup Nandy, Tanmay Kolge, Sachin D. Kore, R. I. Bakhtsingh, (2022), *"Numerical investigation of Magnetic Pulse Welding of D9 Steel Tube to SS316LN End Plug using Lagrangian Finite Element and Smoothed Particle Hydrodynamics (SPH) and its Experimental Validation",* https://doi.org/10.22541/au.165244698.83840654/v2

8. **Deepak Kumar**, Shafeeque E. S., Sachin D. Kore, Arup Nandy, (2022), *"Electromagnetic Crimping on Threaded Surface: FEM Modelling, Validation and Effects of Pitch and Discharge Energy on Deformation in an Empirical Relation",* https://doi.org/10.48550/arXiv.2105.07165
9. **Deepak Kumar**, Sachin D. Kore, Arup Nandy, *"Joining of Tubes by Electromagnetic Forming: A review*" (Under preparation)

- **Book Chapters**

1. **Deepak Kumar**, Sachin D. Kore, Arup Nandy, (2021), *"Finite Element Modelling of Electromagnetic Crimping of Copper-Stainless Steel Tube-to-Tube Joint"*, In: K. Pandey, R. Misra, P. Patowari, U. Dixit, (eds), Recent Advances in Mechanical Engineering. Lecture Notes in Mechanical Engineering. Springer, Singapore, http://doi.org/10.1007/978-981-15-7711-6_11
2. **Deepak Kumar**, Chinmay Morajkar, Sachin D. Kore, Arup Nandy, (2023) *"Comparison of Two Different Non-Coupled Multi-Step Simulation Techniques for Strength Prediction of an Electromagnetically Crimped Cu-SS Tube-to-Tube Joint with a Smooth Interface*", In: A. Chakrabarti, S. Suwas, M. Arora, (eds), Industry 4.0 and Advanced Manufacturing. Lecture Notes in Mechanical Engineering. Springer, Singapore, https://doi.org/10.1007/978-981-19-0561-2_28
3. **Deepak Kumar**, Sachin D. Kore, Arup Nandy, (2022) *"Electromagnetically Assisted Adhesive Joining: A Novel Hybrid Joining Method",* In: R. Kumar, A. Prasad, A. Kumar, (eds), Smart Manufacturing Processes for Sustainable Development in Industry 4.0 Era, CRC Press- Taylor & Francis (Accepted),

- **Presentations / Conference attended**

1. **Deepak Kumar**, Sachin D. Kore, Arup Nandy, (07-09 February 2020), *"Finite Element Modelling of Electromagnetic Crimping of Copper-Stainless Steel Tube-to-Tube Joint"*, The 1st International Conference on Recent Advancement of Mechanical Engineering, ICRAME 2020, NIT Silchar, India.
2. **Deepak Kumar**, Sagar Pawar, Sachin D. Kore, Arup Nandy, (04-08 May 2020), *"Comparison of Coupled and Non-Coupled Finite Element Models for Joining of Cu-SS Tubes by Electromagnetic Forming"*, 1st Virtual ESAFORM Conference and 23rd International Conference on Material Forming, ESAFORM 2020, Brandenburg University of Technology (BTU) Cottbus-Senftenberg, Cottbus, Germany.

3. Shafeeque E. S., **Deepak Kumar**, Sachin D. Kore, Arup Nandy, (11-12 June 2021), *"Finite Element Modelling of Electromagnetic Crimping on Threaded Surface*", 3rd International Conference on Sustainable Manufacturing, Materials and Technologies, ICSMMT 2021, Coimbatore, India.
4. **Deepak Kumar**, Chinmay Morajkar, Sachin D. Kore, Arup Nandy, (10-11 January 2022), *"Comparison of Two Different Non-Coupled Multi-Step Simulation Techniques for Strength Prediction of an Electromagnetically Crimped Cu-SS Tube-to-Tube Joint with a Smooth Interface"*, 2nd International Conference on Industry 4.0 and Advanced Manufacturing, I-4AM 2022, IISC Bangalore, Karnataka, India.
5. **Deepak Kumar**, Avinash Chetry, Sachin D. Kore, Arup Nandy, (29 June-01 July 2022), *"Study of Interfacial Waviness Formation and Jetting Phenomenon during Magnetic Pulse Welding using Smoothed Particle Hydrodynamics (SPH)",* ME@75 Research Frontiers Conference, IISC Bangalore, India.
6. **Deepak Kumar**, Kunalan Murthy, Sachin D. Kore, Arup Nandy, (28-29 October 2022), "*Effect of Thread Angle besides Pitch and Discharge energy in Electromagnetically Crimped Threaded Surfaced Tube-to-Tube Joint: Experimental and Numerical Investigation along with ANOVA Analysis to Assess the Relative Contribution of the Process Parameter*", 2nd International Conference & Exposition on Mechanical, Material and Manufacturing Technology, ICE3MT2022, Hyderabad, India.
7. Sagar Pawar, **Deepak Kumar**, Sachin D. Kore, Arup Nandy, (28-29 October 2022), "*Effect of Die Conductivity on Electromagnetic Forming of Tube*", 2nd International Conference & Exposition on Mechanical, Material and Manufacturing Technology, ICE3MT2022, Hyderabad, India.

References

[1] Schürmann, H., (2007), Konstruieren mit Faser-Kunststoff-Verbunden. Springer Verlag, https://doi.org/10.1007/978-3-540-72190-1

[2] M. Kleiner, M. Geiger, A. Klaus, (2003), Manufacturing of Lightweight Components by Metal Forming, CIRP Annals, 52 (2), 521-542, https://doi.org/10.1016/S0007-8506(07)60202-9.

[3] Barnes, T. A., Pashby, I. R., (2000), Joining techniques for aluminium spaceframes used in automobiles: Part I — solid and liquid phase welding, Journal of Materials Processing Technology, 99 (1–3), 62-71, https://doi.org/10.1016/S0924-0136(99)00367-2.

[4] Kalpakjian, S., (1995), Manufacturing engineering and technology. Reading, Mass: Addison-Wesley

[5] Barner, K., Luo, X.J., Song, XP et al. Correlation between the trap state spectra and dielectric behaviour of CaCu3Ti4O12. Journal of Materials Research 26, 395–406 (2011). https://doi.org/10.1557/jmr.2010.28

[6] NOBUTADA OHNO, SECTION 4.6 - Kinematic Hardening Rule with Critical State of Dynamic Recovery, Editor(s): JEAN LEMAITRE, Handbook of Materials Behavior Models, Academic Press, 2001, Pages 232-239, https://doi.org/10.1016/B978-012443341-0/50025-9

[7] K. Osakada. Effects of Strain Rate and Temperature in Forming Processes of Metals. Journal de Physique IV Proceedings, 1997, 07 (C3), pp.C3-XXXVII-C3-XLIV. ff10.1051/jp4:1997302ff. ffjpa00255375f] [Rajeev Kapoor, Sia Nemat-Nasser, Determination of temperature rise during high strain rate deformation, Mechanics of Materials, Volume 27, Issue 1, 1998, Pages 1-12, https://doi.org/10.1016/S0167-6636(97)00036-7

[8] Dalai, B., Moretti, M.A., Åkerström, P. et al. Mechanical behaviour and microstructure evolution during high strain rate deformation of AA7075-T651. SN Appl. Sci. 4, 251 (2022). https://doi.org/10.1007/s42452-022-05141-6

[9] Skubisz P, Lisiecki Ł, Paćko M, Skowronek T, Micek P, Tokarski T. Effect of high strain rate beta processing on microstructure and mechanical properties of near-β titanium alloy Ti-10V-2Fe-3Al. Proceedings of the Institution of Mechanical Engineers, Part L: Journal of Materials: Design and Applications. 2018;232(3):181-190. doi:10.1177/1464420715619447

[10] Siliang Yan, He Yang, Hongwei Li, Xuan Yao, Microstructure Evolution and Flow Localization Characteristics of 5A06 Alloy in High Strain Rate Forming Process, Procedia Engineering, Volume 81, 2014, Pages 1198-1203, https://doi.org/10.1016/j.proeng.2014.10.097.

[11] Dewsnap, G. G., (1971). High Energy Rate Forming. In: Beadle, J.D. (eds) Metal Forming. Production Engineering Series. Palgrave, London. https://doi.org/10.1007/978-1-349-01188-9_9

[12] Richardson, D. B., Blanzymski, T. Z., Gregory, E. N., Hutchinson, A. R., Wyatt, L. M., (1994), 16 - Manufacturing methods, Editor(s): Edward H. Smith, Mechanical Engineer's Reference Book (Twelfth Edition), Butterworth-Heinemann, 16-1-16-112, https://doi.org/10.1016/B978-0-7506-1195-4.50020-8.

[13] Woo, M. A., Kim, H. K., Park, H. G., Kim, Y. H., Song, W. J., Kim, J., (2017), Numerical and experimental study on electrohydraulic forming process, Procedia Engineering, 207, 311-316, https://doi.org/10.1016/j.proeng.2017.10.780

[14] Daehn, G., (2006), High-Velocity Metal Forming, Metalworking: Sheet Forming, 14B, ASM Handbook, Edited By S.L. Semiatin, ASM International, 405–418, https://doi.org/10.31399/asm.hb.v14b.a0005127

[15] Maxwell, J., (1873). A Treatise of Electricity and Magnetism. Macmillan and Co. Publishers to the University of Oxford.

[16] Brower, D. H., (1966). Electromagnetic Devices. US Patent 3,231,842.

[17] Lamb, H., (1883), On Electrical Motions in a Spherical Conductor. Philosophical Transactions of the Royal Society of London, 174, 519–549, http://www.jstor.org/stable/109415

[18] Heaviside, O., (1951), Electromagnetic Theory. The Complete & Unabridged Edition.

[19] Psyk, V., Risch, D., Kinsey, B., Tekkaya, A., Kleiner, M., (2011), Electromagnetic forming - a review, Journal of Materials Processing Technology, 211, 787–829, https://doi.org/10.1016/j.jmatprotec.2010.12.012

[20] Lorentz, H., (2013), Versuch einer Theorie der electrischen und optischen Erscheinungen in bewegten Körpern (Cambridge Library Collection - Physical Sciences). Cambridge: Cambridge University Press, https://doi.org/10.1017/CBO9781139381406

[21] Dietz, H., Lippmann, H. J., Schenk, H., (1967), Theorie des Magneform-Verfahrens: Erreichbarer Druck. Elektronische Zeitschrift ETZ-A 88 (9), 217–222

[22] Ethan Thibaudeau, Brad L. Kinsey, (2015), Analytical design and experimental validation of uniform pressure actuator for electromagnetic forming and welding, Journal of Materials Processing Technology, 215, 251-263, https://doi.org/10.1016/j.jmatprotec.2014.08.019

[23] Bruno, E. J., (1968), Ed. High-Velocity Forming of Metals, Rev. Edn., ASTME, Dearborn, Michigan

[24] Belyy, I.V., Fertik, S.M., Khimenko, L.T., (1977), Spravochnik Po Magnitno-impul' Snoy Obrabotke Metallov [Electromagnetic Metal Forming Handbook]. English translation by Altynova, M.M., online available at http://www.mse.eng.ohiostate.edu/~Daehn/metalforminghb/index.html

[25] Bühler, H., von Finckenstein, E., we. Bemessung von Sickenverbindungen für ein Fügen durch Magnetumformung, 104. Werkstatt und Betrieb, 45–51

[26] Bertholdi, W., Daube, J., (1966), Die elektrohydraulische und die elektromagnetische Umformung von Metallen. Urania—Gesellschaft zur Verbreitung wissenschaftlicher Kenntnisse

[27] Erdösi, J., Meinel, M., (1984), Elektrische Hochgeschwindigkeitsbearbeitung. Fertigungstechnik und Betrieb 34 (10), 600–601

[28] Saha, P.K., (2005), Electromagnetic forming of various aircraft components. SAE Technical Papers 114, 999–1009, part 1, https://doi.org/10.4271/2005-01-3307

[29] Wilson, F.W., (1964), High-Velocity Forming of Metals. Prentice-Hall Inc

[30] Balanethiram, V. S., Daehn, G. S., (1994), Hyperplasticity: Increased forming limits at high workpiece velocity, Scripta Metallurgica et Materialia, 30 (4), 515-520, https://doi.org/10.1016/0956-716X(94)90613-0.

[31] Birdsall, D. F., (1961), Magnetic forming! What is it. Am. Mach./Metalwork. Manufacturing, 105 (6), 117-121.

[32] Faes, K., Kwee, I., De Waele W., (2019), Electromagnetic Pulse Welding of Tubular Products: Influence of Process Parameters and Workpiece Geometry on the Joint Characteristics and Investigation of Suitable Support Systems for the Target Tube. Metals, 9(5), 514, https://doi.org/10.3390/met9050514

[33] Zittel, G., (2010), A historical review of high speed metal forming, 4th International Conference on High Speed Forming, March 9th-10th 2010 Columbus, Ohio, USA, 2–15. http://dx.doi.org/10.17877/DE290R-8687

[34] Kapil, A., Sharma, A., (2015), Magnetic pulse welding: an efficient and environmentally friendly multi-material joining technique, Journal of Cleaner Production, 100, 35-58, https://doi.org/10.1016/j.jclepro.2015.03.042.

[35] Aizawa, T., Okagawa, K., Kashani, M., (2013), Application of magnetic pulse welding technique for flexible printed circuit boards (FPCB) lap joints, Journal of Materials Processing Technology, 213 (7), 1095-1102, https://doi.org/10.1016/j.jmatprotec.2012.12.004.

[36] Mori, K., Bay, N., Fratini, L., Micari, F., Tekkaya, A. E., (2013), Joining by plastic deformation, CIRP Annals, Volume 62 (2), 673-694, https://doi.org/10.1016/j.cirp.2013.05.004..

[37] Weddeling, C., Koray O., Peter Haupt, D., Tekkaya, A. E., (2015), Analytical methodology for the process design of electromagnetic crimping, Journal of Materials Processing Technology, 222, 163-180, https://doi.org/10.1016/j.jmatprotec.2015.02.042.

[38] Weddeling, C., Woodward, S. T., Marré, M., Nellesen, J., Psyk, V., Tekkaya, A. E., Tillmann, W., (2011), Influence of groove characteristics on strength of form-fit joints, Journal of Materials Processing Technology, 211 (5), 925-935, https://doi.org/10.1016/j.jmatprotec.2010.08.004.

[39] Sapanathan, T., Raoelison, R. N., Buiron, N., & Rachik, M. (2016), Magnetic Pulse Welding: An Innovative Joining Technology for Similar and Dissimilar Metal Pairs. In (Ed.), Joining Technologies. Intech Open, https://doi.org/10.5772/63525

[40] Rowland, A., (1967), Metal forming by magnetic means. Proceedings of the Conference on Electrical Methods of Machining and Forming, 192-197,

[41] Kumar, R., and Kore, S. D. (September 18, 2019). "Effect of the Field Shaper Geometries in Electromagnetic Crimping of Tubes on Rods." ASME. J. Manuf. Sci. Eng. November 2019; 141(11): 114501. https://doi.org/10.1115/1.4044516

[42] Simoen, B., Faes, K., De Waele, W., (2017), Investigation of the weldability of copper to steel tubes using the electromagnetic welding process, International Journal of Sustainable Construction and Design, 8(1), https://doi.org/10.21825/scad.v8i1.6811

[43] Massalki, T. B., Murray, J. L., Bennet, L. H., Baker, H., and Kacprzak, L., (1986), Binary Alloy Phase Diagrams, American Society for Metals, Metals Park, Ohio, Vols. 1 and 2.

[44] Patra, S., Arora, K., Shome, M., and Bysakh, S., (2017), Interface characteristics and performance of magnetic pulse welded copper-Steel tubes, Journal of Materials Processing Technology, 245, 278-286, https://doi.org/10.1016/j.jmatprotec.2017.03.001.

[45] Shankar, V., Gill, T. P. S., Mannan, S. L., (2003), Sadhana 28, 359. https://doi.org/10.1007/BF02706438

[46] Chard, E., (1998), Welding Metallurgy of Stainless Steels. Springer, New York

[47] Salamati, M., Soltanpour, M., Fazli, A. et al. (2019), Processing and tooling considerations in joining by forming technologies; part A—mechanical joining. International Journal of Advanced Manufacturing Technology, 101, 261–315, https://doi.org/10.1007/s00170-018-2823-y

[48] Lueg-Althoff, J., Lorenz, A., Gies, S., Weddeling, C., Goebel, G., Tekkaya, A.E., Beyer, E., (2014), Magnetic Pulse Welding by Electromagnetic Compression: Determination of the Impact Velocity. Advanced Materials Research, 966–967, 489–499. https://doi.org/10.4028/www.scientific.net/amr.966-967.489

[49] Kumar, R., Kore, S. D., (2018), Studies on Effect of Surface Profiles and Field Shaper Geometries on Electromagnetic Crimping of Tubes on Rods, Doctoral Thesis, IIT Guwahati, India. http://gyan.iitg.ernet.in/handle/123456789/1470

[50] Fan, Z., Yu, H., Meng, F., Li, C., (2016), Experimental Investigation on Fabrication of Al/Fe Bi-Metal Tubes by the Magnetic Pulse Cladding Process, International Journal of Advanced Manufacturing Technology, 83, 1409–1418. https://doi.org/10.1007/s00170-015-7671-4

[51] Kore, S. D., Date, P. P., Kulkarni, S. V., Kumar, S., Rani, D., Kulkarni, M. R., Desai, S. V., Rajwat, R. K., Nagesh, K. V., Chakravarty, D. P., (2011), Application of Electromagnetic Impact Technique for Welding Copper-to-Stainless Steel Sheets, International Journal of Advanced Manufacturing Technology, 54, 949–955. https://doi.org/10.1007/s00170-010-2981-z

[52] Kumar, D., Kore, S. D., Nandy, A., (2022), A Study on the Effect of Process Parameters on the Joint Strength and Leak Tightness in Electromagnetically Assisted Adhesive Cu-SS Tube-to-Tube Joining Through Statistical Analysis, International Journal of Adhesion and Adhesives, 103136. https://doi.org/10.1016/j.ijadhadh.2022.103136

[53] Psyk, V., Risch, D., Kinsey, B., Tekkaya, A. E., Kleiner, M., (2011), Electromagnetic Forming- A Review, Journal of Materials Processing Technology, 211, 787–829. https://doi.org/10.1016/j.jmatprotec.2010.12.012

[54] Bahmani, M., Niayesh, K., Karimi, A., (2009), 3D Simulation of magnetic field distribution in electromagnetic forming systems with field-shaper, Journal of Materials Processing Technology, 209, 2295–2301, https://doi.org/10.1016/j.jmatprotec.2008.05.024

[55] Homberg, W., Marré, M., Beerwald, C., (2006), Kleiner, M. Joining by Forming of Lightweight Frame Structures, Advanced Materials Research, 10, 89–100 https://doi.org/10.4028/www.scientific.net/AMR.10.89

[56] Al-Ahmad, N., (1980), Das Fugen rotationssymmetrischer Formelemente durch Umformen mit Impulsmagnetfeldern. Dr.-Ing. Dissertation, Ingenieurhochschule Zwickau.

[57] Kleiner, M., Brosius, A., (2006), Determination of flow curves at high strain rates using the electromagnetic forming process and an iterative finite element simulation scheme. CIRP Annals, 55, 267–270, https://doi.org/10.1016/S0007-8506(07)60413-2

[58] Eguia I, Zhang P, Daehn GS (2004) Improved crimp-joining of aluminum tubes onto mandrels with undulating surfaces. In: Proceedings of 1st International Conference on High Speed Forming - ICHSF2004, pp 161–170

[59] Park YB, Kim HY, Oh SI (2005) Design of axial/torque joint made by electromagnetic forming, Thin-Walled Structures, Volume 43, Issue 5, 2005, Pages 826-844, https://doi.org/10.1016/j.tws.2004.10.009.

[60] Hwang W S, Kim N H, Sohn H S, Leeb J S Electromagnetic joining of aluminum tubes on polyurethane cores, Journal of Materials Processing Technology, Volume 34, Issues 1–4, 1992, Pages 341-348, https://doi.org/10.1016/0924-0136(92)90126-D.

[61] Marre, M. B. (2004). Einfluss der Geschwin-digkeit beim kraftschlussigen Fugen rohrformiger Werkstucke durch elektromagnetische Kompression. 11.Paderborner.

[62] S. Kore, J. Imbert, Y. Zhou, M. Worswick, 19 - Electromagnetic pulse welding of magnesium to aluminium sheets, Editor(s): Liming Liu, In Woodhead Publishing Series in Welding and Other Joining Technologies, Welding and Joining of Magnesium Alloys, Woodhead Publishing, 2010, Pages 367-379, https://doi.org/10.1533/9780857090423.2.367.

[63] Kleiner, M., Marré, M., Beerwald, C., Homberg, W., Löhe, D., Barreiro, P., & Schulze, V. (2006). Investigation of force-fit joints produced by electromagnetic tube compression. Production Engineering, 13, 227-230.

[64] Cui, J., Wang, S., Yuan, W. et al. Effects of Standoff Distance on Magnetic Pulse Welded Joints Between Aluminum and Steel Elements in Automobile Body. Automotive Innovation 3, 231–241 (2020). https://doi.org/10.1007/s42154-020-00104-2

[65] Messler, W. S., (1995) Joining of advanced materials. SAMPE J 31: 25–30

[66] Hammers T, Marré M, Rautenberg J, Barreiro P, Schulze V, Biermann D, Brosius A, Tekkaya AE (2008), Influence of mandrel's surface and material on the mechanical properties of joints produced by electromagnetic compression. In: Proceedings of the 3rd International Conference on High Speed Forming ICHSF 2008, Dortmund, Germany, pp 245–256. https://doi.org/10.2374/SRI08SP151

[67] W.S. Hwang, J.S. Lee, N.H. Kim, H.S. Sohn, (1993), Joining of copper tube to polyurethane tube by electromagnetic pulse forming, Journal of Materials Processing Technology, Volume 37, Issues 1–4, 83-93, https://doi.org/10.1016/0924-0136(93)90082-H.

[68] Buhler, H. v. (1968), Fugen durch Magnetumformung. Werkstatt und Betrieb 101 (4), 209–215.

[69] Weddeling C, Walter V, Haupt P, Tekkaya AE, Schulze V, André K (2015), Joining zone design for electromagnetically crimped connections, Journal of Materials Processing Technology, Volume 225, 2015, Pages 240-261, https://doi.org/10.1016/j.jmatprotec.2015.06.009.

[70] Weddeling C, Woodward S, Nellesen J, Psyk V, Marré M, Tekkaya AE, Daehn GS, Tillmann W (2010), Development of design principles for form-fit joints in lightweight frame structures. In: Proceedings of 4th International Conference on High Speed Forming-ICHSF-2010, pp 137–148 http://dx.doi.org/10.17877/DE290R-8741

[71] Hammers T, Marré M, Rautenberg J, Barreiro P, Schulze V, Biermann D, Brosius A, Tekkaya AE (2009), Influence of Mandrel's Surface and Material on the Mechanical Properties of Joints Produced by Electromagnetic Compression. Steel Research International, volume 80, Issue 5, 366–375. https://doi.org/10.2374/SRI08SP151

[72] Psyk, V., Tekkaya, A.E., (2009), Significance of semi-finished part properties regarding the forming result of electromagnetic compression processes. In: Proceedings of the 6th international conference on electromagnetic processing of materials, Dresden. Pp. 715-718

[73] Ramesh kumar, Kore, S. D. (2018), Effects of surface profiles on the joint formation during magnetic pulse crimping in tube-to-rod configuration. International Journal of Precision Engineering and Manufacturing volume 18 (8), 1181-1188. https://doi.org/10.1007/s12541-017-0138-9

[74] Ramesh Kumar, Kore, S. D. (2018), Electromagnetic Crimping in Tube-to-Cylinder Configuration: Influence of the Base Profiles on the Joint Quality. Journal of Testing and Evaluation 46 (3) https://doi.org/10.1520/JTE20160531

[75] Buhler H., E. v. (1969), Beitrag zur Herstellung von Ummantelungen und Sickenverbindungen rohrformiger Teile durch Magnetumformung. Bander Bleche Rohre 10 (7), 413–418.

[76] Kumar, R., Rajak, A. K., Kore, S. D, Numerical and Experimental Study of Electromagnetic Crimping, 8th International Conference on High Speed Forming, ICHSF 2018, http://dx.doi.org/10.17877/DE290R-19058

[77] Ashish Kumar Rajak, Sachin D. Kore, (2018), Numerical simulation and experimental study on electromagnetic crimping of aluminium terminal to copper wire strands, Electric Power Systems Research, Volume 163, Part B, 744-753, https://doi.org/10.1016/j.epsr.2017.08.014.

[78] D. Kaushik and M. J. Thomas, (2020), Numerical Modelling and Analysis of the Effects of Process Parameters on Pulsed Electromagnetic Crimping, IEEE International Conference on Plasma Science (ICOPS), 2020, pp. 351-351, https://doi.org/10.1109/ICOPS37625.2020.9717416.

[79] Khadija Sofi, Mohammed Hamzaoui, Hassan El Idrissi, Ahmed Nait Sidi Moh, Denis Jouaffre, Abdelkrim Hamzaoui, (2020), Electromagnetic pulse generator: An analytical and numerical study of the Lorentz force in tube crimping processes, CIRP Journal of Manufacturing Science and Technology, 31, 108-118, https://doi.org/10.1016/j.cirpj.2020.10.002

[80] Bühler, H., Bauer, D., (1968), Ein Beitrag zur Magnetumformung rohrförmiger Werkstücke. Werkstatt und Betrieb 110 (9), 513–516

[81] Golovashchenko, S., (2001), Methodology of design of pulsed electromagnetic joining of tubes. In: Proceedings of the 2nd Global Symposium on Innovation in Material Processing and Manufacturing: Sheet Materials, TMS Annual Meeting, New Orleans

[82] Golovashchenko S (2001), Methodology of design of pulsed electromagnetic joining of tubes. In: Proceedings of the 2nd Global Symposium on Innovation in Material Processing and Manufacturing: Sheet Materials. TMS Annual Meeting, New Orleans

[83] Vanhulsel, P. & Van Wonterghem, M. & De Waele, W. & Faes, K., (2011), Groove design for form fit joints made by electromagnetic pulse crimping, International Journal of Sustainable Construction and Design 2(3), p.432-441. https://doi.org/10.21825/scad.v2i3.20535

[84] Brown,W.F., Bandas, J., Olson, N.T., (1978), Pulsed magnetic welding of breeder reactor fuel pin and closures. In: Proceedings of the AWS 59th Annual Meeting , New Orleans, USA

[85] Shribman, V., Tomer, Y., (2006), Magnetic pulse technology for improved tube joining and forming. Tube & Pipe Technology, 91–95.

[86] Hisashi, S., Isao, S., Sherif, R., Hidekazu, M., (2009), Numerical study of joining process in magnetic pressure seam welding. Transactions of JWRI 38 (1), 63–68

[87] Uhlmann, E., Ziefle, A., (2010), Modelling pulse magnetic welding processes—an empirical approach. In: Proceedings of the 4th International Conference on High Speed Forming—ICHSF 2010 , Columbus, pp. 108–116, online available at https://eldorado.tu-dortmund.de/handle/2003/27193.

[88] Kore, S.D., Imbert, J., Worswick, M.J., Zhou, Y., (2009), Electromagnetic impact welding of Mg to Al sheets. Science and Technology of Welding and Joining 14 (6), 549–553 https://doi.org/10.1179/136217109X449201

[89] Z. Fan, H. Yu, C. Li, (2016), Interface and grain-boundary amorphisation in the Al/Fe bimetallic system during pulsed-magnetic-driven impact, Scripta. Materialia. 110, 14–18. https://doi.org/10.1016/j.scriptamat.2015.07.035

[90] Wu, X., and Shang, J. (2014), An Investigation of Magnetic Pulse Welding of Al/Cu and Interface Characterization, ASME. Journal of Manufacturing Science and Engineering, 136(5), 051002. https://doi.org/10.1115/1.4027917

[91] Okagawa, K., Aizawa, T., (2004), Impact seam welding with magnetic pressure for aluminum sheets. Material Science Forum 465–466, 231–236 https://doi.org/10.4028/www.scientific.net/MSF.465-466.231

[92] Göbel, G., Kaspar, J., Herrmannsdörfer, T., Brenner, B., Beyer, E., (2010), Insights into intermetallic phases on pulse welded dissimilar metal joints. In: Proceedings of the 4th International Conference on High Speed Forming—ICHSF 2010 , Columbus, pp. 127–136, online available at https://eldorado.tudortmund.de/bitstream/2003/27191/1/17.pdf.

[93] H. Geng, J. Mao, X. Zhang, G. Li, J. Cui, (2019), Formation mechanism of transition zone and amorphous structure in magnetic pulse welded Al-Fe joint, Materials. Letters. 245, 151–154. https://doi.org/10.1016/j.matlet.2019.02.118

[94] Kore, S.D., Date, P.P., Kulkarni, S.V., (2007), Effect of process parameters on electromagnetic impact welding of aluminum sheets. International Journal of Impact Engineering 34, 1327–1341 https://doi.org/10.1016/j.ijimpeng.2006.08.006

[95] Kore, S.D., Date, P.P., Kulkarni, S.V., Kumar, S., Rani, D., Kulkarni, M.R., Desai, S.V., Rajawat, R.K., Nagesh, K.V., Chakravarty, D.P., (2009), Electromagnetic impact welding of copper-to-copper sheets. International Journal of Material Forming, 3, 117–121. https://doi.org/10.1007/s12289-009-0661-z

[96] Watanabe, M., Kumai, S., Aizawa, T., (2006), Interfacial microstructure of magnetic pressure seam welded Al–Fe, Al–Ni, and Al–Cu lap joints. Materials Science Forum (Vols. 519–521, pp. 1145–1150). Trans Tech Publications, Ltd. https://doi.org/10.4028/www.scientific.net/msf.519-521.1145

[97] Elsen, A., Ludwig, M., Schaefer, R., Groche, P., (2010), Fundamentals of EMPTwelding. In: Proceedings of the 4th International Conference on High Speed Forming—ICHSF 2010 , Columbus, pp. 117–126, online available at https://eldorado.tu-dortmund.de/handle/2003/27192

[98] Nassiri, A., Chini, G., Kinsey, B., Spatial stability analysis of emergent wavy interfacial patterns in magnetic pulsed welding, CIRP Annals, Volume 63, Issue 1, 2014, Pages 245-248, https://doi.org/10.1016/j.cirp.2014.03.023.

[99] Cui, J., Sun, G., Li, G., Xu, Z., Chu, P.K., (2014), Specific wave interface and its formation during magnetic pulse welding. Applied Physics. Letter 105, 221901 https://doi.org/10.1063/1.4903044

[100] Ben-Artzy, A., Stern, A., Frage, N., Shribman, V., Sadot, O., (2010), Wave formation mechanism in magnetic pulse welding. International Journal of Impact Engineering 37(4), 397–404 https://doi.org/10.1016/j.ijimpeng.2009.07.008

[101] Lee, K.J., Kumai, S., Arai, T., Aizawa, T., (2007), Interfacial microstructure and strength of steel/aluminum alloy lap joint fabricated by magnetic pressure seam welding. Material Science and Engineering A 471, (1-2) 95-101. https://doi.org/10.1016/j.msea.2007.04.033

[102] Psyk, V., Gershteyn, G., Demir, O.K., Brosius, A., Tekkaya, A., Schaper, M., Bach, Fr.- W., (2008), Process analysis and physical simulation of electromagnetic joining of thin-walled parts. In: Proceedings of the 3rd International Conference on High Speed Forming ICHSF—2008, Dortmund, pp. 181–190, https://eldorado.tu-dortmund.de/handle/2003/27091

[103] Aizawa, T., Matsuzawa, K., Okogawa, K., Ishibashi, M., (2014), Parallel seam welding of aluminum sheets by magnetic pulse welding method with collision between metal jets. Materials Science Forum 767, 171-176. https://doi.org/10.4028/www.scientific.net/MSF.767.171

[104] Stern, A., Aizenshtein, M., Moshe, G., Cohen, S.R., Frage, N., 2013. The nature of interfaces in Al-1050/Al-1050 and Al-1050/Mg-AZ31 couples joined by magnetic pulse welding (MPW). Journal of Materials Engineering and Performance 22, 2098-2103 https://doi.org/10.1007/s11665-013-0481-7

[105] Raoelison, R.N., Racine, D., Zhang, Z., Buiron, N., Marceau, D., Rachik, M., (2014), Magnetic pulse welding: interface of Al/Cu joint and investigation of intermetallic formation effect on the weld features. Journal of Manufacturing processes 16 (4), 427-434. https://doi.org/10.1016/j.jmapro.2014.05.002

[106] Zhang, Y., Babu, S., Prothe, C., Blakely, M., Kwasegroch, J., LaHa, M., Daehn, G.S., (2011), Application of high velocity impact welding at varied different length scales. Journal of Materials Processing Technology 211 (5), 944–952. https://doi.org/10.1016/j.jmatprotec.2010.01.001

[107] Haiping, Y.U., Zhidan, X.U., Zhisong, F., Zhixue, Z., Chunfeng, L.I., (2013), Mechanical property and microstructure of aluminum alloye steel tubes joint by magnetic pulse welding. Material Science and Engineering A 561, 259-265. https://doi.org/10.1016/j.msea.2012.11.015

[108] Haiping, Y.U., Zhisong, F., Chunfeng, L.I., (2014), Magnetic pulse cladding of aluminium alloy on mild steel tube. Journal of Materials Processing Technology 214 (2), 141-150. https://doi.org/10.1016/j.jmatprotec.2013.08.013

[109] Faes, K., Baaten, T., De Waele, W., & Debroux, N. (2010), Joining of copper to brass using magnetic pulse welding. In Proceedings of th 4th International conference on High Speed Forming (pp. 84–96). Dortmund, Germany: Technische Universität Dortmund. Institut für Umformtechnik.

[110] Gallio G, Lombardi M, Rovarino D, Fino P, Montanaro L. Influence of the mechanical behaviour of different adhesives on an interference-fit cylindrical joint. International journal of adhesion and Adhesives 2013;47:63–68. https://doi.org/10.1016/j. ijadhadh.2013.09.021

[111] Schmidt, V., 1976. Untersuchung der magnetischen Induktion, Stromdichte und Kraft-wirkung bei der Magnetumformung. Dr.-Ing.-Dissertation, Universität Stuttgart

[112] Alf, F., (1963), Verfahren zur Verminderung der bei der Metallumformung durch Magnetfelder erforderlichen Kräfte. Auslegeschrift, 1157320

[113] Uhlmann, E., Hahn, R., (2003), Pulsed magnetic hot forming of magnesium profiles. Production Engineering 10 (2), 87–90

[114] Yu, H. and Li, C., (2007), "Effect of Coil Length on Tube Compression in Electromagnetic Forming," Trans. Nonferrous Met. Soc. China, 17(6), pp. 1270-1275. https://doi.org/10.1016/S1003-6326(07)60261-1

[115] Yu, H., Li C., Liu, D., and Mei, X., (2010), "Tendency of Homofeneous Radial Deformation During Electromagnetic Compression of Aluminium Tube," Trans. Nonferrous Met. Soc. China, 20(1), pp. 7-13. https://doi.org/10.1016/S1003-6326(09)60089-3

[116] Yu, H., (2006), "Buckling Criteriation and Deformation Analysis of Electromagnetic Tube Compression [D]," Harbin Institute of Technology, Harbin, pp. 70-71. (in Chinese)

[117] Yu, H., Li, C., Zhao, Z., and Li, Z., (2005), "Effect of Field Shaper on Magnetic Pressure in Electromagnetic Forming," J. Mater. Process. Technol., 168(2), pp. 245-249. https://doi.org/10.1016/j.jmatprotec.2005.01.001

[118] Khan, M. R., Hossain, M. M., Sharma, A., and Kumar, S., (2019), "Predicting the Effect of Field Shaper in Electromagnetic Welding Using FEM," Arab J. Sci. Eng., 44, pp. 1129-1136. https://doi.org/10.1007/s13369-018-3430-9 220

[119] Bahmani, M., Niayesh, K., and Karimi, A., (2009), "3D Simulation of Magnetic Field Distribution in Electromagnetic Forming Systems with Field-Shaper," J. Mater. Process. Technol., 209, pp. 2295-2301. https://doi.org/10.1016/j.jmatprotec.2008.05.024

[120] Zhang, P., Kimchi, M., Shao, H., Gould, J. E., and Daehn, G. S., (2004), "Analysis of the Electromagnetic Impulse Joining Process with a Field Concentrator," AIP Conference Proceedings, 712(1), 1253. https://doi.org/10.1063/1.1766701

[121] Junjia Cui, Guangyong Sun, Junrui Xu, Zhidan Xu, Xiaodong Huang, Guangyao Li, A study on the critical wall thickness of the inner tube for magnetic pulse welding of tubular Al–Fe parts, Journal of Materials Processing Technology, Volume 227, 2016, Pages 138-146, https://doi.org/10.1016/j.jmatprotec.2015.08.008.

[122] Joern Lueg-Althoff, Joerg Bellmann, Soeren Gies, Sebastian Schulze, A. Erman Tekkaya, Eckhard Beyer, Influence of the flyer kinetics on magnetic pulse welding of tubes, Journal of Materials Processing Technology, Volume 262, 2018, Pages 189-203, https://doi.org/10.1016/j.jmatprotec.2018.06.005.

[123] ASTM International. (2016) E8/E8M-16a Standard test methods for tension testing of metallic materials. West Conshohocken. https://doi.org/10.1520/E0008_E0008M-16A

[124] Faes, K., Waele, W. D., Müller, M., Cramer, H. (2014) Design of electromagnetic pulse crimp torque joints. Proceedings of the 6th International Conference on High Sped Forming ICHSF 2014, Daejon, Korea. 39-50.

[125] Fazzolari, F., A., 2 - Sandwich Structures, Editor(s): Haim Abramovich, (2017) Stability and Vibrations of Thin Walled Composite Structures, Woodhead Publishing, Pages 49-90, ISBN 9780081004104, https://doi.org/10.1016/B978-0-08-100410-4.00002-8.

[126] Rosato, D., Rosato, D., 4 - PRODUCT DESIGN, Editor(s): Dominick Rosato, Donald Rosato, (2003) Plastics Engineered Product Design, Elsevier Science, Pages 198-343, https://doi.org/10.1016/B978-185617416-9/50005-3.

[127] Zhidan Xu, Junjia Cui, Haiping Yu, Chunfeng Li, Research on the impact velocity of magnetic impulse welding of pipe fitting, Materials & Design, Volume 49, 2013, Pages 736-745, ISSN 0261-3069, https://doi.org/10.1016/j.matdes.2012.12.059.

[128] Hassan A. Abdulhadi, Syarifah N. Aqida, Izwan Ismail, (2019) Tool Failure in Die Casting, Reference Module in Materials Science and Materials Engineering, Elsevier, ISBN 9780128035818, https://doi.org/10.1016/B978-0-12-803581-8.10483-7.

[129] L'Eplattenier, P., Cook, G., Ashcraft, C., Burger, M., Imbert, J., and Worswick, M., 2009, "Introduction of an Electromagnetism Module in LSDYNA for Coupled Mechanical-Thermal-Electromagnetic Simulations," Steel Res. Int., 80(5), pp. 351–358.

[130] Neugebauer, R., Psyk, V., and Scheffler, C., 2012, "Simulation of Electromagnetically Formed Joints," 5th International Conference on High Speed Forming, Dortmund, Germany, April, pp. 219-228 http://dx.doi.org/10.17877/DE290R-14394

[131] Neugebaeur, R, Bouzakis, K.-D., Denkena, B., Klocke, F., Sterzing, A., Tekkaya, A. E., and Wertheim, R., 2011, "Velocity Effects in Metal Forming and Machining Processes," CIRP Ann. Manuf. Techn., 60(2), pp. 627-650.

[132] Maria, C., 2009, Technology of EHIS (Stamping) Applied to Production of Automotive Parts. Saint-Petersburg State Polytechnical University, Department of Applied Mathematics.

[133] Eric, A. S., and Steven, J. H., 2008, "The Use of LS-DYNA® Models to Predict Containment of Disk Burst Fragments," 10th International LS-DYNA® Users Conference, Michigan, USA. 221 Ls-Dyna Keyword User's Manual Version 971, Livermore Software Technology Corporation, Livermore, 2007.

[134] NIST/SEMATECH e-Handbook of Statistical Methods, 2012, p. 2.6.5.2.2.

[135] Amancio-Filho S, Santos J., 2009, "Joining of polymers and polymer–metal hybrid structures: recent developments and trends," Polymer Engineering and Science" pp. 1461–76. https://doi.org/10.1002/pen.21424

[136] Petrie., E. M., 2007, Handbook of Adhesives and Sealants, Second Edition (The McGraw-Hill Companies, Inc.). https://www.accessengineeringlibrary.com/content/book/9780071479165

[137] Martinsen K, Hu SJ, Carlson BE., 2015, "Joining of dissimilar materials," CIRP Ann – Manuf Technol, 64, pp. 679–99. http://dx.doi.org/10.1016/j.cirp.2015.05.006

[138] da Silva LFM, Pirondi A, O.chsner A, editors. 2011, Hybrid adhesive joints, 6. Berlin, Heidelberg: Springer Berlin Heidelberg; http://dx.doi.org/10.1007/978-3-642- 16623-5

[139] Gallio, G., Lombardi, M., Rovarino, D., Fino, P., Montanaro, L., 2013, "Influence of the mechanical behaviour of different adhesives on an interference-fit cylindrical joint," Int J Adhes Adhes, 47,pp.63-68. https://doi.org/10.1016/j.ijadhadh.2013.09.021

[140] Ufferman, B., Abke, T., Barker, M., Vivek, A., Daehn, G. S., 2018, "Mechanical properties of joints in 5052 aluminum made with adhesive bonding and mechanical fasteners," Int J Adhes Adhes, 83, pp. 96-102. https://doi.org/10.1016/j.ijadhadh.2018.02.030

[141] Meschut G, Janzen V, Olfermann T., 2014, "Innovative and highly productive joining technologies for multi-material lightweight car body structures." J Mater Eng Perform, 23, pp. 1515–23. http://dx.doi.org/10.1007/s11665-014-0962-3

[142] Gallio, G., Marcuccio, G., Bonisoli, E., Tornincasa, S., Pezzini, D., Ugues, D., Lombardi, M., Rovarino, D., Fino, P., Montanaro, L., 2014, "Study of the interference contribution on the performance of an adhesive bonded press-fitted cylindrical joint," Int J Adhes Adhes, 53, pp. 89-96, https://doi.org/10.1016/j.ijadhadh.2014.01.008.

[143 Kawamura, H., Sawa, T., Yoneno, M., Nakamura, T., 2003, "Effect of fitted position on stress distribution and strength of a bonded shrink fitted joint subjected to torsion," Int J Adhes Adhes, 23, pp.131–40. https://doi.org/10.1016/S0143-7496(03)00005-8

[144] Dragoni, E., Mauri P., (2002), Cumulative static strength of tightened joints bonded with anaerobic adhesives, Proc Inst Mech Eng Pt L J Mater Des Appl, 216(1), pp. 9-15. https://doi.org/10.1177/146442070221600102

[145] Corigliano, P., Ragni, M., Castagnetti, D., Crupi, V., Dragoni, E., Guglielmino, E., (2019), Measuring the static shear strength of anaerobic adhesives in finite thickness under high pressure, Journal of Adhesion, https://doi.org/10.1080/00218464.2019.1704271

[146] Ragni, M., Castagnetti, D., Dragoni, E., (2018), Experimental validation of a simple shear strength model for hybrid friction-bonded interfaces," International Journal of Adhesion and Adhesives , 83, pp. 130-136. https://doi.org/10.1016/j.ijadhadh.2018.02.026.

[147] Castagnetti, D., Dragoni, E., (2016), Experimental Investigation and Model Validation of the Shear Strength of Hybrid Interfaces up to Complete Failure, Journal of Adhesion, 92:7-9, pp. 679-697. https://doi.org/10.1080/00218464.2015.1115740

[148] Castagnetti, D., Dragoni, E., (2014), Adhesively-bonded friction interfaces: Macroscopic shear strength prediction by microscale finite element simulations, International J Adhes Adhes, 53, pp. 57-64. https://doi.org/10.1016/j.ijadhadh.2014.01.016.

[149] Castagnetti, D., Dragoni, E., (2013), Experimental Assessment of a Micro-Mechanical Model for the Static Strength of Hybrid Friction-Bonded Interfaces, J Adhes, 89:8, pp. 642-659. https://doi.org/10.1080/00218464.2012.747179

[150] Dragoni, E., Mauri, P., (2000), Intrinsic static strength of friction interfaces augmented with anaerobic adhesives, Int J Adhes Adhes, 20(4), pp. 315-321. https://doi.org/10.1016/S0143-7496(99)00062-7.

[151] Dario Croccolo, Massimiliano De Agostinis, Pierfranco Mauri, Giorgio Olmi, (2014), Influence of the engagement ratio on the joint strength of press fitted and adhesively bonded specimens, Int J Adhes Adhes, 53, 80-88, ISSN 0143-7496, https://doi.org/10.1016/j.ijadhadh.2014.01.017.

[152] Croccolo, D., Agostinis, M. D., Fini, S., Olmi, G., Paiardini, L., Robusto, F., (2020), "Influence of the interference level and of the assembly process on the shear strength of loctite 648 anaerobic adhesive," Journal of Adhesion, 96(1-4), pp. 90-112. https://doi.org/10.1080/00218464.2019.1681268

[153] https://www.henkel-adhesives.com/ (accessed on 18th October 2020)

[154] S. Kalpakjian and S. R. Schmid, (1992), Manufacturing Processes for Engineering Materials, 2nd Ed. Addison-Wesley Publishing Company, New York, USA,

[155] J. Renart, J. Costa, C. Sarrado, S. Budhe, A. Turon, A. Rodríguez-Bellido, (2015), 5 - Mode I fatigue behaviour and fracture of adhesively-bonded fibre-reinforced polymer (FRP) composite joints for structural repairs, Editor(s): A.P. Vassilopoulos, Fatigue and Fracture of Adhesively-Bonded Composite Joints, Woodhead Publishing, 121-147, ISBN 9780857098061, https://doi.org/10.1016/B978-0-85709-806-1.00005-7.

[156] Adhesive handbook third edition, Sina Ebnesajjad and Arthur H. Landrock, https://doi.org/10.1016/C2013-0-18392-4

[157] A. Sethuramiah, Rajesh Kumar, Chapter 3 - Dry Wear Mechanisms and Modeling, Editor(s): A. Sethuramiah, Rajesh Kumar, Modeling of Chemical Wear, Elsevier, 2016, Pages 41-68, https://doi.org/10.1016/B978-0-12-804533-6.00003-2.

[158] B19 - Wear mechanisms, Editor(s): M.J. Neale, Lubrication and Reliability Handbook, Butterworth-Heinemann, 2001, Pages 1-3, https://doi.org/10.1016/B978-075065154-7/50113-3.

[159] "Air Under Water (AUW) - Bubble test and immersion leak testing," ATC inc., [Online]. Available: http://www.atcinc.net/bubble-test.asp.

[160] A. Loosveld , W. De Waele , K. Faes and O. Zaitov, (2012), Leak tigtness of magnetic pulsed crimped joints, Maters thesis, Ghent university, Belgium. https://doi.org/10.21825/scad.v3i3.20580

[161] D. Croccolo, M. de Agostinis & N. Vincenzi (2011), Experimental Analysis of Static and Fatigue Strength Properties in Press-Fitted and Adhesively Bonded Steel–Aluminium Components, Journal of Adhesion Science and Technology, 25:18, 2521-2538, https://doi.org/10.1163/016942411X580207

[162] J. Renart, J. Costa, C. Sarrado, S. Budhe, A. Turon, A. Rodríguez-Bellido, 5 - Mode I fatigue behaviour and fracture of adhesively-bonded fibre-reinforced polymer (FRP) composite joints for structural repairs, Editor(s): A.P. Vassilopoulos, Fatigue and Fracture of Adhesively-Bonded Composite Joints, Woodhead Publishing, 2015, Pages 121-147, https://doi.org/10.1016/B978-0-85709-806-1.00005-7.

[163] Mannan, S.L., Chetal, S.C., Raj, B. and Bhoje, S.B. (2003) Selection of Materials for Prototype Fast Breeder Reactor. Transactions-Indian Institute of Metals, 56, 155-178.

[164] Babkin L T, albertov K K, Sannikov D V, Yashunskii A Y, Peslyak O K, Sealing of fuel elements for nuclear reactors by resistance butt welding, Welding International, Volume 14 (2), 2000. 162-164 https://doi.org/10.1080/09507110009549158

[165] Harinath Y V, Gopal K A, Murugan S, Albert S K, Journal of Nuclear Materials 435 (1-3) (2013) 32-40. https://doi.org/10.1016/j.jnucmat.2012.12.023.

[166] Murugan A, Sai S R, Raju R, Lakshminarayanan A K, Albert S K, (2017), Adv Electron Forum 24, 40. https://doi.org/10.4028/www.scientific.net/aef.24.40

[167] Cui, J.; Sun, G.; Li, G.; Xu, Z.; Chu, P.K. (2014), Specific wave interface and its formation during magnetic pulse welding. Applied Physics Letter 105, 221901.

[168] Shankar, V., Gill, T.P.S., Mannan, S.L. et al. (2003), Solidification cracking in austenitic stainless-steel welds. Sadhana 28, 359–382 https://doi.org/10.1007/BF02706438

[169] chard E.: Welding metallurgy of stainless steels, Springer Verlag, New York, 1998.

[170] Brooks J.A. and Thompson A.W.: Microstructural development and solidification cracking susceptibility of austenitic stainless-steel welds, International Materials Reviews, 1991, vol. 36, no. 1, pp. 16-44.

[171] Srinivasan, G., Divya, M., Albert, S.K. et al. (2010), Study of Hot Cracking Behaviour of Nitrogen-Enhanced Austenitic Stainless Steels using Varestraint and Hot Ductility Tests. Weld World 54, R322–R332, https://doi.org/10.1007/BF03266746

[172] S. Noh, R. Kasada, N. Oono, N. Iwata, and A. Kimura: Fusion Eng. Des., (2010), vol. 85, pp. 1033–37

[173] Raoelisona RN, Sapanathan T, Buiron N, Rachik M (2015), Magnetic pulse welding of Al/Al and Al/Cu metal pairs: consequences of the dissimilar combination on the interfacial behaviour during the welding process. Journal of Manufacturing and Process, 20, 112–127. https://doi.org/10.1016/j.jmapro.2015.09.003

[174] R. Shotri, K. Faes, A. De, (2020), Magnetic pulse welding of copper to steel tubes–Experimental investigation and process modelling, Journal of Manufacturing Processes, 58, 249-258, https://doi.org/10.1016/j.jmapro.2020.07.061.

[175] Nikolaos E. Karkalos, Angelos P. Markopoulos, (2018), Determination of Johnson-Cook material model parameters by an optimisation approach using the fireworks algorithm, Procedia Manufacturing, 22, Pages 107-113, ISSN 2351-9789, https://doi.org/10.1016/j.promfg.2018.03.017.

[176] Do Young Kim, Dong Min Kim, OBum Kwon, Hyung Wook Park, (2021), Simulation of the round insert face milling process of AISI 316LN stainless steel with machining-based plastic behavior modelling, Proc IMechE Part B: J Engineering Manufacture, Vol. 235(3) 443–454, https://doi.org/10.1177/0954405420958845

[177] Kumar, S., Dey, G.K., & Sharma, A. (2019), An Investigation on Weldability of Flared D9 Tube to Cylindrical SS316L (N) Plug Using Electro-Magnetic Compression Welding. Open Access Library Journal, Vol.6 No.5, 2019 DOI: 10.4236/oalib.1105465

[178] Kumar, S., Dey, G.K. and Sharma, A. (2020), Optimisation of Process Parameters in Electromagnetic Welding of D9 Tube to SS316 L (N) Plug. Open Access Library Journal, 7: e6346. https://doi.org/10.4236/oalib.1106346

[179] 43. Furth,H.P., Levinne,M.A. and Waniek,R.W., (1979), Production and Use of High Transient Magnetic Field-II, Review of Scientific Instruments 28(11):7768-7770,

[180] Kulkarni, M.R., Kolge, T., Kumar, D. et al. (2022), Magnetic Pulse Welding of D9 Steel Tube to SS316LN End Plug. Trans Indian Inst Met 75, 171–182, https://doi.org/10.1007/s12666-021-02413-4

[181] G. Abrahamson, (1960), J. Appl. Mech. Trans. ASME 28 (4), 519–528,

https://doi.org/10.1115/1.3641777.

[182] A. Bahrani, T. Black, B. Crossland, (1967), The mechanics of wave formation in explosive welding, Proc. R. Soc. Lond. A 296 (1445), 123–136.

[183] J. Hunt, (1968), Philos. Mag. 17 (148) 669–680, https://doi.org/10.1080/14786436808223020.

[184] G. Cowan, O. Bergmann, A. Holtzman, Metall. Mater. Trans. B 2 (11) (1971) 3145–3155, https://doi.org/10.1007/BF02814967.

[185] J. Robinson, Philos. Mag. 31 (3) (1975) 587–597, https://doi.org/10.1080/14786437508226540.

[186] 51. D. Hay, (1979), Explosive welding: applications and techniques, High-Pressure Science and Technology, Springer, 1813–1836.

[187] Wu, X., Shuai, J., Shan, K., Xu, K., Di, Y., (2020), Hydraulic Burst Test of X52 Pipes with Defects or Nozzle Repair Structure, ASME Journal of Pressure Vessel Technology, 142(5): 054505, https://doi.org/10.1115/1.4047562

[188] Bahrani, A. S., Black, T. J., Crossland, B., (1967), The Mechanics of Wave Formation in Explosive Welding, Proceedings of the Royal Society A: Mathematical, Physical, Engineering Sciences 296, 1445, 123-136.

[189] Victor S., Blakely, M., (2008), Benefits of the Magnetic Pulse Process for Welding Dissimilar Metals, Welding Journal 87 (9), 56-59.